Investigation des Interactions Toxine-Cellule et du Confinement des Récepteurs dans la Membrane Cellulaire

Maximilian U. Richly

Maximilian U. Richly

Doctoral Thesis

Investigation of Toxin-Cell Interactions and Receptor Confinement in the Cell Membrane

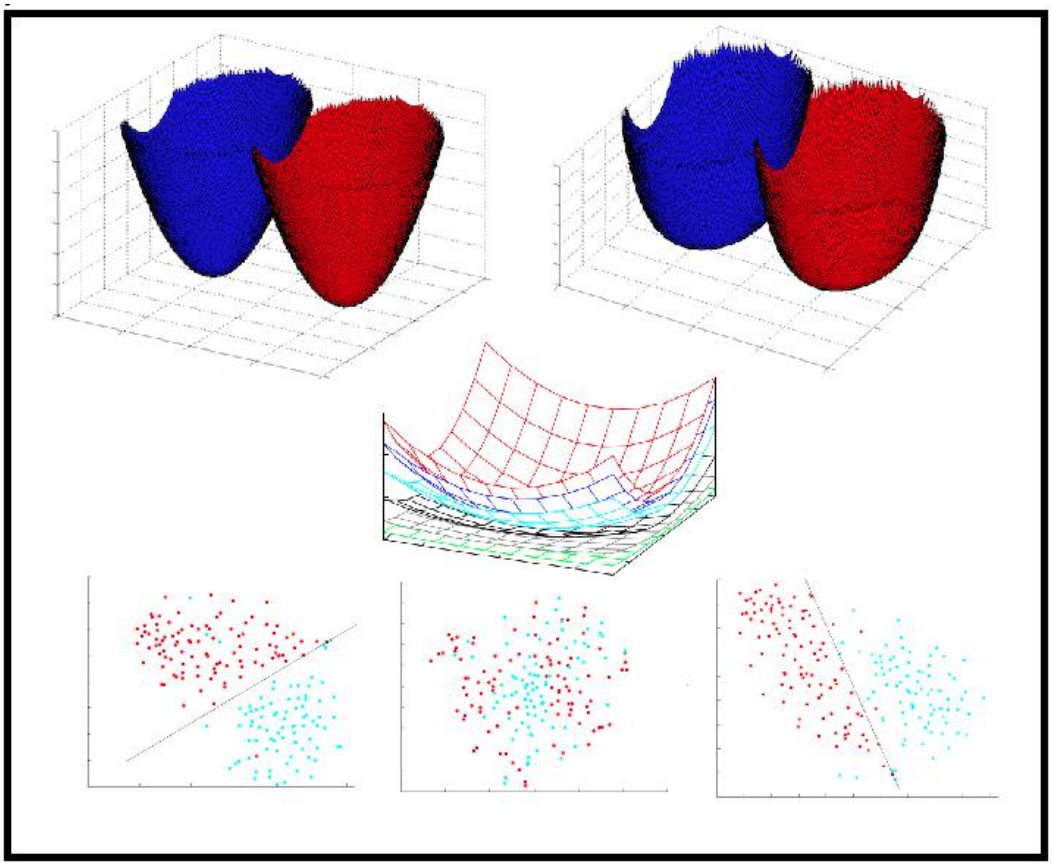

LABORATOIRE D'OPTIQUE ET BIOSCIENCES
ECOLE POLYTECHNIQUE

Ecole Polytechnique

Doctoral Thesis

Physics

Investigation of Toxin-Cell Interactions and Receptor Confinement in the Cell Membrane

Author:
Maximilian U. Richly

LABORATOIRE D'OPTIQUE ET BIOSCIENCES
Ecole Polytechnique, CNRS UMR7645, INSERM U1182

Defense on March 26, 2015

Jury Members

Patricia Bassereau	President
Laurence Salomé	Reviewer
Olivier Thoumine	Reviewer
Henri-Jean Drouhin	Examinator
Didier Hilaire	Examinator, DGA Representative
Didier Marguet	Examinator
Michel Popoff	Examinator
Antigoni Alexandrou	Thesis Advisor

"All life is an experiment. The more experiments you make the better."

Ralph Waldo Emerson

Acknowledgements

A physics thesis is not written in isolation, and this thesis in particular has only been possible thanks to the contribution of countless people during the past three years, and for some even longer than that. To anyone that has directly or indirectly helped me along the way, I address my deepest gratitude. This is as much your work as it is mine. Although I cannot thank everyone by name, since that list is far too long to fit on this page, I would like to mention some people in particular.

I am grateful to the reviewers Laurence Salomé and Olivier Thoumine, the president Patricia Bassereau, and the examiners Henri-Jean Drouhin, Didier Hilaire, Didier Marguet, and Michel Popoff who all graciously accepted to be part of my jury. Having written the thesis, I can imagine the non-negligible work constituting a review of my manuscript.

My eternal gratitude also goes to my wonderful advisor Antigoni for all she has done for me, and especially for fighting to bring me to Polytechnique in the first place, and being a mentor to me for the past three years. On that note, I also thank Jean-Louis Martin for helping Antigoni make my arrival at the Laboratoire d'Optique et Biosciences possible. Without their trust in me, I would not have obtained the funding for my thesis generously provided by the Direction Générale de l'Armement and the Triangle de la Physique.

I sincerely thank all the collaborators from other research groups that shared the journey of investigative research with us. Chloé Connan, Marie Voillequin, Serge Pauillac and Michel Popoff for discussing research goals and supplying me with toxins and cells, especially when the occasional fungal contamination decimated my cell cultures. Jean-Marc Allain without whom the beautiful experiments on cells in microfluidic flow would not have been possible. I would also like to thank Antoine Le Gall, Nicolas Fiszman, Nathalie Westbrook, and Karen Perronet, with whom I was fortunate enough to publish my first paper as a first author, and also Flavie Gillant for continuing this collaboration with her work. I also thank Thierry Gacoin and Jean-Pierre Boilot for providing access to their laboratory and the know-how, and the means to produce the nanoparticles I have used throughout this work. A big thank you also to Denis Grebenkov for agreeing to be my tutor. Furthermore, I would like to mention Mohamed El Beheiry, who programmed the latest version of the Bayesian inference algorithm and allowed me to use it. Without it, chapter 5 would look a lot different.

A special thank-you I reserve for Silvan, whose work I continued and who tirelessly worked with me during my first year to get me up to speed. Special recognition also goes out to Jean-Baptiste for his extensive contribution on the work we did on Bayesian inference and hopping energies, for his crucial guidance on data clustering and classification, and for the numerous inspiring discussions, both scientific and recreational.

A big thank you is to the people in my research group that have accompanied and guided me throughout the last three years. I would particularly like to thank Cédric Bouzigues for all the valuable insights and hands-on discussions. Paul, Cédrik-Roland, Markus, Rachid, Rivo, Mouna, and Chao, who, without fail, would always be there to help or

motivate when the going got tough. I am also immensely thankful to Amanda and Dana, Laurène, and Jean and Solène with whom I had a lot of fun working on projects that are, unfortunately, not represented in this thesis.

My gratitude also goes out to my fellow graduate students that have come on this adventure alongside me. The ones I saw finish before me: Guillaume, Ivan, Pierre, Laura, Thibault, Stéphane, Lucille, and Laura, who all told me the journey is worth it. The ones who are yet to reach their destination: Marianne, Nelly, Kamel, Floriane, Lamiae, Claire, Marco, Olga, and Pierre, to whom I in turn say the journey is worth it. And the post-PhD in-betweeners: Max, Guillaume, Vincent, Guy, and Julien, who, like me, know it is worth it.

I also thank everyone with whom I shared my time at the LOB, for making this laboratory such an incredible place to work in, and anyone I may have forgotten to mention. My memory fails me more often than I would like to admit.

Finally, thank you to my family and friends. You know who you are.

Contents

List of Figures

List of Tables

Abbreviations

ACh	**A**cetyl**ch**oline
AIC	**A**kaike **I**nformation **C**riterion
AICc	**A**kaike **I**nformation **C**riterion **c**orrected
AFM	**A**tomic **F**orce **M**icroscope
AOD	**A**cousto-**O**ptical **D**eflector
APTES	(3-**A**mino**p**ropyl)Tri**e**thoxy**s**ilane
ATP	**A**denosine **Tri**p**h**osphate
AVE	**A**verage **V**alue **E**stimator
BFGS	**B**royden-**F**letcher-**G**oldfarb-**S**hanno
BI	**B**ayesian **I**nference
BIC	**B**ayesian **I**nformation **C**riterion
BIDT	**B**ayesian **I**nference **D**ecision **T**ree
BoNT	**Bo**tulinum **N**euro**t**oxin
CFTR	**C**ystic **F**ibrosis **T**ransmembrane conductance **R**egulator
CHOx	**Ch**olesterol **Ox**idase
CM	**C**ulture **M**edium
CPϵT	***C**lostridium **P**erfringens* **E**psilon **T**oxin
CSαT	***C**lostridium **S**epticum* **A**lpha **T**oxin
DHM	**D**igital **H**olographic **M**icroscope
DLS	**D**ynamic **L**ight **S**cattering
DMPE	**D**i**m**yristoyl-sn-glycero-3-**p**hospho**e**thanolamine
DOF	**D**epth-**o**f-**F**ield
DOPE	L-α-**dio**leoyl**p**hosphatidyl**e**thanolamine
DRM	**D**etergent **R**esistant **M**embrane
EGFR	**E**pidermal **G**rowth **F**actor **R**eceptor

EM-CCD	**E**lectron **M**ultiplying **C**harge-**C**oupled **D**evice
FCS	**F**luorescence **C**orrelation **S**pectroscopy
FLIM	**F**luorescence-**L**ifetime **Im**aging
FPT	**F**irst **P**assage **T**ime
FRAP	**F**luorescence **R**ecovery **A**fter **P**hotobleaching
FRSK	**F**etal **R**at **S**kin **K**eratinocytes
FWHM	**F**ull-**W**idth-at-**H**alf-**M**aximum
GFP	**G**reen **F**luorescent **P**rotein
GPI	**G**lyco**p**hosphatidyl**i**nositol
HASM	**H**uman **A**rtery **S**mooth **M**uscle
HC	**H**eavy **C**hain
LatB	**Lat**runculin **B**
LC	**L**ight **C**hain
LFA	**L**ymphocyte **F**unction-associated **A**ntigen
LOB	**L**aboratoire d'**O**ptique et **B**iosciences
MD	**M**olecular **D**ynamics
MDCK	**M**adin-**D**arby **C**anine **K**idney
MM	**M**inimal **M**edium
MME	**M**ean **M**aximal **E**xcursion
MSD	**M**ean **S**quared **D**isplacement
NAP	**N**eurotoxin-**A**ssociated **P**rotein
NP	**N**ano**p**article
NRK	**N**ormal **R**at **K**idney
NTNHA	**N**on**t**oxic **N**on-**H**em**a**gglutinin
OM	**O**bservation **M**edium
PCA	**P**rinciple **C**omponent **A**nalysis
PDF	**P**robability **D**ensity **F**unction
PFT	**P**ore **F**orming **T**oxins
PSD	**P**osition **S**ensing **D**etector
PSF	**P**oint **S**pread **F**unction
PV	**P**article **V**elocimetry
QD	**Q**uantum **D**ots
QPD	**Q**uadrant **P**hoto**d**iode

SEM	**S**canning **E**lectron **M**icroscope
SMase	**S**phingo**m**yelin**ase**
SNR	**S**ignal-to-**N**oise **R**atio
SPT	**S**ingle-**P**article **T**racking
STED	**ST**imulated **E**mission **D**epletion
STORM	**ST**ochastic **O**ptical **R**econstruction **M**icroscopy
syt	**Sy**napto**t**agmin
TCR	**T**-**c**ell antigen **r**eceptor
TEM	**T**ransmission **E**lectron **M**icroscope
TKR	**T**yrosine **K**inase **R**eceptor
TM	**T**rans**m**embrane
t-SNE	**t**-distributed **S**tochastic **N**eighbor **E**mbedding
YFP	**Y**ellow **F**luorescent **P**rotein

To my parents, who succeeded in the impossible task of raising me, for their endless support.

Preface

Biophysics as an independent research field is quite young, the term *"Biophysics"* itself only having been coined in 1892 by Karl Pearson in his book *The Grammar of Science* [1]. Craig Venter, heading one of the first two groups to sequence the human genome [2], declared *"If the 20th century was the century of physics, the 21st century will be the century of biology."* [3]. However, it will not be biology alone, but, more importantly, the disciplines that lie at the interface of biology and all other sciences. A prediction that places biophysics at the heart of many amazing new discoveries that this century has yet to produce.

The study of how toxins and proteins in general interact with cells is one of the fields requiring an interdisciplinary approach. This interaction happens first and foremost at the membrane of the cell. Almost like the "brain" of the cell, the membrane detects external stimuli and triggers the cascade of events that eventually lead to a response from the cell. As such, its importance the cell's life and behavior cannot be overstated.

This thesis reflects this multidisciplinary approach and applies it to studying the dynamics of toxin-cell interactions and is a continuation of previous work done by Silvan Türkcan in his thesis *Investigation of the Cell Membrane Architechture by Single-Molecule Tracking of Peptidic Toxins*, in which he demonstrated the confinement of the ϵ- and α-toxin receptors, the toxins being produced by *Clostridium perfringens* and *Clostridium septicum*, respectively, in lipid raft domains on MDCK cells. Here, we pick up where this previous work left off, expand on the nature of receptor confinement by investigating more closely the receptor dynamics while destabilizing the domains and by applying an external force to the system. Additionally, the shape of the confinement potentials experienced by raft receptors in the domain, extracted using the novel analysis tool of Bayesian inference, is compared to that experienced by non-raft receptors to gain a deeper understanding of the nature of the confinement. Furthermore, the field of application of the Bayesian inference algorithm used to analyse the observed trajectories is broadened to include optical trap calibration, further validating this new application of Bayesian inference. Finally, the technique of single particle tracking in two dimensions on the cell membrane is extended to track in three dimensions, and used to visualize the trajectory of botulinum toxin into intestinal epithelial cells.

Several collaborations made this work possible. These include working with Jean-Baptiste Masson at the Physics of Biological Systems Unit at the Institut Pasteur and Mohamed El Beheiry at the Laboratoire Physico-Chimie at the Institut Curie on

analysing data, and implementing the inference algorithm. The hopping, raft destabilization, and clustering analyses were also conducted in collaboration with Jean-Baptiste Masson. The work on calibrating optical tweezers was done in collaboration with Karen Perronet and Nathalie Westbrook at the Laboratoire Charles Fabry at the Institut d'Optique. Antoine Le Gall and Nicolas Fiszman were the graduate students who obtained the optical tweezers data. Cells and toxins were provided by Michel Popoff at the Institut Pasteur along with the insight on which aspects of toxin dynamics are the most interesting to explore. The nanoparticles were synthesised in collaboration with Thierry Gacoin and Jean-Pierre Boilot at the Laboratoire de Physique de la Matière Condensée at Ecole Polytechnique. The work done using hydrodynamic flow on cells was done with the help of Cédric Bouzigues and in collaboration with Jean-Marc Allain at the Laboratoire de Mécanique des Solides at Ecole Polytechnique.

The aim of this work is to extend the scope of previously used techniques to explore the diversity of environments experienced by receptors targeted by toxins and proteins to interact with the cell.

- Chapter 1 introduces the cell membrane, the current models for membrane compartmentalisation and the techniques used to investigate the membrane.
- Chapter 2 introduces the experimental setup, equipment and methods used in this work.
- Chapter 3 proposes and discusses the use of the Bayesian inference algorithm as a new method for calibrating optical traps.
- Chapter 4 investigates the dynamics of toxin receptors in lipid rafts, by destabilizing domains, applying a hydrodynamic force, and observing hopping events.
- Chapter 5 compares the confinement potential of raft and non-raft proteins.
- Chapter 6 uses three-dimensional single-particle tracking to observe the action of botulinum toxin on intestinal epithelial cells.
- Chapter 7 provides a summary of the work and a discussion of possible future work in this field.

Chapter 1

Cellular Membrane Structure

Biology is the study of complicated things that have the appearance of having been designed with a purpose.

Richard Dawkins

Contents

1.1 The Cell Membrane

All cells possess a barrier that separates them from the outside world. This barrier is called the cell membrane or plasma membrane, without which cells and life itself would

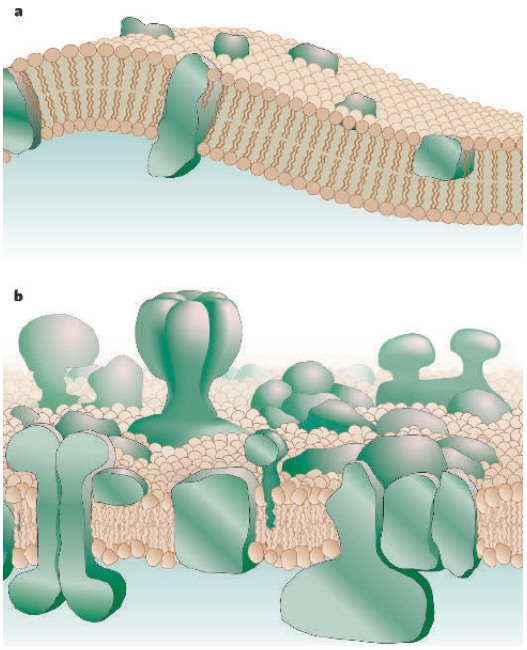

Figure 1.1: Fluid mosaic model vs. present plasma membrane model. (a) shows the plasma membrane according to the 1972 fluid mosaic model of Singer and Nicolson. (b) shows the present view of the plasma membrane, where proteins are significantly more crowded and densely clustered. Figure reproduced from [6].

be impossible. According to Singer and Nicolson [4], who proposed the Fluid Mosaic Model in 1972, the membrane is a sea of lipids that allows the proteins to diffuse freely within it. A similar model to relate diffusion coefficients in the cell membrane and size of membrane proteins, resulted from the work of Philip Saffman and Max Delbrück [5]. This model views the lipid membrane as a layer of viscous fluid within a less viscous bulk liquid. However, although the membrane does act like a two dimensional plane in which proteins can move, there are a number of different structures that act as obstacles to a diffusing protein and provide some in-membrane compartmentalisation. These are described in more detail in section 1.3. Some of these models are still under close scrutiny and the subject of controversy. What we can be certain of, however, is that the membrane is far more densely crowded with proteins than supposed by Singer and Nicolson [6]. Figure 1.1 shows a comparison between the initially assumed and presently accepted protein prevalence within the plasma membrane.

1.1.1 Structure and Composition

Cells produce around 500 to 1000 different lipids, which constitute approximately half of the mass of the cell membrane. The lipids form a bilayer approximately 5 nm thick providing an environment for lateral movement of membrane proteins, as well as an interface for transport and communication between the cell exterior and interior. There are estimated to be around one million lipids in one square micrometer of cell membrane and one billion in an entire cell. Among all these lipids, are specialized proteins floating in the two-dimensional plane that is the membrane. This section will detail and elaborate

on the components that make up this mini universe and their contribution to the plasma membrane structure.

1.1.1.1 Lipids

Lipids contribute to roughly 50% of the cell membrane in terms of mass [7]. They are amphiphilic, meaning that they have a hydrophilic and a hydrophobic end. This provides them with the ability to spontaneously form bilayers in water. The hydrophilic polar head of the lipids prefers contact to water, whereas the hydrophobic tail groups, being non-polar, experience unfavourable interactions with the surrounding H_2O. The energetically preferred configuration is, therefore, a structure of lipid molecules with the head group facing the water, and the tail groups at the interior of the structure.

Phospholipids are the most common type of lipids found in the plasma membrane. Among these are phosphatidylcholine, phosphatidylethanolamine, phosphatidylserine, phosphatidylinositol and phosphatidic acid. Lecithin was the first phospholipid to be discovered in 1847 by Theodore Nicolas Gobley. Phospholipids are characterised by a polar head group attached to two non-polar hydrocarbon tails. One of the tails is saturated, whilst the second has a *cis*-double bond and is unsaturated. This structural characteristic of the tail groups makes it more difficult for the phospholipids to pack together. The layer itself is, therefore, harder to freeze and thinner. Regions with mainly unsaturated lipids form in model membranes a, so called, liquid-disordered phase [8, 9]. This effect is graphically depicted in figure 1.2.

Sphingolipids, first discovered in brain extracts in the 1870s, have saturated tails. These allow them to assemble more tightly and produce taller and more packed membrane environments. Biophysicists call this type of lipid configuration in model membranes a solid-like liquid-ordered phase [7, 10]. Model membrane regions that have saturated lipids as major components form these gel-like environments. The major sphingolipids are sphingomyelin and glycosphingolipids.

Sterols are the third major constituent of cell membranes. Although these do not form bilayers independently, they will, when mixed with other bilayer-forming lipids, produce a liquid-ordered state in model membranes. The most prominent of the sterols is cholesterol, which consists of a rigid ring structure, a polar hydroxyl group and a short non-polar hydrocarbon chain. Cholesterol inserts itself in the lipid bilayer in line with the other lipids, the hydroxyl group acting as the head. The presence of cholesterol reinforces the structural integrity of the membrane. It renders the membrane less permeable and modulates membrane packing thereby controlling membrane fluidity. It also enhances membrane rigidity by maximising the contact between its cholesterol ring and the adjacent hydrocarbon chain, thereby restraining the hydrocarbon chain from motion.

The lipids themselves also experience diffusion throughout the membrane. The diffusion coefficient of the lipid 1-palmitoyl-2-oleoyl-sn-glycero-3 phosphocholine was measured by Gaede and colleagues in multilamellar liposomes, and found to be of the order of

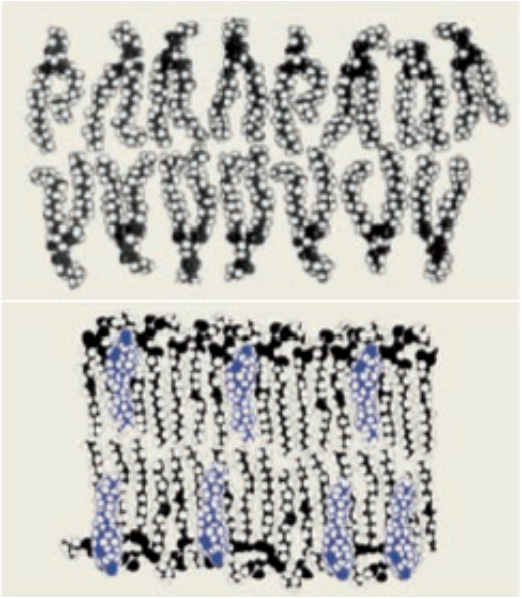

Figure 1.2: Liquid unordered vs. liquid ordered membrane phases. A schematic of lipid configurations in membranes. The top bilayer is composed of glycerophospholipids with unsaturated hydrocarbon chains producing a liquid-disordered phase. The bottom bilayer has a significant sterol and sphingolipid component, forming a more rigid liquid-ordered phase. Figure reproduced from [7].

1 $\mu m^2/s$ [11]. Similar values for lipids were obtained in studies using single particle tracking (SPT) and fluorescence recovery after photobleaching (FRAP) techniques [12].

By extensively studying model membranes containing different classes of lipids, biophysicists have identified these regions of liquid order and liquid disorder (see figure 1.2). When adding mixtures of phosphoglycerolipids, glycosphingolipids, and sterols, the two latter have been found to spontaneously form domains of higher order [8, 9]. The size of these clusters ranges from nanometres to micrometres [13, 14].

1.1.1.2 Membrane Proteins

Lipids provide the building blocks and structure of the cell membrane. It is, however, mainly the proteins that reside within the membrane that provide the functionality. Depending on the type and species of the cell, the relative amount of proteins that make up the cell membrane can range from 25% to 75% in terms of mass. For a membrane with a protein composition of about 50%, there are about 50 lipids per protein.

The proteins fall into different classes depending on how they are anchored in or to the membrane. **Transmembrane proteins** stretch across the boundary. Like lipids, they are amphiphlic with hydrophilic regions exposed to the water and hydrophobic regions that pass through the bilayer. Receptors, for example, that bind signalling molecules and transmit the signal across the membrane to the cell interior are transmembrane proteins. This functional asymmetry is reflected in the orientational asymmetry of the protein within the bilayer. Among the exposed hydrophilic groups of the protein,

there will always be a cytosolic area and non-cytosolic area, that are separated by the hydrophobic connector region.

For most transmembrane proteins, the membrane-traversing region is composed of α-helical polypeptide chains. Depending on how many there are, the protein can either be a single-pass or a multi-pass protein. In single-pass proteins, the polypeptide chain crosses the membrane once, whereas in multi-pass transmembrane proteins the polypeptide chain crosses multiple times. Transmembrane proteins can also rely on a β-barrel structure instead of α-helices to traverse the membrane.

Other types of cell membrane proteins include proteins that are embedded in just one of the two lipid layers of the membrane, either in the inner or outer leaflet. These can be anchored either via an amphiphilic α-helix, via a covalently attached lipid chain, or via a **glycosylphosphatidylinositol (GPI) anchor**. Receptors attached via GPI anchors can be recognised by adding phospholipase C, which cleaves these anchors and releases the proteins.

Lastly, proteins can also be attached to the cell membrane simply by association with other proteins already attached. Their structures do not extend into the interior of the membrane. Instead they attach to anchored proteins via non-covalent bonds. These proteins are know as **peripheral membrane proteins**, whereas the ones directly anchored are known as **integral membrane proteins**.

The dynamics of membrane proteins are multifold. Moving in the membrane, some have a tendency to assemble into larger complexes. An example of one of these complexes is the photosynthetic reaction center of the bacterium *Rhodopseudomonas viridis*, which Deisenhofer and colleagues found to consist of four subunits, each having five α-helices, and a cytochrome [15].

As mentioned above, we know that the model of membrane proteins diffusing freely is over-simplified, however, proteins do undergo two-dimensional diffusion within the membrane. Firstly, proteins experience rotational diffusion by spinning around their membrane-perpendicular axis [16]. Additionally, proteins diffuse laterally in the membrane. The first observation of lateral diffusion was reported in 1970, when Frye and Edidin observed the movement of fluorescently labelled surface antigens [17]. In their experiment, they artificially fused mouse cells and human cells, and observed how the differently labelled human and mouse antigens diffused across the entire hybrid cells. Lateral diffusion rates can easily be measured using ensemble measuring techniques like FRAP explained in section 1.5.1.2. However, ensemble measurements are disadvantaged when investigating the factors affecting diffusion. Using single particle tracking (explained in section 2.1), the movement of a single molecule can be observed, and structures or obstacles influencing its motion, detected.

The lateral diffusion that membrane proteins experience is influenced by the cell's ability to confine these in certain areas in its membrane bilayer. A more detailed account of confinement domains is given in section 1.3, yet, proteins can also be assigned to general parts on the cell surface. Intestinal epithelial cells, for instance, maintain an asymmetric distribution of certain plasma membrane proteins on their surface. The so-called tight

junctions prevent the diffusion of these proteins from the apical membrane to the basal and lateral membranes and vice-versa. Likewise, the asymmetric lipid distribution on the sides of the tight junction is actively maintained, resulting in a similarly uneven lipid organisation. This region assignment can also be achieved in the absence of a tight junction. Sperm cells of mammals, for example, have been shown to have at least three distinct antigen regions on their surface [18].

1.1.2 Function

The cell membrane performs numerous tasks. As the barrier between the cell's inner workings and the surroundings it is responsible for the transport of materials and information across the border. **Transport of material** is achieved via movement into the cell by diffusion, active transport or endocytosis. **Transport of information** is achieved by receptors binding signalling molecules and passing the information on by triggering signaling pathways in the cell.

The plasma membrane displays different permeabilities depending on the molecule in question. Main factors dictating the rate of **diffusion** are the molecule's size and its solubility in oil. The smaller and more hydrophobic it is, the quicker it will diffuse across the membrane. Charged molecules, on the other hand, consistently experience a much higher resistance to diffusion across the membrane with respect to uncharged molecules.

Ions and other polar molecules, therefore, need to be introduced into the cell via **active transport**. Specialized transmembrane proteins move such solutes across the membrane. These transport proteins specialise in the transport of one type of molecule (ions, sugars, amino acids). Mutations in the genes coding for a certain transport protein can prevent the cells from performing active transport of the respective molecules, and can cause serious medical consequences. Transport proteins fall into two main classes: transporters and channels. Transporters actively bind target agents and, via a series of conformational changes, moves these agents across. Channels on the other hand act as controllable pores allowing certain solutes to pass.

Endocytosis is the process by which cells take up macromolecules. Different pathways exist for performing endocytosis. Phagocytosis is used to ingest large particles. This process is mainly used by specialised cells like macrophages and neutrophils that internalise infectious agents and cells that have undergone apoptosis for subsequent digestion. In order to selectively gather target molecules, endocytosis can be receptor-mediated. This allows the cell to uptake even solutes only present at low concentrations. In contrast to receptor-mediated endocytosis, pinocytosis is an untriggered, continuous ingestion of external fluids. The cell dedicates about 3% of its membrane every minute to this form of endocytosis. Like receptor-mediated endocytosis, this process starts at clathrin-coated pits that spontaneously form and, once assembled, rapidly invaginate into the cell and form clathrin-coated vesicles. Additionally, there are other, less well understood, mechanisms of endocytosis. One of these is facilitated by caveolae. These are thought to form lipid rafts and contain the protein caveolin as a major structural component.

Using electron microscopy, these can be seen as flask-shaped pits and domains of varying curvature in the cell membrane [19].

Cellular signalling is the process by which cells emit and detect external signals. Detecting extracellular signals takes place through the binding of a signal molecule to its respective receptor on the membrane, which subsequently becomes active and triggers a signaling pathway in the cell interior. An example of these is the tyrosine kinase receptor (TKR), which is activated by binding growth factor ligands. This induces receptor dimerization and triggers the intracellular signaling pathway. The development of certain types of cancer has been linked to TKR over-activity, triggering the development of cancer-treating drugs inhibiting TKR action [20]. Another example are G-protein coupled receptors, which represent the largest family of membrane proteins. This includes receptors like rhodopsin, a light sensitive protein in the retina of the eye, essential for the process of phototransduction [21]. In section 1.1.1.1, we mentioned that lipids are the major constituents of the membrane. Furthermore, the lipid distribution between the two monolayers of the membrane can be highly differentiated. Consider human red blood cells. These show a high concentration of phosphatidylcholine and sphingomyelin in the outer layer, and phosphatidylethanolamine and phosphatidylserine in the inner monolayers. The phosphatidylserine is negatively charged, producing a charge difference between the two leaflets of the bilayer. This structural detail turns out to be highly important for cellular signalling. *Protein kinase C*, for example, uses this negative charge to bind to the inner leaflet of the membrane as a response to an extracellular signal.

1.2 Cytoskeleton

The cytoskeleton, that spans the interior of the cell, enables the cell to maintain its structure. It is a network of actin filaments, intermediary filaments and microtubules that extend throughout the entire cell. The cytoskeleton is dynamic, constantly in flux, moving, disintegrating and rebuilding. It provides cells with the means to withstand external stress, maintain their shape and in conjunction with the extracellular matrix provides structure to entire organs.

The cytoskeleton *per se* is not part of the plasma membrane. But as it lies directly beneath the membrane it can influence the motion and behaviour of receptors. One example how this is achieved is the picket and fence model of membrane protein confinement described in section 1.3.2.

The actin protein that constitutes the actin filament network exists as a free monomer (G-actin), and as part of microfilaments (F-actin). Actin filaments are perpetually undergoing polymerization and depolymerization. Different agents can be used to promote one or the other. The Arp2/3 complex is one of the nucleating factors that can stimulated actin filament production. It binds to already existing filaments from which new actin can then branch out. Latrunculin, on the other hand, binds monomers and prevents them from polymerizing, and can be used to disrupt the cytoskeleton. We make use of this in chapter 4, to investigate receptor confinement dependence on actin.

Microtubules are formed by the dimerization of the two globular proteins α-tubulin and β-tubulin. Microtubules have a distinct polarity. Since their polymerization proceeds via the addition of dimers, one end of the microtubule will always have the α-subunits exposed, while the other end will always have the β-subunits exposed. These ends are designated as the + and - ends of the microtubule, and serve critical biological funtions. Certain motor proteins, for example, will only move along one direction on the microtubules. Tubulin inhibitors can be used to induce microtubule depolymerization.

Whist the protein composition of the cytoskeleton is mostly identical for all eukaryotic cells, the function and behaviour can differ dramatically depending on species and specialisation of the cell. A prime example of this are muscles cells. During muscle contraction each muscle cell performs an individual contraction, via an army of myosin motors that pull along parallel actin filaments within the cell.

A recent example that beautifully showcases the dynamic behaviour of the cytoskeleton is demonstrated in work done by Jennifer Schwartz-Lippincott and colleagues [22]. They showed spectacular dynamic movement of the actin filament network at the protruding edge of the cell during cell migration across a surface. This study found that the actin, located at the very extreme of the cell during cell propagation, retreats towards a more densely packed actin region just behind the advancing edge of the cell.

The cytoskeletal strands also double as highways for motor proteins transporting cargo from one part of the cell to another. The dynein and kinesin motor proteins, for example, walk along microtubules transporting large cargo like vesicles within the cell. Dynein walks along microtubules towards the minus-end, whereas kinesin moves towards the plus-end. These proteins have been under close scrutiny. A debate over the walking mechanism of kinesin, for example, in which the proposed mechanisms were termed "hand-over-hand" movement and "inchworm" movemement has been resolved to be the former [23, 24]. Moreover, a study investigating the binding and dissociation of kinesin from its microtubule demonstrated that the structural change driving the motion of the motor is triggered by ATP hydrolysis, and not ATP binding [25]. Active transport within the cell is the assumed model for the process we wish to observe using 3D single particle tracking in chapter 6.

1.3 Confinement Models

By observing the diffusion rate of receptors within the membrane, it has been shown that, even taking crowding effects due to the sheer number of proteins into account, the long-term diffusion rate is lower than expected [26]. The logical conclusion is that there are other factors influencing the movement of these receptors. Single-particle tracking techniques (discussed in more detail in section 2.1) have emerged as one of the best ways to study the nature of these additional factors. Using SPT, researchers have discovered that individual proteins diffusing in the membrane experience permanent and transient confinement, and several models have been proposed to explain these phenomena [27] .

1.3.1 Lipid Rafts

In section 1.1.1.1 we talked about the variety of the lipid content in membranes. The difference in their physico-chemical properties gives rise to lipid heterogeneities in the membrane. In live cells, certain types of proteins have been found to reside in detergent resistant parts of the membrane (DRM), termed this way due to their resistance to Triton X-100 [28]. However, more recently the idea of DRMs has been challenged and lipid rafts are, consequently, no longer strictly associated with them. For one, treatment with Triton X-100 has been shown to alter the lipid composition of the domains [29].

The field of lipid rafts is still widely contested and no absolute consensus exists on what constitutes a lipid raft and what not. The points of debate include the size of the domains, the exact lipid composition, and their formation process. Proposed sizes range from small clusters of <20 nm [30, 31] to large raft platforms spanning several hundred nm [32]. Furthermore, the existence of lipid rafts in live cell membranes is also a matter of discussion. This is largely due to the differences observed when comparing model membranes and cellular membranes. In model membranes, transmembrane proteins seem to be excluded from the lipid ordered rafts [33], whereas they can be found in lipid rafts in live cells [34]. There also seems to be a difference between the lipid composition of lipid rafts certain types of membrane proteins prefer [35]. Additionally, the process by which lipid rafts are formed is debated. Do protein clusters assemble the relevant lipids around themselves, or are the assembled lipids recruiting the proteins? In the first case, the term protein-lipid composites would be the preferred term. One may consider this to be a question of semantics, along the lines of the chicken and the egg dilemma, and will, henceforth, refer to the lipid-dependent confinements we observe as lipid rafts.

Lipid rafts display a high concentration of glycosphingolipids. It has been shown that these domains have three to five times the level of cholesterol found in the surrounding membrane. Likewise, sphingolipids like sphingomyelin have a 30% higher prevalence [36]. Lipid rafts in model membranes have been shown to be liquid-ordered domains that are thicker and more tightly packed than the rest of the cell membrane, for reasons detailed in section 1.1.1.1. Lipid-ordered rafts diffuse freely in liquid-disordered state lipids [37].

Certain types of membrane proteins tend to reside in these domains, particularly receptors responsible for signal transduction at the cellular level. Examples include GPI anchored proteins (section 1.1.1.2) [38], cholesterol binding proteins such as caveolins [39], and phospholipid-binding proteins such as annexins [40]. Receptors as well as lipids have the ability to move into and out of the domain depending on the respective partitioning kinetics.

Lipid rafts also play an important role in signal transduction and cell signalling. By harbouring different proteins and changing their composition in response to intra- and extracellular stimuli they can influence specific protein interactions triggering certain signalling pathways [41]. The T-cell receptor, the high-affinity IgE receptor and the B-cell receptor have been shown to migrate to lipid rafts upon crosslinking [42]. Examples of signalling pathways triggered at lipid rafts include the T-cell antigen receptor (TCR)

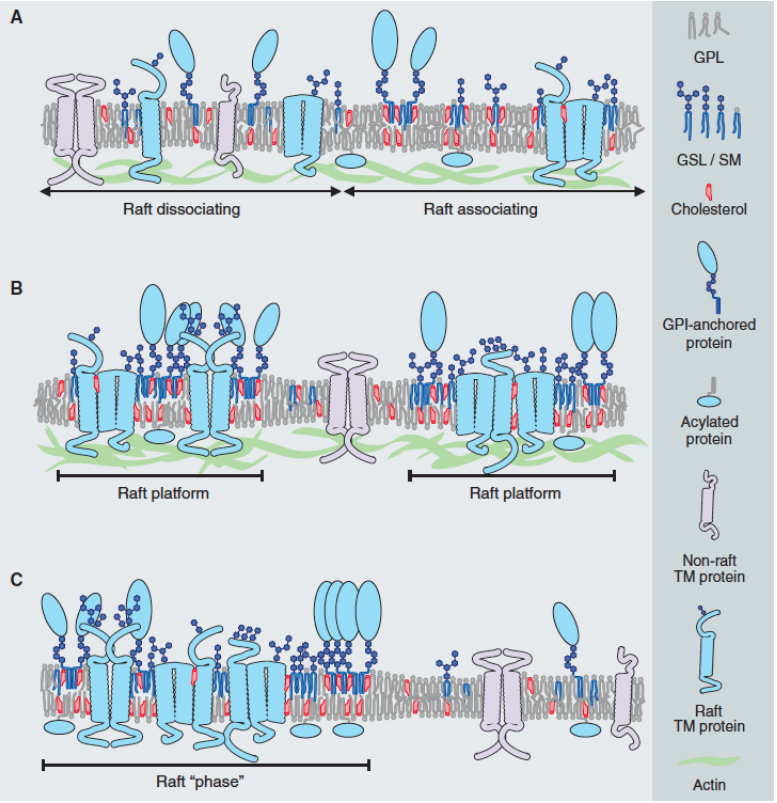

Figure 1.3: Conceptual cartoon of lipid rafts. (A) shows spatially fluctuating distributions of sterol and sphingolipid concentrations provoking assembly of certain lycosylphosphatidylinositol (GPI)-anchored and transmembrane (TM) proteins. Formed rafts in (B) have a visibly higher proportion of sterols and sphingolipids as compared to the lipid composition outside the raft. Lateral heterogenity is accentuated by the difference in membrane thickness. Some transmembrane proteins also have the potential to interact with cellular actin. (C) shows a formed and stable raft that fully contributes to protein sorting within the membrane. Figure reproduced from [45].

signalling [43, 44]. TCR is a lipid raft associated multisubunit immune recognition receptor. The receptor requires accessory molecules and assisting proteins to form an immunological synapse and activate. The fact that these are all found in lipid rafts facilitates this task.

Work by Parton and Richards [46] has revealed that lipid rafts and caveolae play a role in endocytosis (section 1.1.2). They also showed that GPI-anchored proteins translocate to caveolae, which are formed from lipid rafts via the polymerization of caveolins, and undergo endocytosis. This pathway seems to also be exploited by certain viruses and toxins. Cholera toxin, for example, has been shown to take advantage of this path [47]. When subsequently depleting the membrane of cholesterol, the cholera toxin finds other paths to enter the cell [48], suggesting a strong cholesterol dependence.

1.3.2 Picket-and-fence Model

The picket-and-fence model is strongly supported by work by Kusumi and coworkers and suggests that some types of compartmentalisation occurring in the plasma membrane is produced by underlying cytoskeletal filaments [49]. The cytoplasmic domain of transmembrane proteins experiences a steric interaction with the actin meshwork that underlies the plasma membrane. These filaments act as "fences" to confine the motion into corrals and are located just below the membrane in the cytosol. This meshwork produces transient confinement of membrane proteins, which experience a type of motion that has been termed "hop diffusion" [50]. The temporary confinement of the protein, followed by occasional movement to adjacent corrals resembles a hopping movement from corral to corral.

Lipids in the outer monolayer of the membrane have been observed to move in a similar fashion. Fujiwara et al. observed single L-α-dioleoylphosphatidylethanolamine (DOPE) in NRK cells [51]. During these experiments, DOPE was seen to mimic the compartmentalized structure, even though it never transfers to the inner monolayer. Similarly to previously outlined experiments, addition of actin modifying drugs affected DOPE in a similar fashion, whereas modification of the extracellular matrix and its associated proteins does not change DOPE's dynamics. These observations lead to a modification of the "fence" model to include transmembrane proteins anchored to the actin fences and acting as pickets in the membrane. These closely reflect the underlying structure of the fences and can influence lipid movement sterically and by altering the viscous characteristics of the membrane in the vicinity.

For proteins experiencing this type of confinement, the dependence of the protein's movement on the cytosplasmic domain has been demonstrated by deleting the cytoplasmic group of E-cadherin in L cells [52]. Additionally, the dependence on actin has been shown by treating cells with cytocholasin D and latrunculin A that act as actin depolymerization agents [51]. In these studies, destabilization of the actin skeleton resulted in an increase in the average compartment size, while application of jasplakinolide, which acts to stabilize the actin skeleton, resulted in an increase in the average residency time in a confinement domain.

Closer analysis of this phenomenon in different cells showed that the average compartment sizes differed from cell type to cell type [53]. Average domain sizes range from 40 nm for FRSK cells to 700 nm for NRK cells. The macroscopic diffusion coefficients (those on the timescale of several milliseconds) found inside the corrals, however, do not differ significantly and, with values around 0.15 $\mu m^2/s$ [54], display a surprising similarity to the values expected for free diffusion within pure lipid bilayers.

1.3.3 Tethered Proteins

Confinement of membrane proteins and observation of reduced diffusion coefficients can also be attributed to tethering to the cytoskeleton. Compared to other confinement models, this explanation is fairly straightforward. Various proteins, like annexin and

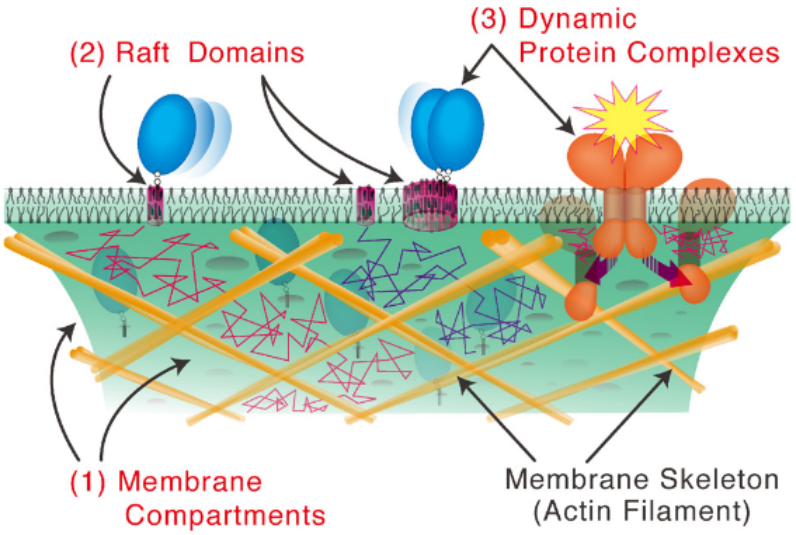

Figure 1.4: Conceptual representation of the picket-and-fence model. The picket and fence model of the plasma membrane predicts transient confinement of transmembrane proteins by actin filaments acting as fences. This figure shows the actin in yellow impeding free diffusion of membrane proteins. We also see that actin cytoskeleton induced confinement and raft confinement coexist in the cell memebrane. Figure reproduced from [55].

dystrophin, interact with the cellular membrane, membrane proteins and the actin network [56]. Similarly, transmembrane proteins may experience tethering to the cytoskeleton. The elasticity of the filaments and the network itself permit the proteins to move in a limited fashion around their point of anchorage, thereby creating the illusion of confinement within a domain.

The epithelial cystic fibrosis transmembrane conductance regulator (CFTR) Cl^- channel is an example of a tethered membrane protein. Verkman and colleagues tracked this protein using fluorescent quantum dots and demonstrated a confined, actin-dependent motion within a spring-like potential [57]. Furthermore, they determined the effective spring constant to be 2.6 ± 0.8 pN/μm. Its movement showed latrunculin dependence, suggesting actin-tethering. Similar experiments combined single-particle tracking and optical tweezers to measure the effective spring constant of tethered LFA-1 adhesion proteins in K562 cells. The spring constants were found to be 2.4 to 8.4 pN/μm.

1.3.4 Protein Induced Confinement

Membrane proteins have also been seen to form **protein clusters**, preferentially in regions of high concentration of cholesterol and sphingomyelin. There is an ongoing debate about the chronological order of the formation of these aggregates: do the lipids cluster and recruit the proteins, or do the proteins assemble and attract the lipids? A collection of proteins pulled together by protein-protein interactions is, in itself, a source of confinement for the individual protein within this group.

Destainville, who has done a significant amount of work on the formation of protein clusters via protein-protein interactions, simulated that protein-protein short-range attraction and long-range repulsion energy on the order of k_BT can lead to the formation of nanoclusters [58]. In his work, Destainville also determines that the diffusion coefficient of an individual protein within a cluster is inversely proportional to the size of said cluster. An example of protein induced confinement is the μ-opioid receptor, a G-protein-coupled receptor, the source of whose exhibited confined motion seems to be long-range interactions with other membrane proteins [59].

An earlier example of receptor clustering is that of acetylcholine (ACh) receptors on muscle cells in work done by Fischbach and coworkers [60]. They used iontophoresis to map the cell surface *in vitro* and measure ACh sensitivity. They detected receptor cluster development in new synapses that formed between embryonic chick spinal cord and muscle cells. Clusters of the receptors were seen as peaks in ACh sensitivity, and formed within a few hours.

Crowding effects due to a large obstacle population in a diffusion medium can also lead to diffusive behaviour that apears to be anomalous. In this case the diffusion coefficient is underestimated with respect to the expected value given the medium viscosity and the diffusing agent's size. $\alpha < 1$ in the anomalous diffusion equation $< r^2 >= 4Dt^\alpha$. The effects of protein crowding on the apparent diffusion coefficient have been reviewed in [61].

1.4 Bacterial Toxin Interactions with the Cell Membrane

Many pathogenic bacteria seek to attack other cells by using soluble protein toxins [62]. These attack the cell either at the membrane or in the cytoplasm. In order to do so, they must interact with the plasma membrane, either to modify the bilayer properties of the membrane, or simply to pass through. Either way, they must target a receptor on the cell surface. To achieve their toxicity, protein toxins have obtained the remarkable ability to adopt two seemingly mutually exclusive states: water soluble and lipid soluble [62]. An example showcasing this ability is given by the family of pore-forming toxins that are also used in this work.

Pore-forming toxins (PFT) are produced as water-soluble monomers that attach to a target receptor, oligomerise and form a protein complex that is inserted into the membrane, forming a pore. Among the PFTs, we distinguish between the α-PFTs and the β-PFTs depending on the structures used to form the pore. α-PFTs use α-helices to form a pore across the membrane, whereas β-PFTs make use of β-sheets to achieve their goal. The mechanism of insertion into the membrane is much better understood for the latter. The monomers combine to form an amphipathic β-barrel that has a hydrophobic exterior and a hydrophilic interior, permitting it to enter the lipid membrane [63]. Depending on the toxin species, there is a large variation in the number of monomers that contribute to the macrostructure and the size of the pores. The number of monomers can range from 7 to 50 and the pore sizes anywhere from 2 to 50 nm [64].

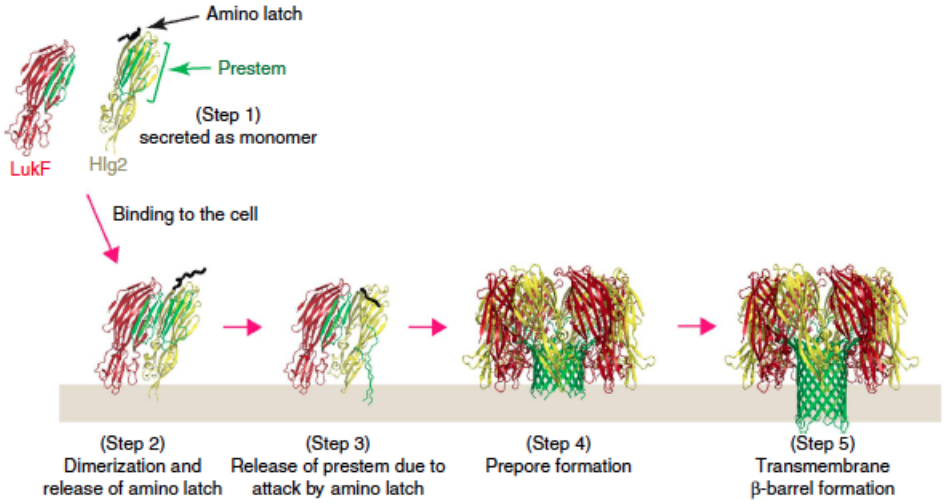

Figure 1.5: Steps of action for pore forming toxins. A schematic of PFT action at the cell membrane. The presented PFT is a two component toxin secreted by *Staphylococcus aureus* and attacks blood cells. The two components are LukF and Hlg2. These soluble monomers bind individually to the cell membrane, oligomerize and unfold a β-barrel into the membrane to pierce a pore into the bilayer. Unfolding begins with the prestem of the Hlg2 monomer extending into the membrane, followed by the assembly of the dimers into an octamere. Figure reproduced from [68].

This work is mainly concerned with the action of two pore-forming toxins and the membrane environment of their receptors, namely the ϵ-toxin of *Clostridium perfringens* and the α-toxin of *Clostridium septicum*. *Clostridium septicum* is a Gram-positive, spore forming bacterium that can cause gas gangrene through the release of exotoxins like **alpha-toxin**. The α-toxin has been shown to exist in two forms. One with a weight of 48 kDa that undergoes cleavage to become the active form of 44 kDa [65]. Furthermore, it has been shown to choose GPI-anchored protein receptors as its target site on the cell membrane [66]. Like *Clostridium septicum*, *Clostridium perfringens* is a spore forming, Gram-positive bacterium. **Epsilon-toxin**, produced by strains B and D, is also a PFT with a much higher toxicity level than the α-toxin, 100 ng/kg versus 10 μg/kg for mice [67].

The bacterial toxins that penetrate the cell membrane to act inside cell all follow a similar mechanism of action [69]. The four step process used by these toxins starts with binding to the membrane. Shiga toxins, for example, achieve this via binding to glycolipids in the membrane [70]. Cholera toxin has been shown to bind with high affinity to ganglioside G_{M1} [71]. Subsequent internalization of the toxins progresses via endocytosis with coated or non-coated vesicles. The third step is the translocation of the toxins from the vesicles into the cytosol and to the target site. The final step in the intoxication involves the action of the toxin at the target site. Diphtheria toxin, for example, blocks protein synthesis by inactivating elongation factor-2 within the cell, thereby provoking cell death [72]. In this work we studied the binding to the membrane and subsequent internalization of the **botulinum toxin** produced by the bacterium *Clostridium botulinum*. More detail on its mode of action is given in section 6.1.

Knowing which receptors are targeted by the toxins and what environment the receptors act in within the membrane is a paramount factor in developing preventions and treatments for toxin related diseases. The studies presented here focus primarily on the membrane structures the relevant receptor proteins find themselves in and the significance of their differences.

1.5 Experimental Methods for Studying the Cell Membrane

1.5.1 Fluorescence Microscopy

The technique that has been used in this work is that of fluorescence microscopy. Fluorescence microscopy uses an optical microscope to detect fluorescence or phosphorescence within a sample.

Fluorescence microscopes function on the principle of illuminating a sample with a specific wavelength. Either an excitation filter is used to filter out unwanted wavelengths, or, as in this work, a monochromatic excitation laser is employed to excite the sample. The photons of this wavelength are absorbed by the fluorescent agents, which will subsequently emit light at a higher wavelength. A dichroic is used to separate the excitation and emission beam paths and the emitted light can be filtered from the excitation light and any other unwanted signals by using an appropriate emission filter. The filtered signal is then observed with a detection system. We use an EM-CCD (electron multiplying charge coupled device) camera. Figure 2.1 shows a conceptual diagram of a fluorescence microscope.

1.5.1.1 Confocal microscopy

Among the types of fluorescent microscopes are wide-field epifluorescent microscopes, or more complicated confocal microscopes that use spatial pinholes at a plane confocal with the sample plane to eliminate out-of-focus light. Confocal microscopes therefore also enable the user to construct three-dimensional structures from the acquired images, with increased axial spatial resolution compared to standard fluorescence microscopy.

Instead of illuminating the entire specimen under observation at once as in wide-field microscopy, the excitation is focused at a single spot in the specimen. This is usually done by focusing a laser beam at a pinhole at a plane confocal with the sample plane. Another pinhole aperture is positioned in front of the detector at a location that is confocal with the laser beam pinhole and the sample plane. Thereby, emission light from the illuminated point in the specimen converges on this point and any other fluorescence within the sample originating from a point not at the point of excitation is largely excluded by the pinhole. A 2D image can then be constructed by scanning over the sample. The achievable frame rate of this method is thus typically not as high as for wide-field fluorescence microscopy. A recent example of a study using confocal microscopy

to study the cell membrane is by Kuriyan et al. who investigated the regulation of the epidermal growth factor receptor (EGFR), by measuring autophosphorylation as a function of the EGFR density in the membrane [73].

1.5.1.2 Ensemble measurements

A relatively simple ensemble technique for measuring lateral diffusion in membranes is **fluorescence recovery after photobleaching** (FRAP). This technique requires a high labelling density on the sample. By selectively photobleaching position dependent fluorescent probes and subsequently observing the signal recovery within the bleached area, the diffusion coefficient of the labels can be calculated using:

$$D = \frac{w^2}{4t_D} \tag{1.1}$$

where w is the radius of the bleached spot and t_D the characteristic recovery time.

FRAP has been used to study the dynamics of proteins within the membrane [74], and the cycling dynamics of plama membrane aquaporins in Arabidopsis roots [75]. Another example is given by Erickson and colleagues [76] who used FRAP to study the *E. coli* Z-ring, which is the cytoskeletal component that contracts during cell division producing two independent bacteria. More specifically, they looked at the FtsZ component of the Z-ring involved in the continual remodelling of the Z-ring. FRAP has also been used to detect domains in the cell membrane and determine the associated domain sizes and diffusion coefficients [77].

Lastly, FRAP has also been used in conjunction with optical tweezers to study the lifetime of adhesive bonds at neuronal contacts. This technique uses an optical tweezer to drag a ligand-coated microsphere over the cell membrane, where the ligands will interact with the receptors. Furthermore, the receptors are labeled with GFP. By photobleaching these, the turnover rate and respective on-rates of ligand-receptor formation can be obtained [78].

Another popular ensemble measurement technique is **fluorescence-lifetime imaging** (FLIM). This technique takes advantage of the fluorescence lifetimes of fluorophores and the effect different environments have on this specific parameter. When a collection of fluorophores are excited, they are transferred to their excited state. Following excitation the fluorophores will produce a fluorescent signal that exponentially decreases with time, as the excited molecules drop back into their ground state. This process, characterized by the fluorescence lifetime, is typically on the order of nanoseconds.

Using techniques like FLIM, the fluorescent signal is recorded for every pixel on the camera and its evolution used to calculate the fluorescence lifetime at the respective position. Since various factors, like pH level, oxygen, temperature and other macromolecules in the vicinity, contribute to the fluorescence lifetime, an image can be constructed using this position-dependent information.

FLIM has been shown to detect liquid ordered and liquid disordered states in model membranes, as well as regions of high cholesterol concentration in live cells [79]. By using the dye di-4-ANEPPDHQ to stain the membranes, this study found that different states of order could accurately be imaged using FLIM. Another study successfully applied FLIM using BODIPY fluorophores to measure the local viscosity in a membrane [80]. Finding an increased lifetime for a higher environmental viscosity, two distinct lifetime populations were found, denoting associated viscosity values of around 160 and 260 cP ($0.16 \text{and} 0.26\ Pa \cdot s$) [80].

Fluorescence correlation spectroscopy (FCS) is a technique which exploits the fluctuations of a fluorescent signal within a microscopic volume. These fluctuations can be used to measure parameters such as diffusion coefficients, hydrodynamic radii or average concentrations. As such, it has become a popular tool for obtaining a deeper understanding of the dynamics of biological and, in particular, cellular systems.

Especially popular in conjunction with confocal microscopy (section 1.5.1.1), FCS illuminates a sample volume with a diffraction-limited laser spot. The fluorophores in the sample solution will randomly diffuse in and out of the excitation volume, thereby producing a fluctuating fluorescent signal. The fluctuating signal produced by the fluorophores can be auto-correlated to yield the autocorrelation function $G(\tau)$, and, hence, distinguishes itself from the uncorrelated background:

$$G(\tau) = \frac{< F(t) \cdot F(t+\tau) >}{< F >^2} - 1 = \frac{< \delta F(t) \cdot \delta F(t+\tau) >}{< F >^2} \tag{1.2}$$

where τ is the lag time, and $F(t)$ the fluorescent signal at time t. This results in a sigmoidal decay curve with a characteristic correlation time that can be related to the average diffusion coefficient in the medium, and consequently to the hydrodynamic radius. Signal amplitude, on the other hand, gives information about the particle concentration.

Given the fact that FCS is usually implemented in conditions such that single molecules move into and out of the excitation volume, so as to maximise the detected fluctuations, it can also legitimately be considered a "multiple single-molecule" technique.

In the context of studying the lateral organisation of the cell membrane, FCS has also found extensive use. By varying the length scales on which FCS is applied (spot-variation FCS), and and exploiting the high time resolution of FCS, one can effectively study the modes of diffusion in the cellular membrane and distinguish between different diffusion models. Additionally, parameters like domain residence times, diffusion coefficients, and domain sizes can be calculated [81, 82]. In this way, for example, an average confinement area radius, for example, of 30 nm for GFP-GPI was obtained in the measured Cos-7 cells.

1.5.2 Super-resolution Microscopy

Fluorescence microscopy as other forms of light microscopy is limited in its resolving power due to the diffraction of light. This limitation was first stated in 1873 by Ernst

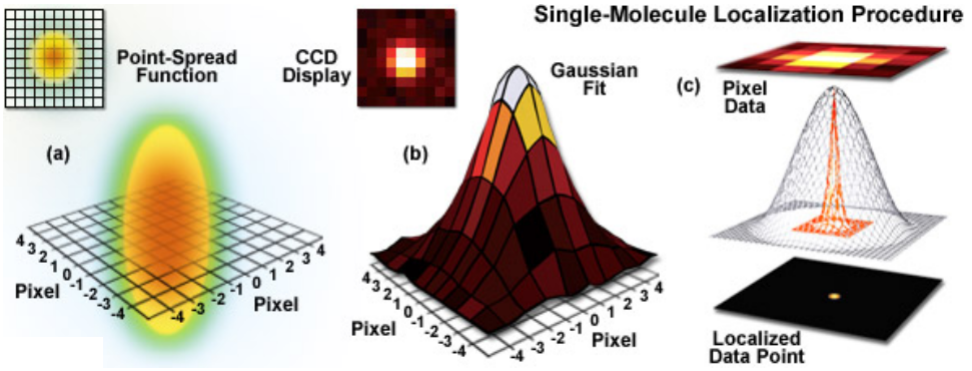

Figure 1.6: Gaussian fit to the point-spread function. The point spread function ias detected on a pixel array (a), and the signal is fit with a Gaussian (b). The emitter can then be localised with an accuracy far beyond the diffraction limit, given by the uncertainty in the position of the Gaussian maxiumum (c). Figure reproduced from [83].

Abbe:

$$r = \frac{1.22\lambda}{NA} \tag{1.3}$$

λ is the wavelength of light, which, for visible light, is around 500 nm. NA refers to the numerical aperture of the objective and is equal to $nsin\theta$ where n is the refractive index of the sample medium and θ the half angle of the cone of light entering the objective. Equation 1.3 is also known as the Rayleigh criterion and sets the limit of resolution for visible light at around 200 nm.

Objects that are smaller than this diffraction limit appear as Airy discs on the acquired image. If two of these objects are closer together than the full width at half maximum of their point spread functions[1] (PSF), they are seen as just one signal. Note that this limit can be surpassed with high signal-to-noise ratios, as demonstrated by Ober and Ward [84]. For single emitters, the position can be determined with an accuracy below the Rayleigh criterion. By approximating the PSF to be a Gaussian and fitting it as such, we obtain the position from the function's maximum with a localisation precision that may be much lower than the full-width-at-half-max of the PSF. This localisation precision is, in a first approximation, proportional to $\frac{1}{\sqrt{N}}$, N being the number of photons of the signal collected. Figure 1.6 shows a schematic of this process. This method for localising a particle is used for single particle tracking and is presented in more detail in section 2.1.

A new generation of optical microscopy has been developed to circumvent this limitation and provide scientists with information well bellow the diffraction limit. In fact, the nobel prize for chemistry in 2014 was given to Eric Betzig, Stefan Hell and William Moerner precisely for their pioneering work in the field of super-resolution microscopy and for bringing "optical microscopy into the nanodimension". These super-resolution techniques and single particle tracking (presented in chapter 2) use the same localisation procedure as described above. The difference being that tracking, as performed in this

[1] The point spread function is the response function of the optical microscope to a point source of light.

work, is done in low density labeling conditions, whereas the super-resolution techniques presented here have found a way to resolve beyond the limit of resolution at high labeling densities.

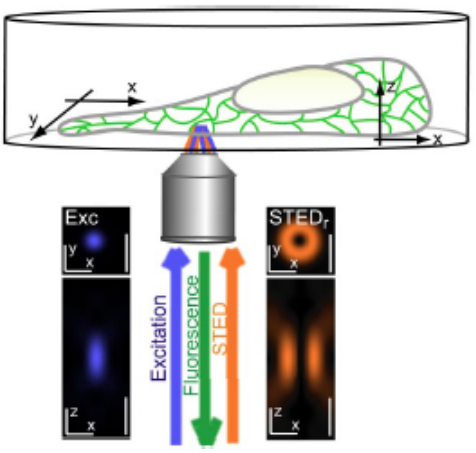

Figure 1.7: Conceptual image of STED. An excitation beam is followed by a doughnut shaped stimulated emission beam that serves to reduce the size of the remaining excitation area. Figure reproduced with modifications from [85].

Super-resolution techniques fall into roughly two categories, depending on the applied strategy for bypassing the limitations of conventional light microscopy. **Deterministic super-resolution techniques** exploit the non-linear responses that most fluorophores exhibit to excitation. An example of this approach is STED (see section 1.5.2.1). **Stochastic super-resolution techniques** take advantage of the stochastic temporal behaviour of different fluorophores. By observing a collection of emitters during changing ON and OFF states, individual emitters can be resolved. PALM and STORM (see section 1.5.2.2) are two examples of this method.

1.5.2.1 Stimulated emission depletion microscopy (STED)

The earliest super-resolution technique developed and extensively used by Stefan Hell, for which he was awarded the Nobel Prize in Chemistry, is **stimulated emission depletion (STED)** microscopy. First, a subpicosecond laser pulse is used to excite a spot of fluorophores on a sample. A second, typically doughnut-shaped, red-shifted STED pulse is then applied to partially de-excite the excited fluorophores via stimulated emission (see figure 1.7). The result is a smaller excited spot on the sample. The lateral resolution achievable with this technique is calculated with equation:

$$\Delta r = \frac{\Delta}{\sqrt{1 + \frac{Imax}{Is}}} \tag{1.4}$$

Δr is the lateral resolution, Δ the full-width at half-max of the PSF, and $\frac{Imax}{Is}$ the ratio of the maximum intensity of the STED pulse and the intensity needed to achieve saturated emission depletion, I_S. So, theoretically, by increasing the peak intensity of the STED pulse, the lateral resolution can be arbitrarily increased. Note that the increase in resolution is only possible due to the non-linearity of the stimulated emission process.

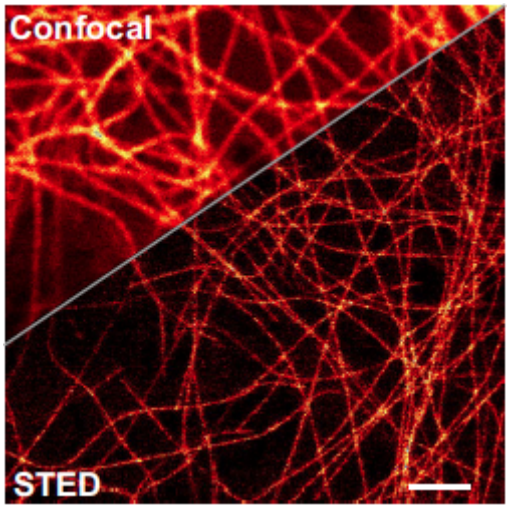

Figure 1.8: Comparison of Confocal and STED resolutions. Difference in resolution that can be achieved with STED compared to confocal imaging. The image shows Citrine-labeled microtubules inside PtK2 cells. Scale bar is 2 μm. Figure reproduced from [85].

The intensities required for this technique to work were initially too high to be applied in live samples. Continuous progress in the choice of probes and experimental implementations, however, have allowed a decrease of the intensity of the STED beam compatible with live samples [86].

Most of the work using STED has been conducted within the research group headed by Stefan Hell. Among the numerous insights made possible with STED, this group has used this new technology to image vimentin and caveolin in live cells to a superior resolution to that achievable with confocal microscopy [87]. An example of a similar study, also conducted in the group of Stefan Hell, that imaged microtubules to sub-diffraction resolution is shown in figure 1.8. In this study, a lateral resolution of around 60 nm was achieved.

STED has also been applied to study the organisation of the cell membrane. In a study using a combination of STED and FCS, syntaxin clusters on neuroendocrine PC12 cells were measured with a focal plane resolution of ~50 nm. Furthermore, an average density of 19.6 clusters per μm^2 and an average cluster diameter of 50-60 nm was measured [88, 89]. Another study combining STED and FCS conducted by Hell and colleagues to study the organisation of the lipid membrane was able to distinguish different diffusion types of lipids on the nanometre scale [31, 90]. In particular, it was found that sphingolipids and GPI-anchored proteins are transiently (10–20 ms) confined in cholesterol-mediated molecular complexes having diameters of <20-nm.

1.5.2.2 Stochastic optical reconstruction microscopy (STORM)

The idea behind PALM and STORM is fairly simple. A given structure within a cell is densely labelled with photoswitchable probes. If these were to be all on (i.e. emitting) simultaneously the individual structures labelled could not be resolved. In PALM and

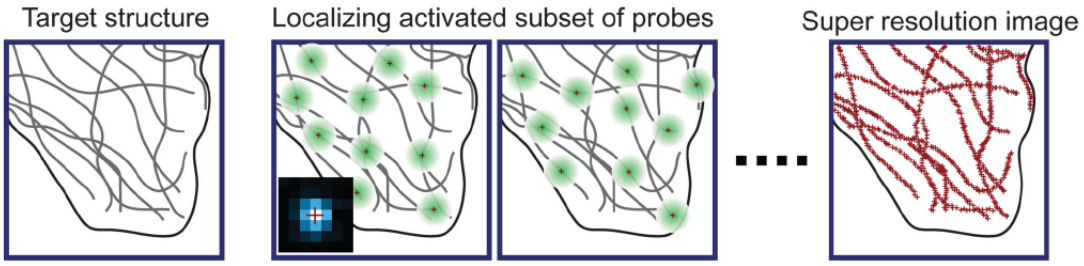

Figure 1.9: Conceptual image of PALM and STORM. Individual emitters are randomly turned on and off in such a way that only a low density of emitters is on at a time. The independent signals are then localised and a sub-diffraction limit resolution is achieved. The process of turning on and off the individual emitters is continued until all emitters have been localised. Figure reproduced from [91].

STORM, however, only a small fraction of the emitters is on at any given time. This produces a series of images in which adjacent emitters are on at different times such that their respective point spread functions (PSFs) do not overlap. The position of the probe can then be determined to a sub-diffraction precision as briefly described in section 1.5.2 and, in more detail, in section 2.2.1. Repeating this process, allows the experimentalist to sample over the entire structure with a resolution beyond the limit of equation 1.3. The principle behind PALM and STORM is explained graphically in figure 1.9.

The various implementations of this technique differ in the way the fluorophores are turned on and off. Whereas PALM uses photoactivatable fluorescent proteins [92], STORM uses two photoswitchable organic fluorophores conjugated with a DNA fragment [93]. In most cases, the turning off of the fluorophores is based on photobleaching.

STORM can be combined with other advanced techniques. **Multicolor STORM** uses different colored fluorescent probes that target different sites. Bates and colleagues demonstrated this approach by imaging microtubules and clathrin-coated pits (CCPs) simultaneously in mammalian cells [94]. By labelling the CCPs with Cy3-Alexa 647 and the microtubules with Cy2-Alexa 647 conjugates, they achieved an imaging resolution of 20 to 30 nanometres.

STORM can also be extended to 3D imaging or **3D STORM**. Resolution in the third dimension can be achieved by using a cylindrical lens that will cause a distortion of the PSF in the x or y direction depending on the emitter location with respect to the focal plane, above or below. The magnitude of the distortion gives information on how far from the focal plane the emitter is located. Using this additional information, probes can be localised in three-dimensional space and a 3D image can be reconstructed. An example of this has been produced by Huang et al., who used this technique to image a network of cellular microtubules [95]. The result of this work can be seen in image 1.10.

FPALM, another stochastic super-resolution technique, has been used to image the membrane protein hemagglutinin (HA) on HAb2 fibroblasts. Using PALM, a resolution of ∼40 nm has been reached and HA clusters from ∼40 nm to several micrometres could be detected [96]. Their dynamics suggested that their formation was likely to be cytoskeleton dependent.

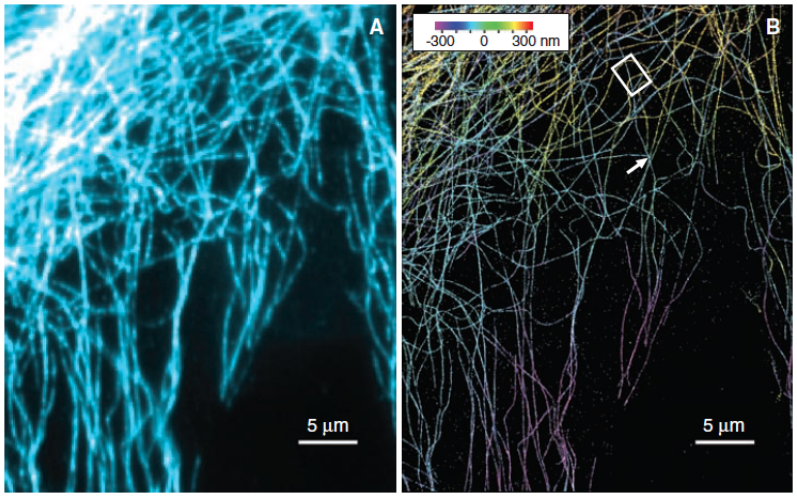

Figure 1.10: 3D STORM images. Microtubule network in a BS-C-1 cell. (A) shows the image obtained with conventional confocal microscopy. (B) is the same image of microtubules attained using 3D-STORM. Figure reproduced from [95].

1.5.3 Holographic Microscopy

Holographic microscopy distinguishes itself from other microscopy techniques in that it uses the information contained within the phase of the light wave in addition to the light intensity. A hologram is produced by an interference pattern established by recombining the beam that has passed through the sample and, thus, has acquired a phase shift, with a previously split off reference beam. From the recorded hologram, a computer algorithm effectively replaces the image forming lens and reconstructs the object image. In terms of optical resolution, a digital holographic microscope can achieve similar values as classical light microscopy, as it is also diffraction-limited. It is, therefore, more suited to imaging cellular morphology, and less suited for studying molecular interactions in the cell membrane.

Digital holographic microscopy (DHM) has been extensively used for live cell imaging. Studies include an investigation by Bernhardt et al. who observed shape changes of live red blood cells from discocytes to echinocytes [97]. Similar experiments made possible by DHM are the study of uneven membrane fluctuations of red blood cells [98] and the measurement of the refractive index of live cells [99].

1.5.4 Electron Microscopy

A method that can bypass the resolution limitations of optical microscopes is electron microscopy. It takes advantage of the wave-particle duality of accelerated electrons which are used as a source of "illumination". The wavelength associated to electrons can be up to 100,000 times smaller than that of visible light. Resolutions of better than 50 pm have been reported [100].

Different types of electron microscopes exist. The **transmission electron microscope** (TEM) is one example of these. It uses a beam of accelerated electrons that are analogous

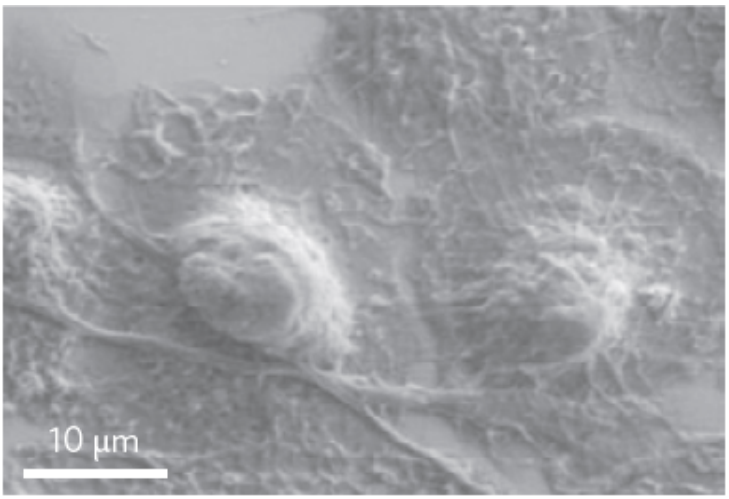

Figure 1.11: SEM image of human monocyte-derived macrophages. Figure reproduced from [101].

to the light beam of an optical microscope. Similarly, electrostatic and electromagnetic lenses, analogous to optical lenses, are employed. The electron beam is focused on a specimen and the transmitted electron are imaged. The way the specimen scatters the passing electrons holds information on the structure of the sample.

Another example is the **scanning electron microscope** (SEM). This uses the focused electron beam to scan the surface. Similar to the TEM, the SEM obtains information from the way the electron beam interacts with the specimen. This interaction produces low-energy secondary electrons, backscattered electrons, and electromagnetic emissions that are used to construct an image. Figure 1.11 shows an example of an image of human monocyte-derived macrophages obtained using a SEM.

The application of electron microscopy in the biological field may be limited as it requires the sample to be largely viewed in vacuum and to be specially prepared making *in vivo* studies impossible. Sample preparation can range from applying a conductive coat, over cryofixation, to dehydration [102]. Yet, it may prove an effective way to study membrane structures below the resolution limit, for example directly observing lipid rafts only tens of nanometres in diameter. Advances in electron microscopy, such as its use in water [103], make this technique more and more attractive for studying cells.

1.5.5 Atomic Force Microscopy

Like the scanning electron microscope, the atomic force microscope (AFM) is a type of scanning probe microscope. First presented in 1986 as an instrument capable of measuring forces as small as 10^{-18} N and spatial resolution on the Ångström scale [104], it uses a cantilever with a sharp tip to scan the surface of a sample. When the tip approaches the sample surface, it experiences a force of mechanical, magnetic, capillary, chemical, electrostatic or other nature. This produces a Hooke type deflection of the tip, which can be measured with a laser beam incident on the top surface of the cantilever. The movement of the reflected laser beam is measured via a position sensitive detector.

AFMs can produce images with resolutions down to fractions of nanometres. This is more than three orders of magnitude smaller than the optical diffraction limit.

These microscopes can reconstruct the surface topography via several different implementations. For biological applications, the constant force and the oscillation modes are the most common. In the constant force mode, the system seeks to maintain the deflection of the tip constant. A feedback loop therefore ensures an appropriate movement in the z direction of the cantilever in response to a change in the surface. The changes in height are recorded and used to reconstruct the topology. The oscillation mode uses the same feedback loop principle to move the cantilever. However, the AFM tip also constantly undergoes a sinusoidal oscillation with contact with the surface at the extreme of the movement.

AFM has been used to image membranes in air as well as in water [105]. This method's ability to function in both media is an important advantage. However, since AFMs need to scan over a sample, image acquisition is slow, and hysteresis effects can produce a distortion of topological features. Nevertheless, high-speed atomic force microscopy has been used to study the dynamics of unlabelled membrane proteins, and observe free diffusion as well as trapping of individual proteins [106].

1.6 Summary

This chapter introduced the cell membrane and its vital role in maintaining cell health and in delimitating the cell interior and exterior. Its main structural components were introduced, lipids and proteins, and the primary functions that the membrane serves were outlined. The cytoskeleton, another major actor in determining cell membrane architecture, has been introduced. The cell membrane, far from being a uniform environment, contains a multitude of confining structures for membrane proteins, for which the major models were presented. Finally, an overview of the principal techniques for studying the cellular membrane were presented and described. Armed with the basic knowledge of the cellular membrane, we progress to the next chapter that will introduce the main experimental techniques used in this work.

Key points:

- The plasma membrane provides a necessary barrier for cells that acts as the interface between the inner workings of the cell and the external environment.
- The cell membrane consists of proteins moving within a sea of lipids.
- Membrane proteins experience confinement caused by factors such as membrane lipid organisation, cytoskeletal filaments, and other proteins.
- The cell membrane can be and has been studied using a variety of techniques like optical microscopy and atomic-force probes.

Chapter 2

Single Particle Tracking and Bayesian Inference

If we knew what it was we were doing, it would not be called research, would it?

Albert Einstein

Contents

Throughout this work, numerous experimental techniques and analysis methods have been used. Each of these will be explained in the appropriate section when necessary. Two approaches, however, have been used extensively and merit a detailed description for the sake of the work's coherence. These two techniques are **single particle tracking** (SPT) and **Bayesian inference** (BI) for trajectory analysis. We used SPT to track different membrane receptors and bacterial peptidic toxins. The obtained trajectories were subsequently analysed with an algorithm based on Bayesian statistics to infer characteristic parameters of the proteins' dynamics. With the BI approach we obtain unique insights into the single particle dynamics unattainable with conventional methods.

2.1 Single Particle Tracking

In section 1.5.1.2 we described techniques such as FRAP that are capable of measuring collective diffusion coefficients of membrane components. SPT uses a labelling density that is low enough to detect single molecules, and thus allows us to go one step further and probe the membrane by looking at the movement of individual membrane components. The data which is extracted in an averaged form in ensemble measurements can, hence, be deconstructed and examined on a case-by-case basis.

Tracking individual particles brings several advantages over observing numerous particles at the same time. Firstly, by looking at the trajectory we see the direct effect of membrane structures on the movement of a diffusing agent. The spatial resolution of FRAP is limited by the minimum size of the diffraction limited laser beam (approximately 0.5 μm), The spatial resolution of SPT can be up to about two orders of magnitude greater than that of FRAP [107]. This allows us to address the movement of previously unresolvable sub-populations. SPT has, numerous times, been shown to be extremely valuable in studying cell membrane heterogeneities [108–110].

So how does SPT work? The membrane receptors we wish to observe cannot be tracked directly *per se*. However, by attaching a probe to the proteins in question we can track the next best thing, namely something directly attached to our target. The kinds of probes that can be used are described in more detail in section 2.1.1. The probe is then detected and tracked for a given amount of time, i.e. for a given series of acquisition time windows. However, there is a trade-off of certainties in determining the particles characteristics during data acquisition. The larger the acquisition time, the more signal can be detected and the better the probe can be localized, but the less temporal resolution we have for following its path.

Similarly to the super-resolution technique STORM described in section 1.5.2.2, the sub-diffractive precision when localising particles can be obtained because only one probe is observed at a time. The labels are smaller than the wavelength of light, so their signals will be recorded as Airy discs. Two particles whose Airy discs overlap will still be unresolvable, but the level of localisation precision that can be reached for a single emitter can reach 1-10 nm depending on the brightness of the probe [111, 112].

Because of the simple two-dimensional geometry, SPT has seen extensive use in studying the cell membrane [113]. Examples of recent studies in which SPT has been used include high-speed tracking (1000 Hz) of the serine chemoreceptor, TSR, in the membrane of *E. coli* bacteria. Most of the cell membranes were found to be partitioned into cytoskeleton-dependent compartments about 300 nm in size [114]. Another advance in SPT that has been made possible by the new superresolution techniques mentioned in section 1.5.2, is high-density SPT [115, 116]. By combining PALM with SPT, Manley and colleagues were able to track the Gag and VSVG membrane proteins wtih a trajectory density of up to 50 μm^{-2} [115]. Combining high-density tracking with recent advances in inference analysis has, furthermore, lead to a powerful approach for mapping the energy and diffusivities on cell membranes [117].

2.1.1 Probes for SPT

Since proteins cannot be visualized individually under an optical microscope and can therefore not be tracked, a probe is needed. The probe is attached to the protein in question and provides a means for observing the protein movement, despite no direct image of the protein itself. To function as an reliable SPT label for obtaining protein trajectories, the tag should ideally be continuously detectable, easy to localise, and not loose this ability. In the case of fluorescent particles, this means that in the ideal case, they should not blink, have a bright emission, and not photobleach.

2.1.1.1 Fluorescent molecules

The most common probes are **organic fluorophores**. These are molecules that re-emit light upon excitation and can be conjugated to a particle of interest for tracking purposes. Popular fluorophores for tracking include cyanine derivatives like Cy5, and Alexa Fluors. An example of SPT using these labels is the study of lipid movement in the membrane of human coronary artery smooth muscle cells (HASM). Here, dimyristoyl-sn-glycero-3-phosphoethanolamine (DMPE) was labeled with Cy5 to detect lipid domains ranging in size from 0.2 to 2 μm [118].

Using genetic engineering, scientists can produce **fluorescent proteins**. The most commonly used of these is the green fluorescent protein, or GFP. As the name suggests, this protein emits bright green light when excited with light in the near UV range. Its wild type form was first discovered in the 1960s by Osamu Shimomura, who consequently was awarded the Nobel Prize in Chemistry in 2008 together with Martin Chalfie and Roger Tsien [119]. The gene that codes for GFP can be modified and combined with another gene that codes for a target protein. This can be transfected into cells, which will express the combination of genes, leading to the production of labelled target molecules. An example of this can be seen in image 4.13, where MDCK cells were transfected with a plasmid coding for GFP-actin. For SPT, one of the earliest uses of GFP and YFP (yellow fluorescent protein) on live cells was for E-Cadherin and the L-Type Ca^{2+} channels [120, 121].

The fact that fluorescent molecules and proteins can easily be directed to a target site make them powerful tools for studying the cell and its membrane. However, a major disadvantage of these probes is the fact that they exhibit photobleaching. Upon exposure to light, the fluorophores will experience photochemical degradation and loose their ability to emit photons. For SPT, this poses a major problem since the period of time a labelled particle can be followed is limited by the bleaching. The fluorescent lifetime can be increased by decreasing excitation intensity and exposure time. The end result, however, is inevitable.

2.1.1.2 Quantum dots

Quantum dots (QD) are inorganic nanocrystals made of semiconductor materials. By adjusting different parameters such as duration, precursor concentration, and temperature during their synthesis, the size of the single crystals can be controlled [122, 123]. This is important since the color of light emitted by these probes depends on their size. More precisely, the frequency of the photons emitted is inversely proportional to the diameter of the QD [122].

When a QD absorbs a photon with an energy higher than its semiconductor band gap energy an electron-hole pair, also called an exciton, is created. The recombination of the electron and hole produces a radiative emission. However, trapped charges prevent this process by introducing non-radiative Auger processes. This phenomenon can be seen as a blinking of the QD at the single particle level [124]. By coating the quantum dots with a high band gap material, this process can be reduced and the quantum efficiency raised to around 90% [125]. Other groups achieve almost complete suppression of blinking by binding thiol groups to the QD [126]. Multiple coating layers have been shown to drastically reduce blinking [127]. However, this is obtained at the expense of elaborate synthesis protocols.

QDs have been used in numerous studies concerning the cell membrane and SPT. The lateral movement of glycine receptors in the membrane of live neuron cells has been studied using QDs [128]. Another example is the study of p-glycoprotein using QD-antibody conjugates on MCF7r breast adenocarcinoma cells [129]. The data obtained was used, among other things, to reconstruct the protein distribution on the membrane. Other groups have also used QDs to observe the internalization of the EGF receptor erbB1 on CHO and A431 cells [130].

2.1.1.3 Rare-earth-doped oxide nanoparticles

Rare-earth-doped oxide nanoparticles for labeling live cells were first used by Alexandrou and coworkers in 2004 [131]. As they do not exhibit blinking and do not photobleach, it is possible to track a labelled protein in the cell membrane for an extended amount of time and obtain uninterrupted trajectories [132, 133]. The nanoparticles can be functionalised with a layer of APTES, whose amine groups can then be used to attach the nanoparticle to amine or thiol groups of a target protein using a cross-linker to form covalent peptide bonds [134]. The nanoparticles are synthesised in water and, hence, do not require complex water solubilization steps as is the case for QDs.

A further advantage of this types of nanoparticles is their long radiative lifetime. With around 1 ms, this can be exploited for delayed detection. However, rare-earth-doped nanoparticles do exhibit a relatively low absorption outside the UV regime, comparable to that of organic fluorophores, and, compared to other probes, have a relatively low quantum yield. Nevertheless, the advantages of these probes largely outweigh their drawbacks. Thanks to the large number of Eu ions in a 30-40 nm nanoparticle, they can be easily tracked with a 50-ms time resolution and a 30-nm localisation precision.

This work makes extended use of Eu-doped nanoparticles, which are described in further detail in section 2.2.

2.1.1.4 Gold and latex beads

Gold beads can also be used as markers in SPT. Unlike the previous examples, these probes act as light sinks and are seen as dark patches on the obtained image. They do not suffer from photobleaching or blinking, but they do have to be at least 15 nm in diameter to be detectable, so typical sizes for detection in a transmission setup range from 30 to 40 nm [135, 136]. Due to these fairly large sizes compared to fluorophores, the possibility of cross-linking must be considered when working with these kind of probes. While typical acquisition times are on the order of 50 ms, Kusumi and colleagues have performed SPT tracking of the phospholipid DOPE with a time resolution of 25 μs per frame on live NRK cells [53, 137]. By exploiting the heating of the probe and the associated change in refractive index in the surrounding medium, extremely small gold particles of 5 nm and even as low as 1.4 nm can be tracked (this technique is called photothermal tracking) [138, 139]

Fluorescent latex beads have also been used as labels in SPT. Various studies have shown that these are effective as labels of membrane proteins such as Concanavalin A receptors or Major Histocompatibility Complex Class I molecules for 2D tracking [140, 141], as well as for 3D tracking in live Swiss 3T3 fibroblast cells [142]. Additional options for polystyrene beads include attachment to membrane receptors of interest and subsequent trapping in an optical trap (the principle of which is explained in section 3.1). One example of this is work done by Oddershede and colleagues who tracked λ-receptors on living *E. coli* bacteria in this way [143].

2.2 Experimental Setup

The experiments presented here were all conducted with an epifluorescent wide-field microscope (see figure 2.1). The setup is fairly standard, but for completeness the conceptual diagram is presented and described in this section.

The microscope used is a wide-field inverted Zeiss Axiovert 100. This uses a 63x oil-immersion objective with a NA of 1.4. Images were collected using a QuantEM:512SC EM-CCD camera manufactured by Roper Scientific. Excitation of the nanoparticles was achieved with a Ar^+-ion laser at 465.8 nm. The nanoparticle subsequent emission was filtered by either a Chroma 617/8M filter or a Chroma 620/10M filter. For image recording, the MetaVue software package is used. Additionally, a piezoelectric device for fine adjustments of the focus was used with step sizes of 100 nm. The laser power was set to 30 mW, which leads to an excitation intensity of 0.25 kW/cm^2 at the sample and images were acquired at a frame rate of 20 Hz (50 ms acquisition time, 1.3 ms readout time).

Coupled Protein	NP-protein coupling ratio	$[VO_4^{3-}]_{NP}$
Epsilon toxin	3:1	7.83 mM
Alpha toxin	5:1	7.83 mM
Streptavidin	11:1	0.10 mM
Botulinum toxin (HcA)	34:1	0.10 mM

Table 2.1: Table of proteins coupled to nanoparticles,coupling ratios, and vanadate concentrations.

All experiments in which cells are involved were conducted in an incubator placed around the microscope at 37°C. In this work, two types of cell lines are used: Madin-Darby canine kidney (MDCK), and IC_{cl2} cells. The culture medium (CM_{MDCK}) for the MDCK and HeLa cells was composed of DMEM with 10% fetal calf serum (FCS) and 1% penecilin-streptomycin. The culture medium for the IC_{cl2} cells (CM_{ICcl2}) is given in appendix A.7.

For experiments, the cells were trypsinated two days earlier and grown on glass coverslips until they were 90% confluent. An observation medium (OM) was used in which the cells resided for no more than 90 minutes during the experiment. The composition of the OM was HBSS with 10 mM HEPES and 1% FCS. The cells were then incubated for approximately 15 minutes with the nanoparticle-labeled proteins. Once these had attached to their respective receptors, the cells are rinsed three times with OM.

The nanoparticles used in the experiments presented in this work are rare-earth doped vanadate nanoparticles, $Y_{0.6}Eu_{0.4}VO_4$. These are coated with a silica layer and functionalized with 3-aminopropyltriethoxysilane (APTES). Using the amine groups of the APTES, the Europium-doped NPs were then coupled, using Bissulfosuccinimidyl suberate, BS_3, as a cross-linker, to various proteins for further use. The BS_3 is first reacted with the NPs in excess, and subsequently, after removing free BS_3, the quantity of proteins corresponding to the desired coupling ratio is added. The entire process is described in detail in [131, 134, 144, 145]. Table 2.1 summarizes the proteins used and their respective NP-protein coupling ratio. For the NPs coupled to streptavidin that are subsequently incubated with biotinylated agents, the concentration of the agent is adjusted to achieve a final 3:1 agent to NP ratio.

2.2.1 Image Recording and Analysis

The photons emitted by our luminescent probes are detected by an EM-CCD (electron multiplying charge coupled device) camera. A charge-coupled device detects photons via an array of capacitors that serve as pixels. These convert incident photons into electrical charges. This way an image at the focal plane of a preceding objective is captured. The electrical charge accumulated on a capacitor is proportional to the incident light intensity and is then read out pixel by pixel.

In the case of an EM-CCD, a gain register treats the signal before reaching the output amplifier. As the name suggests, this serves to multiply the electrons produced in the CCD. The main advantages of this method are a drastic reduction of readout noise

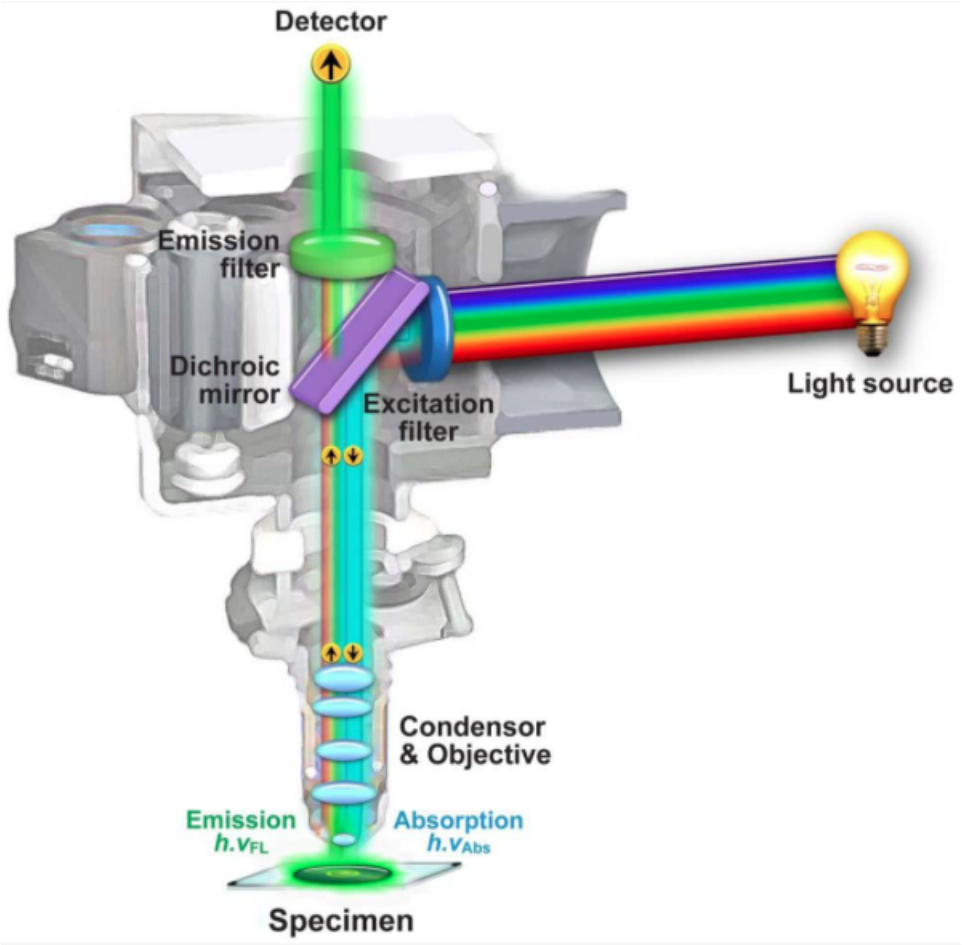

Figure 2.1: Schematic of the experimental setup. Conceptually, the setup for epifluorescent microscopy is quite simple. A light source, which is either monochromatic or made quasi-monochromatic via an excitation filter, is used to excite a specimen/sample. The sample will consequently emit its own light which will be filtered from the excitation light source via a dichroic mirror and filtered of background signals via an emission filter before being picked up by the detector/camera. The image shows an upright microscope. An inverted microscope was used in this work, which allows easier access to the specimen (for the addition of labels, rinsing, etc.). Figure reproduced from [146].

and a concomitant increase of readout speed for EM-CCDs with respect to conventional CCDs.

The images are sent from the camera to the computer and formatted to be viewed as an image or, more precisely, a pixel array representing the intensity of photons incident on each pixel in the camera. This matrix of photon values is then treated with a MATLAB algorithm that localises the individual nanoparticles seen on the image.

New algorithms for localization and tracking of probes are constantly being developed [147]. In this work, we use a straighforward in-house MATLAB algorithm that is described in detail in [148, 149]. The general procedure is given in this section.

As the nanoparticles have a diameter of around 40 nm, they are smaller than the optical limit of diffraction and seen as a point spread function (PSF). The said MATLAB routine

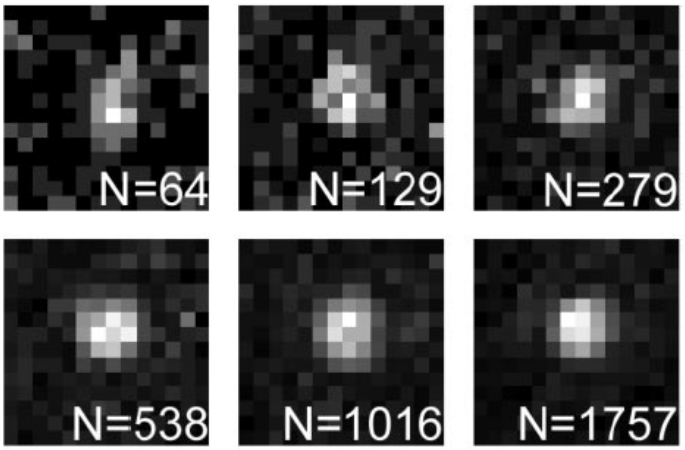

Figure 2.2: Effect of photon number on signal-to-noise ratio. Here we see the effect of signal strength i.e. photon number on the signal-to-noise ratio. The localisation of the probe becomes more precise as the number of photons, N, increases from 64 to 1757. In equation 2.2 this is represented by term A. Reproduced from [150].

fits a two-dimensional Gaussian envelope to the digital pixel signal of the nanoparticle. The position is given by the peak of the Gaussian and the error can be calculated using equation 2.2. This procedure is done for every image in a time sequence of images and the positions are then combined to produce a trajectory. With a 63x objective, which is mostly used in this work, and an EM-CCD camera with 16 μm $\times$ 16 μm pixels, one pixel has the dimensions of 0.254 $\times$ 0.254 μm at the object plane.

Since the image will also contain noise, it is important to consider the signal-to-noise ratio. The main factors contributing to the noise when acquiring images with our system are readout noise and shot noise. The readout noise is the noise intrinsic to the system that we are using for signal acquisition. Readout noise is also present when no signal is present. Looking at acquired images for our experiments and dark images containing only the readout noise, we determined that the intrinsic readout noise of the system is negligible with respect to shot noise.

The number of photons that hit a given pixel during an acquisition interval is determined by Poissonian statistics, which gives rise to the so-called shot noise. Considering the background shot noise, σ_{BG}^2, and the shot noise due to a signal of N photons, $\sqrt{N}$, we obtain for the signal-to-noise ratio:

$$SNR = \frac{N}{\sqrt{\sigma_{BG}^2 + (\sqrt{N})^2}} \tag{2.1}$$

Clearly, the SNR will determine the precision that can be achieved when localising a label during SPT, and consequently also the parameters that can be determined. In order to measure a diffusion coefficient of as low as 0.01 μm^2/s using an acquisition time of 50 ms, a SNR of at least 8 is needed. This result and a more detailed analysis, conducted by Silvan Türkcan, can be found in [148].

The Gaussian fit that is used to determine the position improves in accuracy as more photons are collected. Thompson and colleagues calculated the error in the particle position in terms of the size of the PSF (s), the pixel size (a) and the background noise, (σ_{BG}) [150]:

$$< (\Delta x)^2 >= \underbrace{\frac{s^2}{N}}_{A} + \underbrace{\frac{a^2/12}{N}}_{B} + \underbrace{\frac{4\sqrt{\pi}s^3\sigma_{BG}^2}{aN^2}}_{C} \tag{2.2}$$

In equation 2.2, the term A represents is the photon noise or shot noise of the signal. The effect on A by increasing N, the number of photons, is shown in figure 2.2. B is the pixelisation noise due to the finite size of the camera's pixels. And lastly, C represents the contribution of the background noise to the positioning error. If we consider the shot noise to be the dominating contributor to the positioning error, the localisation error simplifies to $\frac{s}{\sqrt{N}}$.

As mentioned at the beginning of section 2.1, increasing the acquisition time will increase the number of photons collected and therefore decrease our positioning error. However, it will also decrease our time resolution. Additionally, the movement of the probe during acquisition may lead to a distortion of the PSF. Simulations conducted by Türkcan show that the full-width-at-half-max (FWHM) of the probe diffraction pattern starts to increase at acquisition times above 50 ms for diffusion coefficients on the order of 0.1 μm^2 [148]. For SPT experiments, we therefore limit ourselves to acquisition times of no more than 50 ms.

2.2.2 Analysis of SPT Trajectories

Once a trajectory has been obtained, it can subsequently be analysed. As already mentioned, this work makes extensive use of an algorithm based on Bayesian statistics. This will be explained in detail in section 2.3. This section will present the established and alternative analysis methods.

2.2.2.1 MSD analysis

The classic method for analysing the motion of a random walker is the **mean squared displacement** (MSD) analysis [110, 151, 152]. Typically, MSD analysis is used to quantify the diffusion of a particle. In the one-dimensional case, we have the probability density function (PDF) of a particle diffusing over a certain distance during a certain amount of time:

$$P(x,t) = \frac{1}{\sqrt{4\pi Dt}} e^{-\frac{(x-x_0)^2}{4Dt}} \tag{2.3}$$

The PDF describes the probability of finding a particle that started out at position x_0, ending up at position x after a time t.

MSD provides a way to measure and predict the average distance a random walker will have moved after a given time. Again, in a one dimensional space, the MSD is defined

by:

$$MSD(t) \equiv < (x(t) - x_0)^2 > \tag{2.4}$$

The connection between equations 2.3 and 2.4 is that the MSD represents the full width at half-max of the P(x,t) distribution. With time, the MSD increases, as does the width of the PDF as it evolves. Of course, equations 2.3 and 2.4 can be extended to two and three dimensions. For general distances between two points, r, and the respective MSD $< r^2 >$, are used henceforth.

Using equation 2.4 to calculate the distance along which a molecule diffuses during one time step is interesting, but not very useful when analysing single particle trajectories. What is more relevant is to see how the MSD evolves as we vary the number of time steps. Naturally, we would expect the displacement to increase. The case where the MSD is linearly related to time, t, is called normal diffusion or Brownian motion and is represented by equation 2.5a. As described in section 1.3, however, there are numerous factors that influence the movement of proteins within a membrane, act as obstacles or disrupt the normal diffusive process in some way. This will produce sub-diffusive movement where the distance travelled is less than what is expected when assuming normal diffusion. Equation 2.5b represents this by introducing a factor $\alpha < 1$ that accounts for this sub-diffusive motion. The inverse can also be the case where the movement is larger than would be expected for a freely diffusing particle. In this case, the particle may be actively transported and undergo directed motion with a speed v as shown in equation 2.5c. Finally, a particle that moves in a completely confining environment will exhibit an MSD curve that will asymptotically approach the domain size as seen in equation 2.5d.

$$< r^2 > = 2dDt \qquad \text{(Normal Diffusion)} \tag{2.5a}$$

$$< r^2 > = 2dDt^{\alpha} \qquad \text{(Anomalous Diffusion)} \tag{2.5b}$$

$$< r^2 > = 2dDt + (vt)^2 \qquad \text{(Directed Motion)} \tag{2.5c}$$

$$< r^2 > \simeq < r_C^2 > [1 - A_1 e^{-\frac{2dA_2Dt}{<r_C^2>}}] \qquad \text{(Confined Motion)} \tag{2.5d}$$

In equations 2.5, d is the number of dimensions that the particle moves in. This increases the expected MSD as the degrees of freedom for the particle increase. r_C represents the size of the confinement and A_1 and A_2 are constants defined by the confinement geometry. They are derived from the solution of Brownian motion within square corrals [50].

Each of these diffusion types can be graphically represented, which is done in figure 2.3. Here we see the linear relationship between the MSD and time for regular diffusion and the deviation from this case for the other types of motions.

A major disadvantage of the MSD approach, however, is that it only detects the presence, but not the nature of the confinement. The assumed potential of this approach is a box potential, flat everywhere within the domain with infinite confining walls, a picture that

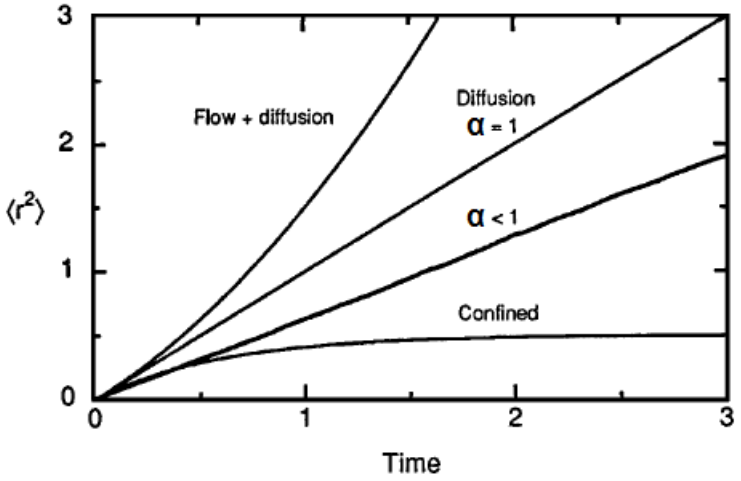

Figure 2.3: MSD curves for different types of diffusion. MSD curves produced with trajectories that undergo directed, normal diffusive, anomalous diffusive and confined motion respectively. Notice how the MSD curve for confined motion reaches an asymtote. Figure reproduced with modifications from [110].

hardly represents reality. Section 2.3 will introduce the approach that is used throughout the rest of this work to obtain confining potentials of arbitrary shape.

2.2.2.2 Non-MSD approaches to trajectory analysis

For detecting confinement, an approach that calculates the time that a particle stays within a circle of a given radius has been used [153, 154]. For confined particles, the probability of staying in a certain area is higher than the same probability for a freely diffusing particle. The probability that a particle diffusing freely stays within a certain radius, r, for a certain time t, can be calculated in terms of the parameters r, t and the particle's diffusion coefficient D [155]. One way to use this is to compare the time the particle spends in a radius r with what is expected for a freely diffusing particle [108].

For confined particles, a characteristic time that can be calculated is the **first-passage time (FPT)**. One way this has been used is via an algorithm that detects FPT variance [153]. It can detect the presence and determine the size of confinement zones from SPT data. Using this method, the movement of LFA-1 receptors on Jurkat cells (clone E6-1) was analysed and the size of the confinement domains compared to known values [153]. Here, Rajani and colleagues first determine if the observed trajectory is in agreement with a correlated random walk (CRW) model. If not, the trajectory is further analysed by calculating the FPT for a range of radii for every point. The variance of the FPT of all sampled radii is then plotted. The position and width of the FPT variance peaks can then be related to the presence and size of any transitory confining domains. First and foremost, the applicability of this technique is in detecting several transitory confinements within a long trajectory.

A similar method to FPT that has been proposed is the **mean maximal excursion method (MME)**. This used the maximal distance covered by a test particle during a

time t as a metric for analysing anomalous diffusion. This method has been shown to more accurately determine the anomalous diffusion exponent, α, in equation 2.5b [156].

An approach to apply SPT data to obtain information on diffusive heterogeneity is the use of **Hidden Markov models** [157, 158]. This approach assumes different diffusive states that the diffusing particle can be in, and between which it switches with certain respective probabilities. This method has been used to demonstrate cytoskeleton-dependent two-state diffusion of the LFA-1 receptor in live T-cells [158].

There are several additional methods for SPT data analysis worth noting. **Spline curve analysis**, for example, extends the MSD approach to respect the geometry of the structure the particle observed is moving in [159]. For analysing particles that seem to undergo directed diffusion, we can correlate the particle's direction of motion at different consecutive points. This can be done by calculating the dot product of consecutive velocity vectors along the particle trajectory [160], a **speed correlation index** so to speak. The more directed the motion is, the more correlated the consecutive velocity vectors are expected to be.

2.3 Bayesian Inference

In section 2.2.2, popular methods for analysing SPT trajectories were described. This section will present an alternative method, of which extensive use is made throughout this work, using an algorithm based on Bayesian inference to analyse trajectories and infer relevant parameters associated with the trajectory. The advantage of this method is that the only input required is a set of local displacements, in our case a trajectory. Additionally, this method, in contrast to MSD analysis, does not reject a large part of the information contained in the trajectory through averaging and by using moments of the point distribution. The output of the program is the overall diffusion coefficient or the diffusivity field, and, for trajectories exhibiting confinement, the force field or confinement potential. The technique was developed by Jean-Baptiste Masson, together with Antigoni Alexandrou, Silvan Türkcan and Didier Casanova, and is described in further detail in reference [133, 161].

2.3.1 Inference of parameters

The model of the movement of the membrane proteins within the two-dimensional environment used by the Bayesian inference (BI) algorithm, starts by assuming Langevin dynamics. We thus construct the equation of motion by assuming three sources of influence on the motion, the simplest representation of a diffusing particle in a potential field. A stochastic diffusivity term, $\sqrt{2D\gamma^2}\xi$, a dissipative drag term proportional to the velocity, $-\gamma\mathbf{v}$, and an arbitrary force term, $-\nabla V(\mathbf{r})$, combine to form the equation of motion:

$$\frac{d^2\mathbf{r}}{dt^2} = \sqrt{2D\gamma^2}\xi - \gamma\mathbf{v} + \mathbf{F} \tag{2.6}$$

The friction of coefficient, γ, is related to the diffusion coefficient, D, via the fluctuation-dissipation theorem, $\gamma = \frac{k_B T}{D}$. $\mathbf{r}$ is the particle position, and ξ is the stochastic zero-average Gaussian noise. Additionally, in the case of conservative force fields, $\mathbf{F} = -\nabla V(\mathbf{r})$.

For confined receptors moving in the plasma membrane we assume steady state conditions, i.e. $\frac{d^2\mathbf{r}}{dt^2} = 0$, since the typical time for relaxation of the velocity to local equilibrium is $\tau = \frac{m}{\gamma} \simeq [10^{-18} - 10^{-10}]$ s. We therefore use Smoluchowski's overdamped approximation for the motion of biomolecules in the cell membrane [162]. This gives us the overdamped Langevin equation:

$$\frac{d\mathbf{r}}{dt} = \sqrt{2D}\xi - \frac{\nabla V(\mathbf{r})}{\gamma} \tag{2.7}$$

The evolution of the transition probability is given by the associated Fokker-Planck equation: [163]:

$$\frac{\partial P(\mathbf{r}_{n+1}, t_{n+1}|\mathbf{r}_n, t_n)}{\partial t_{n+1}} = -\nabla \cdot [\frac{\nabla V(\mathbf{r})}{\gamma} P(\mathbf{r}_{n+1}, t_{n+1}|\mathbf{r}_n, t_n) - \nabla(D(\mathbf{r}) P(\mathbf{r}_{n+1}, t_{n+1}|\mathbf{r}_n, t_n))] \tag{2.8}$$

In order for equation 2.8 to be analytically solved, the force and diffusion coefficient need to be locally constant. The trajectory therefore needs to be split up into $i \times j$ subdomains in each of which $\nabla V(\mathbf{r})$ and D are constant. Since the problem will be solved with constant diffusivities in each mesh, the nature of the stochastic integrals (Itō, Stratanovich) is not important as they will all lead to the same result. Then, after solving the Fokker-Planck equation, we obtain the probability for the particle taking a step n to $n+1$ as a function of the trajectory parameters (diffusion coefficient and forces):

$$P((\mathbf{r}_{n+1}, t_{n+1}|\mathbf{r}_n, t_n)|\mathbf{D}_{ij}, \mathbf{F}_{ij}) = \frac{e^{-\frac{(\mathbf{r}_{n+1} - \mathbf{r}_n - \mathbf{F}_{ij}(t_{n+1} - t_n)/\gamma_{ij})^2}{4(D_{ij} + \frac{\sigma^2}{(t_{n+1} - t_n)})(t_{n+1} - t_n)}}}{4\pi(D_{ij} + \frac{\sigma^2}{(t_{n+1} - t_n)})(t_{n+1} - t_n)} \tag{2.9}$$

σ represents the standard deviation of the Gaussian noise and is used to model all sources of noise, shot noise, pixelization, readout noise, etc. $\mathbf{F}$ is $-\nabla V$. The indices ij represent the respective parameter values in the subdomain at column i and row j in the square grid.

We now know the probability for each consecutive step within the trajectory. The process being Markovian, we can multiply all the probabilities for all $N-1$ steps in the trajectory, and obtain the overall probability for the trajectory, T, in terms of $\mathbf{D}_{ij}$ and $\mathbf{F}_{ij}$:

$$P(T|D, \mathbf{F}) = \prod_{i,j=1}^{i_{max}, j_{max}} P(T|D_{ij}, \mathbf{F}_{ij}) \tag{2.10}$$

$P(T|D_{ij}, \mathbf{F}_{ij})$ in equation 2.10 is given by:

$$P(T|D_{ij}, \mathbf{F}_{ij}) = \prod_{n:\mathbf{r}_n \in S_{ij}} P((\mathbf{r}_{n+1}, t_{n+1}|\mathbf{r}_n, t_n)|D_{ij}, \mathbf{F}_{ij}) \tag{2.11}$$

where S_{ij} represents subdomain ij. So all the probabilities, defined by equation 2.9, for consecutive steps lying in a specific subdomain are multiplied together to obtain an expression for the probability of the trajectory subset that is located in that subdomain (equation 2.11). Then, all the probabilities associated with the individual subdomains are multiplied together to obtain the overall probability for the trajectory in terms of all parameters (equation 2.10).

At this point we have calculated the probability of our trajectory as a function of the various parameters, and can use Bayes' theorem ($P(A|B) = \frac{P(B|A)P(A)}{P(B)}$), to obtain the probability of each of the parameters, Q, given the observed trajectory, T:

$$P(Q|T) = \frac{P(T|Q)P_0(Q)}{P_0(T)} \tag{2.12}$$

$P_0(Q)$ is the *prior probability* of the parameter Q before the trajectory T is observed. For our purposes it is equal to 1 in the range of realistic values. Alternatively, one can also use Jeffreys prior as done by Masson et. al in [117]. $P_0(T)$, the *evidence of the model*, is a normalisation constant and also set to 1 as it is the same for all possible parameter values and, hence, does not affect their probabilities. $P(T|Q)$ is the *likelihood*, which we calculated using the Fokker-Planck equation, and effectively determines the probability of seeing the experimental data (i.e. the trajectory observed) within an environment described by the inferred characteristics (i.e. the parameters). Finally, $P(Q|T)$, the *a posteriori* probability of the inferred parameters given the observed trajectory. The inferred values are the values determined while maximising $P(Q|T)$ in the multiparameter space $\{Q_i\}$. The maxima are determined using a Broyden–Fletcher–Goldfarb–Shanno (BFGS) algorithm.

In order to determine the uncertainty of the values for the individual parameters obtained, a Monte Carlo sampling is performed. This stochastically changes the values of the parameters around the inferred value and recalculates the overall probability of the trajectory. This is repeated several thousand times and the probabilities around the maximum are sampled. As we move away from the optimal value, the probability decreases in both directions and we obtain *a posteriori* probability distribution for the parameter. Examples are shown in figures 2.4C and D. The width of this distribution gives us the uncertainty of our determined value and its maximum is the determined parameter value.

It is also worth mentioning that the BI algorithm only infers forces if these are truly present. In previously conducted work [161], the algorithm was used on a trajectory produced with a simulated flat box-potential. The inferred forces on the flat potential were all negligible with broad *a posteriori* probability distributions that included 0.

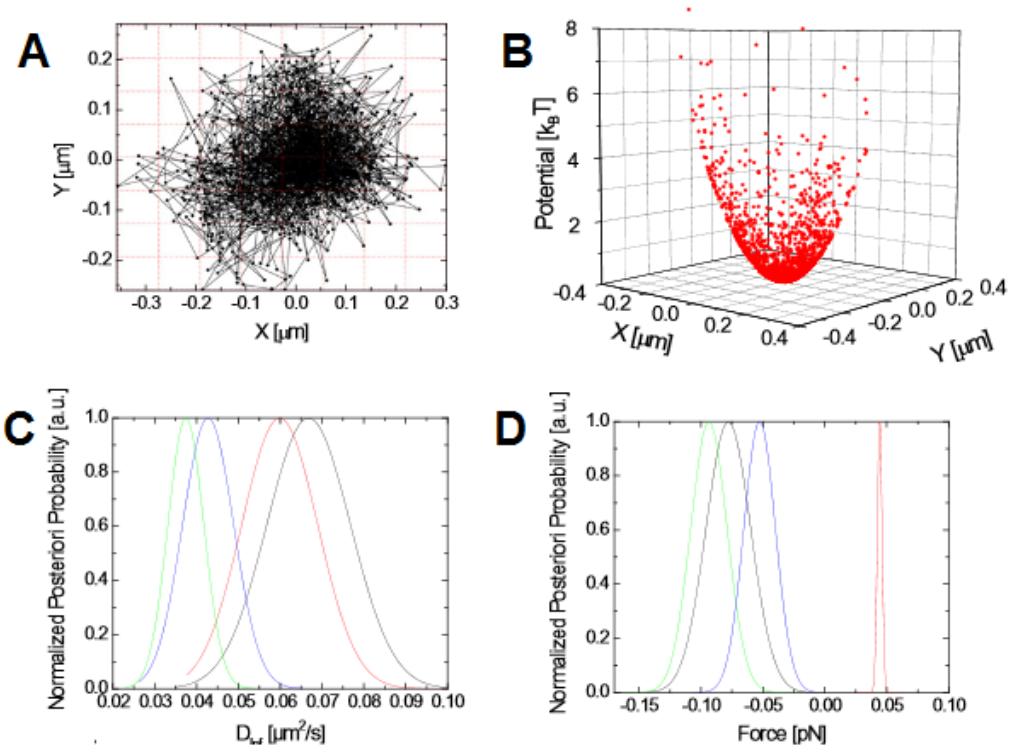

Figure 2.4: Example trajectory with inferred potential and *a posteriori* distributions. Trajectories exhibiting confinement (A) are used as inputs for the BI algorithm, which infers the relevant parameters that define the shape of the confinement potential (B). Each of the parameters has a probability distribution whose maximum is the inferred value and whose width provides us with that values uncertainty. (C) shows these distributions for diffusion coefficients, and (D) for inferred forces. Figure reproduced from [161].

Furthermore, reference [161] showed that Bayesian inference outperforms both the MSD and the residence-time analysis approaches.

2.3.2 Parameter Bias

In [161], Türkcan et al. describes a bias during the determination of trajectory parameters. This bias is dependent on the factor u,

$$u = \frac{D\Delta t}{A} \tag{2.13}$$

where D is the diffusion coefficient, Δt is the step size between consecutive points determined by the experimental acquisition time, and A the domain area.

u quantifies the extent of the extracted parameters' bias. It is a measure of comparison between the distance travelled during one step and the size of the confinement domain i.e. it quantifies how close the particle approaches the limit of the domain for when the particle moves. As the step size becomes larger the fact that it is not a freely diffusing particle will result in an underestimation of the diffusion coefficient, D. This underestimation then results in an overestimation of the confinement strength, since, as

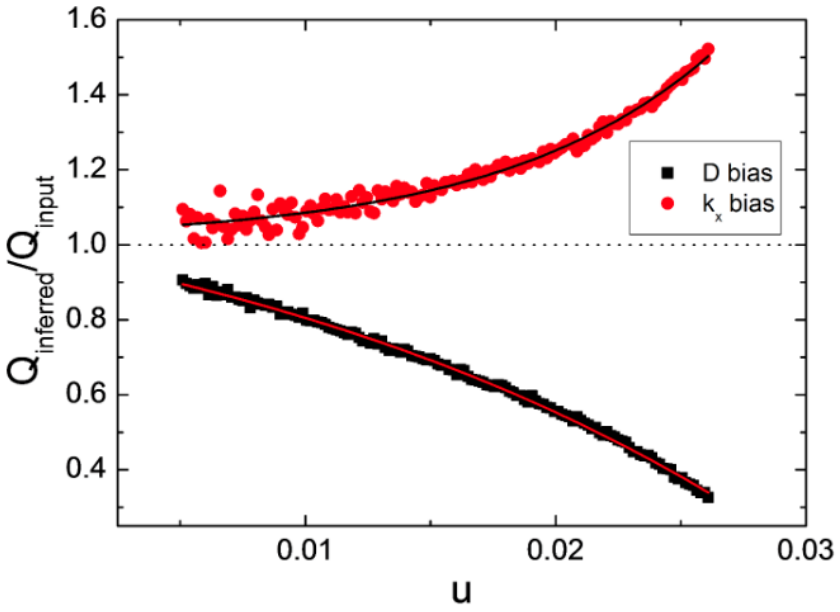

Figure 2.5: Bayesian inference algorithm bias curves. Example of the bias curves used for the analysis of trajectories recorded with optical tweezers in chapter 3. The bias is represented as the ratio of the inferred parameter to the input parameter value. The red labels show a progressive overestimation of the effective spring constant, k_x. Similarly, the black labels show a progressively underestimated diffusion coefficient. The data is then fit with a curve from which the bias can then be calculated and corrected for, for the experimental data. Bias curves obtained from simulated trajectories for $\Delta t = 91.8\ \mu s$ and $D = 0.3\mu m^2/s$. The trap stiffness $k_x = k_y$ was varied from 10^{-6} to 0.2 pN/nm. Trajectory lengths were simulated with 3000 points and data points are calculated as the averages of 30 numerical trajectories for each u value.

.

equation 2.7 shows, the diffusion term and the term for the confinement potential can compensate for each other. It has been shown that the accessible information decreases exponentially with rising u [164].

This bias effect can be simulated and corrected for. By numerically producing trajectories with appropriate input parameters and then using the Bayesian inference algorithm to infer these parameters, the discrepancy between the original values and the inferred values can be determined. This process can then be repeated for a range of u values by altering the potential and the bias of the parameters with respect to u can be determined. The results are then summarized in a bias curve as seen in figure 2.5 from which the bias for a parameter can be obtained. Note that these bias curves are only valid for the particular experimental parameters for which they have been calculated and must be determined again for each new set of experiments.

2.3.3 Variations of the algorithm

Throughout this work different versions of the Bayesian inference algorithm have been used, depending on their relevance and individual advantages and disadvantages, a common approach in Bayesian inference analysis. In each case it will be clarified which

Bayesian Inference Algorithm Versions

	Subdomains	Potential	Diffusion Coeff.	# of Q
Version 1	square grid	polynomial	global	$\frac{(\nu+1)(\nu+2)}{2}$
Version 2	square grid	polynomial	per subdomain	$\frac{(\nu+1)(\nu+2)}{2} - 1 + n$
Version 3	Voronoi grid	per subdomain	per subdomain	2n

Table 2.2: Table of different Bayesian Inference Algorithm versions used. The versions of the Bayesian inference algorithm used differ in the way they split the trajectory into subdomains (square grid or Voronoi grid), in the way they determine the potential (polynomial or subdomain specific), and in the assumption made for the diffusion coefficient (global or subdomain specific). ν is the order of the polynomial and n the number of subdomains.

version has been used and why, but an overview of the different capabilities is presented here in table 2.2. For all versions, the underlying principles outlined in section 2.3.1 uphold.

Version 1 and *version 2* [132, 161] use a different **domain partitioning** method than *version 3*. *Versions 1* and *2* divide the trajectory into square grids, the size of which is determined by taking the step length, $\sqrt{D\Delta t}$, the expected displacement during the time interval Δt, into account. The length of a subdomain is typically taken to be $1.5 \times \sqrt{D\Delta t}$ to ensure that a significant portion of trajectory points adjacent in time fall into the same subdomain. *Version 3*, on the other hand, proceeds in performing a k-means clustering algorithm (appendix B.1) to determine the position of cluster centroids and divides the trajectory points via Voronoi tessellation (appendix B.2). The main difference is that the Voronoi partitioning produces a more irregular pattern and can assign values over the entire area of the trajectory, even low-sampled regions, via the value of the nearest cluster centroid. It also uses a higher resolution where the concentration of points is higher.

Additionally, *versions 1* and *2* infer a polynomial when determining the potential shape. This means that the order of the polynomial extracted is determined by the experimenter. The output data are then simply the coefficients of the terms in the polynomial (see section 3.4.1 for more details on this). *Version 3* on the other hand infers the forces in each subdomain. The forces simply being the negative slope of the potential, the algorithm integrates over these to obtain the potential landscape. The advantage of the former approach is that it requires less computing time, because the number of inferred parameters is smaller, and, provided the potential is indeed polynomial, can give a more accurate representation. The latter, however, is more flexible in representing potentials of arbitrary shape.

Lastly, there is the difference in inferred diffusion coefficients. The diffusion coefficient can either be determined globally for the entire trajectory, or per subdomain. Determining a global diffusion coefficient provides less information on diffusive heterogeneities within the domain, but, provided the heterogeneities are small, may yield a more accurate number for the overall diffusivity. Assuming a global diffusion coefficient is fully justified in the case of a particle diffusing in water for example (see chapter 3).

The difference of the versions remains, firstly, in the way the domain is partitioned and how sub-domains are determined, and, secondly, in the choice of the output parameters. The output potential is either a polynomial, or relative potential values of sub-domains. Similarly, the diffusion coefficient can be inferred either globally or separately for each subdomain.

Other versions of the BI algorithm exist. These were not used in this work, but they do deserve to be briefly mentioned. An earlier version of the algorithm performed a square grid partinioning of the domain and inferred the forces in each domain to obtain force maps of the confinement [132]. *Version 3* of the algorithm, developed by Jean-Baptiste Masson and Mohamed El Beheiry, can also create a "quad-tree" subdomain mesh, whereby regions of higher data concentration are divided into a larger number of subdomains to obtain a higher spatial resolution [165].

2.4 Summary

This chapter introduced and explained the technique of single particle tracking referred to in chapter 1. Furthermore, the means to achieve SPT, the probes needed, the equipment and the imaging and analysis capabilities were detailed. We then presented how the, thus obtained, trajectories can be analysed. Either by considering the MSD curve, or by using an algorithm based on Bayesian statistics to infer trajectory parameters, which makes better use of the information available in the trajectory. This second option is what is made most use of throughout this work for analysing and comparing protein trajectories. This chapter along with the previous ones conclude the general background to the work presented and give us the necessary tools to dive into the presentation and discussion of the experimental findings.

Key points:

- Single particle tracking is a powerful tool for investigating the cell membrane architecture and its influence on receptor motion.
- Rare-earth doped nanoparticles present an ideal label for single particle tracking experiments due to their photostability and fluoresence lifetime.
- The trajectories obtained can be analysed with MSD curve to obtain information of the type on diffusion experienced.
- Using Bayesian statistics to infer relevant parameters of the receptor trajectory provides a powerful method for confined trajectory analysis, especially for investigating the confinement potential.

Chapter 3

Calibrating optical tweezers with Bayesian inference

If you can't measure something, you can't understand it. If you can't understand it, you can't control it. If you can't control it, you can't improve it.

H. James Harrington

Contents

Bayesian inference, as described in section 2.3, can also be used as a technique to calibrate optical tweezers. In fact, several advantages reveal themselves when using this approach compared to classical calibration methods. In this chapter, the apparatus and theory of optical tweezers are presented, followed by examples of recent scientific discoveries that have been made possible thanks to this technique. Then, an exposé of the conventional methods used to calibrate the setup is offered, and finally, the results of calibrating an experimental setup with Bayesian inference are presented and compared with the results obtained with the conventional methods. Additionally, results of simulations conducted to showcase the reasons for the superiority of the Bayesian inference approach are outlined and explained.

The content of this chapter has been published in reference [166].

3.1 Optical Tweezers

Optical tweezers have, since their conception in the 1970s by Arthur Ashkin [167], been an integral part of a biophysicist's repertoire for single molecule manipulation, and measuring and applying forces on the pico-Newton scale [168]. On the most basic level, optical tweezers use a laser to trap a micron-sized bead at the focus of the beam. The bead experiences two types of forces. The radiation pressure of the light acting in the direction of propagation, and a force due to the refraction of light within the bead. The rays refracted inside the dielectric bead (Figure 3.1) produce a change in momentum of the laser photons, which is compensated for by the movement of the bead. The figures show that the compensating motion of the bead is always towards the higher light intensity, i.e. the focus of the beam. Along the beam direction, the equilibrium position is slightly displaced from the focus due to the radiation pressure.

For small displacements of the bead from the equilibrium position, the divergence of the laser can be approximated to be linear and the displacement of the bead is proportional to the restoring force. This is analogous to a mechanical spring that, provided it is not extended beyond its elastic limit, will produce a restoring force proportional to its extension.

A quadrant photodiode (QPD), consisting of four individual optically active areas, is typically used to measure the displacement of the bead with respect to the trap centre by detecting the light transmitted around the bead. QPDs measure the difference in the left-right and top-bottom output voltages of their photodiode array to calculate the position change of the laser beam. This is then used to infer the bead displacement. The values given by the QPD are in Volts and need to be converted to micrometres before proceeding to trap calibration with Bayesian inference.

Being able to resolve forces at the pico-Newton level and step sizes at the nanometre scale has allowed biophysicists to gain insight into a variety of biological processes. It

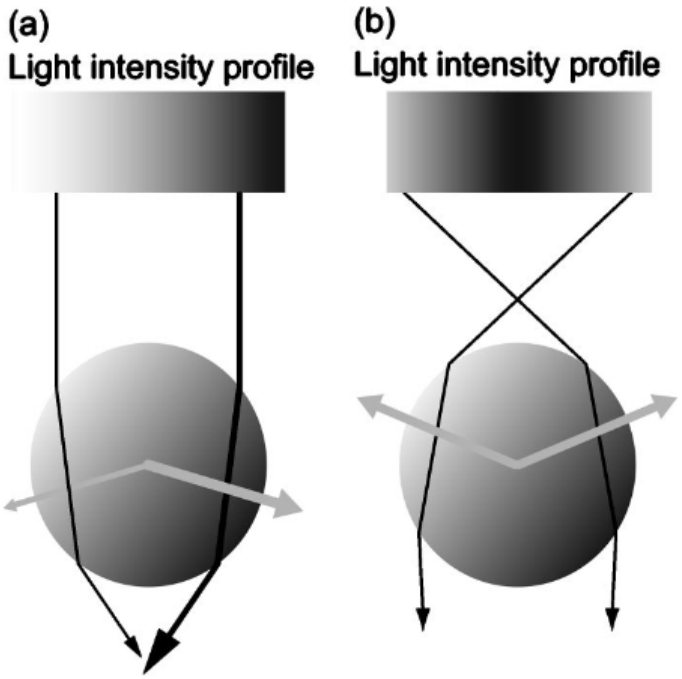

Figure 3.1: Laser ray geometry within a dielectric bead. The rays are refracted within the bead. The change of impulse given to the photons is compensated by an equal and opposite impulse on the bead. (a) shows that a lateral movement away from the centre produces a net force towards the centre of the beam. (b) shows a similar reaction to movement of the bead away from the focus of the beam along the beam's axis. Figure reproduced from [169].

has, for example, been possible to study the **elastic properties of DNA** [170, 171], and to unzip single DNA strands [172]. In 1996 Bustamante and coworkers stretched single molecules of double stranded DNA (dsDNA) [173]. They discovered that, at a force of approximately 65 pN, the molecules undergo a transition to a longer stable form and contract again as soon as the applied force drops below 65 pN.

Similarly, the **dynamics of molecular motors** [174–176], like Myosin-V, that was found to have a stepping length of approximately 36 nm, have been investigated [177, 178]. Moreover, numerous studies on the controversial stepping mechanism of the kinesin motor have been conducted [23, 179], determining a center-of-mass step size of around 10 nm for the protein's hand-over-hand walk [180].

Optical tweezers have been used to trap polystyrene and silicon beads, as well as biological matter (e.g. bacteria). By attaching molecules of interest to the beads, scientists have, among other things, been able to study the **mechanics of protein un-folding** [181]. One example is the work of Marqusee et al. who have succeeded in performing a complete unfolding and refolding of individual *Escherichia coli* ribonuclease H (RNase H) molecules [182]. By mapping the forces required, the energy landscape of RNase H was reconstructed. Similar expermients were done on titin by Bustamante and colleagues [183]. Using optical traps, this team was able to measure forces of 20 to 30 pN that were required to unfold the polypeptide. Even *in vivo* experiments conducted on

live cells are possible with optical traps [184]. In 2013, the trapping and manipulation of red blood cells in living mice was demonstrated by Li and coworkers [185].

The field of optical tweezers is highly dynamic and the boundaries of what is possible are continuously being expanded [186, 187]. Magnetic tweezers have been shown to produce multiplexed measurements and have been used in several biological applications [186, 188]. Another novelty is the development of an optical stretcher. This setup consists of a dual-beam that is used to deform micrometer-sized soft matter particles like cells. This technique has been used by Guck et al. to monitor the deformability changes in mouse fibroplasts and human breast epithelial cells transforming from normal to cancerous [189].

3.1.1 Multiple-beam Traps

More advanced techniques have been proposed that use multiple traps to manipulate objects. Visscher and colleagues [190] have done work with two kinds of multi-beam optical traps: the dual-beam trap and the time-sharing trap. The dual beam trap, as the name suggests, is just a trap comprised of two laser beams acting as traps. These are produced by splitting a single laser beam with a polarizing beam-splitting cube, producing two orthogonally polarized beams.

The time-sharing optical trap uses a slightly more complicated setup. This method is able to produce several simultaneous trapping lasers by scanning the laser position back and forth within the sample plane. If this is done quickly enough, the laser produces multiple steady-like illuminations at the desired trap locations. A second laser is then used for position detection of the beads.

Recent work by Rief and coworkers used a maximum likelihood approach to calibrate a dual-beam setup [191]. They reported that an additional advantage of this technique is to obtain parameter values of more sophisticated experiments, such as the viscoelastic properties of tethered proteins between the two traps. Multiple tweezers have made it possible to study new experimental geometries, measure independent forces simultaneously and even bend micron-sized structures. An example of the latter is a study of microtubule stiffness [190], previously impossible with single beam traps.

3.2 Conventional Methods to Calibrate Optical Tweezers

There are several methods that have been used to calibrate optical tweezers, each with their respective advantages and drawbacks.

In addition to the single beam methods presented here, it is worth mentioning that there are also techniques that use a second, low-power laser for independent position detection of the trapped bead [192, 193]. This approach has the advantage of having measurement system independent of the trapping laser. This provides a way to measure the absolute bead position, and not only the relative position of the bead with respect to the beam.

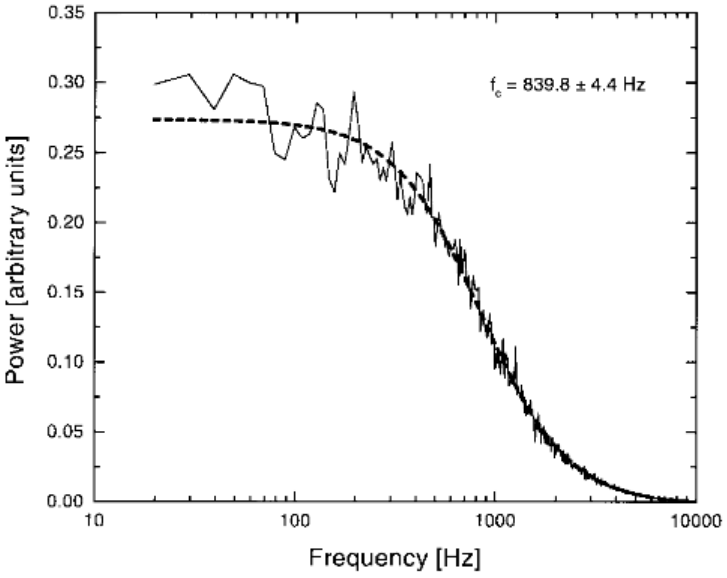

Figure 3.2: An example of a power-spectrum fit with a Lorentzian. Figure reproduced from [190].

One advantage is that the position measuring system is easier to calibrate, the setup, however, is fairly complicated to set up, as the added complications of combining and separating the two lasers quickly outweigh the added advantages.

Here, the Bayesian inference calibration approach will be compared to the power spectrum method and the equipartition method. However, for completeness, the step response method, the drag force method and the escape force method are also presented.

3.2.1 Power-spectrum method

The Power-spectrum method is arguably the most widely used method for calibrating an optical tweezers setup [194, 195]. It performs a Fourier transform on the random thermal motion, $\mathbf{r}(\mathrm{t})$, of the bead within the trap. A Lorentzian curve is then fit to the resulting data from which the cut-off frequency can be deduced:

$$P(f) = \frac{k_B T}{2\gamma\pi^2(f^2 + f_c^2)} \tag{3.1}$$

This cut-off frequency, f_c, can be related to the one-dimensional effective spring constant of the trap via the following equation , where γ is the drag coefficient:

$$f_c = \frac{k_x}{2\pi\gamma} \tag{3.2}$$

Obtaining the correct value for the effective spring constant is thus dependent on the accuracy of the additional parameters required. Notably, the values of the medium

viscosity, η, in which the bead resides and the bead radius, a, are needed, the drag coefficient being given by $\gamma = 6\pi\eta a$.

An advantage of this technique is its ability to detect slight imperfections, like beam misalignment or a non-Gaussian beam, in the setup. In these cases, the spectrum becomes non-Lorentzian or can produce peaks at specific noise frequencies.

3.2.2 Equipartition method

Similarly to the power-spectrum method, the equipartition method takes the one dimensional random thermal motion of the trapped bead and calculates the corresponding mean squared displacement [169]. This is then used to calculate the potential energy of the bead in the trap and equate it to its thermal energy according to the equipartition theorem:

$$\frac{1}{2}k_B T = \frac{1}{2}k_x\langle x^2\rangle \tag{3.3}$$

Some drawbacks can already be identified. This method requires a large information content within the data. To obtain a faithful representation of the potential after averaging, very long trajectories are necessary. Additionally, this technique is highly susceptible to mechanical drift of the setup. For data sets that contain drift, the $\langle x^2\rangle$ term will be overestimated and, consequently, the effective spring constant will be underestimated. Care must also be taken that the bead only explores the region within the trap that can be approximated to be harmonic, provided the beam is Gaussian.

3.2.3 Step-response method

The step-response method calibrates the trap by applying a sudden displacement to the trap and observing the recovery of the bead towards the trap centre [196]. This motion is described by the exponential recovery equation 3.4 characterised by a time constant τ. τ is related to the trap stiffness k by equation 3.5

$$x = x_{step}(1 - e^{-t/\tau}) \tag{3.4}$$

$$\tau = \frac{6\pi\eta a}{k} \tag{3.5}$$

.

Here, again, care must be taken that the initial step taken is not too large and that the bead remains in the linear region of the trap.

3.2.4 Drag-force method

The drag-force method uses a drag force for calibration [197]. The trap is moved at a constant velocity, v, moving the bead through the medium and producing a constant force on the bead according to Stokes' law, equation 3.6.

$$F_{drag} = 6\pi\eta a v \tag{3.6}$$

This displaces the bead from the centre until the restoring force of the trap equals the drag force. At that point, the displacement, Δx, can be measured and the two forces can be equated. The effective spring constant of the trap can be calculated via the following equation:

$$k_x = \frac{6\pi\eta a v}{\Delta x} \tag{3.7}$$

3.2.5 Escape-force method

The escape-force method, similar to the drag-force method in section 3.2.4, moves the bead through the solution to apply a force until the bead escapes the trap [198–200]. The minimum force required for the escape of the bead is thus determined. This is a fairly rudimentary method compared to the other approaches, as the calibration takes place at the trap's border. Yet, the force at the trap border can still be determined to about 10%.

3.3 Experimental setup

Experimental trajectories used for calibration were recorded by Antoine Le Gall and Nicolas Fiszman in the group of Karen Perronet and Nathalie Westbrook at the Laboratoire Charles Fabry in the Institut d'Optique.

The trajectories of the trapped beads were obtained using an inverted microscope (Olympus IX70) with an oil-immersion objective (Olympus PlanApo 60X, NA=1.45). For bead trapping and detection a Nd:YAG laser (Quantum Laser, model Forte 1064, TEM00, 1W cw) was used. The laser beam was diffracted with an acousto-optic deflector (AOD) (Intra Action Corp. DTD-274HA6) located in a plane conjugated with the back focal plane of the objective. A feedback loop was put in place to ensure a constant laser intensity at the entrance of the objective during experiments.

The transmitted light was collected using a high numerical aperture condenser (Olympus Aplanat Achromat, NA = 1.4) and directed toward a QPD (SPOT-9DMI, OSI Optoelectronics) situated in a plane conjugated with the back focal plane of the microscope objective. The cutoff frequency of the QPD is a few kHz (5-10 kHz depending on the incident laser power). The four readings of the QPD were digitised simultaneously with

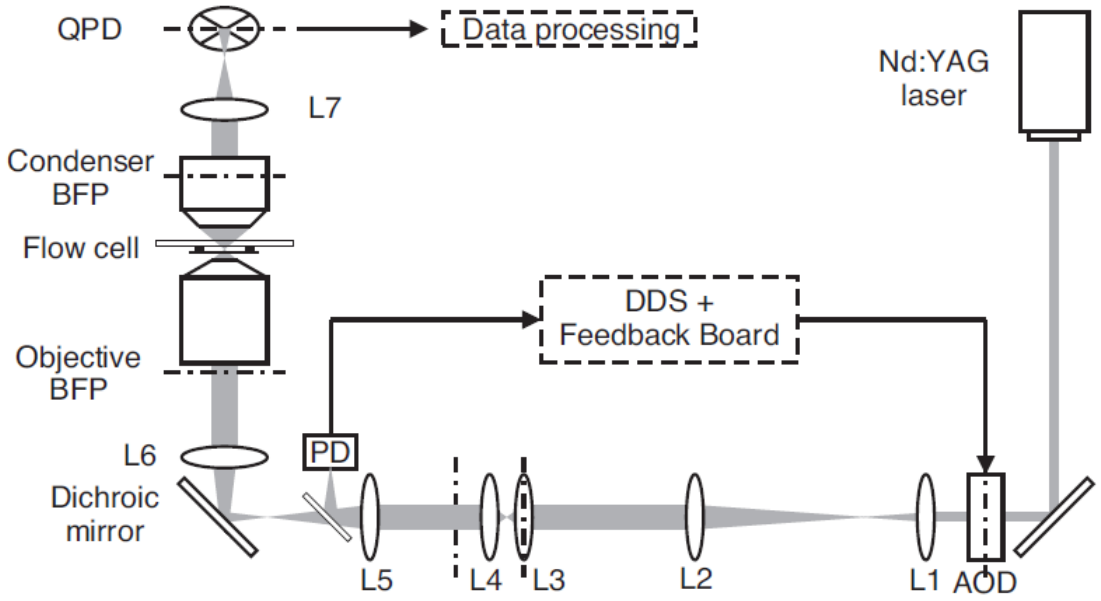

Figure 3.3: Conceptual diagram of the optical trap setup. A diagram of the optical trap setup used to record the two sets of experimental trajectories used in the analysis. An acousto-optical deflector (AOD) is used for trap deflection in experiments using step-response calibration. A photodiode (PD) is used to probe and maintain the laser power constant via a feedback board and a direct digital synthesiser (DDS) that controled the AOD. To fill the entire pupil of the objective, a beam expander was inserted in the beam path (L1 and L2). A quadrant photodiode (QPD) measures the signal transmission in a plane conjugate to the back focal plane of the microscope objective. Conjugate planes are represented by dotted lines. Figure reproduced from [196].

a sampling rate of 65,536 Hz using a Delta Sigma DAC (National Instrument, PCI 4474). Subsequent processing of the data was done using LabView 8.2 and the displacement signals were normalized by the sum of all quadrant readings before calibration. Bangs Laboratories supplied the silica beads (SS03N, 1 μm diameter).

QPD calibration during experiments was done using the step-response method [196]. The QPD can only register bead motion relative to the trap centre and not absolute motion, since it is located in a plane conjugated with the condenser back focal plane. Therefore, during step-response calibration, displacing the trap rapidly with the AOD produces a spike of the QPD signal. The displacement can be correlated to the signal peak yielding the QPD conversion factor from V to μm.

For the complete optical setup refer to [196].

The inference was done as explained in section 2.3. Unless otherwise indicated, every sixth point of the trajectories sampled at 65,536 Hz were taken for reasons explained in section 3.4.2.

The power spectrum analysis was done with a MATLAB algorithm as described in [201, 202]. For the short trajectories of figure 3.6, some of the input values had to be chosen outside the recommended range for the program to work.

3.4 Bayesian inference for calibrating optical tweezers

3.4.1 Determining the trap spring constants

We already outlined the principle of the Bayesian inference algorithm [132, 133, 161, 203] and its general application in section 2.3. Assuming that the trapping potential is of second order within the area of the trajectory, as is further discussed in section 3.6.2, we used a second-order polynomial of the form below to infer the shape of the potential:

$$V_{2^{nd}order} = C + C_x x + C_y y + C_{xx} x^2 + C_{xy} xy + C_{yy} y^2 \tag{3.8}$$

The first-order coefficients we obtain consistently have negligible values, leaving us with the second order coefficients. From these, we deduce the spring constants in the x and y direction, respectively.

$$k_x = 2C_{xx} \tag{3.9}$$

$$k_y = 2C_{yy} \tag{3.10}$$

Figure 3.4A shows an example input trajectory, and figure 3.4B shows the potential we infer.

Naturally, the obtained spring constant values, along with the obtained diffusion coefficients, undergo the bias correction described in section 2.3.2. However, due to the extremely high sampling rate during trajectory acquisition and the resulting low u value (~ 0.02), this correction remains minor.

3.4.2 Non-instantaneous response of photodiode

QPDs with a finite cut-off frequencies used to acquire bead positions suffer from a "memory effect" due to the non-instantaneous response time of the diode [194]. The response function of the photodiode, $g(t)$, can be described by an instantaneous response fraction $\alpha^{(diode)}$ and a non-instantaneous term with a characteristic decay time τ:

$$g(t) = \alpha^{(diode)}\delta(t) + (1 - \alpha^{(diode)})\frac{1}{\tau}e^{-\frac{t}{\tau}} \tag{3.11}$$

The signal detected by the QPD is then given by equation 3.12, where $S(t)$ is the actual signal and $S^{(det)}$ is the recorded signal.

$$S^{(det)} = \int_{-\infty}^{t} dt' \cdot g(t - t') \cdot S(t') \tag{3.12}$$

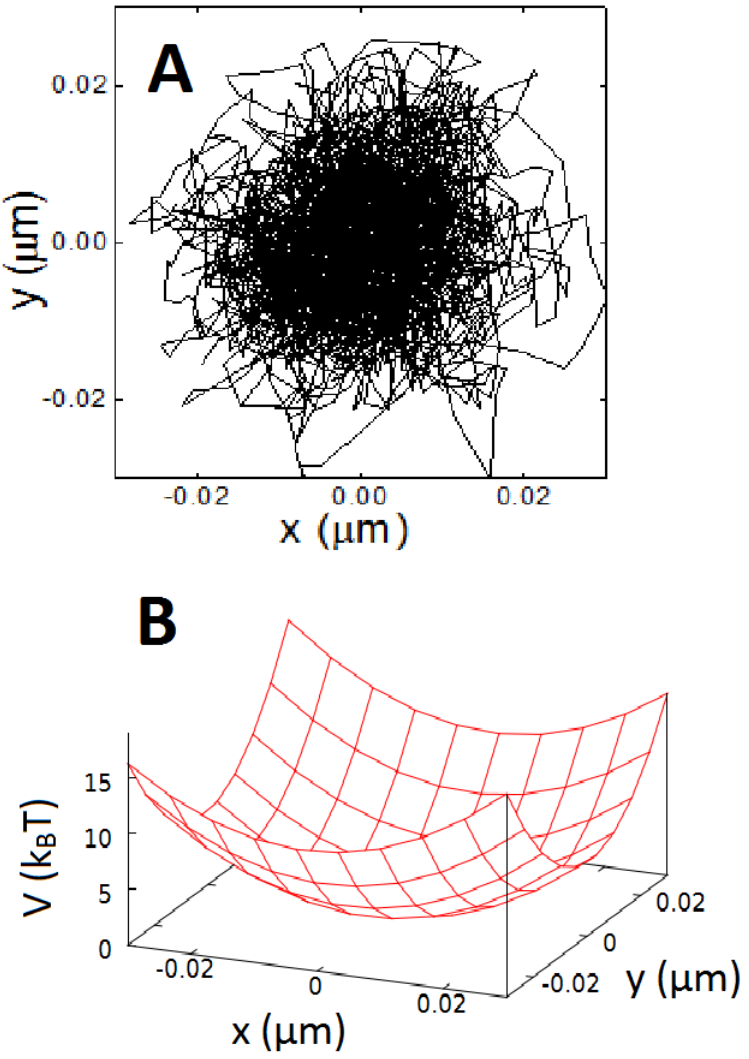

Figure 3.4: Bayesian inference algorithm input and output. The Bayesian inference algorithm only needs a trajectory (A) as an input. It then uses the information contained in the trajectory to extract the confinement potential (B) experienced by the bead in the trap.

The acquisition rate for bead positions was 65,536 Hz. Given that the cut-off frequency of the photodiode was a few kHz, we considered that by taking every sixth point of the trajectory we were effectively eliminating the non-instantaneous contribution, since the residue of the response due to the previously recorded point will have sufficiently decayed. This was verified by adding the non-instantaneous response to simulated trajectories. Analysing these after taking only every sixth point confirmed a sufficient decay by determining the correct trap stiffness. However, it should be noted that the bias correction needs to be adjusted accordingly as the time step size increases six-fold.

3.5 Performance of the Bayesian inference Calibration

3.5.1 Simulated Trajectories

To simulate experimental trajectories the same method as in reference [132] was used. A program using C simulates Brownian motion in a confining potential field. Random steps in the x and y direction were produced using a Gaussian distribution with a width of $\sqrt{2D\Delta t}$. D and Δt were chosen to reproduce experimental conditions. During the time step Δt the particle takes 10,000 non-averaged sub-steps. The confining potential is represented by $V(x,y) = \frac{1}{2}kx^2 + \frac{1}{2}ky^2$. From this, the position dependent confining force is calculated and the resulting displacement is added to each step. Positioning noise was neglected for this case. Figure 2.5 shows that applying Bayesian inference to these simulated trajectories yields the correct trap spring constant provided the deterministic bias is corrected.

3.5.2 Effect of drift on the calibration accuracy

As previously mentioned in section 3.2.2, the equipartition method may be prone to underestimate the effective spring constant of a trap due to an overestimation of the $< x^2 >$ term. This could be a consequence of mechanical drift in the experimental setup. Here, we test the effects of a constant drift on the ability of the equipartition method and the Bayesian inference method to extract the correct trap spring constants from a set of simulated trajectories.

The results of these tests are shown in figure 3.5. Each data point is the result of averaging the results of 20 trajectories. The drift builds up linearly during the duration of the entire trajectory. The simulated trajectories analysed with the equipartition method were 45,000 points long with a step size of 15.3 μs. As outlined is section 3.4.2, for analysis with Bayesian inference every sixth point was taken and the analysed trajectory had a length of 7,500 points with a step size of 91.8 μs. The diffusion coefficient, D, used was 0.3 μm^2/s and the effective spring constant, k_x, 0.06 pN/nm.

The obtained values for k_x with respect to the input value diverge drastically for the equipartition method, as the drift increases. For low drifts, the ratios of $k_{x_{determined}}$ to $k_{x_{input}}$ for both methods are virtually identical and close to 1. However, as drift increases to 5 nm over the length of the trajectory, the equipartition method results already experience a 5% divergence from the true value, whereas the Bayesian inference method still obtains the correct value for k_x. Between 5 nm drift and 10 nm drift, the equipartition method results diverge drastically and finish at being more than 30% off the correct value. The Bayesian inference method, on the other hand, ends up only 5% off the actual input value.

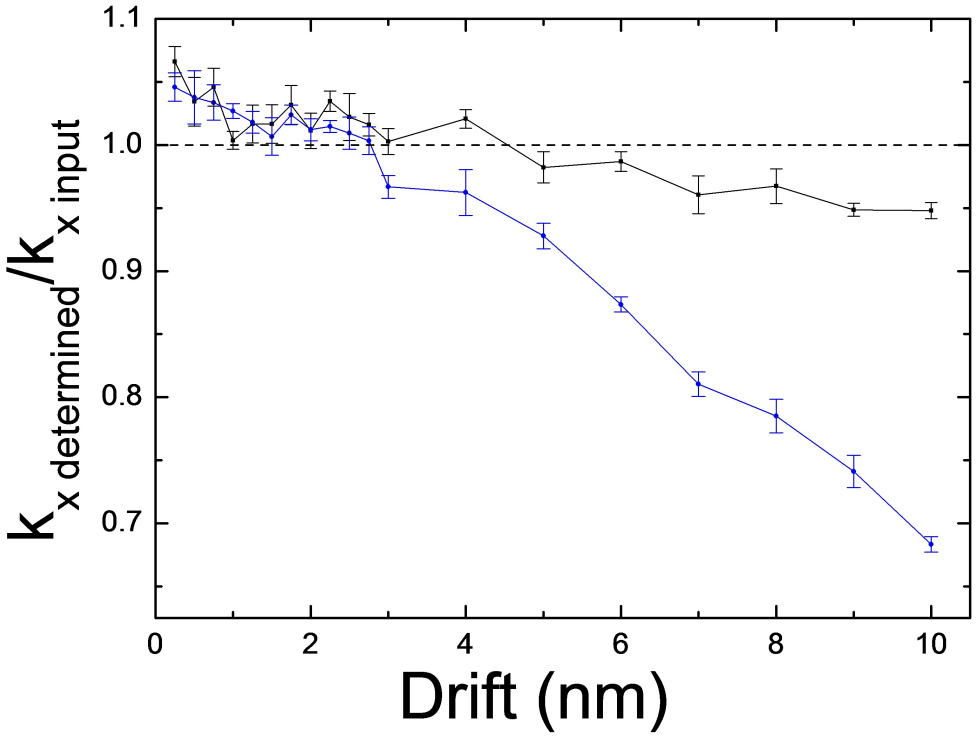

Figure 3.5: Drift dependence of optical tweezer calibration methods. A drift is simulated over the entire length of a trajectory. For each drift 20 trajectories are simulated and are then analysed with the equipartition method (blue) and the Bayesian inference method (black). The artificial drift produces a large bias in the effective spring stiffness determined by the equipartition method.

3.5.3 Dependence on information content

For the Bayesian inference to obtain reliable values, a trajectory length of approximately 1000 points is needed. However, the algorithm can obtain acceptable results (with a correspondingly greater uncertainty) for as little as a few hundred points. To compare this ability to the capacities of the equipartition and the power-spectrum method, a series of simulations were conducted, using numerically computed trajectories of varying lengths. Similar to the trajectories simulated in section 3.5.1, the initial trajectory parameters (i.e. diffusion coefficient, k_x, etc.) were chosen in accordance to experimental observations ($D = 0.3\mu m^2/\text{s}$, $k = 0.06$ pN/nm), and the data points are obtained by averaging the results for 20 trajectories.

Figure 3.6A shows how the different calibration techniques compare for varying trajectory lengths. The determined value of k_x by each approach is normalised with respect to the input value. We see that, as the information content (i.e. the trajectory length) decreases, the power-spectrum method begins to diverge most strongly from the true value. For short trajectories, there is a significant bias associated with the values determined by the equipartition method. Meanwhile, the Bayesian inference algorithm continues to obtain values close to the real values for as little as 100 points.

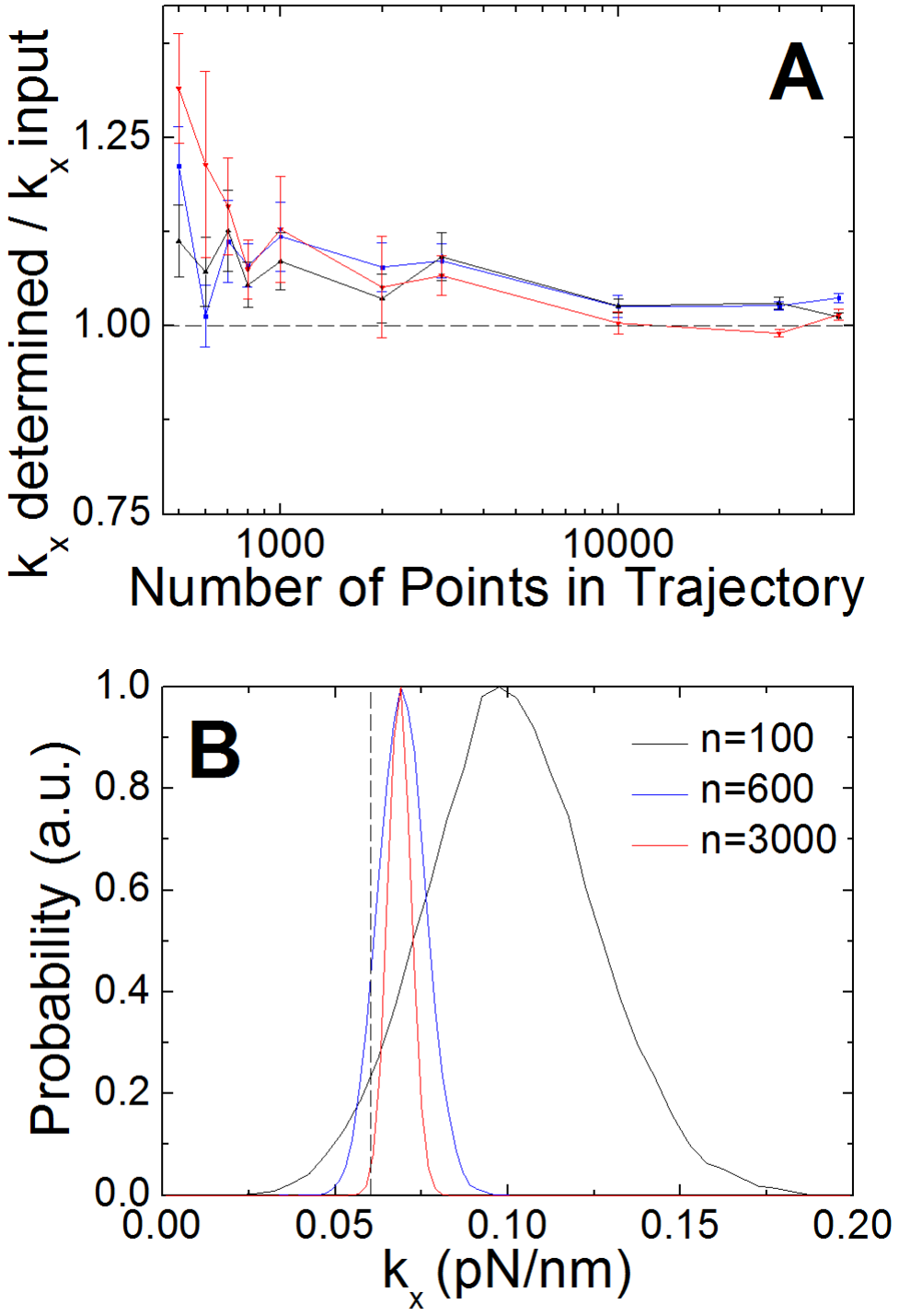

Figure 3.6: Trajectory length dependence of optical tweezer calibration methods. Trajectories with different lengths were simulated. The equipartition, the power-spectrum, and the BI method were then used to extract the trap's spring constant. In (A) the data show the effectiveness of the equipartition method's (blue), the power spectrum method (red) and the Bayesian inference method (black) in determining the input spring constant. (B) shows the *a posteriori* probability distribution of three trajectories analyses with Bayesian inference. Note the increase in bias and distribution width (i.e. error) as the number of points per trajectory decrease.

What is not shown in figure 3.6A is that the power spectrum algorithm used [201] increasingly fails to obtain any value at all for decreasing input trajectory points. By 500 points per trajectory, about one quarter of trials fail.

Figure 3.6B gives a somewhat deeper insight into the reaction of the Bayesian inference algorithm to low-information input. The curves depict the *a posteriori* probability distributions of the three k_x values determined from three different trajectory lengths. The input value for k_x was 0.05 pN/nm. We see a slight bias for the values determined from trajectories of length 600 and 3000 points. We also note that the distribution is broader for the shorter trajectory representing a larger uncertainty of the determined value. The *a posteriori* distribution obtained from a 100-point trajectory displays both a larger bias and width. We note, however, that the increased bias can be accounted for via the bias correction explained in section 2.3.2.

For trajectories of 600 points or less, it was still necessary to address the memory effect as described in section 3.4.2. However, to avoid wasting precious information, we continued using every 6th point to remove the non-instantaneous QPD response, but also sampled all consecutive sets of every sixth point. These were then recombined to obtain a trajectory of the initial length.

3.6 Calibration of Experimental Trajectories

Two sets of experimental data were used. The first set consisted of trajectories recorded with different laser powers ranging from 60 mW to 500 mW. The second set of trajectories was recorded with varying distances between the trapped bead and the cover slip surface. The potentials inferred using the Bayesian inference algorithm are shown in figure 3.7. Figure 3.7A displays the potentials for varying laser powers. As the laser power increases, the curvature of the potential increases and the effective spring stiffness rises as well, in line with expectations. The potentials determined for various bead heights in figure 3.7B show an increase in potential curvature as height decreases and the bead approaches the surface. As the bead approaches the surface, the effective viscosity it feels increases [194, 204, 205]. Consequently, the diffusion coefficient decreases as the distance to the surface decreases and the determined spring constant increases. It is also worth considering that, for large distances from the surface, spherical aberrations may affect trap stiffness due to the refractive index change at the coverslip-water interface [206].

3.6.1 Comparison between BI, equipartition, and power-spectrum calibration results

Figure 3.8 shows the quantitative results of the three methods for determining the effective trap spring constant in the x direction. As expected, we found a linear relation between the laser power and the determined spring constant [167, 200, 207]. In both the cases of changing laser power and trap height, in figures 3.8 A and B respectively,

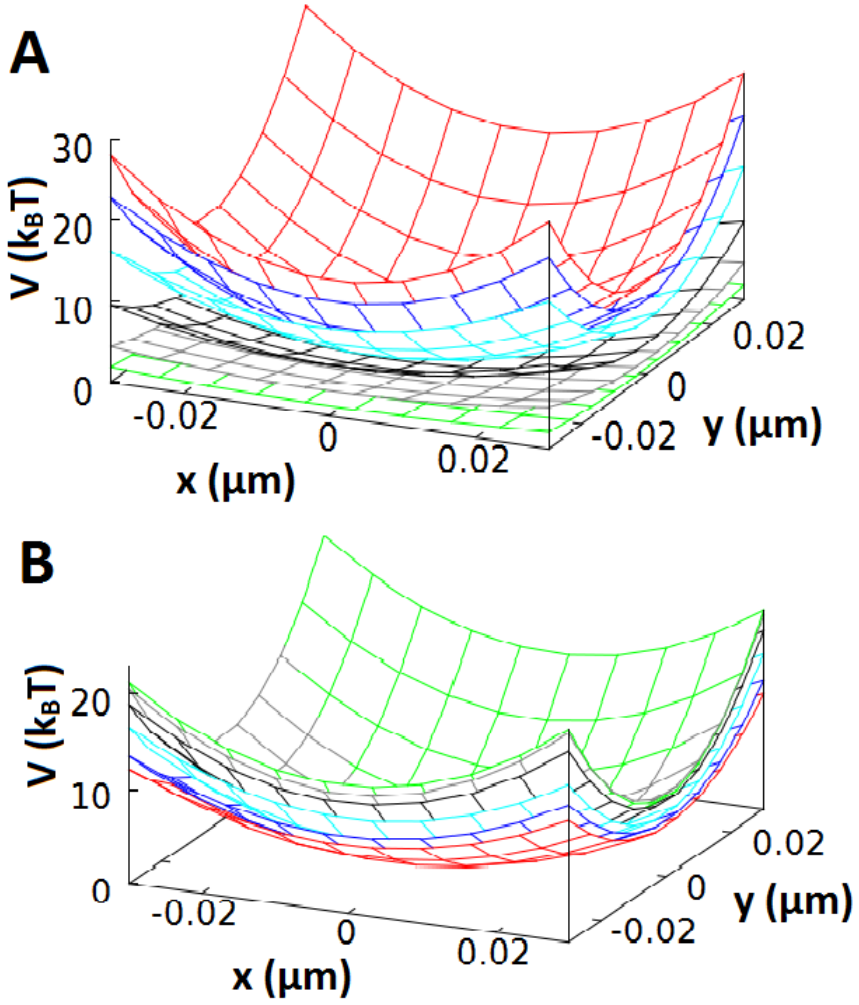

Figure 3.7: Potentials inferred from the experimental trajectories. Inferred potentials from two sets of experimental trajectories. (A) set of trajectories with changing laser powers (60, 138, 251, 377, 466, 500 mW)(k_x from 0.007 to 0.08 pN/nm), increasing from green to red. (B) set of varying bead heights (21.5, 16, 11, 6, 4, 2 μm)(k_x from 0.04 to 0.06 pN/nm). Bead heights decrease from red to green.

the equipartition method and Bayesian inference method obtain similar results. However, the power-spectrum method, especially for the changing heights in B, displays a significant divergence from the results obtained by the other two methods.

The most probable reason for this discrepancy is the dependence of the power-spectrum method on extra parameters for calculating the effective spring constant. When considering equations 3.1 and 3.2, we see that the radius of the bead is required. When performing the calibration, we used the nominal bead radius of 500 nm as quoted by the supplier. However, using dynamic light scattering (DLS), we find a maximum of 436 nm with a full width at half-maximum of 184 nm (see figure 3.9). This could explain the overestimation of the spring constant by the power-spectrum method.

On the other hand, Bayesian inference does not require any input parameters other than the trajectory. In fact, the bead radius can be determined from the diffusion

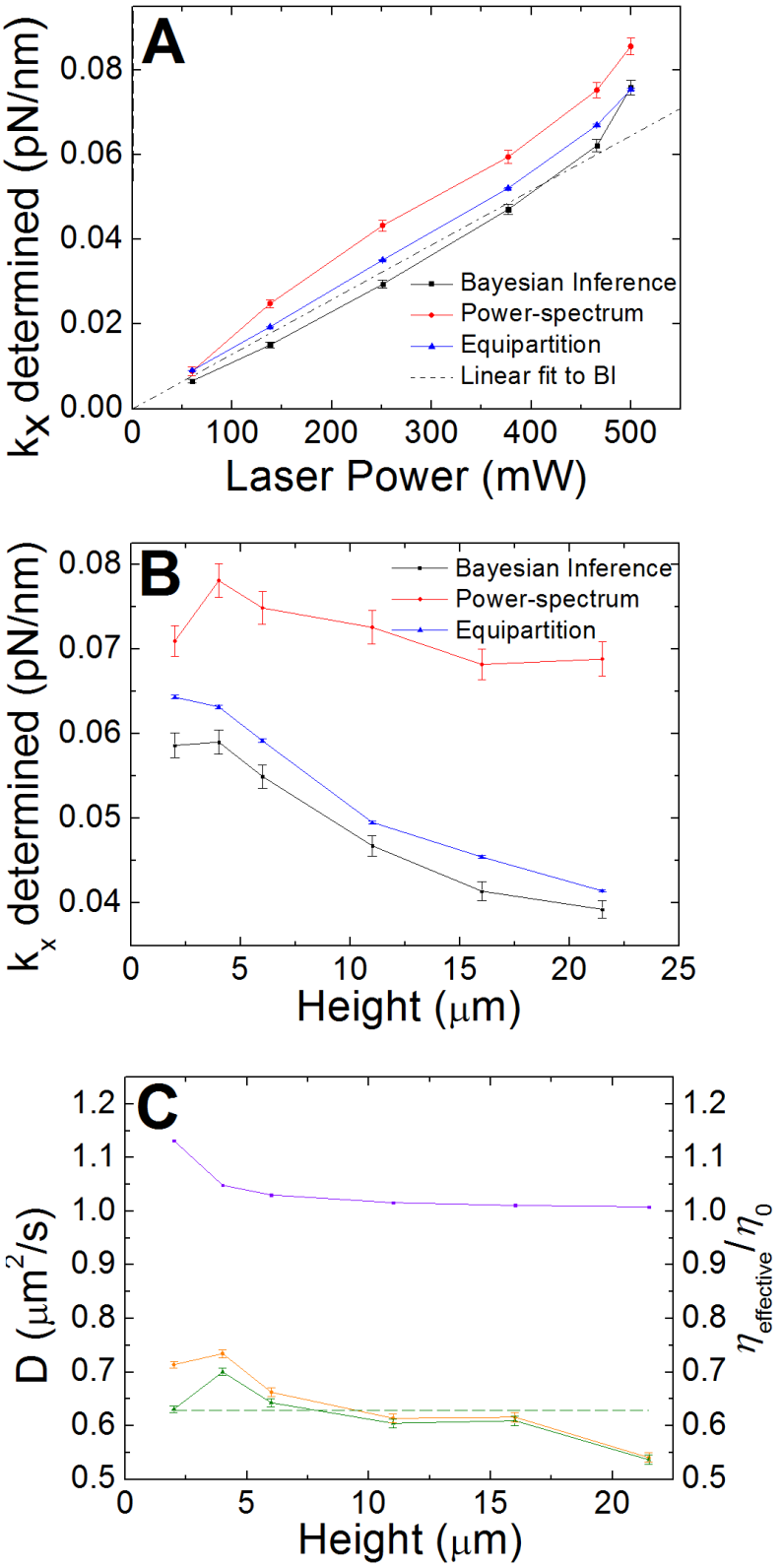

Figure 3.8: Experimental results for calibrating with different methods. Results determined for k_x with the equipartition (blue), the power-spectrum (red), and the Bayesian inference method (black). (A) Results for the data set of changing laser powers. (B) are the results for changing bead heights. (C) shows how the diffusion coefficient can be determined by considering how the effective viscosity experienced by the bead changes as a function of distance to the surface.

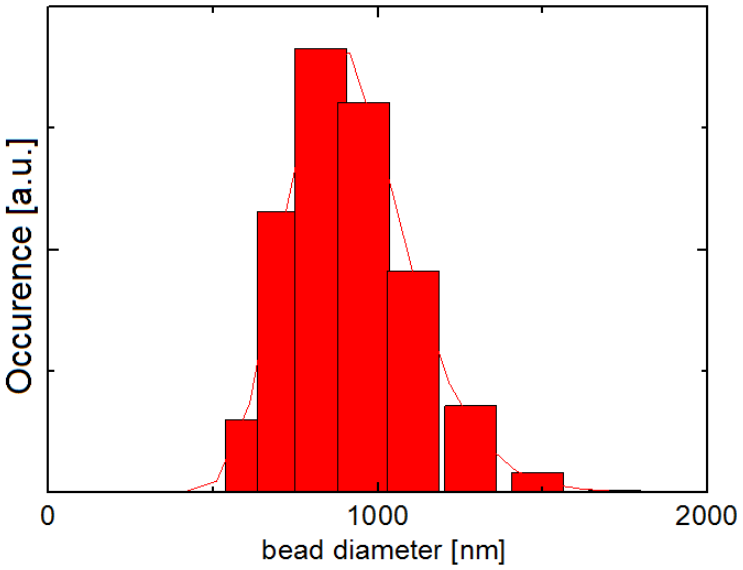

Figure 3.9: Dynamic light scattering distribution of bead sizes. Bead diameter distribution determined using dynamic light scattering (DLS). The distribution maximum is at 872 nm giving a most likely bead radius of 436 nm.

coefficient found via Bayesian inference. Taking the diffusion coefficient, $D = 0.62 \pm 0.01$ $\mu m^2/\text{s}$, determined as discussed below, we can use the Einstein-Stokes equation and water viscosity at 20°C, $\eta = 10^{-3}\ Pa \cdot s$, to calculate the bead radius. The radius was, in this way, determined to be 358 ± 4 nm. Given the polydispersity of the bead solution and that DLS overestimates the contribution of larger particles [208], the determined bead radius is compatible with the DLS measurements.

The power spectrum-method can also be used to determine the bead radius. The y-intercept of the Lorentzian from equation 3.1 can be used to obtain the diffusion coefficient. If we take another look at equation 3.2, and consider the fluctuation dissipation theorem, $D = k_B T/\gamma$, we notice that when we set $f = 0$ we obtain the following equation for the bead diffusion:

$$P(0) = \frac{D}{2\pi^2 f_c^2} \tag{3.13}$$

.

From this relation, the diffusion coefficient and the radius can be determined. However, for data at low frequencies there is usually a significant amount of noise which does not permit an accurate determination of the diffusion coefficient. With this approach, we obtain a bead radius of 154 ± 5 nm is obtained. This value is clearly much lower than what was obtained using DLS or Bayesian inference.

An alternative method for determining the bead radius has been proposed by Gosse and Croquette [209], which is based on the observation that the power spectrum of velocity fluctuations asymptotically approaches a value proportional to the diffusion coefficient at high frequencies. The asymptotic value, however, can only be determined if the cut-off frequency of the acquisition system is much higher that that of the trap. Usually,

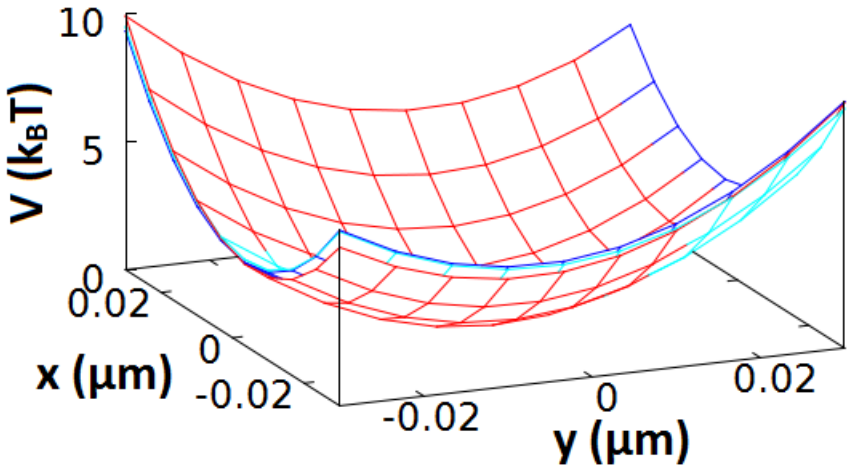

Figure 3.10: Second, fourth and sixth order potentials extracted from an experimental trajectory. Second (red), fourth (dark blue) and sixth order (light blue) potentials are superimposed to show that there is no significant difference between the determined potentials. This demonstrates that the additional parameters provided by the fourth and sixth order potentials do not contribute and the potential is truly second order.

for trap stiffnesses of approximately 10^{-4} pN/nm ($f_c \approx 2$ kHz for a 1-μm bead), the cut-off frequency of most used QPD is too low for allowing an exact determination of the diffusion coefficient and, hence, bead radius.

As discussed above, the distance of the bead from the surface modifies the effective viscosity felt by the bead. This dependence can be calculated using Faxen's law [205], equation 3.14, in which R is the bead radius and h the distance to the surface.

$$\eta_{Faxen}(R/h) = \frac{\eta_0}{1 - (\frac{9R}{19h}) + (\frac{R^3}{8h^3}) - (\frac{45R^4}{256h^4}) - (\frac{R^5}{16h^5}) + ...} \tag{3.14}$$

The orange curve in figure 3.8C shows the diffusion coefficients determined by the Bayesian inference method for the data set of changing bead heights. We can use equation 3.14 (purple curve) to correct the height-dependent change in diffusion coefficient. The corrected diffusion coefficient is depicted by the green curve.

3.6.2 The trapping potential is a second-order potential

In order to confirm that the potential observed is truly a second order potential, we also ran the Bayesian inference algorithm assuming fourth- and sixth-order potentials. The resulting second-order parameters found did not change significantly compared to the values already obtained assuming a second-order potential, and the additional third- to sixth-order parameters were all of negligible magnitude.

Figure 3.10 shows the second-, fourth- and sixth-order potentials extracted using a sample input trajectory. Clearly the potentials do not differ significantly from one

another, meaning that a second order potential is a satisfactory representation of the confinement potential experienced by the bead inside the optical trap.

The fact that we can extract a full potential from the trajectory permits us to determine if there are any deviations from the expected parabolic potential. The additional linear and cross terms, as well as the possibility to extract a potential of higher order can serve to determine the presence of aberrations in holographic optical traps [210], or for considering regions within the trap where the linear force approximation does not apply [211].

3.7 Discussion and Conclusion

In this chapter we demonstrated that, using Bayesian inference, we can calibrate an optical tweezers setup using, as the only inputs, the observed bead trajectory. The optical trap produces a harmonic potential and the corresponding polynomial can be inferred. This gives an accurate estimate of the effective spring constant.

When comparing the effectiveness of the Bayesian inference algorithm to two standard calibration methods, we saw several advantages in using Bayesian inference. Firstly, Bayesian inference does not require additional parameters. The power-spectrum method, on the other hand, requires the bead radius and the fluid viscosity. Inexact knowledge of these can distort the results obtained using this method. Furthermore, the Bayesian inference algorithm is significantly less affected by mechanical drift of the setup than the equipartition method. Where the later already displays a grossly underestimated trap stiffness for a drift of several nanometres, the former still remains close to the true value.

Finally, the Bayesian inference method requires the least amount of points to perform a calibration. This may prove crucial in cases where the trap calibration is performed post-experiment and the bead escapes the trap. Being able to perform a calibration with a minimum number of points can, therefore, be critical for exploiting the experiment.

Key points:

- Optical tweezers are an essential tool for studying biophysical phenomena.
- Bayesian inference can be used to infer confinement potentials and effective spring constants of optical traps.
- The results using the Bayesian inference method are less affected by drift than the equipartition method.
- The Bayesian inference algorithm only requires a trajectory and no extra input parameters. It thus requires less input information than the power-spectrum method.
- The potentials obtained with the Bayesian inference algorithm can be used to determine deviations from a perfect harmonic potential.

Chapter 4

Membrane Receptor Dynamics

See now the power of truth; the same experiment which at first glance seemed to show one thing, when more carefully examined, assures us of the contrary.

Galileo Galilei

Contents

4.1 Peptidic Toxin Receptors Confined in Lipid Rafts

To set the stage, a brief introduction of the previous work done by Silvan Türkcan will be given. Alternatively, this can also be consulted in publications [133, 148, 161]. Most of the results presented in this chapter were published in references [203] and [212].

The ϵ- and α-toxins of the bacteria *Clostridium perfringens* (CPϵT) and *Clostridium septicum* (CSαT) respectively, are both pore-forming toxins, of extreme virulence (100 ng/kg and 10 μg/kg in mice respectively [67, 213]) (see section 1.4 for more background information on toxins). These toxins, produced as monomers by the bacteria, need to oligomerize to act on cells. For the prototoxin of CPϵT, the C- and N-terminals are cleaved to obtain the active form. One active toxin monomer can oligomerize with other active monomers in the vicinity to form the pore lethal to the cell. This pore has been determined to be formed by seven two-stranded β-sheets that combine after insertion to form a β-barrel [213]. Therefore, to facilitate this process, it can be hypthesised that the bacteria have evolved to produced toxins that attack receptors that are grouped in lipid raft domains [133, 148]. The precise receptor targeted by CPϵT in MDCK cells is a 36-kDa membrane protein, potentially the same that is targeted by the Hepatitis A virus [214, 215].

Previous work [133] has shown that the CPϵT and CSαT receptors in MDCK cells find themselves confined in domains in the cell membrane that range from 0.01 to 0.8 μm^2 in size. The receptors diffuse in these domains with an average diffusion coefficient of 0.13 $\mu m^2/s$. Thanks to the Bayesian inference algorithm described in section 2.3, the potential responsible for the confinement was also studied, found to be harmonic with a mean effective spring constant of 0.4 pN/μm (94 $k_BT/\mu m^2$). This harmonic shape is possibly due to:

- A lipid composition, gradually changing between the centre and the border of the domain, producing a changing solubilization energy of the protein in its membrane environment.
- A gradually changing thickness of the membrane across the raft microdomain producing a varying hydrophobic mismatch, i.e. leading to hydrophobic protein groups becoming exposed to water as they move further away from the domain centre. Indeed, previous work has demonstrated a thickness difference between the raft and non-raft phase [216].
- Or, a combination of the two.

The observed domains remained stable and free motion has never been observed.

Furthermore, it has also been demonstrated that these confinement domains are cholesterol and sphingomyelin (see section 1.1.1.1) dependent. Adding cholesterol oxidase (CHOx) or sphingomyelinase (SMase) abruptly decreases the toxin receptor confinement suggesting the source of confinement to be lipid rafts [133]. Although extensive work has been done on model membranes, several controversies remain and studies on live

cells are precious. In this chapter, we aim to further investigate this phenomenon and use a series of experimental approaches to gain a deeper understanding of the structural and energetic aspects of receptor confinement in live MDCK cells.

4.2 Evolution of Diffusivity and Potentials during Raft Destabilization

Previous work has used the BI scheme to extract force maps from receptor trajectories [132]. We again make use of the BI algorithm (section 2.3) to obtain diffusivity and potential maps. The approach can be adapted to observe the evolution of the confinement potential after the addition of raft domain disruptive agents like CHOx and SMase. All CHOx and SMase incubation experiments in this section were performed on the same day on cells grown in identical conditions.

In order for the inference scheme to apply, it should be possible to consider that the system is in equilibrium. If this is not the case, the Fokker-Planck equation (equation 2.8) does not follow from the assumed model equation (2.7) of overdamped Langevin motion. To observe the evolution of the inferred parameters we take a time window to selecting a subset of sampled data for inferring parameters (for derivation and details see [203]). By progressively inferring parameters along the time axis of the trajectory, we can see how the confinement potential and diffusivity evolve.

We must therefore find appropriate timescales that both respect the requirement of system equilibrium and sufficient sampling of the trajectory space. Keeping this in mind, three time scales, τ_{m}, τ_{inf}, and $\tau_{\mathrm{V,D}}$, are defined.

Temporal BI timescales:

- $\tau_{\mathrm{m}} = \mathrm{L}^2/\mathrm{D}$ is the characteristic time of the receptor motion in confinement. It is the typical time required for the receptor to move across a distance comparable to the domain size. L is the typical domain size and D the average diffusion coefficient of the confined receptor. A typical value of τ_{m} is about 1 s.
- $\tau_{\mathrm{inf}} \sim \{\langle \mathrm{N}_{i,j} \rangle \geq \mathrm{N}_{min}\}$ is the typical time needed to acquire at least a sufficient amount of sampled points, N_{min}, in each subdomain to obtain meaningful values with the BI algorithm. $\mathrm{N}_{i,j}$ is the number of points in each subdomain acquired during the time of the inference window τ_{inf}. Previous work has shown that a sufficient number is about 15 [133, 217].
- $\tau_{\mathrm{V,D}}$ is the time required for a significant local alteration of the potential or diffusive field.

In order for the temporal inference scheme to work, the following condition must be fulfilled:

$$\tau_{\mathrm{m}} < \tau_{\mathrm{inf}} < \tau_{\mathrm{V,D}} \tag{4.1}$$

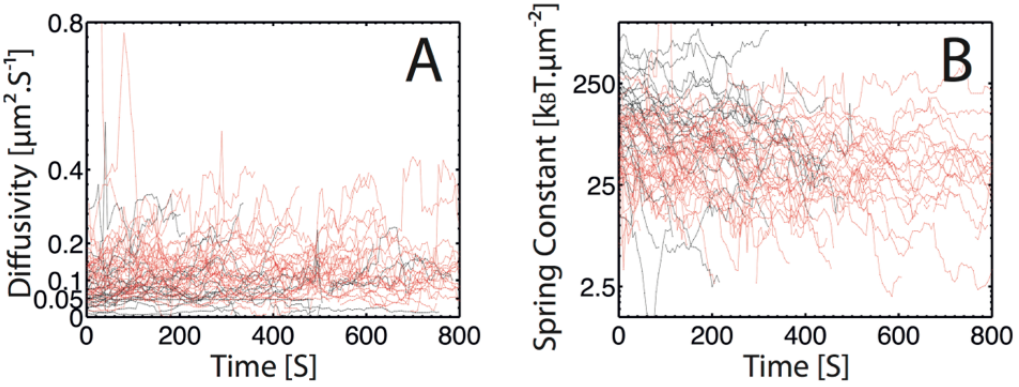

Figure 4.1: Fluctuations of the diffusivity and domain spring constant with time. The diffusivity (A) and strength of confinement (B) i.e. the spring constant display strong fluctuations during the action of cholesterol oxidase (black) and sphingomyelinase (red).

This means that the time to acquire enough points to perform the inference analysis, τ_{inf}, must me sufficiently small that the diffusive and potential fields do not change ($\tau_{inf} < \tau_{\text{V,D}}$), and yet large enough to allow the receptor to explore a sufficient portion of the confinement domain ($\tau_{inf} > \tau_{\text{m}}$).

To satisfy the above assumptions, the size of the window is chosen such that a doubling of its size does not produce a relative change of inferred parameters of more than 20%. We found that the variation of the potential and diffusive fields was sufficiently slow so that we respect the condition of equation 4.1. The temporal window was chosen to be $\tau_{inf} = 40$ s with a shift step of 5 s between subsequent inferences. This produced values of $N_{i,j}$ ranging from 15 to 100 depending on the inference window τ_{inf} and the domain analysed. Drift during long trajectories was eliminated by subtracting the average positions from the trajectories for each window.

During experiments, the movement of the ϵ-toxin receptors is observed via the attached luminescent $Y_{0.6}Eu_{0.4}VO_4$ nanoparticles. The samples are observed for several minutes before CHOx or SMase addition and then continue to be observed during enzyme action. Observations before, during and after enzyme addition were, hence, performed on the *very* same receptors.

Enzyme solutions used were either 20 U/mL cholesterol oxidase or 10 U/mL sphingomyelinase in minimal medium (MM)(HBSS+10 mM HEPES). To quantify the amount of cholesterol and sphingomyelin reacting in the 30 minutes of experimentation, a cholesterol quantification kit (Invitrogen) and a sphingomyelinase quantification assay kit (Amplex® Red, Invitrogen) were used. In the cell lysates that were incubated with CHOx or SMase, 30% less cholesterol and 45% less sphingomyelin were found, respectively. Note that these values are for the entire cell, however, we expect similar values from the plasma membrane.

We see that, after CHOx and SMase addition, both the average diffusivity and effective spring constant undergo strong fluctuations (see figure 4.1). Despite these fluctuations, however, we see a clear increase in diffusivity. Table 4.1 summarizes this result.

	Initial ($\mu m^2/s$)	End ($\mu m^2/s$)	N
CHOx	0.063 ± 0.01	0.18 ± 0.02	27
SMase	0.066 ± 0.06	0.27 ± 0.02	40

Table 4.1: Table of diffusivity evolution after cholesterol oxidase and sphingomyelinase addition. Change in average diffusion coefficients produced by adding cholesterol oxidase (CHOx) or sphingomyelinase (SMase) for N receptors studied. Errors given are standard errors on the mean.

To verify that the change in motion of the receptors was truly due to the structural change of the lipid raft domains, we conducted control experiments on transferrin receptors (these same receptors are further investigated in chapter 5). These are well known to mainly reside outside of rafts [218]. We observe the movement of these membrane proteins before and after CHOx addition, and from the hop-diffusion trajectories that we obtain, we extract the diffusion coefficients. The mean diffusivities we find are 0.15 ± 0.02 (N=26) $\mu m^2/s$ and 0.12 ± 0.02 (N=16) $\mu m^2/s$ before and after CHOx incubation, respectively, clearly demonstrating no significant change in mean diffusivity for this non-raft membrane protein.

As already demonstrated in previous work [133], the potentials of the studied proteins within lipid rafts are well described by a harmonic potential. We can therefore attribute an effective spring constant to the potentials to quantify them. Additionally, we can also look at the effect of CHOx and SMase on the potentials and the effective spring constant. Figure 4.1B shows this effect and table 4.2 summarizes the change in potential due to the added enzymes.

The evolution of the effective spring constants and the diffusivities is also summarized in figure 4.2. It shows, that for all the frames analysed, as the CHOx and SMase act, the spring constants become progressively weaker, while the diffusivity increases. These changes in diffusivity and spring constant are produced by a change in the lipid structure of the domain. We may thus attribute theses changes to a decrease in the solubilization energy gradient produced by the enzyme action.

	Initial ($k_BT/\mu m^2$)	End ($k_BT/\mu m^2$)	N
CHOx	237 ± 44	35.4 ± 7.7	27
SMase	206 ± 90	10.5 ± 4.1	40

Table 4.2: Table of potential evolution after cholesterol oxidase and sphingomyelinase addition. Change in average effective spring constant produced by adding cholesterol oxidase (CHOx) or sphingomyelinase (SMase) for N receptors studied. Errors given are standard errors on the mean.

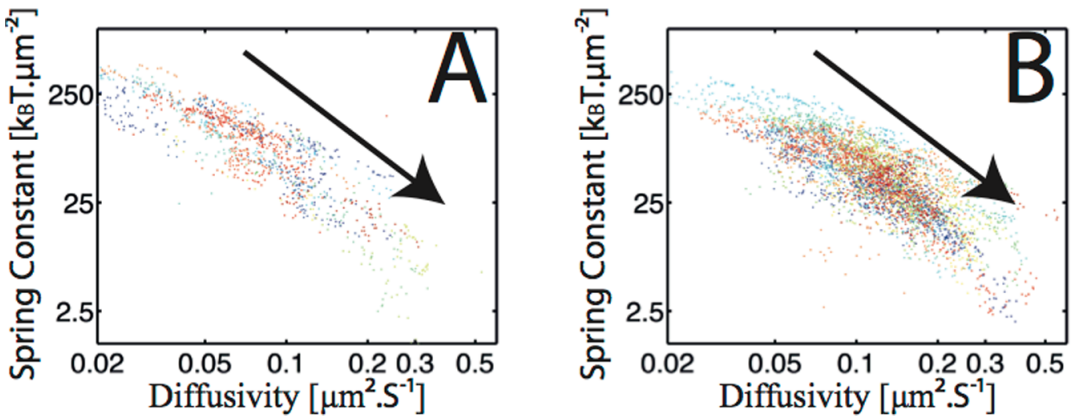

Figure 4.2: Temporal evolution of spring constant and diffusivity in domains during raft destabilization. Temporal evolution trend (see arrows) of confinement potential spring constants and diffusivities of ϵ-toxin receptors after the addition of cholesterol oxidase (A) and sphingomyelinase (B). The induced raft destabilization leads to a decrease in spring constant and an increase in diffusivity. All data points of the same color represent the evolution the evolution for one receptor.

4.3 Interdomain Hopping of Receptors

Throughout all experiments, we have never seen a ϵ-toxin or α-toxin receptor not confined. On occasion, however, we do observe receptors moving from one raft to an adjacent lipid raft. "On occasion" because certain conditions need to be met for this to happen. The rafts need to be in close proximity of each other and the receptor needs to have enough energy to overcome the energy barrier between the two domains. This energy, which we term the "hopping energy", that is required for such an event to take place, and it can tell us more about the energy landscape experienced by a receptor in a lipid raft. It is also worth noting that it is highly unlikely that this hopping phenomenon is produced by a detachment of the ϵ-toxin from its receptor, as the dissociation constant for these two proteins is very low with a K_d of 3.8±1.9 nM [219]. Likewise, we never observe the toxin dissociating from the receptor during experiments, not even when exposed to forces of several pN (see section 4.4).

4.3.1 Extraction of fourth-order potentials

To study the potential landscape of "hopping trajectories" we can use the BI method to extract a fourth-order (in some cases, like large-distance hopping, we used a sixth-order potential) to obtain the double well of the adjacent potentials. This provides a model of the energy "barrier" between the two domains that needs to be overcome. However, due to the large parameter space of the inferred values, it is not easy to check that we have access to the limit defined by the Fisher information [164, 220]. Therefore, an estimate of the viability of our method in hopping conditions and the error associated with the inferred parameters can only be accessed by conducting simulations. These are discussed in section 4.3.2.

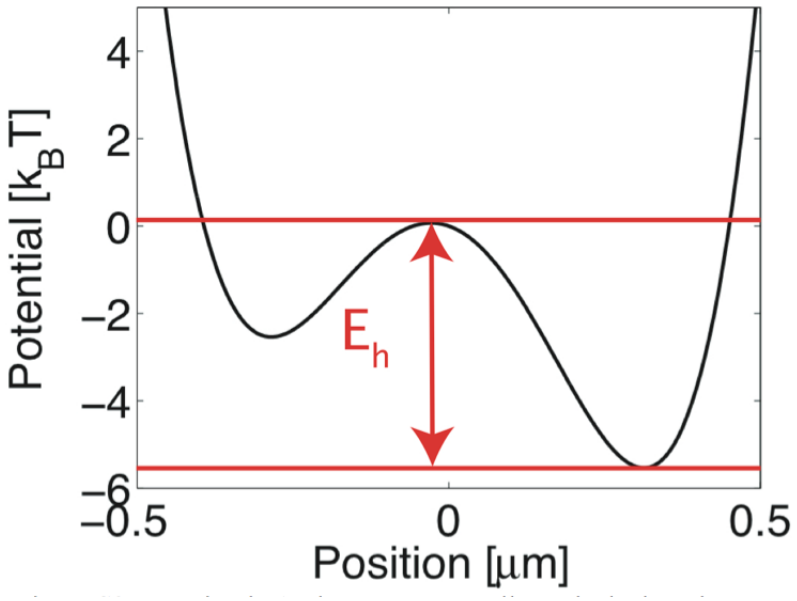

Figure 4.3: Definition of hopping energy for a double well. The energy barrier E_h for hopping from one confinement domain to an adjacent domain is defined as the difference between the maximum height of the potential barrier and the minimum of the lower of the two potential wells.

For the geometry of two-dimensional potential wells we define the hopping energies as shown in figure 4.3. We take the maximum and minimum values along a straight line connecting the two minima of the wells.

4.3.2 Simulations of hopping trajectories

Numerous simulations to test the method's viability in extracting accurate hopping energies were conducted by Jean-Baptiste Masson. A detailed account of these can be consulted in [203]. Here, for completeness, the general principles and the main results are presented.

We use the maximum of the *a posteriori* probability (MAP) density function (PDF) of ΔE in equations 4.2 and 4.3:

$$V(x) = \frac{E_h}{X_{min}^4} x^4 - \frac{2E_h}{X_{min}^2} x^2 \tag{4.2}$$

$$V(x) = \frac{E_h}{X_{min}^4} x^4 - \frac{2E_h}{X_{min}^2} x^2 + ky^2 \tag{4.3}$$

for the 1D and 2D case, respectively, as the estimator for the hopping energy. X_{min} and $-X_{min}$ represent the x-coordinates of the well minima. In equation 4.3, k is the effective spring constant of the harmonic confinement in the y-direction.

For the simulations, the potential outside the wells was set to 0 $k_B T$. Additional positioning noise was introduced with a random value picked from a Gaussian distribution,

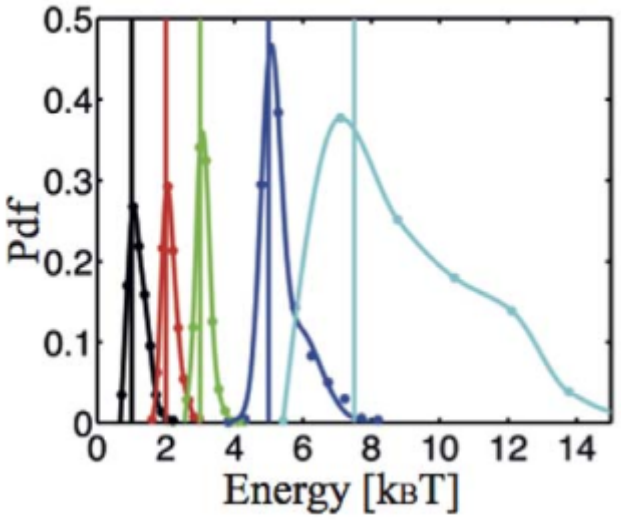

Figure 4.4: Evolution of MAP statistics as a function of E_h. 2D 2000-point trajectories produced with an acquisition time of 25-ms. Double-wells separated by 300 nm, and using a diffusivity of 0.025 $\mu m^2/s$ and a confinement with a spring constant of 0.85 $pN/\mu m$. Colored lines represent the input hopping energy value and the corresponding probability curves are shown in the same color. We see that the true values are accurately inferred. Figure reproduced from [203].

which acted as a placeholder for all sources of error (shot noise, read-out noise, PSF imperfections, etc.)

Bayesian inference accurately infers the input hoppng energy, E_h, in a variety of conditions (see figure 4.4 [203]. The results showed that the MAP estimator outperforms the average value estimator (AVE) of the *posteriori* distribution. Advantages of using the MAP include the fact that the MAP estimator remains unbiased for unique hopping events, with some broadening of the PDF for larger hopping energies. MAP statistics do not have a long distribution tail and all the values are centered around the maximum value.

Changing the lateral confinement by varying the effective spring constant, k, in equation 4.3, does not change the result. Therefore, 1D hopping approximations capture most of the information necessary to characterize the 2D hopping inference behaviour.

As addressed in section 2.3.2, high values of confinement factor u produced by higher diffusivities can produce a bias in the inferred values. For both 1D and 2D trajectories, the inferred hopping energy values decrease with increasing u. However, this effect is deterministic and can be compensated for.

4.3.3 Experimental results

Figure 4.5 shows an example of a hopping trajectory together with the corresponding inferred diffusivity and potential maps. What is interesting to note, in addition to the double-well potential, is that there is an increase in diffusivity between the two wells. We

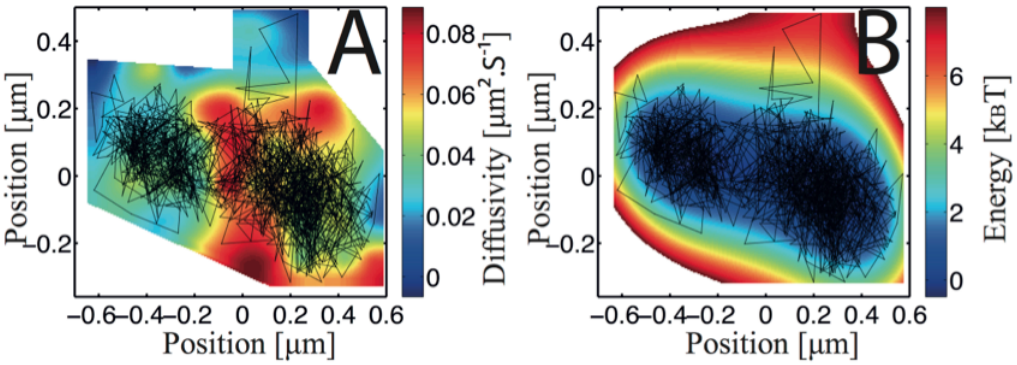

Figure 4.5: An example of a hopping trajectory. The hopping trajectories, like this one, are analysed with Bayesian inference assuming a fourth-order polynomial potential. Using a bi-harmonic interpolation between the mesh values, the diffusive (A) and potential (B) maps can be inferred.

extract a range of hopping energy values from our experimental data. Their distribution is shown in figure 4.6. We see that there are two distinct peaks in the distribution representing two kinds of hopping events. A lower typical hopping energy of $\langle E_h \rangle = 0.54 \pm 0.05 k_B T$ (N=18) related to multiple back and forth receptor hops before arriving in the new confinement domain. These can be interpreted as movement of the receptor between different substructures within the lipid raft, possibly during coalescence of rafts. The higher average hopping energy we see with a value of $\langle E_h \rangle = 2.64 \pm 0.25 k_B T$ (N=15) is associated with the receptor hopping once or only a few times between two distinct lipid rafts. This higher hopping energy value sets a lower limit for the solubilization energy difference between the raft and non-raft phase.

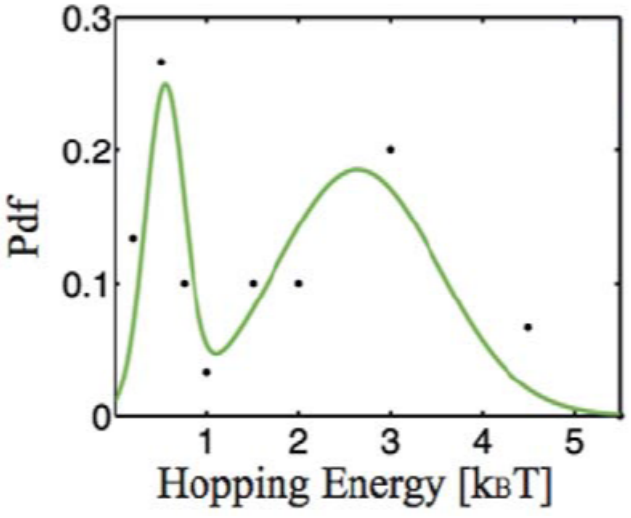

Figure 4.6: Probability density function of hopping energies. The probability density function of the hopping energies displays two distinct maxima at 0.54 and 2.64 $k_B T$.

4.4 External Force Application on Receptors

So far the movement of the receptors has been investigated under equilibrium conditions without the influence of external forces. But what happens when a force is applied to a receptor? How does this influence the movement? Will the cell react? And what happens after the force application is stopped?

This can be tested in a fairly simple and straightforward manner by placing the system, that is the nanoparticle-coupled toxin bound to cells, into microchannels. After the cells adhere to the surface inside the microchannels, a flow can be applied to pass over them. This flow will act on the nanoparticles, which will adopt the role of a sail by amplifying the force exerted on the receptor by the flow. By allowing the flow to push on the NPs, which will, in turn, push on the bound receptors, we investigate the dynamic membrane receptor response to an external force, and the results are quite surprising and enlightening. Figure 4.7 depicts a schematic cartoon of this setup.

4.4.1 Experimental setup

The microscope used to observe cells under a microfluidic flow including camera, software and general peripheral equipment was the same as described in section 2.2. Additionally, two types of syringe pumps were used for injecting solutions into the microchannels. The syringe pumps (Harvard Apparatus and KD Scientific) were used to inject liquid using a set of SGE Analytical Science syringes. The syringes were sized 500 μL and 10 mL. Tubing (Adtech) had dimensions of 1.07 mm and 0.56 mm for outer and inner diameter, respectively, and was used to connect the syringes on the pumps to the microchannel sample. Additional tubing was used at the channel exit to lead the used solution to a plastic container for collection and subsequent disposal.

As the microchannel material we used polydimethylsiloxane (PDMS). The microchannels were attached to a glass microchip to seal the channel. The protocol for the production of these channels is detailed in appendix A.2, and the preparation protocol by cell injection of the sample channels in appendix A.3.

The prepared sample channel is connected to three input syringes: one large syringe with the flow solution consisting of observation medium, a second syringe containing the nanoparticle-labeled toxins, and a third containing the relevant reactant solution. This last solution is used in the relevant control experiments and added halfway through the experiment to test the cell reactions to flow before and after addition of a specific agent.

Multiple flows are always applied throughout the experiment starting with the lowest flow rate and finishing with the largest. Each flow is announced with a short sequence of white light images to confirm the presence of cells and to subsequently determine the exact starting point of the applied force.

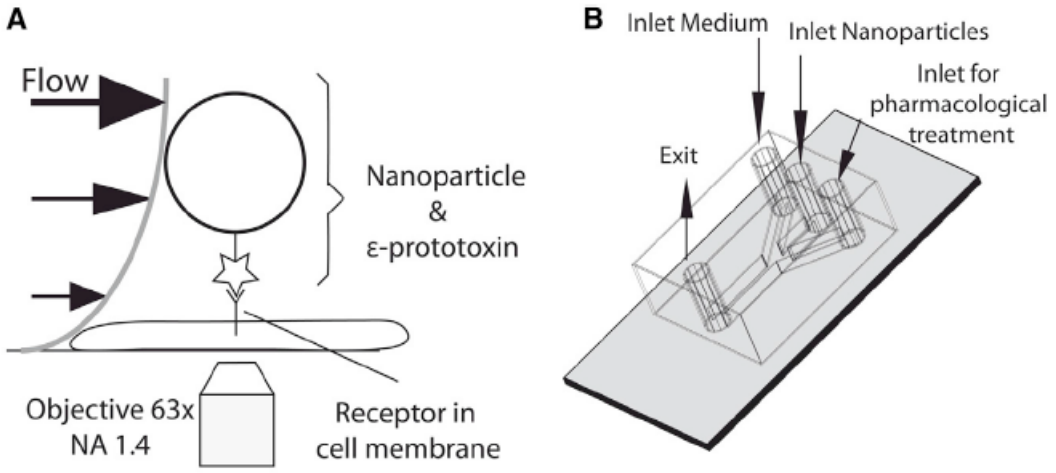

Figure 4.7: Conceptual image of receptor-bound nanoparticle in a flow and sketch of microchannel geometry. (A) shows a conceptual graphic of the system. The NPs are coupled to the toxin, which in turn binds to its receptor in the cell membrane. The flow that is applied acts mainly on the relatively large NP. (B) is a depiction of the microchannel geometry. The channel possesses multiple inlets for flow fluid and reactant injection, and a single exit.

4.4.2 Determination of the flow speed around NPs

The syringe pumps inject liquid in units of μL/min. Clearly this does not tell us anything about the velocity of liquid that the NPs will be exposed to and the resulting force. We therefore use particle velocimetry (PV) to accurately determine the flow speed at the precise distance of the attached NP from the glass.

First, we prepare a typical experiment and permit the conjugated nanoparticles to bind to their respective receptors. Then, a flow is applied with a solution containing unbound NPs. We then measure the speed of unbound particles in flow in the same focal plane as the bound nanoparticles to obtain the relevant flow speed.

We should note, however, that, for flow speeds, v_{flow} used during the experiment, the velocity of unbound NPs flying past is too large for effective speed measurement. Speed measurements are, therefore, performed at low flow rates up to 0.6 μL/min. This data is then evaluated and extrapolated to obtain the flow velocities for higher flow rates. The results are represented in figure 4.8. The conversion factor obtained from a linear fit of the data was $3.2 \pm 0.8 \times 10^{-4} \frac{\mathrm{m}}{\mathrm{s}} / \frac{\mu\mathrm{L}}{\mathrm{min}}$.

The depth of field (DOF) of our microscope objective is 500 nm and our measuring range is $[z - DOF/2, z + DOF/2]$. Since our measurements are conducted in close proximity to the cell surface, the NPs that we are observing (in the range $[z, z + DOF/2]$) will experience a Poiseuille flow with a twist. The boundary in this case is not a no-slip boundary but the cell membrane, a viscous medium with a non-zero slip length. If we use the Poiseuille profile to estimate the flow velocity at the NP position just above the cell assuming a no-slip boundary for the cell surface, we will obtain an underestimation of the flow velocity by as much as 20%, which is still within the error bars of the velocities

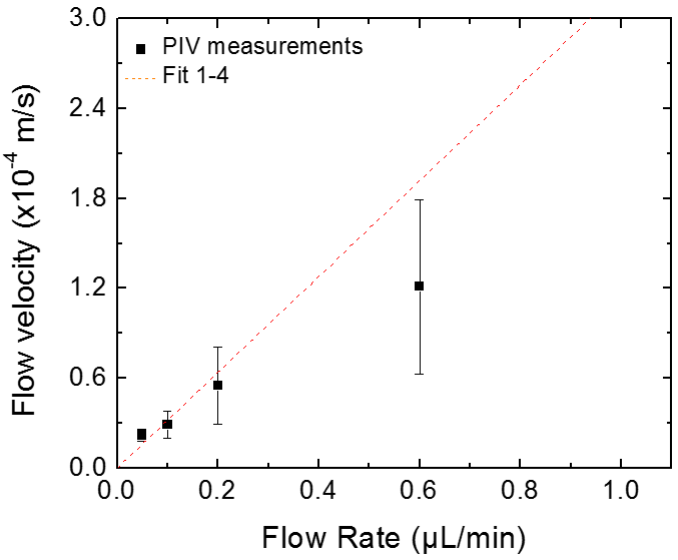

Figure 4.8: Calibration curve relating injection rate to flow velocity in the microchannel. This curve represents the relationship between the injection rate of liquid into the channel and the flow speed of the liquid at the position of the NPs observed. The errors are the standard deviation of the 10, 10, 53, and 8 measurements for the flow rates of 0.05, 0.1, 0.2, and 0.6 $\frac{\text{m}}{\text{s}}/\frac{\mu\text{L}}{\text{min}}$, respectively.

determined. This is mirrored in the fact that measured velocities are larger than would be predicted by the Poiseuille equation. We can, however, assume a virtual zero-flow boundary that would provide us with the observed velocity in the absence of a cell. Using the following equations, which represent the Poiseuille flow profile and average flow velocity, we can calculate the position of this virtual boundary.

$$v(z) = v_{mean}(-\frac{4}{h^2})(z^2 - hz) \tag{4.4}$$

$$v_{mean} = \frac{3U}{2A} \tag{4.5}$$

h is the height of the channel, 30 μm, A the cross-section area of the channels (30 $\mu m \times 400\ \mu m = 12,000\ \mu m^2$), and U the flow rate. Using these values, we obtain a distance, z, of 800 ± 200 nm from our PV measurements. We can take this height to be the slip length, since the NP-membrane distance is negligible in comparison.

Typically, for equation 4.6, the viscosity, η, needs to be adjusted to an effective viscosity, η_{eff}, when the particle is in the presence of a boundary. However, in our case, the NP radius (approximately 30 nm), is more than 25 times smaller than the distance to the virtual no-slip boundary. The adjustment to the viscous field around the NP is, therefore, negligible and we can assume that $\eta_{eff} = \eta_{water} = 0.001\ Pa \cdot s$.

Flow-rate (μL/min) to Force Conversion

	Force (pN)	Error on Force (pN)	% Error
2.5	0.42	0.05	12
5	0.83	0.2	24
7.5	1.2	0.4	33
10	1.7	0.7	41
15	2.5	1.6	64
20	3	3	100
30	5	7	140
50	8	18	225

Table 4.3: Table relating flow rates to forces on NP. This table lists the range of flow rates used during experiments and the corresponding forces experienced by the NPs. The error on the force is determined from the error on the velocity of the nanoparticle and its radius, where the overall error is dominated by the later.

4.4.3 Receptor response

With the flow speeds determined in section 4.4.2, we can now determine the force that acts on a nanoparticle using the Stokes equation:

$$\mathbf{F}_d = 6\pi\eta r \mathbf{v}_{flow} \tag{4.6}$$

where r is the NP radius. Once the flow is turned on, this is the force experienced by the receptor. Table 4.3 gives the flow rates used and the corresponding forces.

We observe that the receptor is displaced in the flow direction, reaches an equilibrium position, and returns towards its initial position as soon as the flow is stopped 4.9B. These flow cycles can be observed simultaneously for several receptors, allowing a multiplexed acquisition of data (figure 4.9A). An example of this type of flow cycle is shown in figure 4.9B. Here a flow rate of 7.5 μL/min (flow speed: 0.002 m/s) is applied and displaces the receptor by as much as 2.1 ± 0.3 μm. The displacement is calculated by averaging all the positions of the equilibrium phases before and during flow, as indicated by the solid and dashed blue line, respective, and then taking the difference between these averages.

The displacement at the start of the flow cycle in figure 4.9B can be fitted with a straight line (*red line*), the slope of which can be related to the displacement speed, v_{disp}, of the receptor, which in this case is 0.52 ± 0.03 $\mu m/s$. Using this, the total displacement L_{disp} (2.1 ± 0.3 μm quoted above), and the diffusion coefficient of the protein D ($0.16 \pm 0.01 \mu m^2$ /s), the Péclet number can be calculated:

$$Pe = \frac{\text{advective transport rate}}{\text{diffusive transport rate}} = \frac{L_{disp} v_{disp}}{D} \tag{4.7}$$

The Péclet number quantifies the rate ratio of advective transport to diffusive transport. We obtain a Péclet number of 7, confirming that the displacement of the receptor is indeed due to the hydrodynamic drag force, and not the Brownian motion.

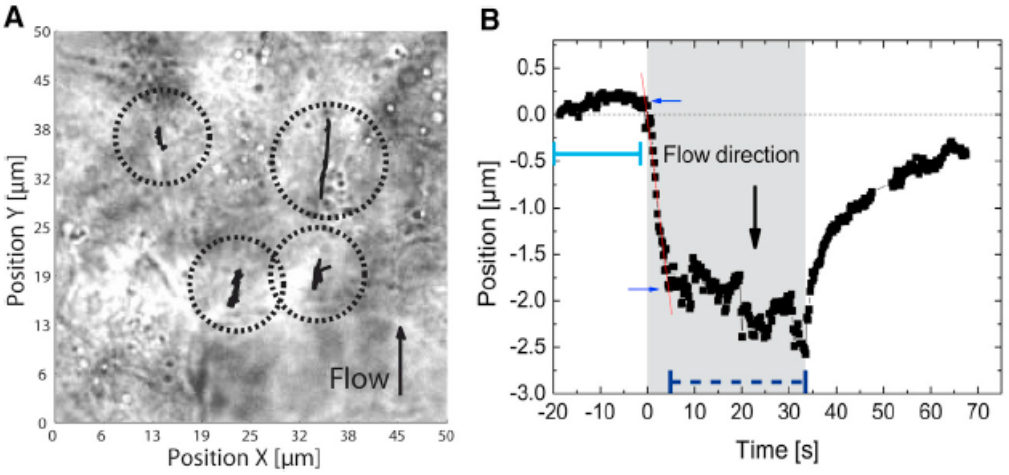

Figure 4.9: A bird's-eye-view of trajectories on cells and of a flow cycle. (A) Four receptor trajectories as observed with the fluorescence microscope overlaid on a white-light transmission image of the cells. We see that several trajectories can be recorded simultaneously. (B) Example of a flow cycle experienced by a receptor. The receptor is displaced in the flow direction encountering some barrier and returns close to its initial position as soon as the flow ceases. The grey rectangle indicates the time period during which a flow is applied. The blue and red lines are explained in the text.

The fact that the receptors return close to their initial positions after the flow is stopped is the most intriguing result. Clearly there is some elastic barrier that is responsible for this motion. The investigation of the nature of this barrier is continued in section 4.4.8. What is also interesting to note, is that the displacement until equilibrium during flow is reached is proportional to the applied force (i.e. to flow). Figure 4.10 shows the results of multiple flow cycles with progressively higher force applied. We notice the larger displacements following larger flow rates, but also that, sometimes, not all the displacement is reversible. This may be due to a non-reversible deformation of the barrier, or a 'hopping' event over the barrier to go on and encounter a subsequent barrier. It could also be that the receptor is initially not in contact with a boundary and needs to travel an initial distance to encounter the first obstacle.

Looking at the flow cycles in figure 4.10 D-F, we can extract the displacements and associated forces to find the effective spring constant of the barrier, k_{eff}. The result of this can be seen in figure 4.10 G-I and provides us with an average value of 2.5 ± 0.6 pN/μm (N=17). The order of magnitude of this value does not change for different receptors and the forces we apply are all below 8 pN, insufficient for deforming the membrane into a tubule [221].

What is also worth noting is that, during the displacement, the receptors sometimes move perpendicularly to the flow direction (4.9A). This can be attributed to obstacles encountered by the moving receptor, either within the cell membrane, or in the cytoplasm underneath. In around half the cases these obstacles correspond to structures seen with white-light transmission, and mostly the non-parallel movement is produced by the cell boundary.

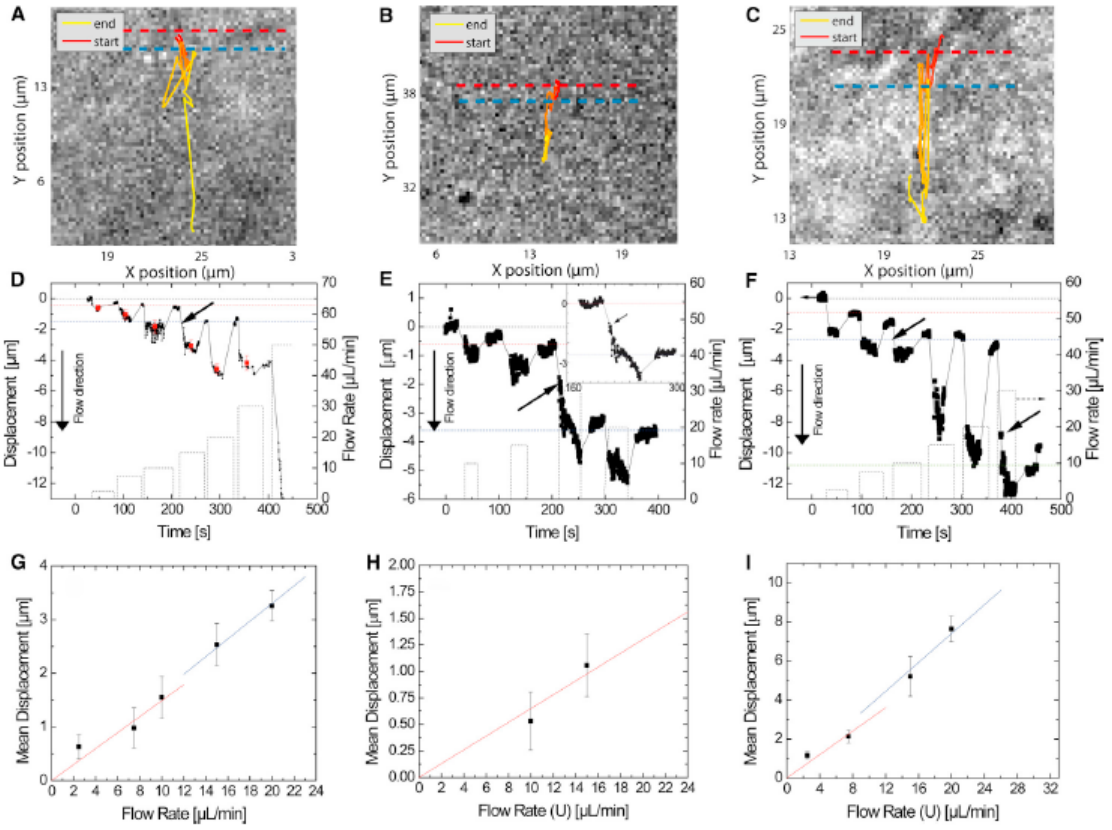

Figure 4.10: Multiple flow cycles and calculation of effective spring constants. (A-C) Recorded images of receptor trajectories during multiple flow applications. (D-F) Displacements observed during multiple flow cycles. The increasing displacement following increasing force magnitudes is visible and used to calculate the effective spring constants of the restoring barriers by linear regression analysis as in figures G-I.

4.4.4 Displacement of confinement domain together with the receptors

The toxin receptors we observe are confined in domains with an average diameter of 700 nm [133]. During the receptor motion under flow, we observe that the size of the confinement domain is not affected by the application of a force. Looking at the RMS displacement of the receptor in the direction perpendicular to liquid flow, we find values of 0.09 ± 0.02 μm (N=11), 0.14 ± 0.03 μm (N=11), and 0.08 ± 0.02 μm (N=11) for before flow, during flow at equilibrium, and after flow, respectively. Furthermore, we can also use the BI method (see section 2.3) to infer the potentials from the trajectories of the receptors in each of these cases. An example of a result of this analysis is shown in figure 4.11. We see that the extracted potential as well as the domain size do not change significantly.

As previously mentioned in section 4.1, the confinement potential the receptor experiences is well described by a second-order potential. The spring constants and diffusion coefficients determined for the domains before, during and after flow are comparable with these previously determined values [133]. These results indicate that the toxin receptors are displaced together with their confining raft domains, although it can not

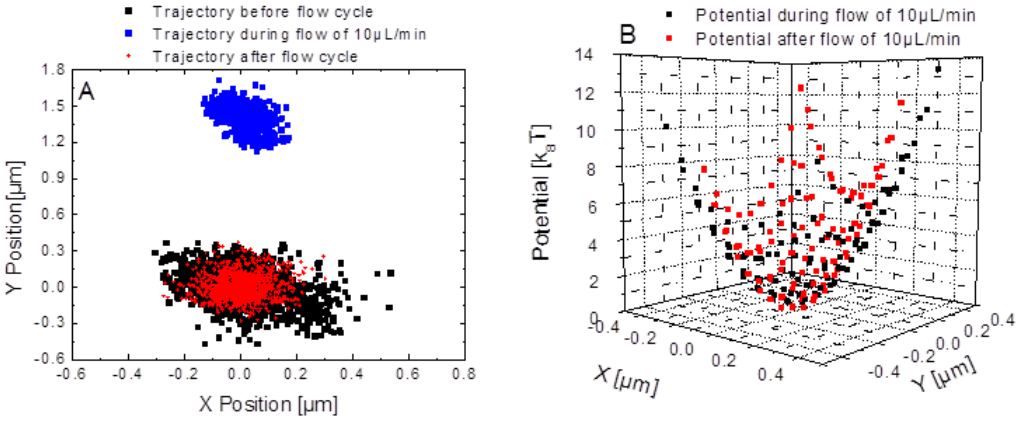

Figure 4.11: Domains and confinement potentials with and without flow. (A) Example trajectory of a CPϵT receptor before (black), during (blue) and after (red) flow. Domain sizes before and after flow are 0.35 ± 0.03 μm and 0.24 ± 0.03 μm, respectively. Likewise, diffusion coefficients are found to be 0.068 ± 0.002 μm^2/s and 0.051 ± 0.002 μm^2/s, respectively. (B) Corresponding inferred potentials with spring constants of 0.44 ± 0.03 pN/μm and 0.91 ± 0.06 pN/μm during and after flow, respectively.

be excluded that hopping to an adjacent domain takes place during the application of a force.

4.4.5 Effect of flow on a NP adsorbed to the glass surface

The first control experiment that needs to be conducted is to measure the signal response of a nanoparticle adsorbed to the glass surface during flow. The quite significant receptor response to a force was shown in section 4.4.3. Ergo, when performing the same flow experiment on a simple NP adsorbed to the glass surface we would expect a much weaker response, if not no response at all.

During experiments on cells, the maximum flow rate applied was 30 μL/min. Using this flow rate on NPs attached to the glass surface we see (figure 4.12) that the movement of the probe does not change significantly when exposed to a flow. Its apparent movement is an order of magnitude smaller than the displacement of the receptors on the cell surface, and is dominated by positioning noise, which is slightly higher in the flow environment. No displacement is seen and the RMS value of the motion perpendicular to the flow is 0.056 μm, also negligible.

4.4.6 Cell stability during flow

Since the fundamental idea behind force application is to induce a change in the target agent, we have to perform several control experiments to ensure that the changes we do observe are not linked to other unobserved changes induced by the flow. The main objective of the control experiments is to verify that the flow does not induce structural changes of the cell, internally and externally, that may be the source of receptor

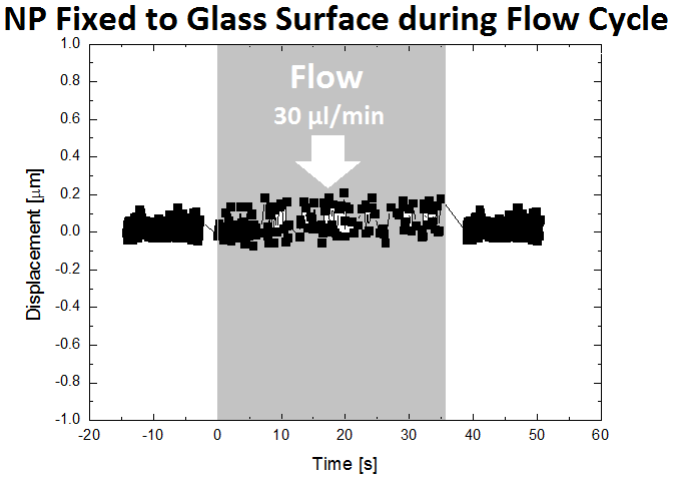

Figure 4.12: Flow cycle actin on a NP non-specifically attached to a glass surface. Flow cycle applied to a nanoparticle attached non-specifically to the glass surface. There is no displacement recorded. The additional noise is produced by the flow in the channel.

movement. Therefore, in the following, we present evidence that the cells are unaffected by the magnitude of the flow during typical flow application times, when NPs are not attached to membrane receptors.

4.4.6.1 Observing actin during flow

To determine if there are any structural changes of the cell during the course of the experiment, we transfected the cells with a reduced expression GFP-β actin plasmid. This allowed us to image the cells, and the actin within, during flow cycles. The protocol for the transfection can be found in appendix A.4.

Figure 4.13 shows the results of this experiment. The yellow overlap of the cell with (red) and without (green) flow shows that there is no significant structural reaction of the cell

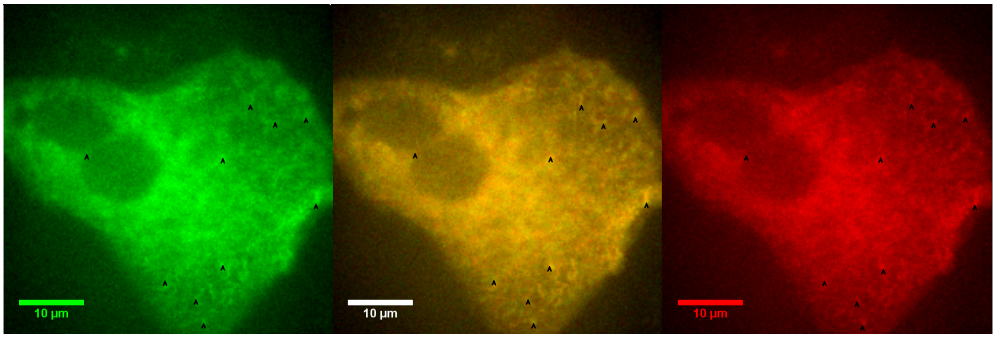

Figure 4.13: Cell labeled with EGF-actin in flow. An example of an EGF-actin labeled cell before flow (*green*), during flow (*red*) and an overlap of the two (*middle*). There is no significant difference between the actin structure and the cell outline in the two cases. Additionally, taking measurements at selected points on the cell (black arrows) gives a maximum displacement of 0.36 ± 0.06 μm (N=10) confirming that any movement seen in the presence of NP labeling is due to the receptor being displaced.

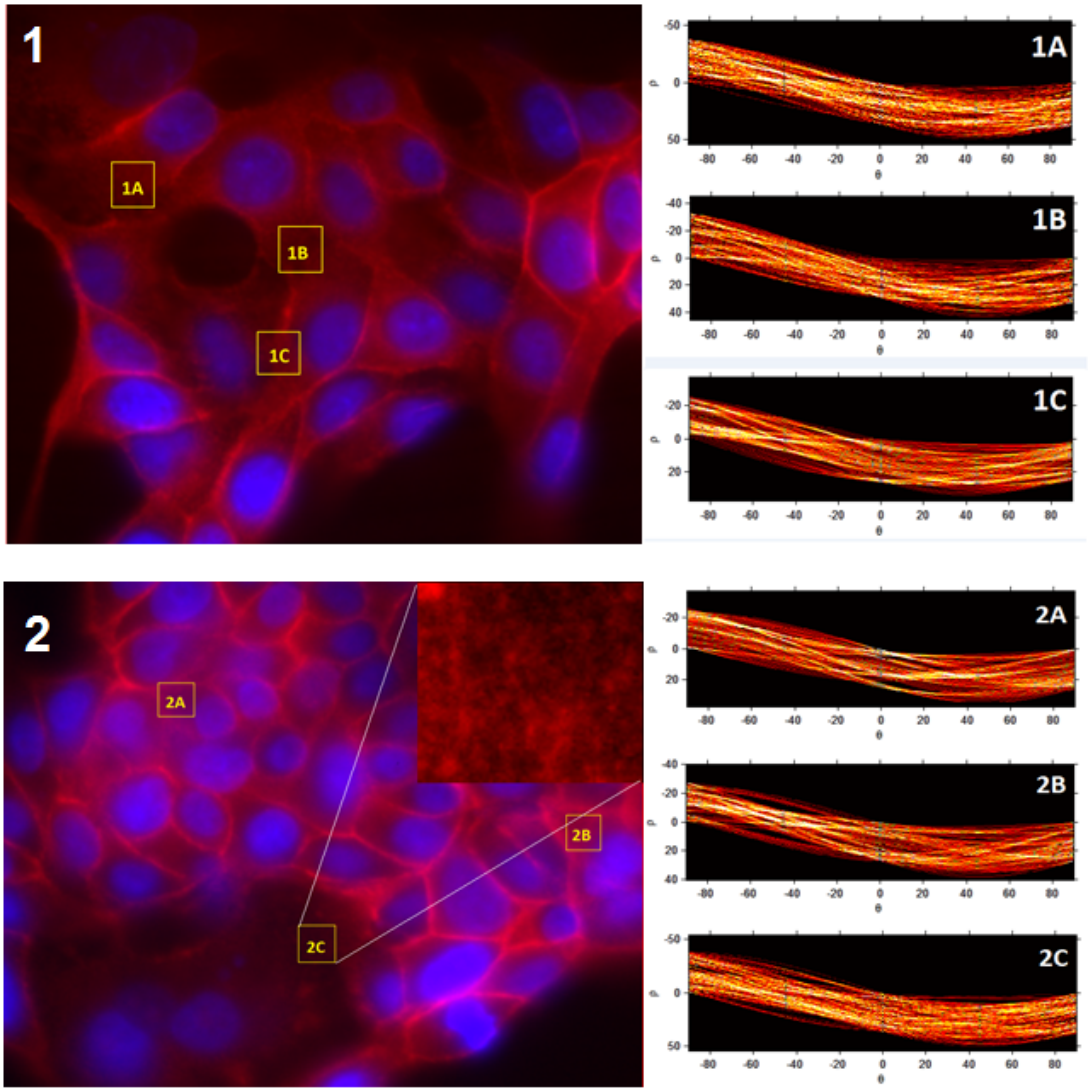

Figure 4.14: Hough transforms of actin filaments of phalloidin-rhodamine and DAPI treated cells before and after flow. We fixed two populations of cells before and after exposure to flow and stained them with phalloidin-rhodamine and DAPI. The DAPI-stained nuclei are shown in blue and the phalloidin-rhodamine stained actin is shown in red. Selected actin regions in both populations before flow (1) and after flow (2) are then analysed with a Hough transform to detect any change in actin orientation due to typical flow application.

and the actin within the cell to the highest flow (30 μL/min) applied during experiments. Notable features of the cell actin were localised and their positions compared in the different conditions. The average displacement of these actin segments measured was 0.36 ± 0.06 μm (N=10), significantly less than the movement of NP-labeled receptors during flow.

Additionally, we fixated cells and performed actin labeling with phalloidin-rhodamin before and after flow cycles. The exact protocol for this procedure can be found in appendix A.5. Simultaneously, the nuclei of the cells were stained with DAPI. This was done for a population of cells that had undergone a flow cycle and a population that had NOT undergone a flow cycle. Typical regions (81.9×81.9 μm) were analysed by

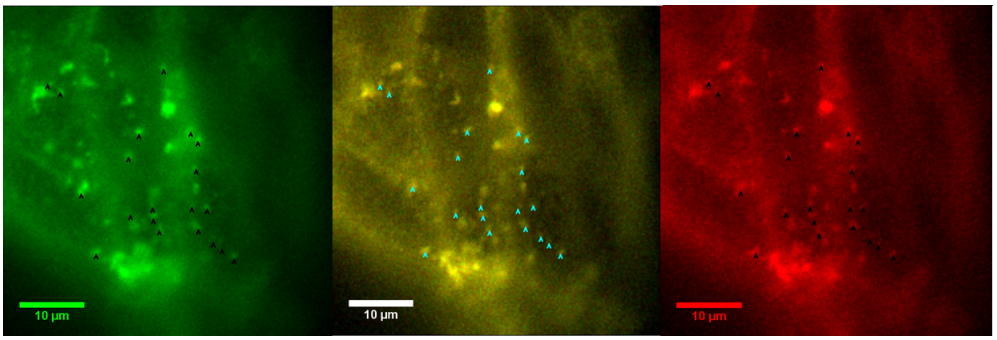

Figure 4.15: BODIPY-labeled sphingomyelin within lipid rafts on cell membrane. We implanted BODIPY-labeled sphingomyelin in the plasma membrane. The cell displayed is shown before flow (*green*), during flow (*red*) and as an overlap of the two images (*middle*). We see no visible difference between the images and measuring selected points on the cell surface (*arrows*), we obtain a negligible average displacement of the rafts of 0.34 ± 0.03 μm (N=20 on 6 cells).

performing Hough transforms to determine any change in the actin structure induced by the flow cycle.

The results of the phalloidin-rhodamine staining and the Hough transforms are summarized in figure 4.14. We see that the Hough transforms performed reveal that neither before nor after flow is there a preferential orientation of the actin filaments in the cells.

4.4.6.2 Observing lipid rafts during flow

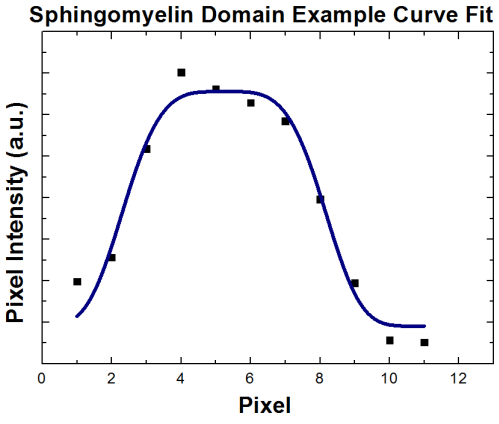

Figure 4.16: Fitting the domain size of labelled rafts. Pixel intensity across a sphingomyelin-BODIPY labeled domain fitted with: $I(x) = background + I_{max}e^{-(\frac{x-x_c}{2w})^4}$. The domain lengths/widths were taken to be equal to the half-width at half-maximum of the fitted curve (length of one pixel is 254 nm).

We also conducted a **labeling of rafts with sphingomyelin-BODIPY for observation during flow cycles**. MDCK cells were incubated with a sphingomyelin-BODIPY complex, effectively labeling sphingomyelin-rich regions in the plasma membrane, as seen in figure 4.15. In these trials, the receptors were not labeled with NPs. The cells were then exposed to 30 μL/min flow rate and the raft response was measured. As in figure 4.13, we see that the flow does not have any significant effect on the membrane structure. Measuring the change in the position of the rafts indicated with the black arrow heads, we obtain an average displacement of $0.34 \pm 0.03\mu$m (N=20 on 6 cells). Again, significantly less than the receptor displacement. The protocol for sphingomyelin labeling is given in appendix A.6.

To obtain some insight into the size of the domains, the BODIPY signal profile was fit with the function given below:

$$I(x) = background + I_{max} e^{-(\frac{x-x_c}{2w})^4} \tag{4.8}$$

where x_c is the centre of the profile and w determines its width. Since the domains are typically not perfectly circular, the long and short axes are fit. The length for the two axes is then taken to be the half width at half-max of the fitted curve. An example of such a fit is shown in figure 4.16. This gives us a distribution of domain lengths, widths, and areas summarized in figure 4.17. The average length, width and area of the domains are 384±11 nm, 316±10 nm, and 0.37±0.004 μm^2, respectively. The average area obtained is in strong agreement with the raft area of 0.40±0.05 μm^2 observed in [133].

It is also worth mentioning that previous related work conducted by Silvan Türkcan investigated the response of fluorescent cholera-toxin-labeled lipid rafts under flow [148]. To achieve this monosialotetrahexosylganglioside (GM1) clusters were labeled with a cholera toxin-Alexa488 complex. A flow of 2.5 μL/min is applied and the displacements of the individual patches were measured. The average displacement of the GM1 clusters was found to be 0.2 ± 0.1 μm (N=21 on 8 cells). Figure 4.18 provides a summary of the results.

4.4.6.3 Observing microtubules during flow

For the sake of completeness, it is also worth noting that within the context of this investigation, previous work has also been conducted by Silvan Türkcan on the visualisation of microtubules during flow. To achieve this, cells were transfected with EB3-GFP DNA. A flow of 50 μL/min was then applied and the microtubules and the positions of notable features (see figure 4.19) on the cell were measured. The average measured displacement of the microtubules was 0.3 ± 0.2 μm (N=60 on four cells). It was observed that the most drastic displacements were observed at cell protusions and the edge of the cell.

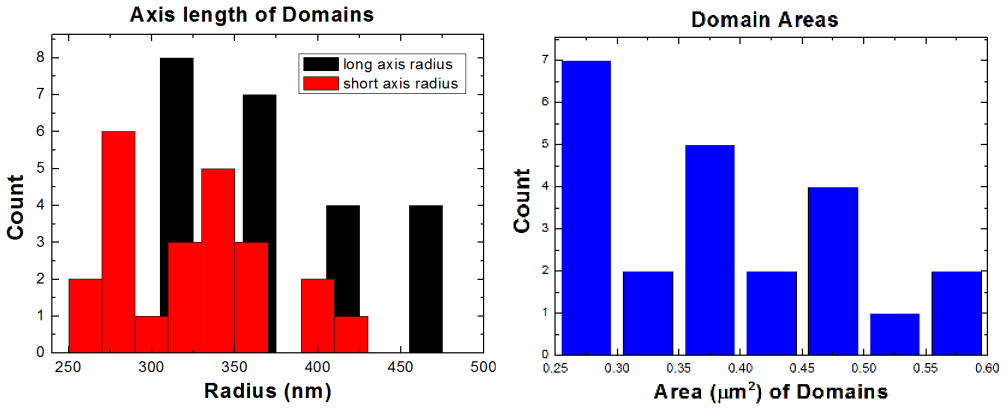

Figure 4.17: Histogram of domain sizes and areas. Histogram of the domain lengths (A) and areas (B). Average value for long and short axis are 384 nm and 316 nm respectively. Average domain area is 3.71 μm^2 (N=23).

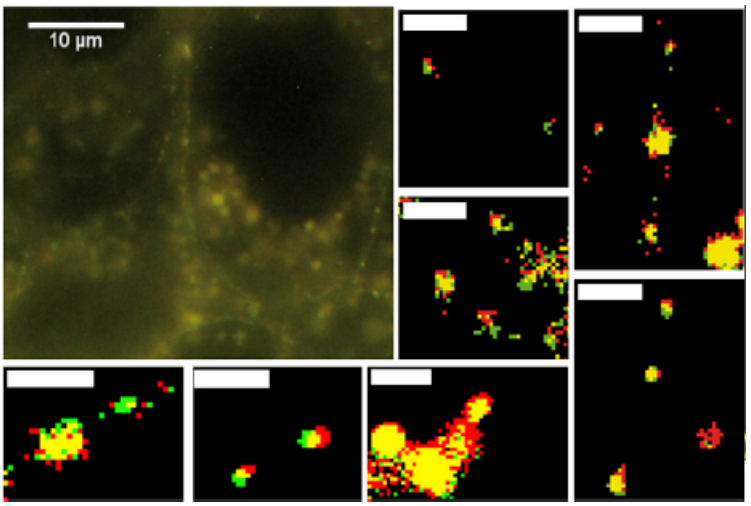

Figure 4.18: Cholera toxin-Alexa488 labeled GM1 clusters. The small images show the positions of the GM1 clusters in the large image under flow. Red clusters are without flow while green clusters are with a flow rate of 2.5μL/min. The average displacement was found to be 0.2 ± 0.1 μm (N=21 on 8 cells). The white scale bars in the small images are 2 μm.

Displacements in the centre of the cell, where the movements of receptors are typically measured, were typically much smaller than the measured average.

4.4.7 Cell treatment with Cholesterol Oxydase

In section 4.2 we discussed the effect of COase addition to receptor dynamics within a raft. To further investigate the phenomenon discovered in section 4.4.3 of raft and receptor displacement during flow, we observed CPϵT receptors during flow cycles before and after COase addition to the cells.

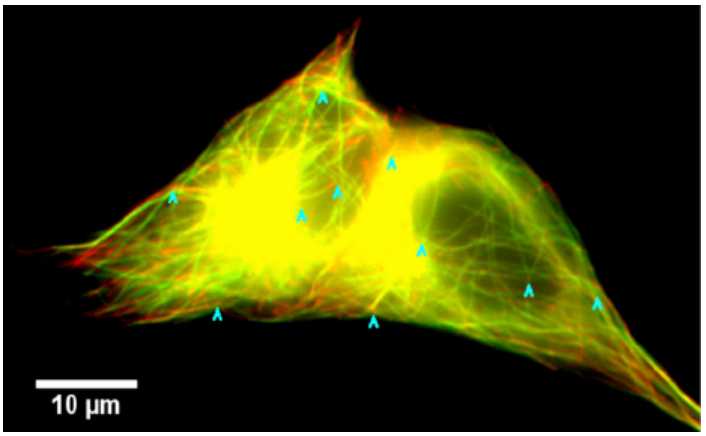

Figure 4.19: EB3-GFP labeled microtubules in a cell. Image of a cell's microtubules labeled with EB3-GFP without flow (*red*) and with a flow (*green*) of 50 μL/min. The position of individual features were measured (arrows) and gave an average displacement during flow of 0.3 ± 0.2 μm (N=60 on four cells).

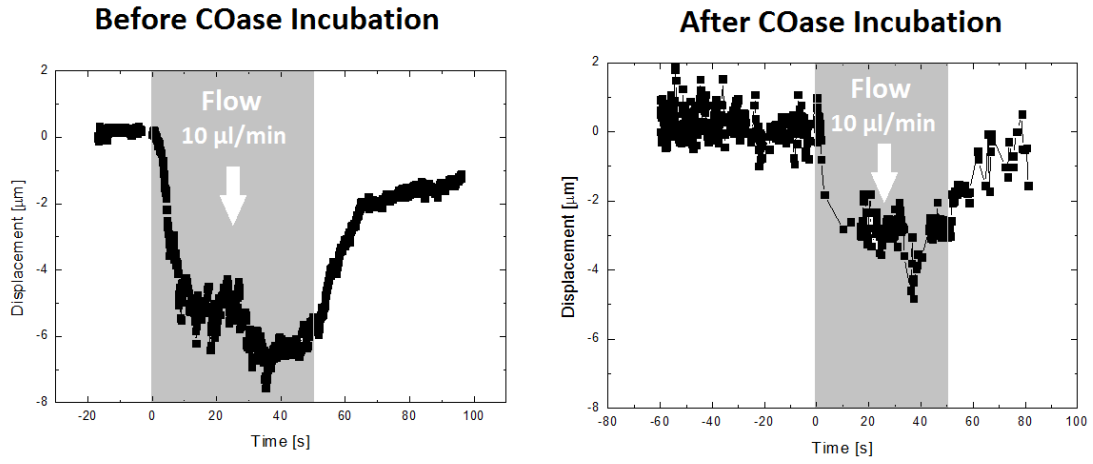

Figure 4.20: Flow cycle for a receptor in a cholesterol oxidase treated cell. Treating a cell with COase destabilizes the lipid raft platforms. This causes a less confined behaviour of the contained receptors. However, the receptors remain confined and still experience the same kind of behaviour under flow, as the two figures show. Furthermore, as expected, the COase treated cell receptor displays a less confined trajectory.

The general shape of the receptor response to the force does not change. The receptor is still displaced in the direction of flow, reaches an equilibrium position and returns as soon as the flow is stopped (see figure 4.20). Yet, when looking closer we see that some important changes have taken place. In section 4.4.3, we calculated the RMS displacement of the receptor in the direction perpendicular to the flow to be 0.09 ± 0.02 μm (N=11), 0.14 ± 0.03 μm (N=11), and 0.08 ± 0.02 μm (N=11) before flow, during flow equilibrium and after flow, respectively. Performing the same analysis on the COase treated cells we obtain RMS values of 0.62 ± 0.21 μm (N=6), 0.65 ± 0.15 μm (N=7), and 0.51 ± 0.08 μm (N=6) before flow, during flow (after equilibrium is reached) and after flow, respectively. These are several times larger than the previous values, supporting the notion that, even though the rafts are destabilized, they still exist and accompany the receptor displacement during flow (see section 4.2, where potential stiffness weakens but does not disappear).

4.4.8 Cell treatment with Latrunculin B

To investigate the nature of the barriers encountered by the membrane receptors, described in section 4.4.3, we treat the cells with latrunculin B (LatB). This acts to destabilize the actin cytoskeleton by sequestering G-actin and preventing F-actin assembly. It is known to bind to monomeric actin with a 1:1 stoichiometry to block actin polymerisation. Any actin dependence of the barriers would, hence, be revealed by a modification of the receptor movement during a flow cycle.

Figure 4.21 shows the effect of LatB on the receptor trajectories. The trajectories after latrunculin treatment (*blue-green*) are clearly much longer than before (*red-yellow*). The larger distances that the receptors are displaced over under an equival force suggests that the barriers are actin dependent and that the associated value for the spring constant

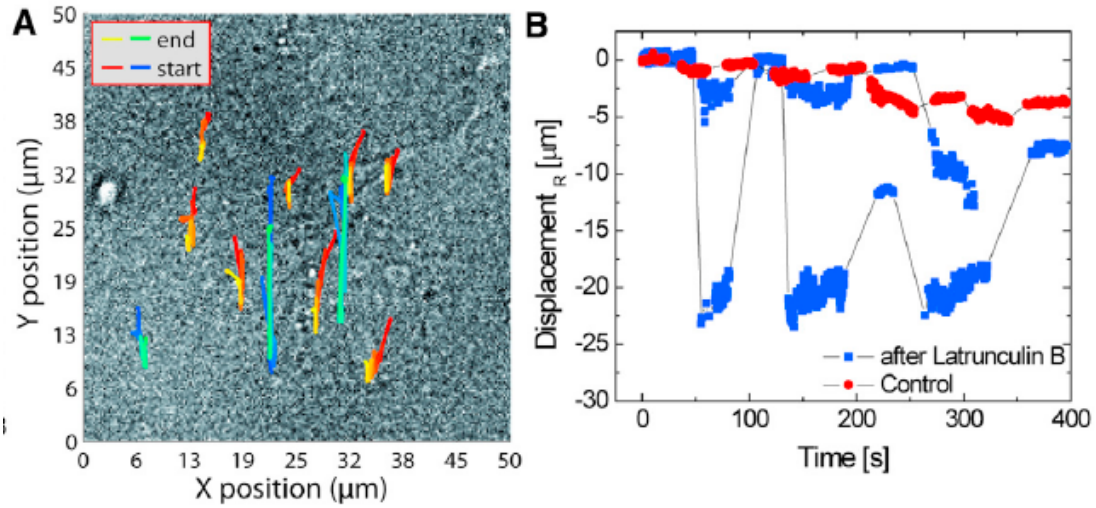

Figure 4.21: Comparing flow cycles for normal cells to cells treated with latrunculin B. (A) The red-yellow curves show the receptor displacements in of a normal cell with progressively higher applied flow rates. Additionally, the receptor displacements for equivalent flows in cells treated with actin-depolymerizing latrunculin B are shown in blue-green. In the second case, the displacements are clearly much larger (B) suggesting that the elastic barriers encountered are actin dependent. The average barrier spring constant changes from 2.5 ± 0.6 pN/μm (N=17) to 0.6 ± 0.2 pN/μm (N=5).

has decreased. Using Hooke's law, we can calculate the average spring constant after latrunculin B incubation and find it to be 0.6 ± 0.2 pN/μm (N=5). Comparing this to the value determined in section 4.4.3, 2.5 ± 0.6 pN/μm (N=17), we determine an 80% decrease in the spring constant value.

Figure 4.22 shows the calculation of the spring constants for two barriers encountered by a receptor. The spring constants in this case are determined to be 0.7 ± 0.09 pN/μm (*red*) and 0.28 ± 0.01 pN/μm (*blue*).

4.4.9 Kelvin-Voigt Analysis of Receptor Displacement

By considering that the displacement of the receptors within the membrane is influenced both by viscous and elastic components, we can analyse the trajectories using the Kelvin-Voigt model of viscoelastic materials to gain a deeper insight into what dictates the movement of the membrane protein. Movement in these types of materials is governed by the following equation:

$$\epsilon(t) = \frac{\sigma_0}{E}(1 - e^{-\lambda t}) = \frac{\Delta L}{L_0}. \tag{4.9}$$

σ_0 represents the constant stress applied by the NP pulling on the receptor equalling F_d/A_0, where F_d is the drag force that is applied on surface A_0. This stress gradually produces the deformation, σ_0/E, expected of a purely elastic material. Here, E is Young's modulus and λ is the relaxation rate given by E/η, η being the viscosity of

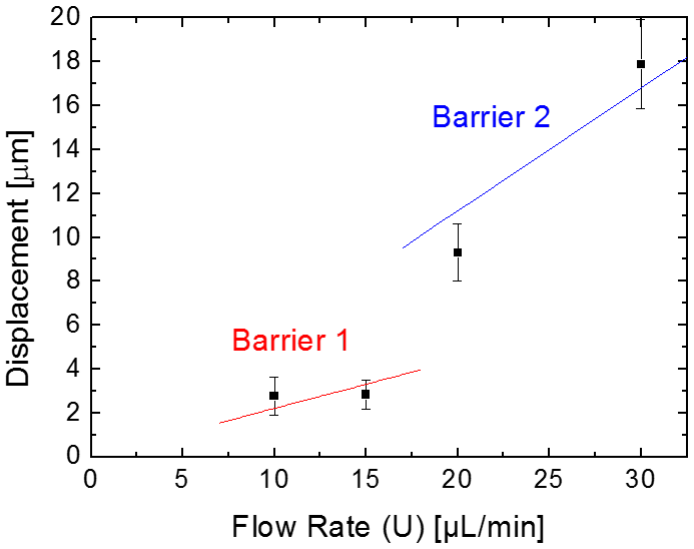

Figure 4.22: Calculation of barrier spring constant after latrunculin B incubation. By plotting the displacement against the applied flow rate we can obtain the effective spring constants of the barriers after LatB incubation. In this case, we find 0.7 ± 0.09 pN/μm (*red*) and 0.28 ± 0.01 pN/μm (*blue*).

the medium. ΔL and L_0 represent the extension and relaxed length, respectively. We expect that the bulk of the elastic, reversible response is due to the elastic strain on the actin filaments, and the viscous response is due to the cell membrane. We exclude membrane bending as a source of elasticity as this would require a higher stress and no global cell shearing was observed during flow under white light.

We analyse the trajectories of the receptors under flow application to full barrier extension and fit these with a curve according to equation 4.9. This was done for receptors under different flow rates. Figure 4.23 shows two examples of fits for flow rates 2.5 μL/min (A) and 20 μL/min (B).

If we first examine the amplitude A of the displacement:

$$A = \frac{\sigma_0}{E} L_0 = \alpha U, \tag{4.10}$$

we can take another look at the reduction of the spring constant value discovered in section 4.4.8. U is the flow rate and α is a factor proportional to $\frac{1}{E}$ taking all the parameters characterising the material into account.

We obtained an α of 0.35 ± 0.11 μmmin/μL (N=6) and 1.04 ± 0.37 μmmin/μL (N=5) for before and after LatB incubation, respectively. Consequently, the Young's modulus has experienced a decrease of 70%, in line with the previously discovered 80% decrease in spring constant value. However, if we look at the average relaxation rates, λ ($= E/\eta$), we obtain from the fits, we find a decrease in λ of around 30% (from 0.54 ± 0.16 s^{-1}(N=6) to 0.39 ± 0.08 s^{-1}(N=5)). The viscosity, η, must therefore also have decreased by 50%$\pm$30%, indicating that the viscosity of the system is dictated by two factors. $\eta_{membrane}$ is the viscosity of the membrane that does not change as it is not affected by the modifications in the actin cytoskeleton, as shown in [133]. The second factor however, η_{actin}, is the

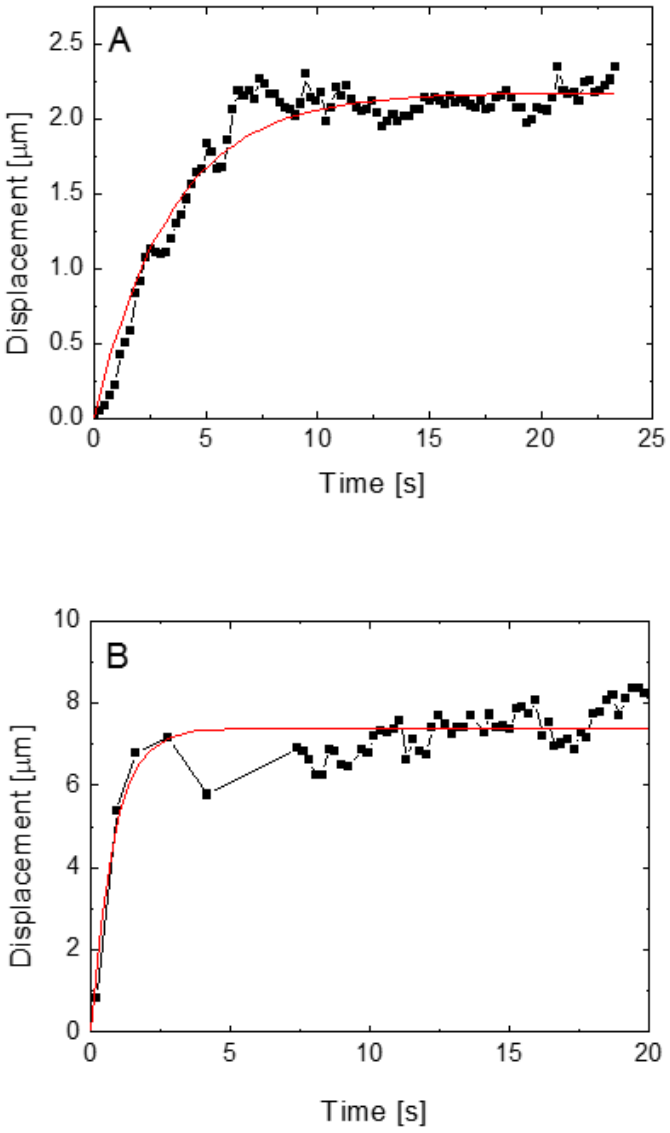

Figure 4.23: Receptor recovery curves for 2.5 μL/min and 20 μL/min flow rate. Recovery of a displaced receptor after the flow has been stopped for an initial flow rate of 2.5 μL/min (A) and 20 μL/min (B), respectively. The red lines are fits with the Kelvin-Voigt model (equation 4.9), yielding a λ of 0.49±0.03 s^{-1} and 1.2±0.2 s^{-1}, respectively.

viscosity related to the viscoelastic network composed of the actin filaments and is reduced by LatB-induced F-actin depolymerization.

4.4.10 Discussion and Conclusion

In this chapter, we used several different approaches to investigate the structure of the cell membrane and the causes of confinement in lipid rafts. First, we studied the effect of raft destabilizing enzymes on the confinement of the receptors and observed the evolution of the confinement potential during this phenomenon. Potential and diffusivity strongly fluctuate after enzyme addition. However, a clear trend towards higher diffusivity and

lower confinement can be seen. This reaction obtained by tracking the receptor motion makes it clear that the CPϵT receptor confinement is strongly dependent on cholesterol and sphingomyelin. The fact that the transferrin receptor, located outside rafts, is not affected further supports this notion. The difference in lipid composition between the environment of raft and non-raft proteins supports the idea that hydrophobic mismatch could play an important role in protein confinement in membranes [222].

We then looked at occasional hopping events that receptor proteins undergo. By using the trajectories of receptors that hop from one confinement domain to an adjacent domain, we extracted the energy required for a receptor to overcome the energy barrier separating the two potential wells representing the lipid raft domains. Furthermore, the fact that receptors are not observed to leave confinement, even in regions where interaction energy values surpass $6k_BT$, gives us a lower limit of the solubilization energy difference between the raft and non-raft phase, which, incidentally, is comparable to other studies [223], which quote energies of approximately 10 k_BT required for inserting a protein into a 5 nm thick lipid membrane. These hopping energies are not extremely high, supporting the idea that the lipid contents of adjacent environments must be similar to lower the energy sufficiently for hopping to take place.

When discussing the origin of the confinement domains, microvilli, and the role of these microscopic protrusions on the cell membrane, must also be considered. Microvilli are on average about 700 nm long and 100 nm wide [224]. The typical sizes of lipid raft domains that we observe in MDCK cells tend to be larger than center-to-center distances between microvilli, a well known feature of epithelial cells, which are around 200 nm [225]. However, similarly to the confinement in lipid rafts, the formation of microvilli has been found to be dependent on the sphingomyelin content of the local membrane [226]. Even a direct correlation of lipid raft presence and microvilli formation has been reported [227]. Therefore, in the absence of conclusive evidence, we cannot rule out the possibility that the confinement potentials observed within lipid rafts could be microvilli-dependent.

Finally, we used a hydrodynamic flow to observe the dynamic reaction of the receptor proteins when exposed to an external force. What we saw, is a readiness of the receptors to move in the flow direction up to a certain equilibrium point. This maximum distance seems to be an elastic limit, since the receptors return to their initial positions, as soon as the flow stops. Furthermore, the displacement is proportional to the flow/force applied and increases even further when the cells are treated with latrunculin B. This means that the receptor displacement distorts actin filaments beneath the membrane, which then exert a restoring force to bring the receptor back to its initial position, when the flow ceases. However, we know from previous work [133] that the observed receptor does not interact with actin. We can thus conclude that another component of the raft, which is displaced together with the receptor, is producing the interaction.

The overall picture these results paint of what is going on at the cell membrane level is the following: The observed CPϵT receptor displays confinement suggests that the receptor is hosted within a lipid raft. In addition to this confinement, there is a second type of interaction between the rafts and the actin cytoskeleton that can be made visible

by applying a force and inducing an interaction with actin barriers. However, it is not the observed receptor that interacts with the actin, but another raft component that is displaced together with the labeled receptor.

In the next chapter, we will further investigate this second kind of confinement by looking at non-raft membrane proteins. These are not confined in lipid rafts and, hence, experience a different type of confinement with a different characteristic potential shape.

Key points:

- The observed receptor confinement is strongly dependent on cholesterol and sphingomyelin. Diffusivity increases while confinement strength decreases when enzymes deplete these two raft constituents. The larger diffusivity can be interpreted to be due to a less dense lipid structure as lipids like cholesterol responsible for packing are removed. Similarly, the raft structure, interpreted as being responsible for producing the confinement forces, is altered.
- Extracting hopping energy from trajectories where receptors switch to adjacent confinement domains provides insight into the energy landscape of lipid rafts and sets a lower limit for the solubilization energy difference between the raft and non-raft phase.
- By using a hydrodynamic flow, a force can be applied on the NP-labeled receptors.
- Under an external force, the receptors are displaced in the direction of the force until an equilibrium position is reached. As soon as the force ceases, the receptors return to their previous positions.
- The receptor displacement is actin dependent. Receptor displacement causes actin distortion, which is responsible for the observed restoring force. As soon as the flow ceases, the restoring force acts to bring the receptor back to the initial position.
- Confinement domains appear to be displaced together with receptors; however, the receptors observed do not seem to be the components interacting with the actin.
- Observed receptors are confined in lipid rafts, which host other proteins capable of interacting with the cytoskeleton.

Chapter 5

Classification of Receptor Confinement

Science is the systematic classification of experience.

George Henry Lewes

Contents

As already eluded to in chapter 1, receptors experience different types of confinement. In chapter 4 we investigated the dynamics of membrane receptors confined in lipid rafts. However, it has also been discovered that the cytoskeleton can produce a motion-limiting effect on membrane constituents that manifests itself as transient confinement and a type of motion termed 'hop diffusion' [51, 54, 228, 229]. One of the proteins that undergoes this phenomenon is the transferrin receptor protein [218, 230]. The differences between the confinement characteristics of the previously explored raft proteins and this non-raft protein are the topic of this chapter.

5.1 Raft vs Non-Raft Membrane Proteins

Many proteins have been seen to reside in lipid-dependent domains [8]. The trajectories of proteins confined within these lipid rafts have already been analyzed with an algorithm using Bayesian inference to extract diffusion coefficient and confinement potential [161]. This potential was found to be well described by a second-order polynomial, after determining that inferring a potential using higher order polynomials did not yield a significant modification in the inferred potential [133]. Furthermore, the receptors were never seen to leave their domains and diffuse freely.

In contrast to these receptors, the transferrin receptor is known to reside outside of lipid rafts, but still experiences a confined-type of diffusive motion with a diffusion coefficient of approximately 0.1 $\mu m^2/s$ within confinement domains of around 0.25 μm^2 in size in normal rat kidney fibroblastic cells [218, 230]. Moreover, during the same studies this membrane protein has been observed to undergo 'hop-diffusion', moving successively from confinement domain to confinement domain with an average residence-time of 29 seconds [218, 230].

These are similar to the values found in this work in MDCK cells, summarized in table 5.1. Values for the diffusion coefficient are consistent with the already published values. On the other hand, the values we find for the confinement domains are larger and vary strongly in size, but nevertheless remain consistent with the previously quoted values. Similarly, the average residence times also fall in the right range. Typical transferrin trajectories are recorded for around 2500 frames, i.e. for approximately 130 seconds, the time interval between frames being 51.3 ms (acquisition time: 50 ms, readout time: 1.3

Average diffusion coefficients and domain areas in MDCK cells

	Diffusion Coefficient ($\mu m^2/s$)	Domain Area (μm^2)
ϵ-toxin receptor (N=77)	0.11 ± 0.007	0.71 ± 0.08
α-toxin receptor (N=20)	0.08 ± 0.02	0.37 ± 0.08
Transferrin receptor (N=65)	0.11 ± 0.01	1.40 ± 0.17

Table 5.1: Average diffusion coefficients and domain areas of analysed trajectories. Area calculated by taking the ellipsoidal area defined by the maximum lengths along the x- and y-axes. Errors are the standard errors on the mean of the sample values for each data set.

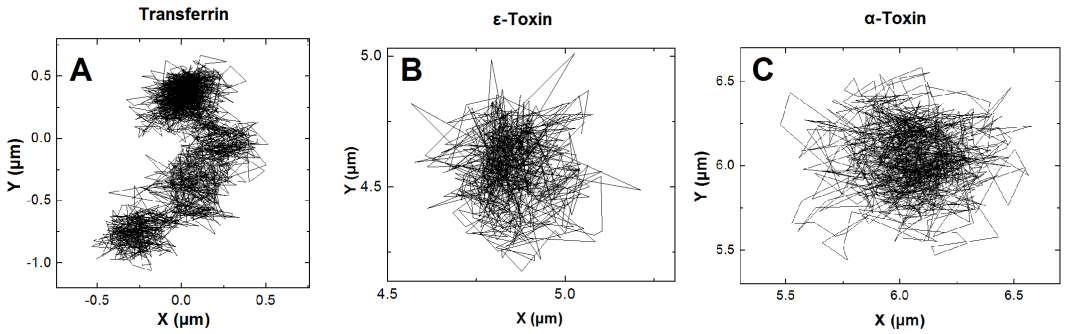

Figure 5.1: Transferrin, ϵ- and α-toxin receptor example trajectories. A, B and C show examples of transferrin, ϵ-toxin and α-toxin receptor trajectories. ϵ- and α-toxin receptors (B and C) are always observed in confinement, whereas transferrin receptors (A) display a form of transient confinement within different adjacent domains.

ms). During this time, domain changes generally occur between one and five times. This is equivalent to average residence times ranging from approximately 20 to 60 seconds.

The manner of movement of the transferrin receptor suggests that it experiences the type of confinement proposed by the picket-and-fence model (see section 1.3.2) of membrane protein confinement [49, 218]. Furthermore, the structural particularities of lipid-dictated confinement and cytoskeleton-dependent confinement suggest that the shape of the confinement potentials should be fundamentally different. For lipid rafts we obtained a harmonic potential. However, for domains limited by actin filaments, we would expect the confinement potential to be flatter in the domain centre and more abrupt at the edges, since encountering an actin barrier, despite the fact that the barrier is elastic, should provide a steeper potential boundary than that produced by a change in lipid composition in lipid rafts, which may be less extreme.

5.1.1 Nanoparticle receptor coupling

The experimental procedure for observing toxin receptors in the cell membrane has already been described in section 2.1. The protocol for observing transferrin receptors is largely the same. One noteworthy difference is the use of streptavidin and biotin to link the transferrin to the NPs. Prior to cell incubation with the NP-transferrin complex, we incubate the NP-streptavidin complex with biotinylated transferrin for one hour at 37° with a molar ratio of 1:3. We believe this ratio is large enough to produce enough couplings for the experiment, and yet small enough to not cause any cross-linking of receptors.

5.1.2 Trajectories

Figure 5.1 shows examples of the trajectories of each of the membrane receptors studied. The ϵ- and α-toxin receptors typically are limited to a single domain, with rare hopping events to adjacent domains. At the same time, the transferrin receptor can be seen to experience temporary confinement and frequently move to adjacent domains.

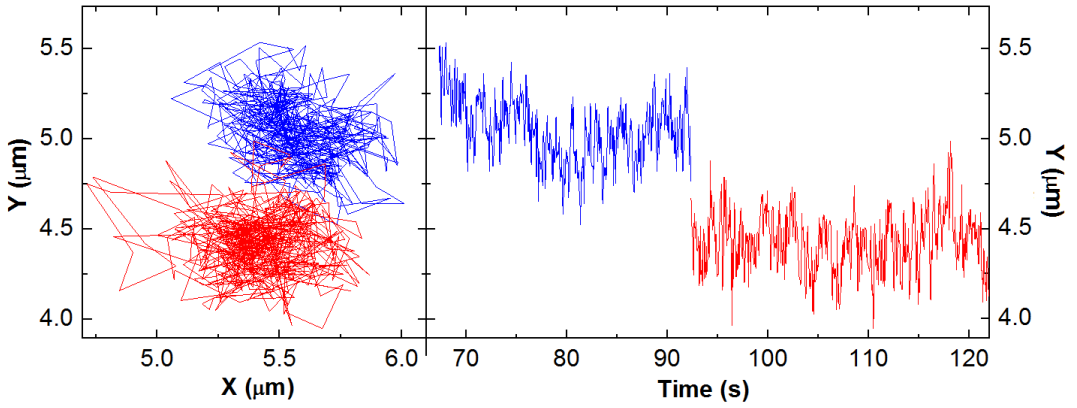

Figure 5.2: Example trajectory of an ϵ-toxin receptor hopping event. The two distinct domains are identified by the red and blue colors. Next to the domains, using the same color code, the evolution of the y-position is shown. The hopping event can clearly be seen to occur shortly after 90 seconds.

For subsequent analysis of the confinement potentials, the individual domains visited by the transferrin receptor need to be identified. To this end the trajectories are separated. This is treated in section 5.2. Typically, the ϵ- and α-toxin receptors we observe do not change confinement domains. As such, their trajectories are directly analysed without further domain identification.

5.1.3 Raft vs. non-raft hopping

In section 4.3 we presented the phenomenon of receptor hopping from one lipid raft to another. As both the hopping of raft-receptors and the hop-diffusion of the transferrin receptors represent a change in confinement domain, it is natural to compare and contrast these two events more closely.

Figure 5.2 shows an example of a hopping trajectory of an ϵ-toxin receptor. The confinement in both domains fluctuates consistently around the centre of the domain. Furthermore, the hopping event is very abrupt. In contrast, figure 5.3, depicting a hopping event of a transferrin receptor, displays a more gradual exploration of the domain. Moreover, the receptor's movement within the domain seems to be less dictated by a restoring force perpetually redirecting it's movement towards the centre. Gradual drifts suggest a flatter potential in the domain's centre with a confining force concentrated at the edges.

ϵ-toxin receptor hopping trajectories will be included in subsequent analyses for further comparison.

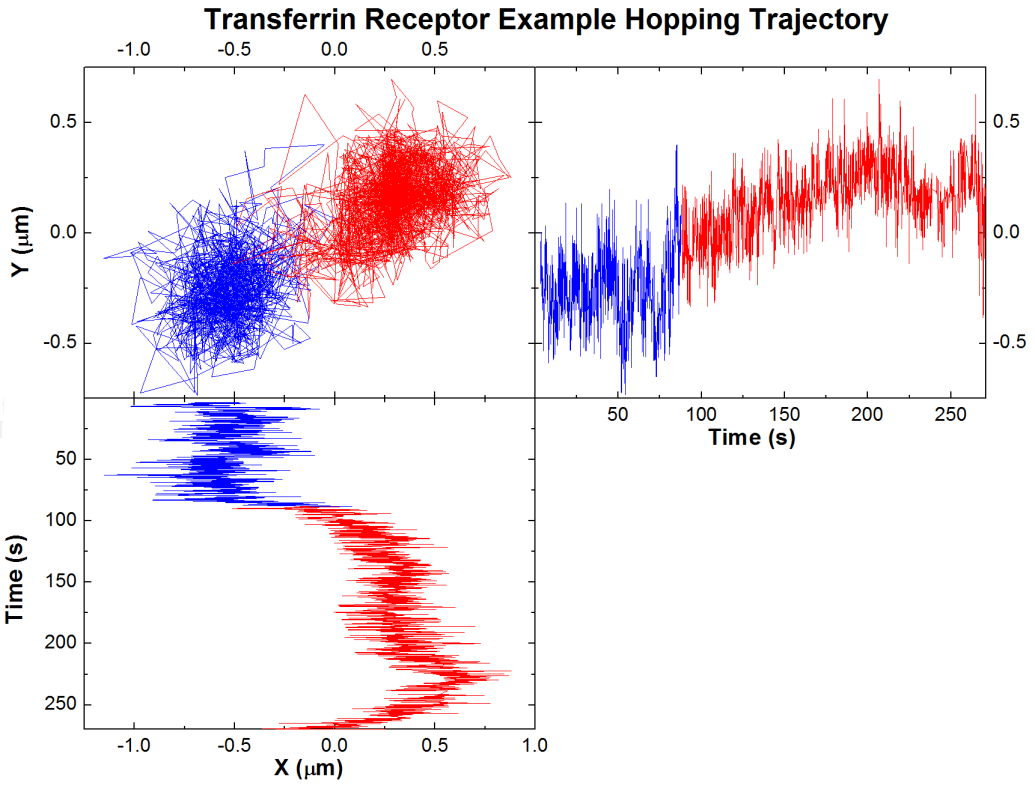

Figure 5.3: Example trajectory of a transferrin receptor hopping event. The two distinct domains are identified by the red and blue colors. Next to and below the trajectory, using the same color code, the evolution of the y- and x-positions are shown. The hopping event can clearly be seen to occur at around 100 seconds.

5.2 Identifying Confinement in Hop-Diffusion Trajectories

5.2.1 Identifying the number of confinement-domains

For some transferrin receptors, like the one in figure 5.3, the number of domains explored is clearly two. However, in other trajectories the receptor explores three domains or more. The number of confinement domains that a receptor undergoing 'hop-diffusion' visits is determined by using the Voronoi version of the Bayesian inference algorithm (see section 2.3.3). The algorithm determines the potential from the input trajectory. The number of minima determined by the algorithm yields the number of confinement domains the receptor passes through.

Figure 5.4 showcases the procedure with two example trajectories. Figure 5.4B and F show the top view of the respective inferred potentials. By looking at the color code for the potenial in 5.4B and F, and the side view of the interpolated inferred potentials in 5.4C and G, two minima are identifyable in the potential in 5.4B and C, and three in 5.4F and G. Having thus determined the number of subdomains, we proceed to splitting the trajectory.

5.2.2 Using k-means to split trajectory points into confinement domains

To standardize the splitting of the trajectories into their subdomains, a k-means clustering algorithm was used to split the entire collection of points into clusters. An explanation of the k-means algorithm is given in appendix B.1. The k-means algorithm is given the determined number of subdomains and proceeds in calculating the clusters of points. Examples of this result are given in figure 5.4D and H. These show a double- (fig. 5.4D) and triple-confinement domain (fig. 5.4H) trajectory, respectively. This also represents the final pre-treatment step of the raw data before analysis along with the single-domain trajectories, and is conducted for both the transferrin trajectories undergoing hop-diffusion and the hopping data of the CPϵT receptor.

The effectiveness of the k-means algorithm in splitting a trajectory moving into two connected domains is explored in section 5.3.2. Furthermore, in later tests (sections 5.3.3, 5.4, and 5.5.3), results from both the simulated split and experimental split trajectories are analysed and compared, as further confirmation of the validity of this approach.

5.3 Decision-Tree Classification of Confinement Potentials

As a first analysis, we use a Bayesian inference decision tree (BIDT) approach to determine if a given trajectory is undergoing free Brownian motion, confined motion in a harmonic potential, or confined motion in a fourth-order potential. The general principle of the BIDT will be explained below. For details on the BIDT method, refer to [217]. As previously determined, confined motion in lipid rafts displays the characteristic motion produced by a harmonic potential [133]. Hence, it is expected that the decision tree will classify these trajectories as produced by a second-order potential. In contrast, we expect the transferrin receptor cytoskeleton barrier-dependent trajectories to have a characteristic abrupt boundary, more closely resembling a fourth-order potential.

The Bayesian decision tree uses three different metrics to differentiate between three models of motion: a second-order potential, a fourth-order potential and free Brownian motion (see equations 5.1). It first applies the Bayesian inference algorithm to determine the inferred characteristic parameters that best correspond to the observed trajectory for each of the models. For each of the models, the respective posteriori probability, given this set of parameters, P(Q|T), is calculated, and its maximum value, which represents the maximum *a posteriori* (MAP) estimator is obtained (refer to section 2.3.1 for details). With this estimator, the relevant metrics are calculated as discussed below, and a decision is made.

The three metrics used are the Bayesian information criterion (BIC) (equation 5.1a), the Akaike information criterion (AIC) (equation 5.1b) and the corrected AIC (AICc)

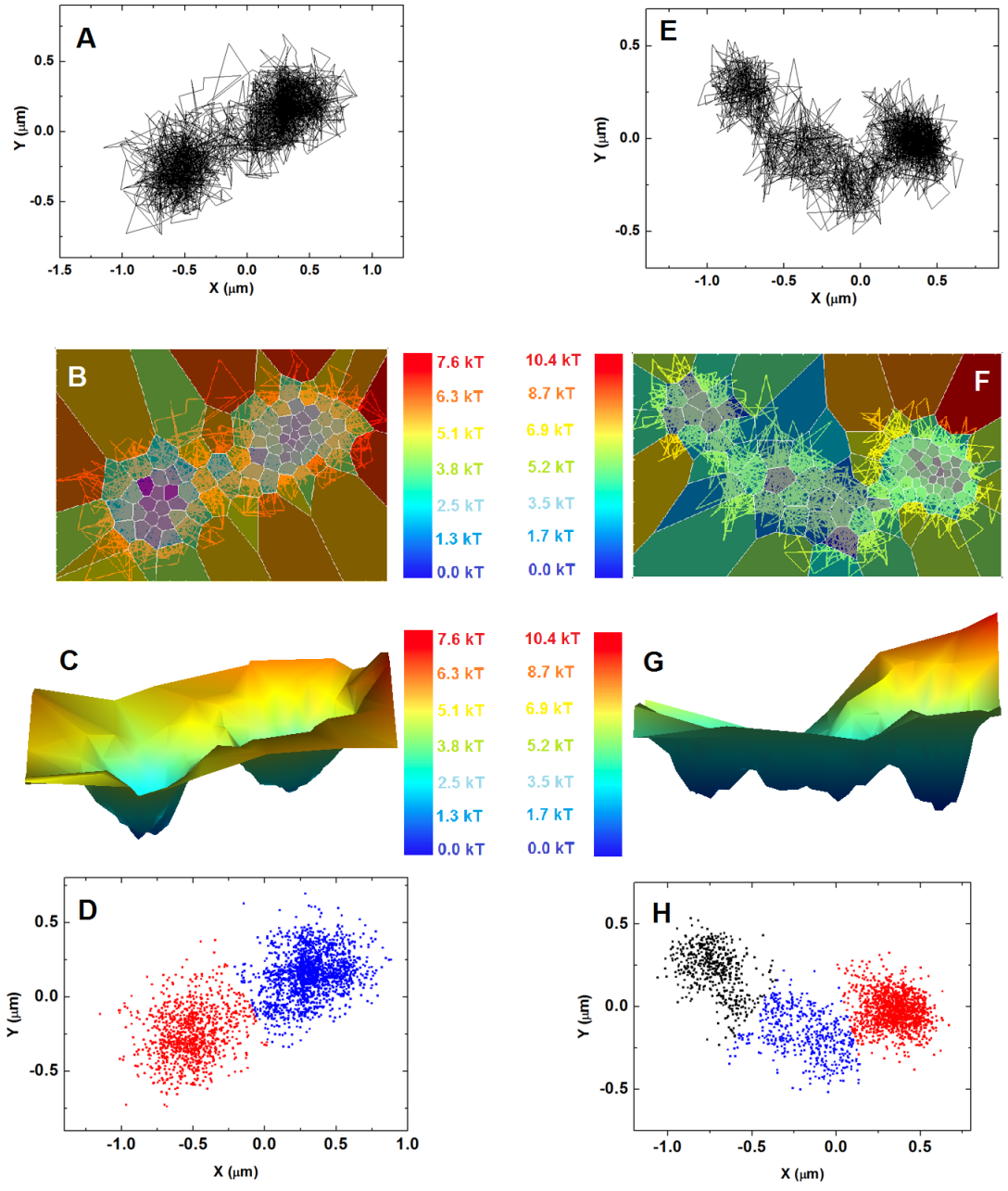

Figure 5.4: Analysis steps for splitting a trajectory into confinement domains. To split a trajectory (A and E) into subdomains, we start by inferring the potentials. The top view of the inferred potentials (B and F) and the side view of the interpolated surface plot (C and G) then give a fairly clear idea of the number of confinement domains contained in the trajectory. Finally, a k-means algorithm is used to split the trajectories into their respective subdomain parts (D and H).

(equation 5.1c).

$$BIC = -2 \cdot \ln(L) + k \cdot \ln(N) \tag{5.1a}$$

$$AIC = -2 \cdot \ln(L) + 2k \tag{5.1b}$$

$$AICc = AIC + \frac{2k(k+1)}{N-k-1} \tag{5.1c}$$

In equations 5.1, k represents the number of degrees of freedom of the used model. This way, a larger number of free parameters is penalized. L is the MAP estimator, and N is the sample size.

The BIC, also known as the Schwarz criterion after Gideon Schwarz, is derived from the leading terms of the asymptotic expansion of the Bayes estimator [231]. It therefore serves as a derived metric from a factor that compares the viability of models based on their probability given an observed data set. The AIC is based on the principle of minimising the information loss calculated by the Kullback-Leibler divergence, $D_{KL}(\phi\|\gamma)$, where a model γ is used to describe the data of some observation ϕ [232]. The AICc is a corrected version of the AIC that includes the finite sample sizes of the datasets in the calculation. The BIC penalises models with a larger number of degrees of freedom more strongly than the AIC/AICc. For sample sizes, N, of eight or more the penalising term in the BIC outweighs that of the AIC/AICc.

All three of these criteria take the number of degrees of freedom into account by adding an additional term penalising larger numbers of free parameters. This in an advantage of this approach with respect to direct likelihood-ratio tests, which may favor models that lead to over fitting. This is important since the number of free parameters between the models ranges from 1, for Brownian motion, to 16, for motion within a fourth order potential.

The lowest number calculated with the metrics gives the determined model for a given trajectory. Türkcan and Masson [217] determined, using simulated trajectories, that the BIC criterion is superior to the AIC and AICc criteria in determining if a trajectory displays confined or free Brownian motion. For simulated trajectories using experimental parameters for the diffusion coefficient, acquisition time and trajectory points of 0.1 μm/s^2, 51.3 ms and ≈1000 points, respectively, BIC correctly classifies close to 100% of all trajectories, whereas AIC and AICc correctly assign only around 50%. On the other hand, for determining if a trajectory exhibiting confinement is produced by a second- or fourth-order potential the AIC and AICc exhibit between 70% and 100% success rates, whereas the BIC systematically classifies all confinement as second-order. Therefore, the BIC is only used to determine the existence of confinement, whereas the AIC and AICc are used in a second step to determine if the confinement is better modelled by a second- or a fourth-order potential. Figure 5.5 show a schematic representation of the decision tree for this process.

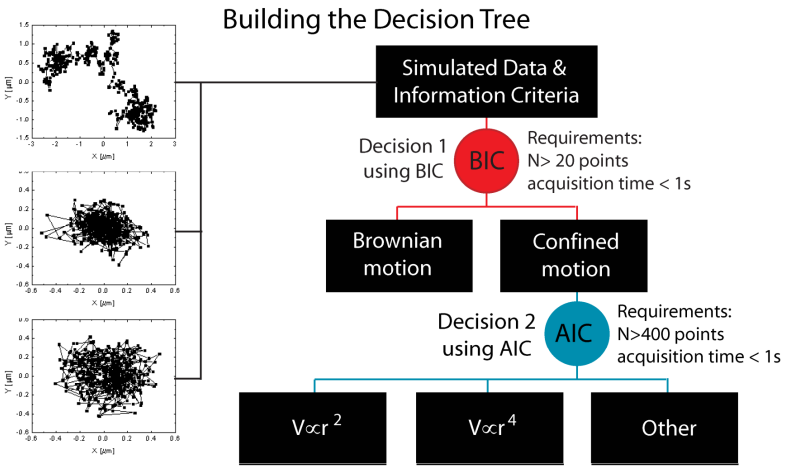

Figure 5.5: Decision-tree of the trajectory classification algorithm. The BIC is used to detect confinement, which is then classified to be better described by a second- or fourth-order confinement potential by the AIC and AICc. Figure reproduced from [217].

5.3.1 Simulated Trajectories

To show that the above metrics also work for trajectories exhibiting hopping and, in particular, that the splitting of transferrin receptor trajectories does not alter the fundamental characteristics that will subsequently be used to compare the two different types of data (second- and fourth-order confinement), we simulate a receptor moving in two adjacent domains with exponential and harmonic potentials. The trajectories are then split using k-means, analyzed and compared.

The trajectories are simulated using two circular domains. Based on the typical values observed in experiments, the radius of the domains is chosen to be $r_0 = 0.5$ μm and the inter-domain distance is chosen to be $\Delta = 1.0$ μm. For both the exponential and harmonic potentials, the potentials are chosen such that their value at $r = r_0$ is $4k_BT$. The receptor is considered to be in a domain, experiencing the potential prevailing in that particular domain until it passes over the perpendicular bisector of the line joining the two domain centres. At that point, it is in the adjacent domain feeling the corresponding potential until it moves back into the previous domain.

The simulated trajectories use two types of potential. Either a harmonic potential as in equations 5.2a and 5.2b with k_{sim} taken to be 0.14 pN/μm,

$$V_x = \frac{1}{2}k_{sim}x^2 \tag{5.2a}$$

$$V_y = \frac{1}{2}k_{sim}y^2 \tag{5.2b}$$

or a flat potential in the center of the domain with an exponential potential commencing at $f \cdot r_0$ and rising up to $4k_BT$ at $r = r_0$ according to equation 5.3.

$$V(r) = \begin{cases} \frac{A_{exp}}{e-1}(e^{\frac{r-f\cdot r_0}{r_0-f\cdot r_0}} - 1), & \text{if } r \geq f \cdot r_0 \\ 0, & \text{if } r < f \cdot r_0 \end{cases} \tag{5.3}$$

In equation 5.3, A_{exp} is the height of the potential at $r = r_0$ and is set to $4k_BT$, and f is the fraction of r_0 at which the potential changes from flat to exponential. In these simulations it was set to $\frac{1}{3}$.

Additionally, to better mimic experimental conditions, positioning noise of 30 nm is added to the simulated trajectory points as well as averaging of intermediate positions during the acquisition time. This averaging serves to simulate the effect the camera produces while it collects photons during the image acquisition time. As work of Destainville and Salomé has shown, this detector time-averaging effect produces a deterministic error in the diffusion coefficients and domain sizes obtained when analysing confined trajectories using MSD [233]. Here, the trajectories are not analysed with MSD. However, it is possible that a similar effect is produced with the BI approach. A parameter bias when extracting second-order potentials has already been discussed in section 2.3.2. For the purposes of this investigation, a mild bias does not alter the comparative results as long as conditions of time-averaging and noise are present in all data sets, including the simulated data.

A graphical representation of the potentials used to simulate the two types of trajectories is given in figure 5.6. Additionally, an example set of trajectories is shown below their respective potentials. For these simulations, a typical diffusion coefficient of 0.1 $\mu m^2/s$ is used. 50 trajectories of each were simulated, giving 100 split trajectories for each condition. After splitting, disconnected trajectory parts due to switching to the second confinement domain and back were recombined to form a single trajectory for a domain.

5.3.2 Classifying Simulated Trajectories

After splitting, the simulated trajectories are then fed into the BIDT algorithm. Figure 5.7 shows the result for the 83 trajectories that were obtained with harmonic potentials and the 100 trajectories that were obtained with exponential potentials. Clearly, the trajectories that were initially produced using a harmonic potential are largely classified as second order, whereas the data produced with the exponential potential has been found to clearly correspond to a fourth-order rather than second-order potential. This confirms that a potential modelled to be flat in the centre with strong repulsion at its borders is classified to more closely resemble a fourth-order potential. It furthermore validates the approach we take to split adjacent-domain trajectories using a k-means algorithm.

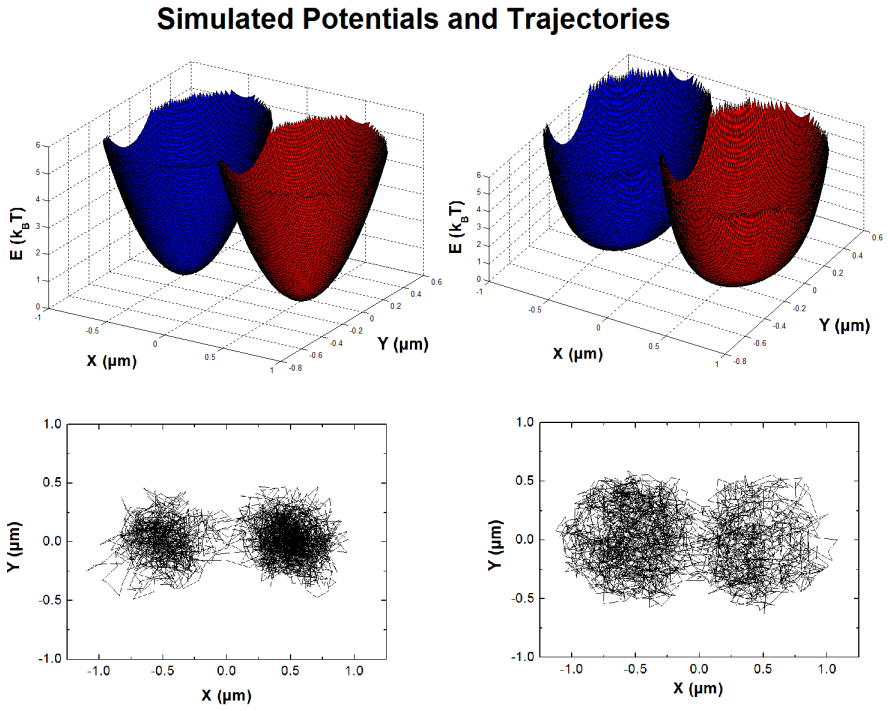

Figure 5.6: Simulated adjacent confinement potentials and resulting trajectories. Adjacent harmonic and exponential (left and right, respectively) potentials used to simulate hopping trajectories. Examples of trajectories are shown underneath their respective potentials. N = 3000, Δt = 51.3 ms, D = 0.1 μm^2/s.

5.3.3 Classifying Experimental Trajectories

We can now take our experimental trajectories and analyse these using the same BIDT approach, after splitting into confinement domains in the case of the transferrin data. The results are summarized in figure 5.8. Again, the data show a clear trend. The ϵ- and α-toxin receptors that reside in lipid rafts clearly show a trend towards motion in a second-order potential confirming previous results in [133]. However, as expected, the transferrin receptors display a behaviour closer to motion in a fourth-order potential.

It should be noted that the number of points, N, per trajectory used in this analysis was always above 500 and in most cases above 800. This ensures that the BIDT algorithm remains in the range of declaring 70% to 100% of trajectories correctly [217].

5.4 Comparing Potential Shapes

To compare the exact shape of the potentials experienced by the receptors investigated we analysed the change in potentials values throughout their domains more closely. For receptors that experience a potential best described by a second-order potential, we would expect a larger change in potential within the center of the domain, whereas potentials with features closer resembling a fourth order potential, the value of the

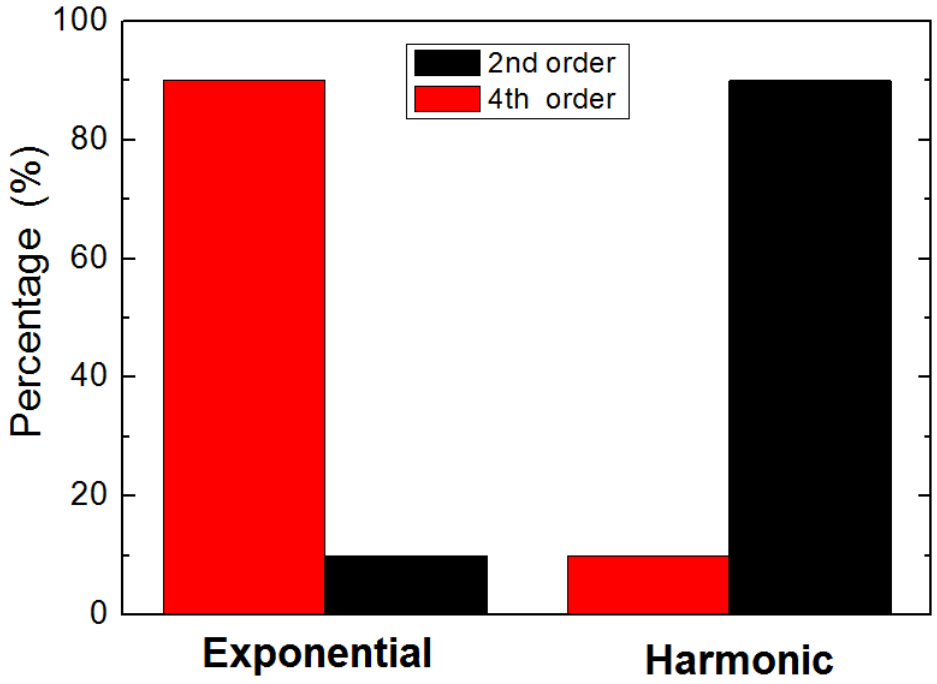

Figure 5.7: Decision-tree results for simulated split trajectories. Using the decision-tree method, the split simulated hopping trajectories are classified into 2nd and 4th order. The trajectories produced using exponential and harmonic potentials were classified by a large majority as fourth- and second-order, respectively. For each case, 50 trajectories were split into 100 individual trajectories, which were then classified. 17 domains of harmonic potentials had to be excluded as not enough data was present in some domains due to a lack of hopping. Using a two-sample t-test with a null-hypothesis that the two distributions have equal means, we can reject the null hypothesis at the 10^{-39}% significance level.

potential will be flatter at first when moving away from the domain centre and then end up steeper at the edges of the domain.

Here, we examine this gradual change by taking into account all the spatially normalised potentials inferred from the experimental trajectories, normalising them, and calculating the average potential at a given radius within a confinement domain. This is done for a range of radii from 0 to the edge of the domain and all radius-dependent values are averaged over all the potentials felt by the respective membrane receptors. This gives us an average value for the increase in potential for each receptor as a function of the distance from the centre of the confinement domain. Figure 5.9 depicts a schematic of this process. The contour rings represent the values at which the values are taken. For each step from a radius r_n to r_{n+1} the difference in the potential, Δz, is calculated and taken as a percentage of the average base value of the potential.

These percentage increases per step away from the confinement domain centre are shown in figure 5.10. The receptors previously classified to reside in second-order potentials are shown in the red/orange colors, while the receptors classified as residing in fourth-order potentials are shown in blue. We see that the increase in the potential close to the domain centre is larger for the former group. On the other hand, on average the transferrin receptor seems to be experiencing a more gradual increase in potential

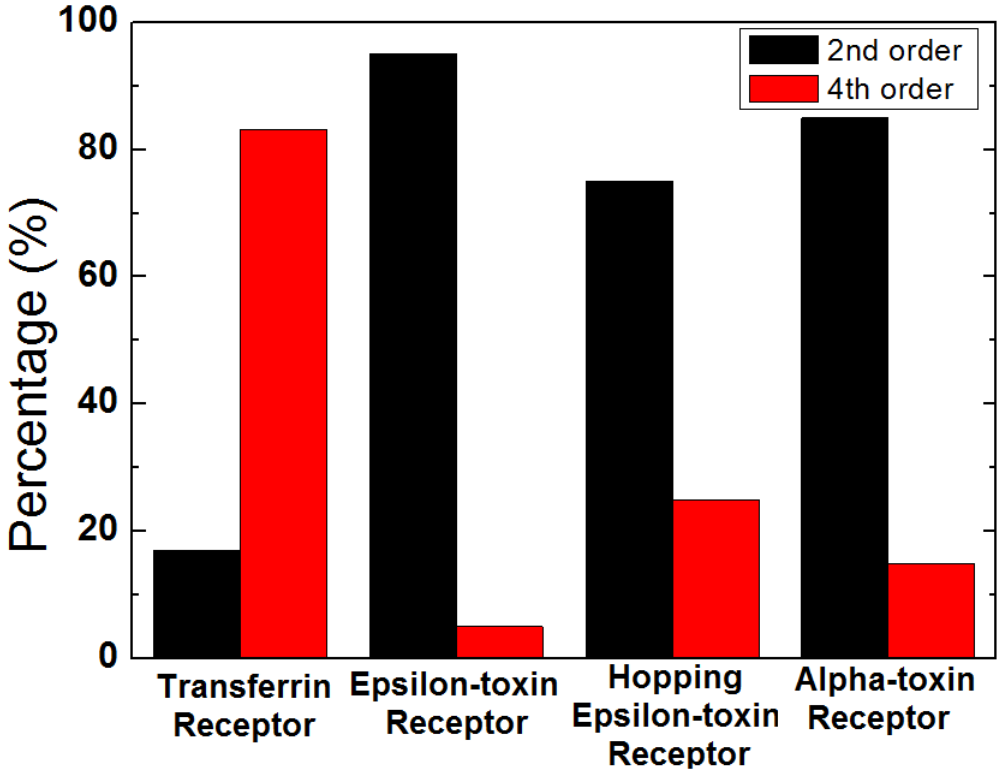

Figure 5.8: Decision-tree results for experimental split trajectories. Using the decision-tree method, the experimental trajectories are classified into 2nd and 4th order. The split transferrin-receptor trajectories are mainly classified as fourth order, while the epsilon-, hopping epsilon-, and alpha-toxin receptor trajectories as second order. 65 transferrin, 40 ϵ-toxin and 20 α-toxin and 12 hopping ϵ-toxin receptor trajectories were analyzed. Using a two-sample t-test with a null-hypothesis that the distribution representing the transferrin receptor has an equal mean compared to each of the other distributions, we can reject the null hypothesis for each case at least at the 10^{-5}% significance level.

and lies closer to the curve representing the flat central potential. Values towards the edge of the potential well become less reliable for all curves since the variability at the domain edges over the entire data set increases. This is due to domain borders being less explored by the receptor and consequently less sampled than centrally lying areas within the confinement domain. However, since the potentials are normalized, the maximum value of all potentials is the same. Therefore, a more gradual initial increase must be compensated by a steeper increase at the edge of the domain.

5.5 Comparison of Potentials using Data Clustering

To exploit the ever growing number of data in single molecule analysis, we can use methods developed in the machine learning community. One way to do this is by clustering the data of the potentials we infer onto a two-dimensional plane in terms of similarity. This is possible because data clustering provides the tools for reducing a high-dimensional data set down to two dimensions while maintaining the maximum possible heterogeneity

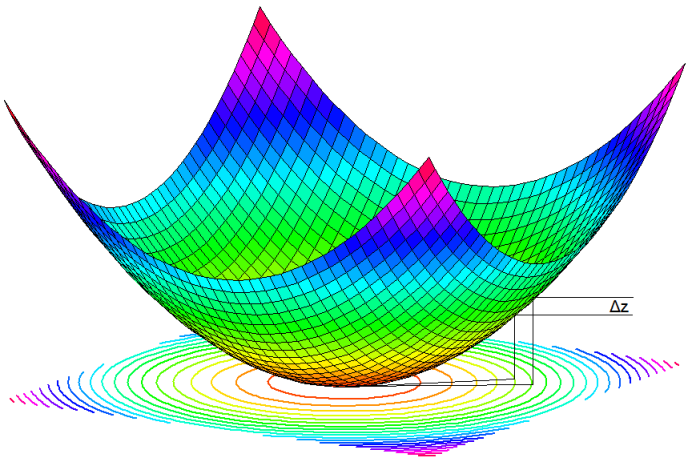

Figure 5.9: Contour plot of confinement potentials used to determine the percentage increase in potential. An example potential with corresponding contour plots underneath representing the steps at which the average potential is calculated. The difference between these values, Δz, is calculated and taken as a percentage of the base value, i.e. the average value of the first radius.

within the data. To achieve this we used a t-distributed stochastic neighbor embedding (t-SNE) algorithm, developed by Van der Maaten and Hinton in 2008 [234]. By first applying a PCA (principal component analysis) algorithm, we reduced the dimensions of the input data while capturing most of the relevant variability. The t-SNE algorithm then plots the remaining samples on a two dimensional surface such that the collective distances between a point and all the other points reflect the "similarities" between the points quantified by a student's t-distribution. A more detailed description of this algorithm is given in appendix B.3, and for the full description refer to [234].

5.5.1 Data preparation for t-SNE clustering

Before applying the t-SNE clustering algorithm, the potentials and diffusivities inferred from the trajectories need to be compiled into a treatable data set. The first step is to analyse the trajectories with the Voronoi version of the BI algorithm. This uses a k-means algorithm (see appendix B.1) to obtain 75 to 100 cluster centroids from which the subdomains will be constructed. The cluster centroids will then be used to produce a Voronoi diagram, which is used to define the subdomains for parameter inference, as explained in section 2.3.3. Figures 5.4B and 5.4F show the Voronoi diagram and the inferred potential values for two trajectories.

The BI algorithm output, i.e. the spatial dimensions of the potential, is normalized, and then used to project the potentials, given as a Voronoi tessellation, onto a 41×41 square mesh in which the individual meshes adopt the values of the corresponding Voronoi meshes using an in-house MATLAB algorithm (see figure 5.11A). The size of each mesh was chosen to be approximately half the size of the smallest typical size of a subdomain produced by Voronoi tessellations of the potentials. The idea is to make the meshes small enough to retain the heterogeneity of the obtained data, yet large enough so as not to

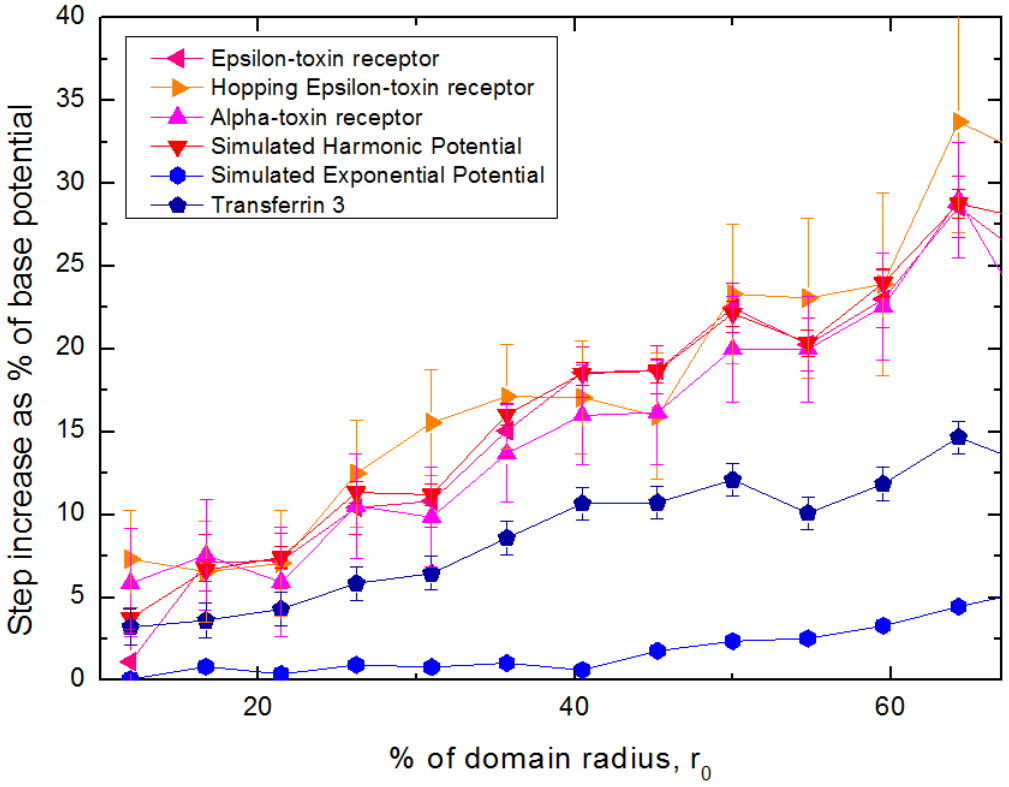

Figure 5.10: Spatial step increases of potentials as a percentage of base potential. The curves in red/orange represent the raft proteins and the simulated harmonic potentials. In blue, we see the non-raft protein and the simulated exponential potentials. The non-raft transferrin receptor clearly lies closer to the exponential potential and both display a lower step increase in potential moving away from the centre of the confinement domain, suggesting a flatter central portion of the confinement potential. Error bars represent the errors on the mean for each calculated mean.

oversample the potential. The individual meshes adopt the values of the confinement potential in the Voronoi meshes they are superimposed on. The potential reconstructed in this way is shown in figure 5.11B. The same is done for a mesh of the diffusivity map of the domain. Next, the meshes are transformed from a 2D matrix of values to a single array of values by concatenating the rows side by side. Doing this for both the potential and diffusivity, yields a 3362-dimensional data set for one input trajectory.

Lastly, a preliminary principle component analysis (PCA) is conducted and the 3362-dimensional data are reduced to 30 dimensions before running the t-SNE analysis on this dimensionally reduced data set. The results of this method are shown in figures 5.13 and 5.14.

Once the data is transformed into a clustered data set, the representation is analysed by eye and, if a set of clusters has precipitated, a line is drawn in between the two clusters to separate them. This boundary represents the condition for classifying the data as being associated either to the characteristics represented by one cluster or the other. Subsequently, the percentage of a given class of data that is on the same side as its assigned cluster is given (tables 5.2, 5.3, and 5.4).

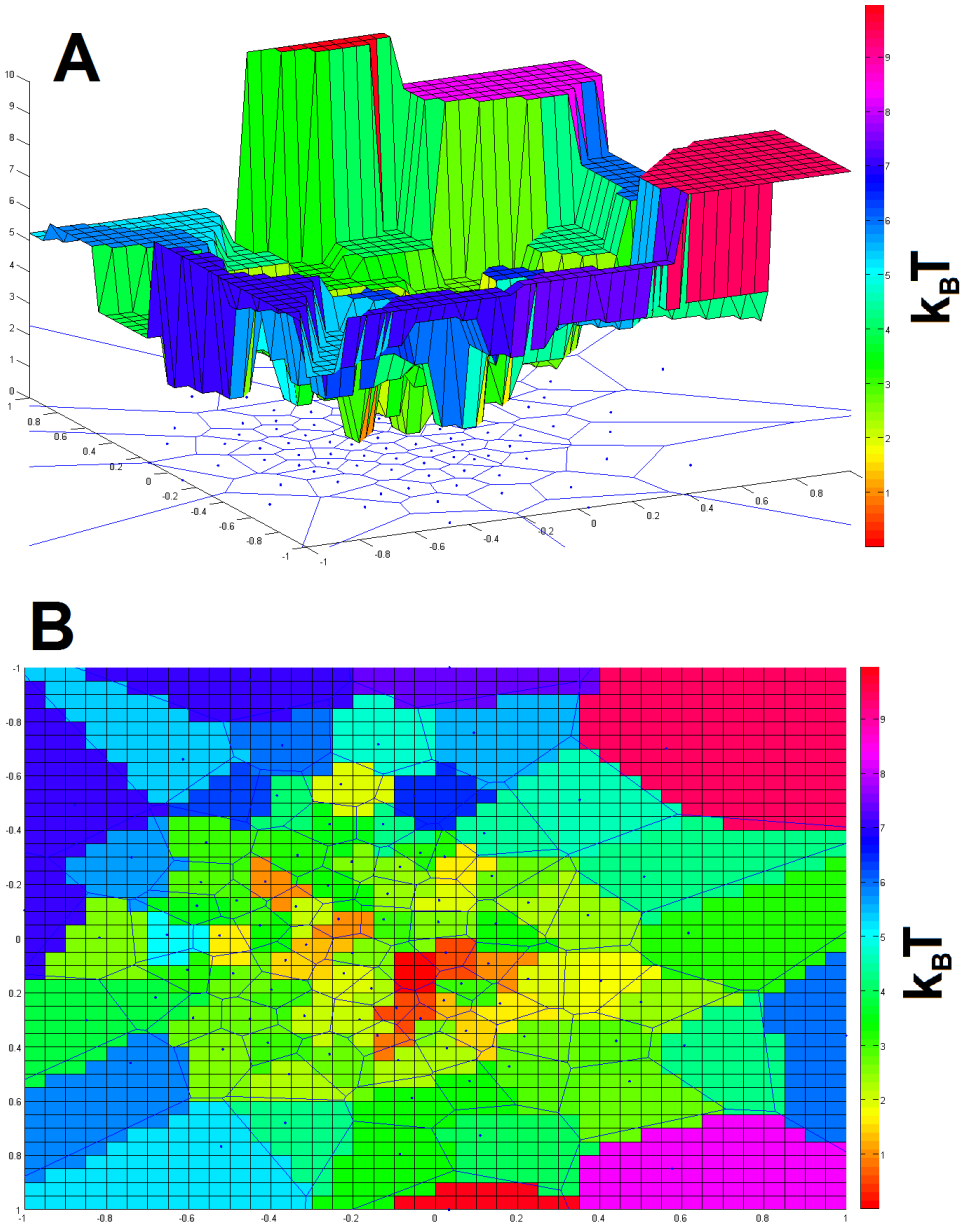

Figure 5.11: Potential data projection on a mesh used for t-SNE clustering algorithm. A is the reconstructed potential of an ϵ-receptor potential obtained using the BI algorithm without interpolation as in figure 5.4 C and G. B is a color-coded top view of the same potential (darker blue colors depict lower potentials). A 41×41 mesh is superimposed to obtain a 1681 dimensioned data set for the potential extracted from a trajectory.

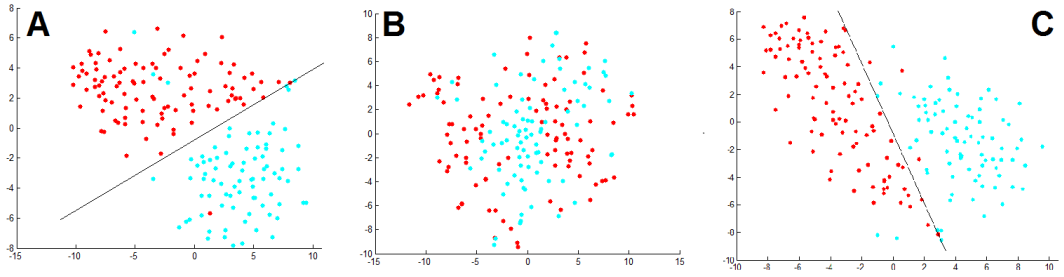

Figure 5.12: t-SNE clusters of simulated data. Cluster plots using only data simulated with an exponential potential (N=100) (red) and a harmonic potential (N=83)(blue). Plots were produced using (A) only the inferred potential map, (B) only the inferred diffusivity map, and (C) a combination of both.

A straight line is chosen for simplicity. However, to optimise further allocation and classification of data, a curved or bent boundary could also be envisaged. k-means was found to be an inadequate method for detecting the data clusters as its only criterion is minimising the distance of the cluster points to the cluster centroids (see appendix B.1). It does not take into account the pre-existing knowledge one has of the various groups of data.

Finally, it should also be noted that adding additional data to cluster or modifying the data sets that are used to produce the clustered data will also have an effect on the shapes of the clusters. For example, adding additional data points to the cluster will, depending on the added data, alter the shape of the cluster since the new similarity relation between the new data point and all the existing data points needs to be recalculated and represented graphically (see appendix B.3 for more detail).

5.5.2 Clustering Simulated Data

As a first step to test the t-SNE based approach to analyse the data, we perform the analysis exclusively on the data produced with the simulated potentials. The BI algorithm produces both a map of the potential within the domain, and a map of the diffusivity. To test the respective efficacies of these two outputs, we cluster the data using only the potential, only the diffusivity, and a combination of the two. The results can be seen in figure 5.12.

Taking purely the diffusivity does not produce a desired splitting of the data into clusters. However, taking only the potential does split the data into two clusters, as does taking a combination of the two parameters. Indeed, for the simulated trajectories used here, the inclusion of diffusivity in the analysis does not produce a significant improvement in the resulting clusters. In both cases, more than 95% of the data falls on the side of its cluster with respect to the placed boundary (see table 5.2). This is not surprising given that the same homogeneous diffusivity was used for both types of simulated trajectories. This, however, may be different for the experimental trajectories.

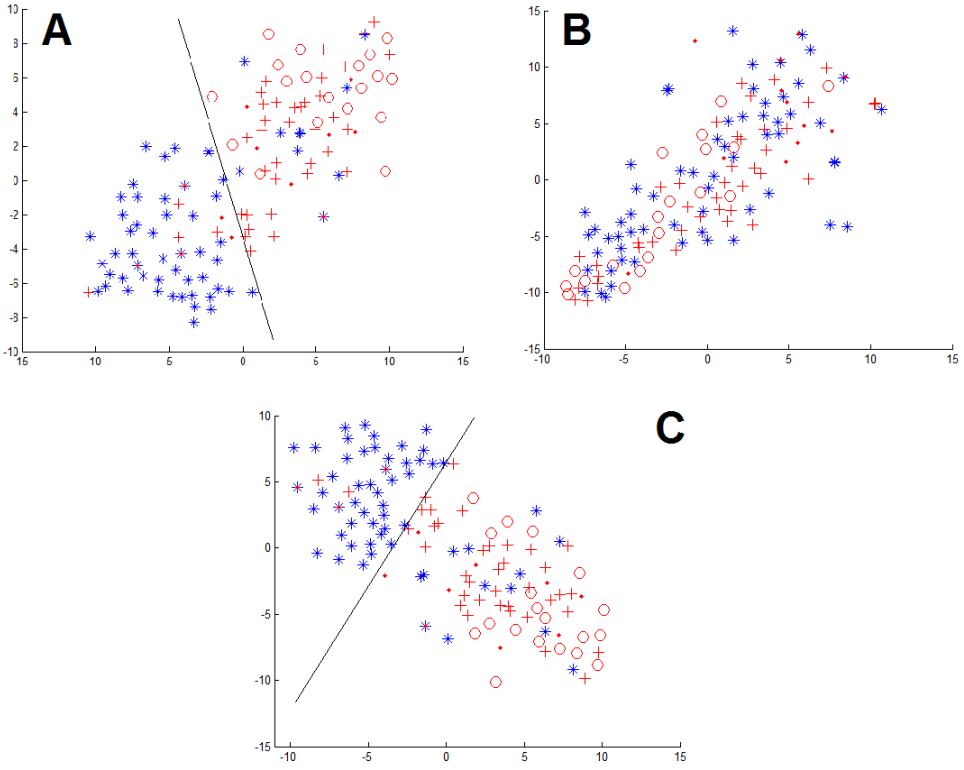

Figure 5.13: t-SNE cluster plot of experimental data. Transferrin ($*$, N=65), epsilon(+, N=40), alpha(◯, N=20), hopping epsilon (•, N=12) potentials are plotted and their clusters separated with a line. We see a clear separation of trajectories previously classified as being due to a second- (red) and fourth-order (blue).

5.5.3 Clustering Experimental Data

Figure 5.13 depicts the clusters of our experimental data points. Again we perform the clustering using the potential only, the diffusivity only, and both. When we only use the diffusivity, we do not see any separation into clusters of the experimental data. However, adding the diffusivity, slightly increases the percentage of points correctly assigned to their cluster (see table 5.3).

The separation of the data demonstrates that the data from the transferrin receptors are fundamentally different from the data of the CPϵT and CSαT receptors, which display a high degree of overlap between each other. Furthermore, this divergence is produced by the shape of the potential and not by the diffusivities experienced by the receptors.

Clustered Simulated Data

	Potential only	Potential and Diffusion
Simulated harmonic potentials	96%	98%
Simulated exponential potentials	99%	96%

Table 5.2: Percentage of simulated data correctly classified with clusters. Percentages of simulated data points that fall onto their respective cluster side after placing a boundary line to delimitate two clusters.

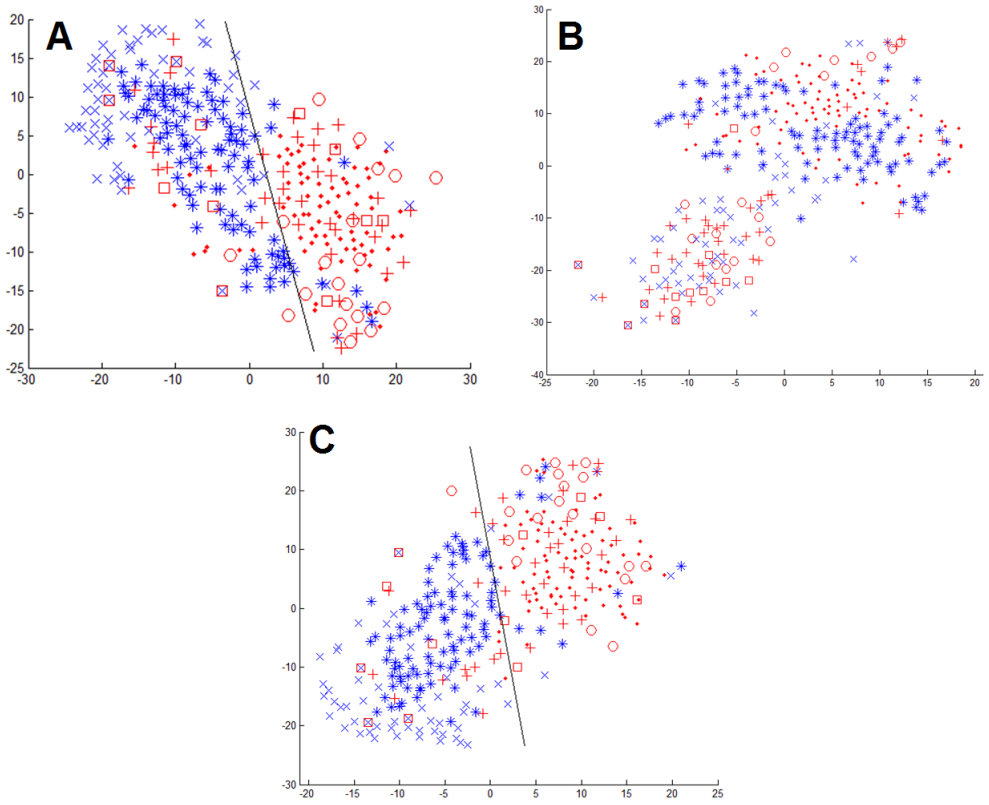

Figure 5.14: t-SNE cluster plot of experimental and simulated trajectories. Transferrin receptor (×, N=65), epsilon-toxin receptor (+, N=40), alpha-toxin receptor (◯, N=20), simulated exponential(∗, N=100), simulated harmonic (•, N=83), hopping epsilon-toxin receptor (□, N=12) potentials are plotted and their clusters separated with a line. We see a clear separation of trajectories previously classified as being due to second- (red) and fourth-order (blue) potentials.

5.5.4 Clustering both Simulated and Experimental Data

We then combine all the data, simulated and experimental and perform the same analysis again as shown in figure 5.14. What we see is that there is primarily a separation of the two clusters representing the simulated trajectories in figure 5.14A and C, representing potential only, and diffusion and potential, respectively. This is expected, since these were produced with two fundamentally different potentials to start out with.

Clustered Experimental Data

	Potential only	Potential and Diffusion
ϵ-toxin receptor	90%	95%
Hopping ϵ-toxin receptor	58%	75%
α-toxin receptor	100%	100%
Transferrin receptor	85%	82%

Table 5.3: Percentage of experimental data correctly classified with clusters. Percentages of experimental data points that fall onto their respective cluster side after placing a boundary line to separate the clusters.

Clustered Experimental and Simulated Data

	Potential only	Potential and Diffusion
ϵ-toxin receptor	70%	70%
Hopping ϵ-toxin receptor	42%	50%
α-toxin receptor	90%	95%
Simulated harmonic potentials	89%	96%
Simulated exponential potentials	91%	91%
Transferrin receptor	94%	92%

Table 5.4: Percentage of simulated and experimental data correctly classified with clusters. Percentages of all data points that fall onto their respective cluster side after placing a boundary line to separate the clusters.

Furthermore, the clusters representing the transferrin receptor potentials are even further away from the separation line than the simulated exponential trajectories. On the other hand, trajectories generated with a harmonic potential fall into the same side of the boundary as the clusters occupied by the alpha- and epsilon-toxin receptor data, and the hopping epsilon receptor data. Again, as in the previous section, this confirms the hypothesis that the potentials previously classified as second and fourth order are truly fundamentally different.

The separation of the clusters is confirmed again to be principally produced by the shape of the potentials and not by the diffusivities. However, as for the previous analysis focussing exclusively on the experimental trajectories, we see a slight improvement in the separation of data if we add the diffusivity to our data sets prepared for clustering (see table 5.4).

What is also interesting to note is that, despite the clustering using only diffusivity not producing the desired splitting of the data, we do see an interesting trend in figure 5.14B. It seems that two clusters have formed. One hosting mainly the simulated data, the other consisting of principally the experimental data. This could be explained by the fact that for the simulated data a uniform diffusion coefficient is used throughout the simulated domain, whereas there certainly is variation of diffusivity within the confinement domains on actual cell membranes, raft or non-raft.

5.6 Discussion

Both the decision-tree approach and the clustering approach suggest that the potentials experienced by raft and non-raft proteins are fundamentally different. By simulating hopping trajectories and then splitting these, we still find that (a) they are classified correctly into trajectories originating from second- and fourth-order potentials, and (b) are scatter-plotted into separate clusters by the t-SNE algorithm. Both these results show that proteins moving in these two types of potentials can be distinguished from each other. Furthermore, the splitting of the trajectories using k-means does not influence our capacity to distinguish between these two types of trajectories.

The decision-tree model, as expected, classified the transferrin receptor potentials as due to a fourth-order potential and the lipid-raft receptors as originating from a second-order potential. When adding these experimental data to the clusters of the simulations they clearly gravitate around the data produced by simulating potentials using an exponential function and a harmonic function, respectively. Likewise, the receptors that reside in lipid rafts associate themselves with the cluster produced using data from harmonic potentials. Note that we could also perform simulations with a fourth-order potential. However, we do not expect any qualitative differences from the simulated results obtained with an exponential potential.

Clustering the data like this not only permits us to visualize differences and similarities between the receptor domain parameters, but it also provides a way to analyse novel data. Any trajectory from an unknown receptor exhibiting confinement could be taken, analysed in the same fashion, and plotted onto the cluster plot. Depending on where on the plot it falls, we can determine a closer similarity to a harmonic or a fourth-order/exponential shape for the confinement potential it experiences, and from this infer a lipid-dependent or cytoskeleton-dependent confinement. This approach still has to be validated using data obtained on difference cell types. Knowing from the initial data what percentage of points tend to fall on which side of the separating line provides a starting point for calculating the probability that an additional point falling on the side of a certain type of potential can be classified as such.

By separating the diffusion data and the potential data while clustering, we have shown that the main contributor to the formation of clusters is the difference in the potentials experienced by the receptors. The diffusivity itself is not a deciding factor in a successful clustering of a data set. However, we do see some improvement in the presented data when it is included, suggesting that the diffusivity structures within the domains do differ in some way, which may be worth investigating further. What is also interesting is that, when only using the diffusivity, the simulated data tends to separate from the experimental data. It is highly likely that this is due to some heterogeneity of the diffusion coefficients across the confinement domains in the case of the experimental data, however, this effect may merit further investigation.

5.7 Conclusion

In this section, we have analysed trajectories recorded from receptors that we determined in the previous chapter to reside in lipid-dependent domains and compared these to trajectories of receptors known to localise outside lipid rafts. Using a decision-tree model and a clustering algorithm, we demonstrated a fundamental difference between the two receptor type confinements. The raft receptors reside in a harmonic potential, while the non-raft receptors experience a potential flatter in the centre of the domain and steeper at its sides. This supports the notion that the confinement models for the two kinds of receptors (lipid rafts and picket-and-fence model) are different. Further work could include an extended comparison of the shape of simulated potentials, and a broadening of the biological scope by looking at other cell and receptor types, possibly

even unknown ones. Using only the diffusivity maps, data clustering may also prove to be useful in analysing the geometric distribution of regions with higher and lower diffusivity within confinement domains.

Key points:

- Transferrin receptor trajectories experience movement through several confinement domains. Individual trajectories can be split into separate confinement domains using a k-means algorithm.
- Trajectories can be analysed using a decision-tree model. This algorithm determines that raft confinement potentials are second-order and non-raft confinement potentials are fourth-order.
- By using a t-SNE clustering algorithm, complex multi-dimensional data can be plotted and compared. Plotting trajectories produced and split from double harmonic and exponential wells shows a separation of the respective data clusters.
- Trajectory data of raft proteins tend to cluster with the harmonic simulated potentials, whereas transferrin receptor data associate with the exponential simulated potentials.
- Diffusivity itself does not produce conclusive cluster plots, but including diffusivity along with potential maps may improve the clustering into seperate areas.

Chapter 6

Botulinum Toxin Transcytosis

Even the humblest creature has to know how to react to the difference between food and toxin if it's to survive. ... Life and some level of intelligent behavior—discerning and doing what's best for one's survival—appear to go hand in hand.

David Darling

Contents

Previously we used SPT for tracking receptor proteins in the cell membrane. Since the receptors are restricted to move within the membrane, the trajectories we obtain remain in a plane and are two dimensional. In this chapter, single particle tracking in three dimensions will be introduced. Along with the established methods, our approach to 3D tracking will be presented and used to investigate the transcytosis of botulinum toxin through live epithelial m-IC_{cl2} cells.

6.1 Botulinum Toxin

Botulinum toxin is considered to be the most virulent of all poisons [235], with a lethal intravenous dose of approximately 1 ng/kg [236]. It is produced by *Clostridium botulinum*, a rod shaped, spore-forming, strictly anaerobic bacterium. Ingestion of either the toxin-producing bacterium or the toxin itself is the cause of the neuroparalytic disease botulism, which manifests itself through paralysis of both voluntary and involuntary muscle groups and finally death due to respiratory failure if left untreated [237]. Botulism can also be caused by colonization of the intestinal tract or a wound infected by *Clostridium botulinum* [238]. There are seven known serotypes of the botulinum toxin, labeled A to G. In this work, we study the actions of serotype A of botulinum toxin (BoNT/A).

The major steps of botulinum toxin action are transcytosis through the cell barriers in the gut into the blood circulation, subsequent transport to the neuromuscular junctions, internalisation of the toxin in neurons, and, finally, disruption of the signalling process between neurons and muscle cells [239]. The details of this process are elaborated on in sections 6.1.1 and 6.1.2 and the main steps are visualized in figure 6.2. In contrast to CPϵT and CSαT that were studied in chapters 4 and 5, BoNT does not cause cell death. Rather, it is able to cross the cell membrane by recognising and taking advantage of transmembrane and transcellular transport processes to enter and cross cells. Precisely through these processes, it is able to, on the one hand, cross through epithelial cells from the intestine into the blood circulation [240, 241], and, on the other hand, subsequently enter the cytosol of cholinergic nerve endings [242, 243].

The structure of BoNT/A consists of two asymmetric subunits, a heavy chain (HC) and a light chain (LC), linked via a disulfide bond. The entire toxin is synthesised as a single chain 150-kDA polypeptide, which is then cleaved by proteases to form the active toxin consisting of the HC and LC. The HC accounts for 100 kDa and the LC for the remaining 50 kDa. Figure 6.1 shows a ribbon diagram of the toxin. The HC part of the toxin is comprised of an N-terminus region and a C-terminus region. The C-terminal is responsible for neurospecific cell binding [244, 245], while the N-terminal effectuates the translocation of the LC into the cytosol by forming channels in the vesicle membrane [246, 247]. The disulfide bond, labeled orange in figure 6.1, is located between the LC and the N-terminal of the HC.

Along with BoNT/A, *Clostridium botulinum* also produces several neurotoxin-associated proteins (NAPs) that serve to protect the toxin from proteolytic digestion in the acidic environment of the gastrointestinal tract during toxicogenesis. BoNT along with these NAPs forms large complexes that have been shown to be more potent than simply the pure form of the toxin. Toxin complexes can vary in molecular weight, but are typically in the range of 203 to 500 kDa. One example of these NAPs is haemagglutinin (He-33), a 33-kDa protein, in the presence of which BoNT/A has been shown to suffer less from enzymatic digestion than in its absence [249]. It has also been suggested that haemagglutinin actively disrupts the intercellular junctions between the epithelial cells of the intestine, thereby facilitating toxin displacement [250]. Another supporting

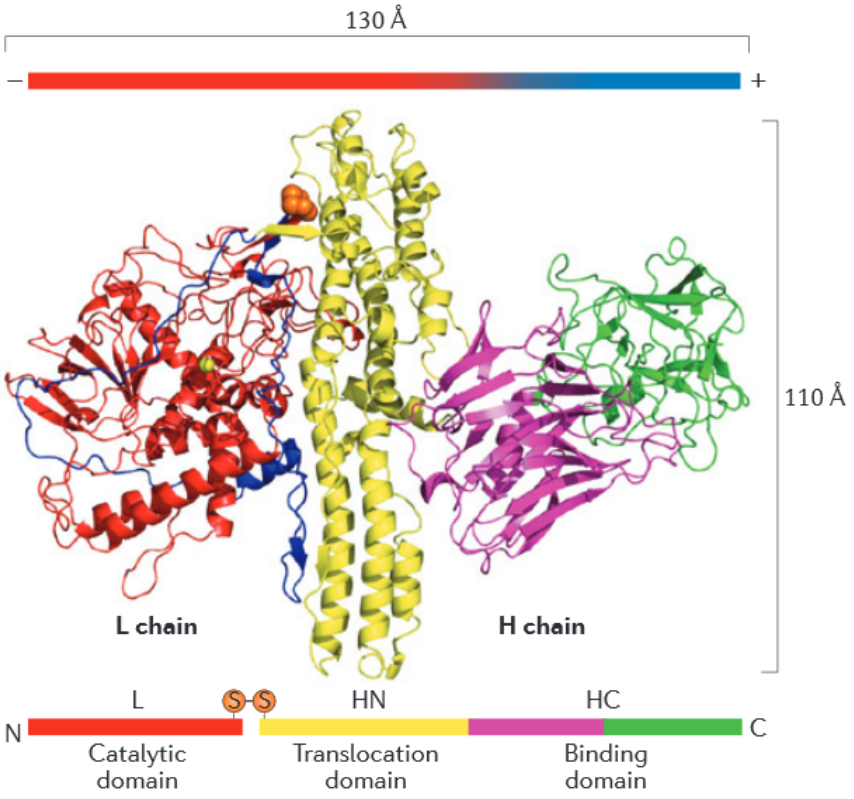

Figure 6.1: BoNT/A structure. It consists of a 50-kDa light chain (LC; L in image) and a 100-kDA heavy chain (HC; HN and HC in image). The latter has an N-terminal domain (H_N; HN in image) and a C-terminal domain (H_C; HC in image). The light chain is shown in red, the heavy chain N-terminal in yellow and the C-terminal in magenta and green. The heavy chain C-terminal is responsible for binding to the toxin receptor, while the N-terminal mediates translocation of the active light chain into the cytosol where it can travel to the site of neurotransmitter release. Figure reproduced from [248].

protein is the 140-kDa nontoxic non-hemagglutinin (NTNHA), which has been found to facilitate trancytosis by shielding BoNT in the gastrointestinal environment [251].

Botulinum toxin has also been widely proposed as a possible treatment solution for various ailments. BoNT/A in particular has been suggested for treating involuntary muscle spasms, focal and segmental dystonias [252], and strabismus [253, 254]. Because it produces a state of flaccid paralysis, BoNT has achieved widespread recognition of its potential use as a muscle relaxant. However, due to its extreme potency, approval for clinical uses of this drug is slow [255]. Nevertheless, the success of crystalline BoNT in the treatment of focal dystonias has resulted in BoNT being considered the main method for combating the condition [256, 257]. More recently, it has even been proposed that treatment with BoNT could even benefit people with conditions such as migraines [258]. It should also be noted that, despite its vast potential in the medical field, due to its extremely virulent nature, BoNT/A has been considered as a biological weapon [259].

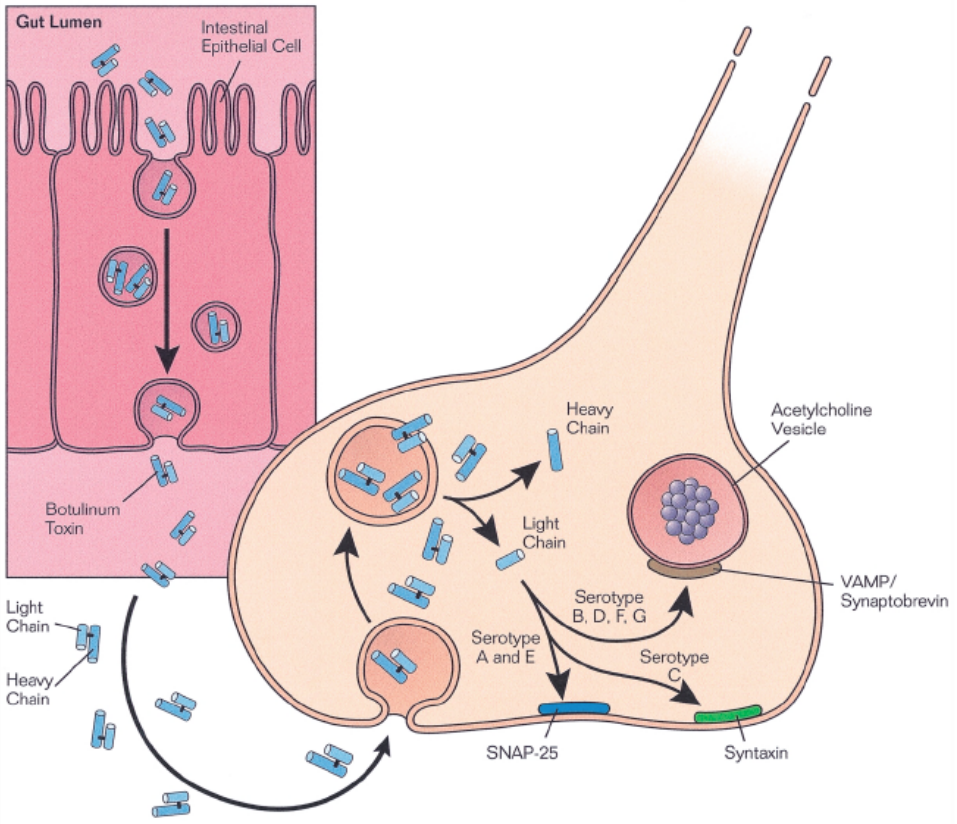

Figure 6.2: Diagram of the journey of an ingested botulinum toxin from the intestine to the active site. After the ingestion of contaminated products, several steps are involved for the botulinum toxin to reach its active site at the neuromuscular junction. The major steps are binding to and transcytosis across the epithelial cells in the intestine, transport via the blood stream to a relevant site on a neuron, and subsequent internalisation. Figure reproduced from [260].

6.1.1 Action at the neuromuscular junction

As stated in section 6.1, the general principle of BoNT action is its ability to cleave proteins essential for neurotransmitter liberation at the neuromuscular junction. In fact, it is capable of blocking exocytosis at all peripheral cholinergic sites, the neuromuscular junction being the best studied. As the body of work in this area increases, a deeper understanding for the entire process has developed and for each of the steps involved more and more substeps are discovered. However, by examining a few key steps the process can be explained in a straightforward manner. In general, four main steps, depicted in figure 6.3B, can be identified:

1. Receptor binding
2. Receptor-mediated endocytosis
3. pH-induced translocation into the cytosol
4. Inhibition of acetylcholine release

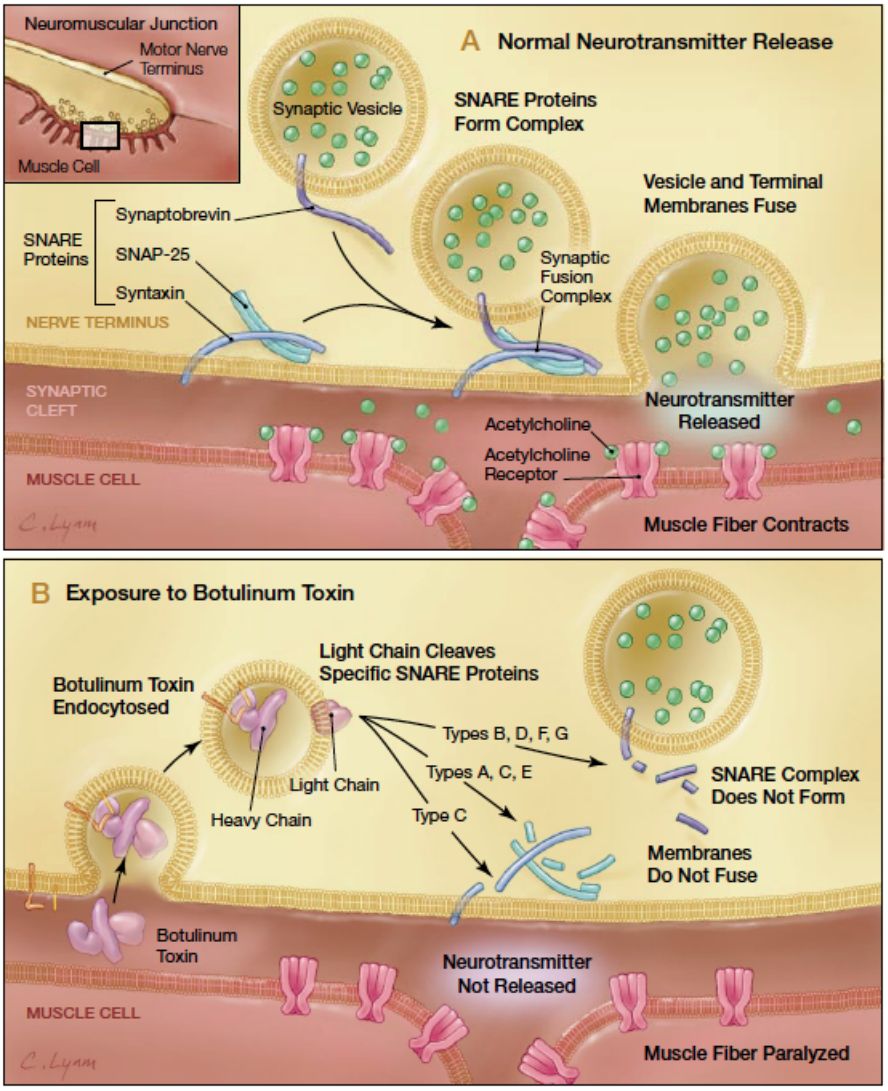

Figure 6.3: Diagram of the action of botulinum toxin at the neuro-muscular junction. The schematic shows a normal functioning neuromuscular juntion (A) and another compromised by the action of BoNT (B), which blocks the release of acetylcholine by cleaving SNAP-25, synaptobrevin, and syntaxin thereby preventing the assembly of the synaptic fusion complex. Figure reproduced from [259].

When arriving at the neuromuscular junction, the first step is the binding of the toxin to its receptor on the cell membrane surface. The exact nature of the receptor remains elusive. However, several studies have concluded that sialic acid-containing molecules, possibly gangliosides, strongly influence toxin activity [261–263]. However, it is unlikely that gangliosides are the receptors to BoNT, since the large distribution of gangliosides in the cell membrane cannot account for the selective binding of the toxin to cholinergic nerve endings. Additionally, it cannot account for the apparent serotype-specific binding of BoNT [264, 265]. One explanation of this is that there are multiple substeps involved in the binding to the receptor. More recent studies suggest that possible receptors that BoNT can target include the synaptic vesicle protein SV2 [266] and synaptotagmins (syt) I and II [267]. For BoNT/A, the preferred receptor has been determined to be SV2C [248, 268].

Subsequent to receptor binding, the toxin is internalized via endocytosis. Proposed pathways for this step include the standard pathway via receptor-mediated endocytosis, after which the receptor-bound toxin finds itself inside a vesicle in the cytosol. Another suggested pathway is one dependent on the neurotransmitter liberation mechanism of the cell. Neurons use vesicles for neurotransmitter transport, which fuse with the cell membrane upon exocytosis (see figure 6.3A). To produce more vesicles, the cells possess a recycling mechanism for membrane retrieval [269, 270]. This retrieval phase could be a possible pathway for toxin internalisation [239]. The fact that syt II is a possible receptor suggests a possible explanation of the initial binding of the toxin. Syt II regulate neurotransmitter release and has a free domain exposed in the lumen of the vesicles. Upon vesicle fusion with the cell membrane this domain may become accessible providing an opportunity for a reaction with the toxin before subsequent internalisation. In support of this hypothesis, a study has shown that increasing the synaptic activity enhances the uptake of BoNT/A [271].

Next, to act in the cytosol, the catalytically active domain, i.e. the LC, must exit the lumen of the endosome. It has been shown that, as for many other agents, the translocation across the vesicle membrane is promoted by a change in pH. This has been demonstrated by the fact that BoNT translocation can be impeded by controlling endosomal pH levels via the introduction of chloroquine and methylamine into neuromuscular junctions [272, 273]. Furthermore, the HC also plays a key role in LC liberation by forming a channel in the membrane and acting as a chaperone in dynamically guiding the LC across.

The common consensus on the substeps involved in the translocation of the LC are:

1. Change in toxin structure produced by a change in pH
2. Insertion of previously inaccessible hydrophobic domains into the membrane
3. Translocation of the LC from the inner to the outer surface of the endosome
4. Reduction of the disulfide bond between the HC and LC
5. Splitting of non-covalent bonds between HC and LC
6. Escape and restoration of LC structure

The final step in the BoNT action sequence follows the release of the LC into the cytosol. Here, the toxin arrives at the site of exocytosis and proceeds to cleave intracellular substrates necessary for vesicle fusion with the membrane. Different serotypes of the toxin act on different proteins. BoNT/A, the serotype studied in this work, cleaves the SNAP-25 protein. Other proteins attacked by serotypes B to G include VAMP and syntaxin. These are essential contributing agents to the SNARE complex that is responsible for mediating vesicle fusion with target membranes. Without this machinery for fusion intact, acetycholine-containing vesicles cannot fuse with the cell membrane to release the neurotransmitter, effectively stopping communication with the muscle cell.

6.1.2 Journey to the active site

In order for BoNT to achieve its goal and block neurotransmitter release, it first needs to arrive at the neuromuscular junction. Since the typical starting point of the toxin is oral ingestion, it needs to reach its final destination from the gastrointestinal tract. Despite this step being a key process during intoxication, the body of work treating this phenomenon is less vast than for the toxin's actions at the neuron. So what are the details of the toxin's journey to its active site?

A number of experiments have been conducted with the aim of shedding light on the transcytosis of BoNT through intestinal epithelial cells. Before internalisation and movement across the cell, the toxin attaches to a binding site on the cell. Efforts to determine how the toxin enters the cell have found that, similar to the process described for BoNT at the neuron, the toxin undergoes receptor-mediated endocytosis [240, 274, 275]. As in the binding of BoNT to neurons, the C-terminal domain of the HC controls the binding process. Studies focussing on HC uptake identified pathway dependencies on dynamin, intersectin, and Cdc42 [276]. Furthermore, it was found that during binding, gangliosides of the GD_{1b} and GT_{1b} series along with SV2C proteins, strongly affect binding and entry of BoNT/A into the cells [275, 277]. Additionally, the non-toxic associated proteins that, along with BoNT, make up the botulinum toxin complex seem to assist in toxin uptake. Further studies have shown binding to be mediated by hemaglutinins HA1 and HA3b interacting with gangliosides and glycoproteins [278, 279].

Attempts have been made to visualize the trancytosis process of BoNT across intestinal epithelial cells [280]. By labeling the toxin with Alexa Fluor 488 it was determined that toxins that entered the cell were rapidly removed from the vicinity of the cell membrane and moved towards the basolateral surface. The time taken for the toxin to cross the cells was quoted to be in the range of 20 to 60 min [275, 280]. A similar, very recent study that examined the translocation of the BoNT/A and NAP complex across polarized Caco-2 cells found the time scale to be on the order of several hours, with a more rapid entry of the BoNT/A complex compared to BoNT/A by itself [281]. However, what no previous study has done, and which is the aim of this investigation, is to track a toxin throughout the entire transcytosis process from internalisation to progression across the cell. Labels like the previously used Alexa Fluor 488 are useful for obtaining the position of the toxin, but cannot be visualized uninterrupted over several minutes and are, therefore, not suitable for tracking applications. The NP we used (and detailed in chapter 2), on the other hand, can be observed for extended periods of time, and, hence, make it possible to record the entire trajectory taken by the toxin across the cell.

After passing through the epithelial barrier, the toxin diffuses in extracellular fluids and enters the lymphatic system before progressing to the blood circulation [282]. How exactly the toxin succeeds in passing through lymphatic and blood vessels is not known.

6.2 3D particle tracking

Several methods have been used for resolving the third dimension during SPT experiments. In this section, we present examples of studies that have made use of different approaches for tracking in 3D. Then the method used for this work will be presented.

6.2.1 Existing methods

One of the earliest proposed techniques for 3D tracking was published by Kao and Verkman [142], and has since been used and adapted in a number of other studies [283, 284]. They achieved tracking of fluorescent particles and fluorescently labeled molecules by implementing a cylindrical lens in their epifluorescence microscopy setup. This produced a circular emission pattern of the point spread function (PSF) when the fluorophore was in focus, but an ellipsoidal signal when the fluorophore finds itself above or below the focal plane. Figure 6.4 shows the images obtained depending on their displacement from the focal plane.

Peters and coworkers performed 3D SPT on the adhesion molecule LFA-1 (Lymphocyte function-associated antigen 1) in K562 cells by using an optical tweezers setup [285]. The position of the protein was obtained by tracking the movement of a trapped polystyrene bead bound to the protein. The bead is kept in the centre of the beam via a feedback system that measures lateral displacement by detecting deflection of the laser beam using a photosensitive detector. The axial direction was resolved by placing the bead behind the focus in the center of the beam. Axial movement of the bead produces a shift in the axial position of the focus position behind the objective and, hence, a change in the intesity that is detected by a photodiode. A similar approach with optical tweezers was taken by Pralle and colleagues [286]. Here, axial displacement is measured by calculating the ratio of the intensity of forward scattered light to the total amount of light read at the detector. This is done by measuring the interference of the unscattered laser light and the forward scattered laser light at the detector.

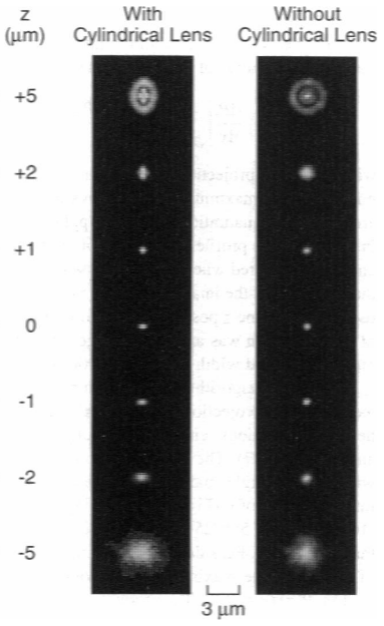

Figure 6.4: Diagram of the fluorescent signal detected using a cylindrical lens. Difference in PSF radius and shape as the fluorophore is displaced from the focal plane. Without the addition of a cylindrical lens, the PSF grows in diameter but remains circular. With the cylindrical lens, the shape is modified along with the size. Figure reproduced from [142].

Confocal microscopy has also been implemented for 3D tracking. Wells et. al. used a confocal microscope with four spatial filters along with a feedback loop for perpetual focusing on quantum dot labeled IgE antibodies [287]. The setup permits observation of two planes axially separated by about 200 nm and four confocal volumes arranged along a tetrahaedral geometry. Using confocal feedback for tracking provides an increased z-range for tracking and can, thus, track the motion of a molecule through the entire volume of a cell. At around the same time, Sun and colleagues proposed a setup called *Parallax*, which uses a pair of closely spaced mirrors and a lens to split the image in two and collimate the image beam [288]. These beams are then used to produce two images of the sample. Using this setup, any lateral movement of the molecule being tracked simply results in an equivalent movement of the image on the detector. When the image is in focus, the two signals overlap. Axial movement, however, manifests itself as producing an out of focus image and a relative displacement from one another of the signals generated by the two beams.

A similar method that images two planes simultaneously for 3D tracking has been proposed by Toprak et. al. [289]. By splitting the signal beam and introducing an extra lens in one of the two beam paths, the focal plane of the two beams relative to each other is shifted. The radius of the ring pattern of a defocused image depends on the axial position, and can be used to determine the out-of-plane position. Extensions and adaptations of this technique have lead to methods that visualize numerous focal planes at the same time [290, 291]. For tracking the trajectory of transferrin receptors, for example, a multifocal plane setup imaging four focal planes simultaneously has been implemented [290]. Another proposed technique taking advantage of the possibility to image multiple planes at once was proposed by Gratton et. al., who use a two-photon microscope setup to trace four circular orbits in a plane just above and below the particle every acquisition cycle [292]. The position of the planes are dependent on the PSF size, which is obtained by fitting one-dimensional Gaussian functions on the intensity profiles of the particle.

The main disadvantages of techniques that split the image beam to visualize multiple image planes is that for each image the signal intensity will be reduced, producing a potentially lower localisation precision and limiting the possible use of fluorophores that photobleach for long term tracking experiments. Moreover, when the direction of motion of the molecule to track is ambiguous, a cylindrical lens or a two plane imaging system is necessary to determine in which direction the axial movement is taking place. In our case, we know that from the moment the toxin binds to the receptor, the principal direction of axial movement will be into the cell and towards the other side. We, therefore, have less of a need for additional confirmation on the direction of toxin propagation.

6.2.2 Our approach: 3D tracking using PSF width

We used the fairly straightforward method of measuring the size of the PSF as the probe moves in the axial direction. As the NP-labeled toxin moves away from the focal plane the radius of the PSF will be altered, which can be exploited to measure the z-position. When the defocussing becomes too strong to correctly localise the NP, we manually

adjust the height via a piezo. The new height can then be determined and the focal height can be reset to the initial PSF width. x and y positions are acquired via the standard procedures, and z positions via this measurement of PSF width.

We calibrated the setup by measuring the signal from immobilized NPs on glass surfaces. Figure 6.5 shows the change in PSF width in terms of the NP displacement from the focal plane. Images were recorded in 0.1 μm steps from 2 μm above the focal plane to 2 μm below the focal plane. The width-at-half-max of the PSF is obtained by fitting the emission pattern with a 2D Gaussian function. In figure 6.5, D is the position at the focal plane at which the smallest value would be expected. When the focal plane lies above the NP (-1 μm to 0 μm), we indeed observe an increase in PSF width. However, when the focal plane lies below the NP the PSF intensity takes on an Airy-like pattern, and a Gaussian fitting algorithm leads to a deceptively low reading of the signal width. Similarly, in the range of A to B in figure 6.5, the PSF shape does not correspond to a Gaussian and Gaussian fitting leads to an erroneous PSF width value.

During experiments, resets are therefore placed closer to the C position of figure 6.5, in order to work in the range of B to D. This way an increase or decrease can be associated with an up or down movement, and resets occur when the PSF width reaches position B. The axial localisation precision of this technique is $\sim$ 200 nm. The working range ($\sim 1\mu$m) could be extended by fitting the PSF with more elaborate functions (e.g. Airy function). This was not implemented for the present experiments.

6.3 Results

The general setup of the epifluorescence microscope is described in section 2.2. For the experiments conducted here, we used NPs coupled to the heavy chain of botulinum toxin A (HCA) with a coupling ratio of 34:1. These were incubated with cells of the intestinal crypt-like cell line m-IC$_{cl2}$ that have been shown to possess a higher affinity for BoNT/A than Caco-2 intestinal cells [277]. These cells originate from the base of small intestinal villi of an L-Pk/Tag1 transgenic twenty day-old mouse foetus. The culture procedure and medium used for these cells are given in appendix A.7. Experiments are then performed at 37°C and with acquisition times of 1 s to obtain a strong signal for PSF fitting, and a laser power of 30 mW. We thus sacrifice localisation precision in the x/y-plane to increase localisation precision in the z-direction.

The HC C-terminal of BoNT/A used was produced and purified using pET-28a-a-c(+) plasmids in *E. coli* cultures in the lab of Michel Popoff. Full details are described in [293]. Toxins were supplied in 20 mM Hepes, 150 mM NaCl and 50% glycerol solution. Before coupling the toxins to the NPs using the process outlined in [148], the HC BoNT/A solution is dyalised to remove the glycerol.

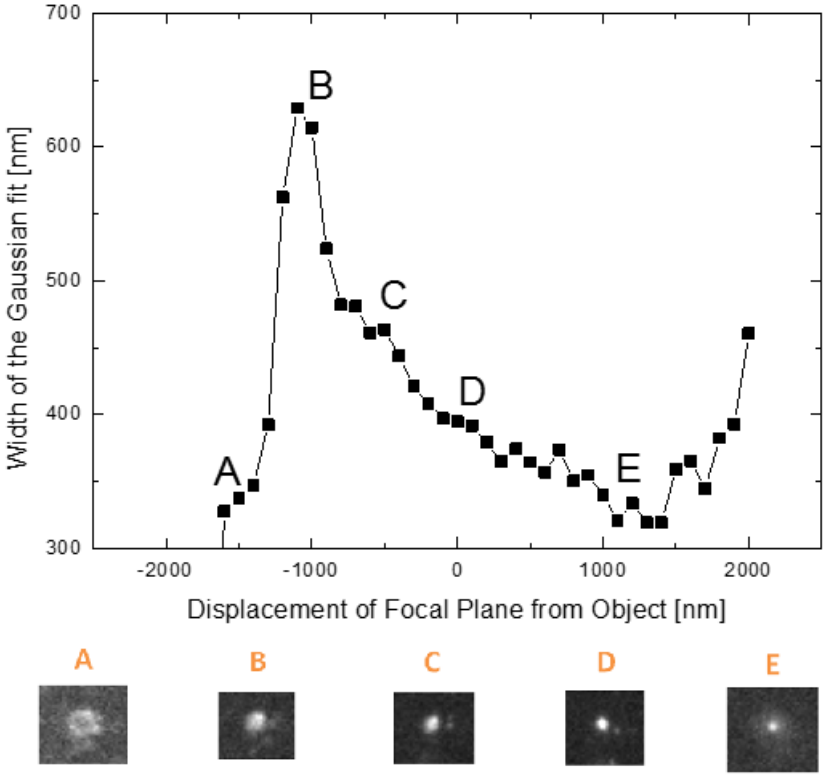

Figure 6.5: Point-spread function width as a function of the emitter distance from the focal plane. Width of the 2D Gaussian fit to the nanoparticle emission images as a function of the position of the objective focal plane. Images of the PSF are shown at points A-E. D (z=0) corresponds to the plane where the nanoparticle is in focus. A 20 mW laser that was focused to approximately 20 μm was used with an acquisition time of 1 s.

6.3.1 Lateral tracking of NP-labeled botulinum toxin at the cell membrane

Before trancytosis of the toxin occurred, we observed HcA-NP conjugates bind to their membrane receptors with an acquisition time of 51.3 ms. Figure 6.6A shows a trajectory obtained at this stage. The trajectories right after binding (black) and 20 minutes later (red) are shown. When plotting their MSD curves (figure 6.6B) both trajectories clearly display confinement. Additionally, we see that the diffusion coefficient of the diffusive motion of the receptor drops from 0.03 $\mu m^2/s$ to practically stationary. This could signal the beginning of entry of the bound receptor into the cell. Compared to times quoted in the previous section 6.1.2 for transcytosis, 20 minutes seems to be a reasonable value for the cell entry initiation.

6.3.2 Axial tracking of NP-labeled botulinum toxin

The tracking method as described in section 6.2.2 involves recording the width of the signal and resetting the z-position manually once the NP-toxin conjugate displacement

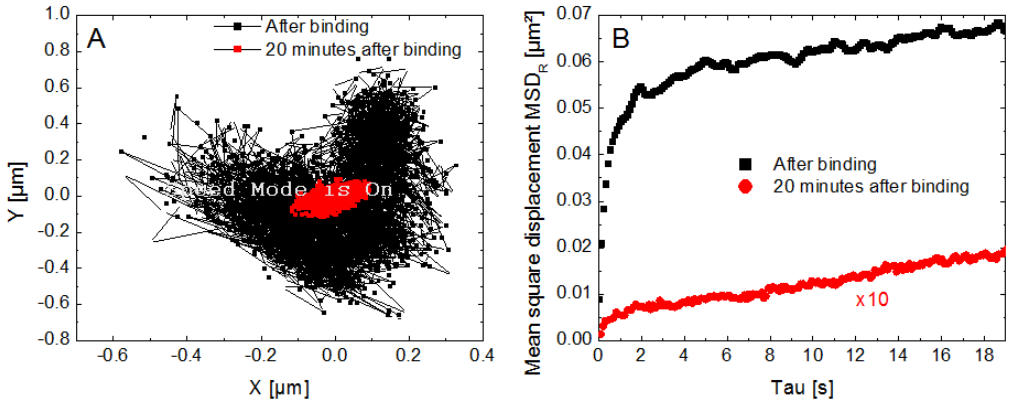

Figure 6.6: HC BoNT/A receptor movement in cell membrane before internalisation. HC BoNT/A receptor trajectory in the membrane of IC_{cl2} cells at 37°. (A) shows the trajectory directly after the NP-toxin complex binds to the toxin receptor (black) and the same trajectory 20 minutes later (red). (B) shows the corresponding MSD curves as a function of lag time (same color code). The smaller confinement domain size is evident. Additionally, there is a decrease in diffusion coefficient.

has reached a certain value. Figure 6.7 show the PSF width values acquired during a tracking experiment. We see that the PSF width increases with frame number. Four jumps are visible. These represent the readjustment of the focal plane to continue tracking in the correct PSF width range. As the adjustment is done manually the width may pass over the inidcated limit. However, the signal is clearly strong enough that a larger width than the limit can still be determined.

The Bayesian inference algorithm cannot be used here for several reasons. Firstly, it is not adapted to three dimensional trajectories as it is designed to extract a 2D potential map of forces from a planar trajectory. Inferring parameters in a third dimension would also require and non-proportional additional amount of computing power. But what is more, the acquisition time of 1 s, used to acquire a strong enough signal for viable out of focus PSF fitting does not provide us with adequate temporal resolution for the BI algorithm to extract any useful information.

Since the experiments were conducted over an extended period of time, mechanical drift of the system is an important factor. Lateral drift is accounted for by recording regular white light images of the cells and observing displacement of set landmarks on the cell close to the site of trancytosis. The resulting displacement is interpolated and the lateral coordinates of the trajectory are corrected accordingly. Furthermore, the axial drift of the setup needs to be measured. As a control experiment to test the stability of the setup during the time of the experiment, we tracked an immobilized NP on a glass coverslip. Figure 6.8 shows the acquired trajectory. The trajectory is recorded during a time of 69 minutes and 6 seconds and displays a vertical drift of 2.3 ± 0.4 μm.

Figure 6.9 shows an example trajectory of a HcA-NP complex entering the cell. The trajectory was recorded during 72 minutes and 30 seconds. The distance it penetrates into the cell is around 4 μm. This displacement is considerably larger than the one due to mechanical drift (figure 6.8). During this time, its average vertical speed is measured

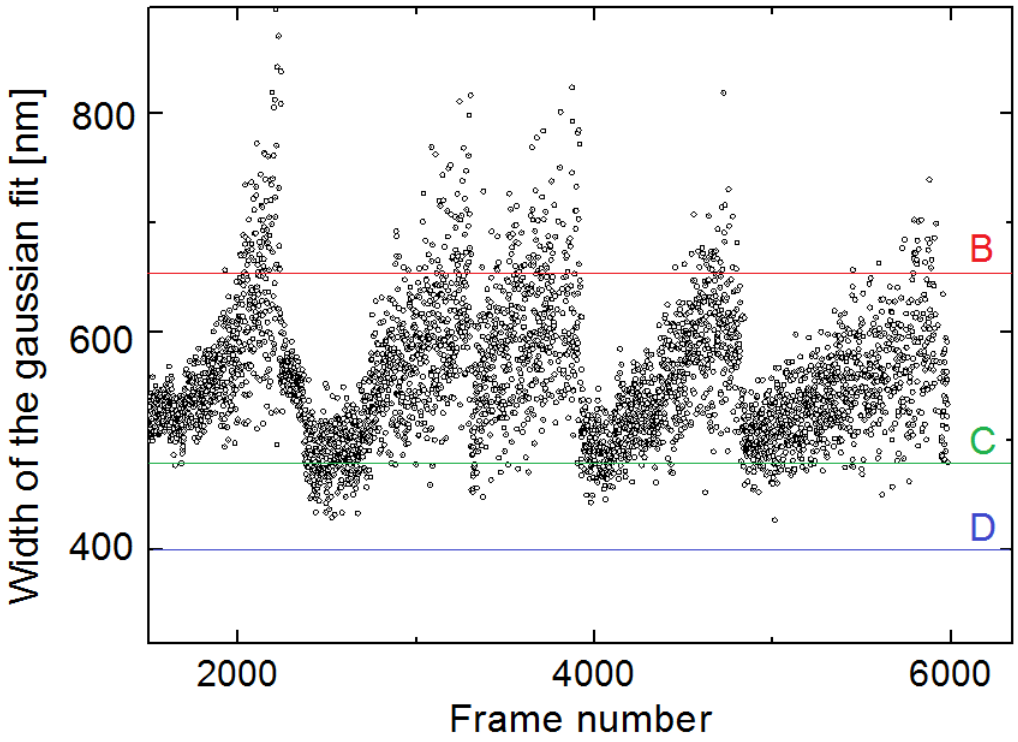

Figure 6.7: Point-spread function width during 3D tracking. Incremental increase of the width of the nanoparticle PSF as the toxin moves downward across the cell. Four manual readjustment of the z position occur resetting the focal plane. The positions B, C, and D from figure 6.5 are indicated by the red, green, and blue lines, respectively.

to be 0.9 ± 0.05 nm/s. Lateral diffusion coefficients are impractical to determine since the long acquisition time would lead to an artificially low diffusion coefficient.

In order to determine the nature of the movement, we can calculate the MSD curve of this trajectory. The result is shown in figure 6.10. Its shape resembles that of directed motion in figure 2.3. This curve is then fit with equation 6.1, assuming a combination of 3D Brownian motion and directed motion with speed v.

$$< r^2 >= (vt)^2 + 6Dt \tag{6.1}$$

We obtain a value of $20 \pm 2.5 \times 10^{-6}$ μm^2/s and 0.001 ± 0.0001 μm/s for the diffusion coefficient, D, and the transport velocity, v, respectively. To obtain meaningful averages, the MSD was only calculated for step lengths up to 700 frames. This directed motion could be produced by microtubule associated motor proteins like kinesin and dyenin. These could actively transport the toxin containing vesicles along microtubule and across the cell. The data presented in this section are preliminary results that need to be confirmed with subsequent experiments to obtain statistical significance.

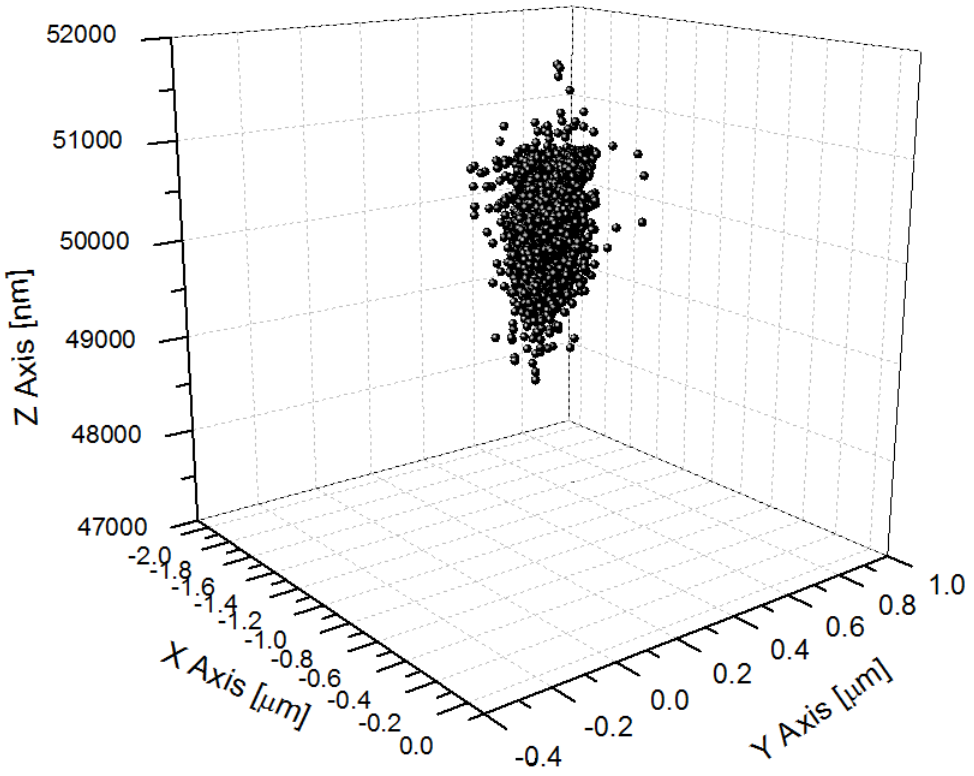

Figure 6.8: Trajectory of stationary NP showing the mechanical drift of the system. Trajectory of a NP stuck to a glass surface. Acquisition occurred during a time of 69.1 minutes. The trajectory starts at the 50 μm position and fluctuates due to mechanical drift of the setup within the range of 49.1±0.2 to 51.4±0.2 μm.

6.4 Discussion and Conclusion

This section presented a simple method for tracking a fluorescent probe in three dimensions that was applied to observing the motion of a HcA-NP conjugate into an m-IC$_{cl2}$ cell. Again, in this case this simplified approach can be used, since the direction of propagation of the tracked toxin is known. Before internalisation, a decrease in receptor motion within the cell membrane is observed. This happens within a time frame that is fairly long but still in accordance with values quoted in the literature for the time required for transcytosis.

The trajectory observed for HcA moving into the cell suggests a directed mode of motion. However, the values found for the diffusion coefficient, $20 \pm 2.5 \times 10^{-6}$ μm^2, and the transport speed, 0.001 ± 0.0001 μm/s, are extremely low compared to vesicle speeds cited in other recent studies, which cite speeds on the order of $\sim$ 10 μm/min [294], or motor protein speed along microtubules, which amounts to several hundred nm per second [295]. However, since our analysis is mainly concerned with the transport speed of the vesicle across the cell and not along microtubules, we expect the observed velocity to be slower than the speed of vesicle along microtubules. In fact, a previous study by Simister et al. [296], which looked at the vesicle transport of immunoglobulin G accross

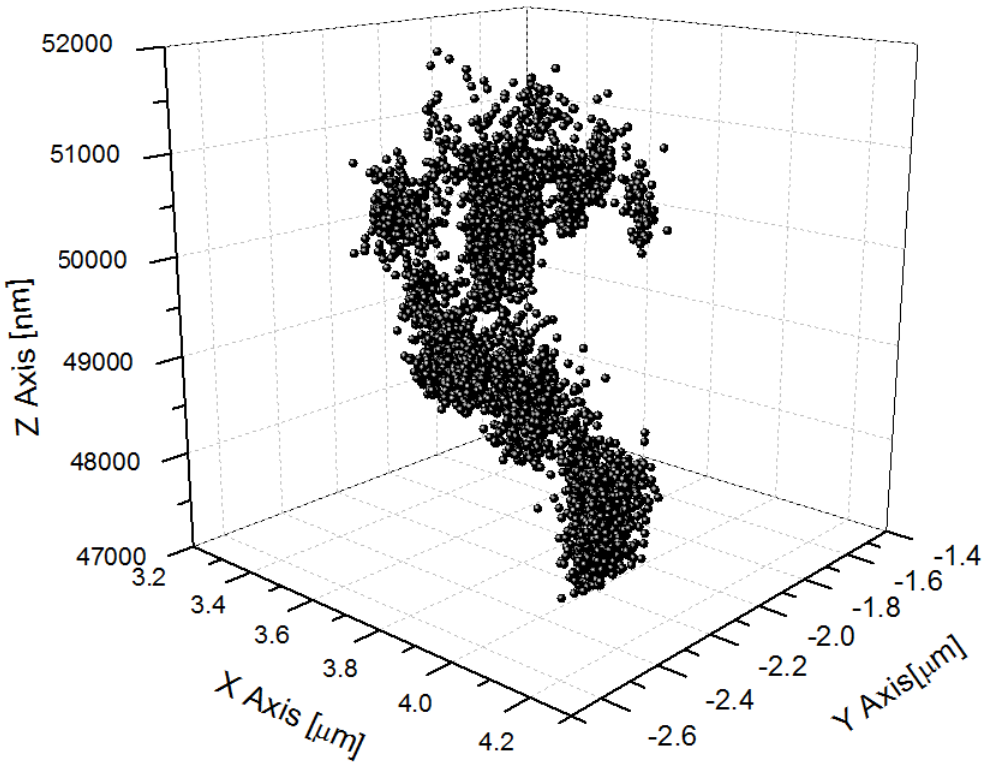

Figure 6.9: 3D trajectory of a Hc BoNT/A entering the cell. HcBoTN/A trajectory through an IC_{cl2} cell. The trajectory starts at the top and moves downward for 72.5 minutes with an acquisition time of 1s.

inner medullary collecting duct (IMCD) rat cells, measured typical transcytosis times in the range of 30 to 200 minutes, in addition to determining a microtubule dependence.

The mechanical drift of the system is comparable in magnitude to the motion of the receptor observed. This could be an important factor contributing to a distortion of the calculated MSD curve and the observed trajectory. Further investigations are required to confirm and understand this discrepancy. The coupling ratio of 34:1 (see section 2.2) of the HcA to the NPs needs to be considered. With this coupling ratio we cannot rule out the possibility of cross-linking. Linking to two different receptors of an observed NP may lead to a modification of the dynamic interaction between the toxin and the cell. However, we expect these potential effects of crosslinking and NP-conjugation to be negligible on the vesicle motion inside the cell. Since the experiments are based on the assumed model transcytosis that the toxin is transported within a vesicle across the cell, being crosslinked to several receptors may have an effect on the internalisation process, but not on the observed trajectory within the cell. Tests with other labels like organic fluorophores could be conducted to test the effect of a coupled NP on the dynamic behaviour of HcA.

Future investigations using this method to track HcA transcytosis dynamics will re quire a setup equipped with a system to correct for this mechanical instability in the z direction. Such a system has recently been acquired by the LOB. It has an independent laser system, that uses a laser incident at an angle at the lower side of the cover slip, to

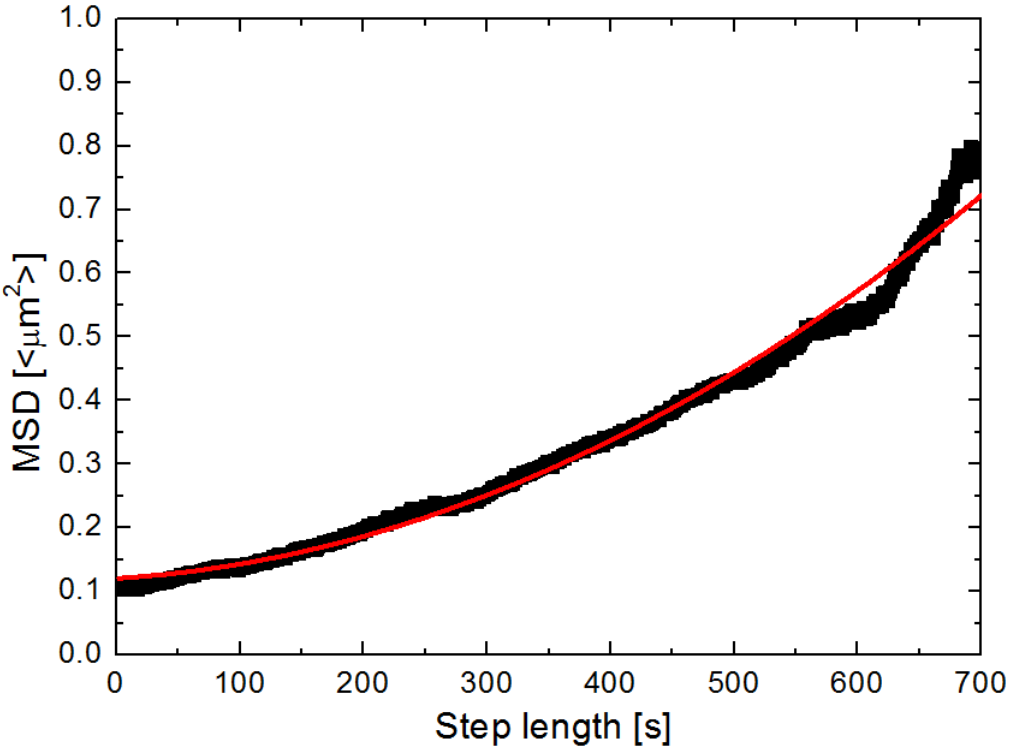

Figure 6.10: MSD curve of the trajectory of a Hc BoNT/A entering the cell . Calculated MSD as a function of delay time for the trajectory in figure 6.9. Assuming 3D diffusion and directed motion according to equation 6.1, yields a velocity of $0.001 \pm 0.0001 \mu$m/s and a diffusion coefficient of $(20 \pm 2.5) \times 10^{-6} \mu\text{m}^2/\text{s}$ (red line).

measure changes in distance between the cover slip and the objective. Any mechanical drift will result in a lateral movement of the reflected beam and can be corrected for. Future experiments include labeling vesicles to confirm these as the transport vehicle, and the labeling or depolymerising of microtubules to investigate their role as the transport paths.

Key points:

- Using rare-earth doped nanoparticles we can track botulinum toxin during trancytosis through intestinal epithelial cells.
- The third dimension can be resolved for 3D tracking by relating the width of the PSF to the NP's displacement from the focal plane.
- The confinement domain of the toxin receptor on the cell surface seems to decrease in size as the toxin approaches internalisation.
- Tracking the toxin we see that it moves approximately 4 μm into the cell during about 70 min.
- MSD analysis suggest that the toxin experience directed diffusion accross the cell.

Chapter 7

Conclusions

To be suspicious is not a fault. To be suspicious all the time without coming to a conclusion is the defect.

Lu Xun

Contents

7.1 Summary

This thesis has presented my work on toxin-cell interactions studied via single-particle tracking of lanthanide-doped nanoparticles ($Y_{0.6}Eu_{0.4}VO_4$) linked to proteins. The observed interactions included that of the ϵ-toxin of *Clostridium perfringens*, the α-toxin of *Clostridium septicum*, the heavy chain of the A serotype of botulinum toxin, as well as that of the protein transferrin with cells. All these were tracked after binding to their respective receptors on the cell membrane. Membrane receptor trajectories were analysed with Bayesian inference based on statistical physics tools to extract the confinement potentials felt by these receptors. In addition, this Bayesian inference technique has been applied to the field of instrument calibration.

In the first chapter, we discussed the present state of knowledge of the interaction interface between cells and toxins/proteins i.e. the cell membrane. Different models of receptor confinement and factors that contribute to non-Brownian motion of receptors were presented. Finally, the main techniques used to study the cell membrane are laid out including recent advances made with each method. Single-particle tracking, the main experimental technique used in this work, was then presented in the second chapter. In addition, the experimental setup as well as the analysis techniques that are typically used to analyse single-particle tracking data were laid out. Bayesian inference,

a superior method for confinement potential extraction and the primary technique for analysing the data in this work, is also described.

We demonstrated that Bayesian inference, by extracting the confining potential from a confined trajectory, can also be used to calibrate an optical-tweezers setup. In fact, when comparing this approach to the primary techniques used, the power-spectrum method and the equipartition method, we discovered several advantages of the Bayesian inference method. For drifts up to 10 nm throughout the trajectory the stiffness of the optical trap determined by Bayesian inference is affected by less than 5%, whereas the equipartition method displays a divergence of up to 30%. Similarly, the length used to calibrate the trap can decrease down to several hundred points with the detected spring constant being only 10% off the actual value, compared to more than 20% for the other methods. In addition, the only input required by the Bayesian inference approach is the bead trajectory. Neither bead radius, nor medium viscosity are necessary.

The techniques presented in chapter 2 were then applied to investigate the dynamic evolution of the confinement domains that the ϵ-toxin receptor finds itself in. By adding cholesterol oxidase and sphingomyelinase we were able to observe the temporal evolution of the destabilization of the raft domains confining the receptor. Upon enzyme addition, we found that receptor diffusivity increases almost 4-fold, while the value of the effective spring constant, characterizing the strength of confinement, drops by a factor of up to 20. The diminished confinement strength can be interpreted as a lowering of the solubilization energy difference in the raft with respect to outside the raft experienced by the protein. Similarly, the higher diffusivity can be attributed to a resulting less dense lipid configuration.

We also investigated the fairly rare events of receptor hopping during which the toxin receptors switch to a different confinement domain and hop from one lipid raft to an adjacent one. Here we found that, by extracting potentials described using a fourth-order polynomial, we can obtain the hopping energy, i.e. the energy of the barrier separating the two potential wells. The two typical values determined were 0.54 k_BT and 2.64 k_BT, representing movement between substructures within a raft, and low-frequency hopping between two different rafts, respectively. This higher hopping energy can be interpreted as the lower limit of the solubilization energy difference between the raft and non-raft phase.

Furthermore, we applied an external force to the receptors to investigate their reaction under non-equilibrium conditions. We observed that the receptors are displaced within the membrane and return to their initial position as soon as the flow is stopped under the action of a restoring force. The data indicate that the receptors are displaced while deforming an elastic barrier, which pulls back the receptor when the force application stops. The displacement and characteristic spring constant of the encountered barrier was found to be actin dependent, since we found that actin depolymerization using latrunculin B produced a decrease in the effective barrier spring constant from 2.5 pN/μm to 0.6 pN/μm. However, since the receptor confinement without flow is not affected by actin depolymerization, we conclude that another raft constituent, possibly another protein co-inhabiting the raft is responsible for the interaction with the cytoskeleton.

We then compared the confinement potentials experienced by raft proteins to that experienced by non-raft proteins, namely transferrin receptors. By simulating trajectories using harmonic potentials, and flat-potentials with exponential borders, and subsequent analysis with a Bayesian inference decision-tree algorithm, we classified the proteins within lipid rafts to be experiencing a second-order potential, and the transferrin receptors to be experiencing a fourth-order potential. This result is consistent with the notion that, in the first case, confinement is produced by the lipid composition of the confinement domains, and, in the second case, by the more abrupt boundary created by cytoskeletal filaments. Furthermore, using the t-SNE clustering algorithm, we graphically represented the degree of similarity of the confining potentials experienced by the receptors. The potentials associated with the transferrin receptors were clearly more similar to the simulated flat potentials with exponential borders, whereas the lipid-raft associated potentials were closer to the simulated harmonic potentials.

Chapters 4 and 5 support a model where receptors are moving within the membrane while interacting with various different cellular constituents that influence the receptor motion. For the cases that we studied, we see that certain receptors find themselves confined in lipid rafts. But in addition to this confinement, there is a secondary actin-dependent boundary that seems to, in turn, confine the lipid-raft domain itself. In the case of force application, it seems as though the raft may overcome this restriction and pass over the elastic boundary. Simultaneously, there are non-raft proteins that are not confined within lipid-dependent domains, yet are subject to this second type of confinement. Additionally, the two types of confinements, preferred by certain receptor types, display two distinct, confinement potential shapes, compatible with the nature of the confinement.

In the final chapter, we investigated the trajectory of the botulinum toxin through intestinal epithelial cells on its way to the active site. In order to do so, we implemented a technique to resolve the axial component of the motion using the changing width of the signal's point-spread-function. Within approximately 20 minutes, the internalisation process was observed to commence. The toxin was seen to undergo directed diffusion for 72 minutes, during which it moved across the cell by about 4 μm. The resulting diffusion coefficient and transport velocity obtained were 2×10^{-5} $\mu m^2/s$ and 0.001 μm/s, respectively. These initial results must be confirmed by subsequent experiments.

7.2 Outlook

One further aspect that can be investigated concerning the application of the Bayesian inference algorithm to the calibration of optical tweezers is its potential to map out the potential landscape and detect asymmetries of the trapping potentials produced by the laser beam. Additionally, the Bayesian inference approach could be applied to even stiffer traps and compared to other methods for trap calibration, like the mentioned step-response and drag-force method.

Concerning the structure of lipid rafts and the confinement potentials created by them, a number of questions still remain unanswered. One of the next steps to be taken is

investigating the lipid distribution in lipid raft domains. Is there a certain geometry to the lipid distribution, or are there regions of higher and lower diffusivity within the rafts? One possible way to investigate this concept is applying the same machine learning approach as used in section 5.5 to cluster data to detect similarities within a data set. This includes clustering of parameters like the skew and the kurtosis of the diffusivity.

Additionally, other cell types and receptor types need to be investigated to determine if the obtained results are consistent features and if, for example, different classes of lipid raft domains exist, providing more or less favourable surroundings for given proteins. Furthermore, the classification algorithm could be extended to test for additional models. In addition to simple diffusion, second-order potentials, and fourth-order potentials, further models that take into account the dynamics of potentials or asymmetries of the potentials could be appended.

Similarly, the application of a force on membrane receptors needs to be continued and applied on other cell types and other receptors, including non-raft receptors like transferrin. This work is presently being conducted by Chao Yu at the Laboratoire d'Optique et Biosciences. Furthermore, the possibility remains to use this microfluidic technique for microscopic force applications in various research areas. An example of this, which is currently also in development at the Laboratoire d'Optique et Biosciences, is measuring k_{off} for two high-affinity proteins by applying a force to lower the energy barrier for dissociation and pulling them apart.

A possible path that remains to be explored is investigating the results obtained in this thesis work using molecular dynamics (MD) simulations. This could provide a new angle on the origin of confinement potentials that the studied proteins experience, and on the roles that lipids, lipid distribution and lipid interactions play in producing this confinement. However, standard molecular dynamics simulations for complex systems as the ones in question here are constrained by the amount of computing resources available. Scientists are thus inhibited in the simulation system, size, and the total time. One way to stretch the performance of MD simulations is using coarse-grained representations of the system. This approach can improve the performance of the simulation by representing groups of atoms instead of each atom individually. This method has already been used extensively by Sansom and colleagues for modelling the protein-lipid interactions, and for studying the factors contributing to protein aggregation within the lipid membrane [297, 298]. More recently, the team around Sansom has used coarse-grain MD simulations to show that the orientation of membrane proteins within the membrane can be predicted exclusively from the protein structure, and is independent of the lipid composition of the membrane [298]. Extending this method for simulating proteins in potentials produced by lipid rafts and actin filaments could provide promising results.

Cryo-electron microscopy could also be a way to reveal previously inaccessible perspectives of the cell membrane. This technology has already been applied on cellular membranes for resolving the membrane structure and the proteins contained within the membrane [102], promising a potential resolution of less than 1 nm for biological specimen.

The next step for the three-dimensional tracking experiments of the HC BoNT/A through epithelial cells is to use a microscope with drift correction in the z-direction. As mentioned in section 6.4, one such system has been acquired by the LOB and is ideally suited for subsequent experiments. Furthermore, it would be useful to confirm the exact path of entry by the toxin and investigate further the nature of the trajectory taken. The nature of the trajectory followed inside cells could be investigated by labelling and verifying co-localisation of the tracked toxin with specific entities in the cell. For example, to confirm that the toxin is transported within vesicles, these could be labelled; to determine if the path taken is along microtubules, these could be depolymerised to verify if the transport through the cells is slowed down. Ultimately, the identification of specific actors important for the transcytosis process may lead to identification of inhibition targets with therapeutic implications.

Appendix A

Experimental Protocols

A.1 Culturing of MDCK cells

Madin-Darby canine kidney (MDCK) cells were grown in a culture medium consisting of DMEM, 10% fetal calf serum, and 1% penicillin-streptomycin in a 5% carbon dioxide environment at 37°C. Cells are typically trypsinated two days before the experiment and put on a glass cover slip to grow up to ∼90% confluence. During experiments, a solution consisting of HBSS, 10 mM HEPES, and 1% fetal calf serum was used. Cell were cultured for no more than 10 weeks (10 trypsinations) and experiments were conducted for no longer than 90 min.

A.2 Production of Microfluidic Channels

The PDMS (Dow Corning STILGARD 184) channels were produced by mixing the bulk material and curing agent with a ratio of 10 parts to 1. The mixture is then poured into a set of channel moulds previously prepared. To eliminate any bubbles that have formed in liquid during mixing, the liquid is centrifuged before pouring and placed in a vacuum bell after pouring. The moulds and the mixture are then placed in the oven to be baked at 70°C. After no less than half a day (approximately six hours), the channels can be cut from the mould using a scalpel and plasma cleaned along with a glass coverslip for 45 s. The mould and the coverslip can then be electrostatically stuck together.

A.3 Cell Injection into Microfluidic Channels

Two days before cells are injected, channels must be covered in culture medium (MC). This permits the PDMS to absorb some of the medium and increases cell viability in the channels.

Cells must be injected into the channels at a very high concentration ($\sim 10^8$ cells/ml). We used a T25 (25 cm^2) box confluent with cells and concentrated them into 300 μL.

These were carefully injected into the channels and left in a 5% carbon dioxide environment at 37°C. The cells attach to the surface after approximately 6 hrs. This is when experiments can be started. Leaving the cells in the channels for more than 12 hrs may lead to cell death as the small space restricts cell viability.

A.4 Actin labeling with GFP

For cell transfection with GFP-β actin, the following reduced expression plasmid was used: *Addgene plasmid 31502; Addgene, Cambridge, MA* [299]. Using the HiSpeed Plasmid Midi Kit by QUIAGEN (Venlo, Netherlands) we extracted the plasmid from an *Escherichia coli (DHα)* bacterial culture. The extracted plasmid concentration was 0.225 μg/μL, determined by the absorption spectrum. We then diluted 5 μL of the plasmid containing liquid in 100 μL of observation medium (see section 2.2) and 3 μL of X-tremeGENE HP DNA Transfection Reagent (Roch Applied Science, Penzberg, Germany). This solution was left to incubate for 15 min at room temperature and then injected in the channels to incubate with the cells for 24-28 hrs.

A.5 Phalloidin-Rhodamine Staining of Cells

The staining of cells with phalloidin-rhodamine in microchannels requires 5 different syringes filled with the following solutions:

1. 4% formaldehyde in phosphate-buffered saline (PBS)
2. marking solution: PBS + 0.125% gelatin
3. marking solution + 1% Triton
4. blocking solution: PBS + 0.25% gelatin
5. staining solution: DAPI (Invitrogen, Carlsbad, CA) diluted by 1:200 in PBS + phalloidin-rhodamine (Invitrogen) diluted by 1:40 in PBS

Injections are at flow rates of ~1-2μL/min so as not to affect the cells. Solution 1 is injected first and incubated for 15 min. Solution 3 is then injected, rinsed after 4 min. with solution 2. Then solution 4 is injected, which is left for 30-60 min. The channels are then rinsed and flooded with solution 5 and left for 45-60 min at 37°C. Finally, the channels are again rinsed with solution 2.

A.6 Raft Labeling with Sphingomyelin-BODIPY

BODIPY FL C12-sphingomyelin (Life Technologies, Carlsbad, CA) is diluted in chloroform:(pure)ethanol (19:1) for a final concentration of 1 mM. 50 μL of this solution are

then dried under Ar and subsequently in vacuum for 1 hr. The complex is then redissolved in 200 μL of pure ethanol. BSA (A2058; Sigma, St. Louis, MO) is prepared at a concentration of 0.34 mg/mL in MM (HBSS + 10 mM HEPES). The sphingomyelin-BODIPY solution is then added, drop by drop, to the BSA solution in a N_2 environment, O_2 free, while vortexing. The resulting solution is then injected into the microchannels and left to incubate with the cells at 4°C for 30-60 min. Cells need to be rinsed before observation.

A.7 m-IC$_{cl2}$ cell cultue

m-IC$_{cl2}$ ells were grown in a culture medium in a 5% carbon dioxide environment at 37°C. Cells are typically trypsinated two days before the experiment and put on a glass cover slip to grow up to ∼90% confluence. During experiments, a solution consisting of HBSS, 10 mM HEPES, and 1% fetal calf serum was used. Cell were cultured for no more than 10 weeks (10 trypsinations) and experiments were conducted for no longer than 90 min.

m-IC$_{cl2}$ cells were cultured in a medium consisting of DMEM/HAM's F12 (Life Technologies) and the following ingredients:

- 2 % heat-inactivated fetal bovine serum (Life Technologies)
- 20 mM HEPES pH7.4
- 5μg/mL transferrin (Sigma)
- 5μg/mL insulin (Sigma)
- 50 nM dexamethasone (Sigma)
- 60nM selenium (Sigma)
- 1nM triiodothyronine (Sigma)
- 10 nM epidermal growth factor (Sigma)
- 2mM L-glutamine (Life Technologies)
- 60nM sodium selenate (Sigma)

Appendix B

Algorithms

B.1 k-means

The k-means clustering algorithm classifies data from a given data set into a given number of clusters by minimising the sum of all distances of all data points to the centroid of their assigned cluster as in equation:

$$\sum_{i}^{k} \sum_{\mathbf{x} \in S_i} ||\mathbf{x} - \mu_\mathbf{i}||^2 \tag{B.1}$$

$\mathbf{x}$ represents the data points, μ_i the centroid of cluster S_i of k clusters. This is done in two principal steps. After determining the number of clusters to be produced, the centroid coordinates are initialised randomly and an optimisation loop begins.

The two main steps in the loop are:

1. assigning each point in the data set to the nearest centroid, hence, producing the sets of clusters
2. given the clusters, the centroids of the clusters are calculated, producing a new set of centroids at which point step 1 is applied again and the points are reassigned to the nearest centroid.

These steps are repeated, constantly minimising the sum of distances from the centroids, until subsequent iterations do not produce changes in the centroid positions any more. The individual steps are shown in figure B.1.

B.2 Voronoi Diagram

Voronoi diagrams, as shown in figure 5.4B and F, are created by using predetermined seed points to segment an area into subsections. The region corresponding to a certain

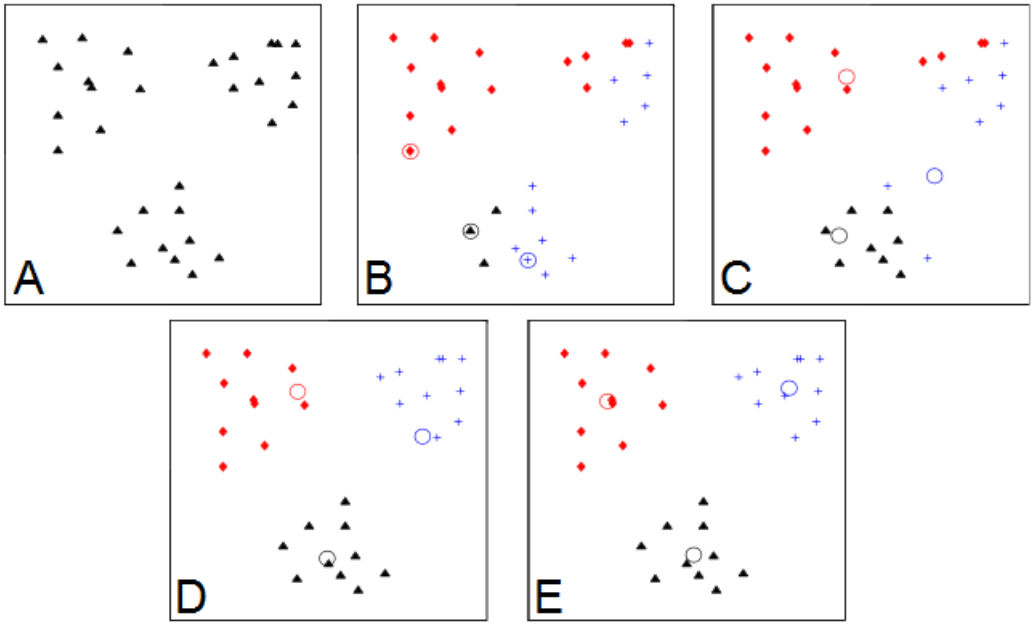

Figure B.1: k-means clustering schematic. (A) Initial input data is (B) combined with centroid positions initialised on random data points, and the data is assigned on a closest neighbour basis. (C) cluster centroids become the positions for the new centroids, and the previous steps are repeated (C,D) for several iterations until (E) the cluster centroids correspond to the present centroid positions. Figure reproduced from [300].

seed point consists of all points closer to that seed point than to all other seed points. The formal definition of this is given by:

$$R_k\{x \in X | D(x, P_k) \leq D(x, P_j) \quad \text{for all} \quad j \neq k\} \tag{B.2}$$

R_k is the set of points that are associated with centroid k. P_i represents the position of centroid i. $D(x, P_i)$ represents the distance between point x and centroid position P_i.

B.3 t-SNE

t-SNE is a technique for visualizing high-dimensional datasets by projecting these on a two- or three-dimensional map. It is a variation of the Stochastic Neighbour Embedding (SNE) method [301], which has been shown to produce results superior to other techniques such as Sammon mapping, Isomap and Locally Linear Embedding [234]. However, as for many visualisation and unsupervised learing techniques, the degree of success of this approach is left to the experimenter to interpret. This section will outline the general principles of t-SNE. For the full description refer to the original publication by van der Maaten and Hinton [234].

Since t-SNE is a modification of the SNE approach, it is useful to remind oneself of the underpinnings of Stochastic Neighbour Embedding. SNE calculates the similarity between two high-dimensional data points x_i and x_j via a Gaussian centered on one of

the points. This "similarity", $p_{j|i}$, represents the probability that x_i would choose x_j as its neighbour if these were picked according to the probability density given by the following Gaussian:

$$p_{j|i} = \frac{e^{-\frac{\|x_i - x_j\|^2}{2\sigma_i^2}}}{\sum_{k \neq i} e^{-\frac{\|x_i - x_k\|^2}{2\sigma_i^2}}} \tag{B.3}$$

$p_{i|j}$ represents this conditional probability in the high-dimensional space, and σ_i is the variance of the Gaussian centred on the data point x_i. Since the density of the data in the parameter space is likely to vary, σ_i is chosen to be different for each point. σ_i is determined by performing a binary search for a value of σ_i that produces a probability distribution, P_i, over all data points with a fixed perplexity. The perplexity can be interpreted as a measure of the effective point density around a point and is determined by the equation:

$$Perp(P_i) = 2^{-\sum_j p_{j|i} \log_2 p_{j|i}} \tag{B.4}$$

Similarly to equation B.3, a conditional probability is calculated for the low-dimensional counterparts of the data using:

$$q_{j|i} = \frac{e^{-\frac{\|y_i - y_j\|^2}{2\sigma_i^2}}}{\sum_{k \neq i} e^{-\frac{\|y_i - y_k\|^2}{2\sigma_i^2}}} \tag{B.5}$$

with the Gaussian variance set to $1/\sqrt{2}$ in this case.

In an ideal case, the low-dimensional representation of the data will yield conditional probabilities $q_{j|i}$ equal to the conditional probabilities $p_{j|i}$. The goal is, hence, to minimize the mismatch between these two quantities. This is done by calculating the Kullback-Leibler divergence over all the data points using:

$$C = \sum_i KL(P_i||Q_i) = \sum_i \sum_j p_{j|i} \log \left(\frac{p_{j|i}}{q_{j|i}} \right) \tag{B.6}$$

and minimizing this quantity via a gradient descent method.

t-SNE addresses two problems by introducing modifications to the SNE approach. Firstly, the cost function is difficult to optimize in the SNE method. However, this can be addressed using symmetric conditional probabilities, $p_{i|j} = p_{j|i}$ and $q_{i|j} = q_{j|i}$, that are calculated using:

$$p_{ij} = \frac{p_{i|j} + p_{j|i}}{2n} \tag{B.7}$$

where p_{ij} is now given by:

$$p_{ij} = \frac{e^{-\frac{\|x_i - x_j\|^2}{2\sigma_i^2}}}{\sum_{k \neq l} e^{-\frac{\|x_k - x_l\|^2}{2\sigma_i^2}}} \tag{B.8}$$

and q_{ij} by:

$$q_{ij} = \frac{e^{-\frac{\|y_i - y_j\|^2}{2\sigma_i^2}}}{\sum_{k \neq l} e^{-\frac{\|y_k - y_l\|^2}{2\sigma_i^2}}} \tag{B.9}$$

This produces a simplified gradient and additionally provides a better representation of high-dimensional outliers in the low-dimensional space.

The second problem that t-SNE addresses is "crowding". This is a problem that arises when seeking to model data initially in a high-dimensional manifold onto a two-dimensional map, which manifests itself by crowing similar points too close to each other to faithfully represent the distances to more dissimilar points.

To overcome this problem, the distribution that is used to compute the conditional probability for the low-dimensional space can be given a heavier tail than the initial Gaussian used for the high-dimensional data. Thereby, moderate distances are modelled as larger distances in the low-dimensional space, and similar data points are less inclined to crowd together. The distribution used is a Student t-distribution:

$$q_{i|j} = \frac{(1 + ||y_i - y_j||^2)^{-1}}{\Sigma_{k \neq l}(1 + ||y_k - y_l||^2)^{-1}} \tag{B.10}$$

Bibliography

[1] K. Pearson. *The grammar of science*. Number vol. 20 in Contemporary science series. W. Scott, 1892.

[2] J Craig Venter, Mark D Adams, Eugene W Myers, Peter W Li, Richard J Mural, Granger G Sutton, Hamilton O Smith, Mark Yandell, Cheryl A Evans, Robert A Holt, et al. The sequence of the human genome. *Science*, 291(5507):1304–1351, 2001.

[3] Craig Venter and Daniel Cohen. The century of biology. *New Perspectives Quarterly*, 21(4):73–77, 2004.

[4] S Jonathan Singer, Garth L Nicolson, et al. The fluid mosaic model of the structure of cell membranes. *Science*, 175(23):720–731, 1972.

[5] PG Saffman and M Delbrück. Brownian motion in biological membranes. *Proceedings of the National Academy of Sciences*, 72(8):3111–3113, 1975.

[6] Donald M Engelman. Membranes are more mosaic than fluid. *Nature*, 438(7068): 578–580, 2005.

[7] Gerrit Van Meer, Dennis R Voelker, and Gerald W Feigenson. Membrane lipids: where they are and how they behave. *Nature reviews molecular cell biology*, 9(2): 112–124, 2008.

[8] Kai Simons, Elina Ikonen, et al. Functional rafts in cell membranes. *Nature*, 387 (6633):569–572, 1997.

[9] Rodrigo F M De Almeida, Aleksandre Fedorov, and Manuel Prieto. Sphingomyelin/phosphatidylcholine/cholesterol phase diagram: boundaries and composition of lipid rafts. *Biophysical journal*, 85(4):2406–2416, 2003.

[10] Deborah A Brown and Erwin London. Structure and function of sphingolipid- and cholesterol-rich membrane rafts. *Journal of Biological Chemistry*, 275(23): 17221–17224, 2000.

[11] Holly C Gaede and Klaus Gawrisch. Lateral diffusion rates of lipid, water, and a hydrophobic drug in a multilamellar liposome. *Biophysical journal*, 85(3):1734–1740, 2003.

[12] Greta M Lee, Akira Ishihara, and Ken A Jacobson. Direct observation of Brownian motion of lipids in a membrane. *Proceedings of the National Academy of Sciences*, 88(14):6274–6278, 1991.

[13] Christian Dietrich, Zoya N Volovyk, Moshe Levi, Nancy L Thompson, and Ken Jacobson. Partitioning of Thy-1, GM1, and cross-linked phospholipid analogs into lipid rafts reconstituted in supported model membrane monolayers. *Proceedings of the National Academy of Sciences*, 98(19):10642–10647, 2001.

[14] Rodrigo F M de Almeida, Luís M S Loura, Alexander Fedorov, and Manuel Prieto. Lipid rafts have different sizes depending on membrane composition: a time-resolved fluorescence resonance energy transfer study. *Journal of molecular biology*, 346(4):1109–1120, 2005.

[15] J Deisenhofer, O Epp, K Miki, R Huber, and H Michel. Structure of the protein subunits in the photosynthetic reaction centre of *Pseudomonas viridis* at 3Å resolution. *Nature*, 318:618–624, 1985.

[16] Richard J Cherry. Rotational and lateral diffusion of membrane proteins. *Biochimica et Biophysica Acta (BBA)-Reviews on Biomembranes*, 559(4):289–327, 1979.

[17] L D Frye and M Edidin. The rapid intermixing of cell surface antigens after formation of mouse-human heterokaryons. *Journal of cell science*, 7(2):319–335, 1970.

[18] Gary R Hunnicutt, Dennis E Koppel, and Diana G Myles. Analysis of the process of localization of fertilin to the sperm posterior head plasma membrane domain during sperm maturation in the epididymis. *Developmental Biology*, 191(1):146–159, 1997.

[19] Toyoshi Fujimoto, Hiroshi Kogo, Ryuji Nomura, and Tomoko Une. Isoforms of Caveolin-1 and caveolar structure. *Journal of Cell Science*, 113(19):3509–3517, 2000.

[20] Mark A Lemmon and Joseph Schlessinger. Cell signaling by receptor tyrosine kinases. *Cell*, 141(7):1117–1134, 2010.

[21] Brian K Kobilka. G protein coupled receptor structure and activation. *Biochimica et Biophysica Acta (BBA)-Biomembranes*, 1768(4):794–807, 2007.

[22] Dylan T Burnette, Suliana Manley, Prabuddha Sengupta, Rachid Sougrat, Michael W Davidson, Bechara Kachar, and Jennifer Lippincott-Schwartz. A role for actin arcs in the leading-edge advance of migrating cells. *Nature cell biology*, 13(4):371–382, 2011.

[23] Charles L Asbury, Adrian N Fehr, and Steven M Block. Kinesin moves by an asymmetric hand-over-hand mechanism. *Science*, 302(5653):2130–2134, 2003.

[24] Ahmet Yildiz and Paul R Selvin. Fluorescence imaging with one nanometer accuracy: application to molecular motors. *Accounts of chemical research*, 38(7): 574–582, 2005.

[25] Edgar Meyhöfer and Jonathon Howard. The force generated by a single kinesin molecule against an elastic load. *Proceedings of the National Academy of Sciences*, 92(2):574–578, 1995.

[26] Stuart J Bussell, Donald L Koch, and Daniel A Hammer. Effect of hydrodynamic interactions on the diffusion of integral membrane proteins: diffusion in plasma membranes. *Biophysical journal*, 68(5):1836–1849, 1995.

[27] Didier Marguet, Pierre-François Lenne, Hervé Rigneault, and Hai-Tao He. Dynamics in the plasma membrane: how to combine fluidity and order. *The EMBO journal*, 25(15):3446–3457, 2006.

[28] Deborah A Brown and John K Rose. Sorting of GPI-anchored proteins to glycolipid-enriched membrane subdomains during transport to the apical cell surface. *Cell*, 68(3):533–544, 1992.

[29] Heiko Heerklotz, Halina Szadkowska, Thomas Anderson, and Joachim Seelig. The sensitivity of lipid domains to small perturbations demonstrated by the effect of Triton. *Journal of molecular biology*, 329(4):793–799, 2003.

[30] Pranav Sharma, Rajat Varma, R C Sarasij, Karine Gousset, G Krishnamoorthy, Madan Rao, Satyajit Mayor, et al. Nanoscale organization of multiple GPI-anchored proteins in living cell membranes. *Cell*, 116(4):577–589, 2004.

[31] Christian Eggeling, Christian Ringemann, Rebecca Medda, Günter Schwarzmann, Konrad Sandhoff, Svetlana Polyakova, Vladimir N Belov, Birka Hein, Claas von Middendorff, Andreas Schönle, et al. Direct observation of the nanoscale dynamics of membrane lipids in a living cell. *Nature*, 457(7233):1159–1162, 2009.

[32] Erin D Sheets, Greta M Lee, Rudolf Simson, and Ken Jacobson. Transient confinement of a glycosylphosphatidylinositol-anchored protein in the plasma membrane. *Biochemistry*, 36(41):12449–12458, 1997.

[33] Prabuddha Sengupta, Adam Hammond, David Holowka, and Barbara Baird. Structural determinants for partitioning of lipids and proteins between coexisting fluid phases in giant plasma membrane vesicles. *Biochimica et Biophysica Acta (BBA)-Biomembranes*, 1778(1):20–32, 2008.

[34] A Pralle, P Keller, E-L Florin, K Simons, and J K H Hörber. Sphingolipid–cholesterol rafts diffuse as small entities in the plasma membrane of mammalian cells. *The Journal of cell biology*, 148(5):997–1008, 2000.

[35] Britta Brügger, Catriona Graham, Iris Leibrecht, Enrico Mombelli, Angela Jen, Felix Wieland, and Roger Morris. The membrane domains occupied by glycosylphosphatidylinositol-anchored prion protein and Thy-1 differ in lipid composition. *Journal of Biological Chemistry*, 279(9):7530–7536, 2004.

[36] Linda J Pike. Lipid rafts bringing order to chaos. *Journal of lipid research*, 44(4): 655–667, 2003.

[37] Andrey Filippov, Greger Orädd, and Göran Lindblom. Lipid lateral diffusion in ordered and disordered phases in raft mixtures. *Biophysical journal*, 86(2):891–896, 2004.

[38] S Chatterjee and S Mayor. The GPI-anchor and protein sorting. *Cellular and Molecular Life Sciences CMLS*, 58(14):1969–1987, 2001.

[39] Teymuras V Kurzchalia and Robert G Partan. Membrane microdomains and caveolae. *Current opinion in cell biology*, 11(4):424–431, 1999.

[40] Eduard B Babiychuk, Katia Monastyrskaya, Fiona C Burkhard, Susan Wray, and Annette Draeger. Modulating signaling events in smooth muscle: cleavage of Annexin 2 abolishes its binding to lipid rafts. *The FASEB journal*, 16(10):1177–1184, 2002.

[41] Kai Simons and Derek Toomre. Lipid rafts and signal transduction. *Nature reviews Molecular cell biology*, 1(1):31–39, 2000.

[42] Caitlin E Sedwick and Amnon Altman. Ordered just so: lipid rafts and lymphocyte function. *Science Signaling*, 2002(122):re2, 2002.

[43] Peter W Janes, Steven C Ley, Anthony I Magee, and Panagiotis S Kabouridis. The role of lipid rafts in T cell antigen receptor (TCR) signalling. In *Seminars in immunology*, volume 12, pages 23–34. Elsevier, 2000.

[44] Claire Langlet, Anne-Marie Bernard, Philippe Drevot, and Hai-Tao He. Membrane rafts and signaling by the multichain immune recognition receptors. *Current opinion in immunology*, 12(3):250–255, 2000.

[45] Daniel Lingwood and Kai Simons. Lipid rafts as a membrane-organizing principle. *Science*, 327(5961):46–50, 2010.

[46] Robert G Parton and Ayanthi A Richards. Lipid rafts and caveolae as portals for endocytosis: new insights and common mechanisms. *Traffic*, 4(11):724–738, 2003.

[47] Lucas Pelkmans and Ari Helenius. Endocytosis via caveolae. *Traffic*, 3(5):311–320, 2002.

[48] Hidehiko Shogomori and Anthony H Futerman. Cholesterol depletion by methyl-β-cyclodextrin blocks cholera toxin transport from endosomes to the golgi apparatus in hippocampal neurons. *Journal of neurochemistry*, 78(5):991–999, 2001.

[49] Ken Ritchie, Ryota Iino, Takahiro Fujiwara, Kotono Murase, and Akihiro Kusumi. The fence and picket structure of the plasma membrane of live cells as revealed by single molecule techniques (Review). *Molecular membrane biology*, 20(1):13–18, 2003.

[50] Akihiro Kusumi, Yasushi Sako, and Mutsuya Yamamoto. Confined lateral diffusion of membrane receptors as studied by single particle tracking (nanovid microscopy). Effects of calcium-induced differentiation in cultured epithelial cells. *Biophysical journal*, 65(5):2021–2040, 1993.

[51] Takahiro Fujiwara, Ken Ritchie, Hideji Murakoshi, Ken Jacobson, and Akihiro Kusumi. Phospholipids undergo hop diffusion in compartmentalized cell membrane. *The Journal of cell biology*, 157(6):1071–1082, 2002.

[52] Yasushi Sako, Akira Nagafuchi, Shoichiro Tsukita, Masatoshi Takeichi, and Akihiro Kusumi. Cytoplasmic regulation of the movement of E-cadherin on the free cell surface as studied by optical tweezers and single particle tracking: corralling and tethering by the membrane skeleton. *The Journal of cell biology*, 140(5): 1227–1240, 1998.

[53] Kotono Murase, Takahiro Fujiwara, Yasuhiro Umemura, Kenichi Suzuki, Ryota Iino, Hidetoshi Yamashita, Mihoko Saito, Hideji Murakoshi, Ken Ritchie, and Akihiro Kusumi. Ultrafine membrane compartments for molecular diffusion as revealed by single molecule techniques. *Biophysical journal*, 86(6):4075–4093, 2004.

[54] Kenichi Suzuki, Ken Ritchie, Eriko Kajikawa, Takahiro Fujiwara, and Akihiro Kusumi. Rapid hop diffusion of a G-protein-coupled receptor in the plasma membrane as revealed by single-molecule techniques. *Biophysical journal*, 88(5):3659–3680, 2005.

[55] Akihiro Kusumi, Takahiro K Fujiwara, Nobuhiro Morone, Kenta J Yoshida, Rahul Chadda, Min Xie, Rinshi S Kasai, and Kenichi G N Suzuki. Membrane mechanisms for signal transduction: the coupling of the meso-scale raft domains to membrane-skeleton-induced compartments and dynamic protein complexes. In *Seminars in cell & developmental biology*, volume 23, pages 126–144. Elsevier, 2012.

[56] Steven J Winder and Kathryn R Ayscough. Actin-binding proteins. *Journal of cell science*, 118(4):651–654, 2005.

[57] Songwan Jin, Peter M Haggie, and A S Verkman. Single-Particle Tracking of Membrane Protein Diffusion in a Potential: Simulation, Detection, and Application to Confined Diffusion of CFTR Cl^- Channels. *Biophysical journal*, 93(3):1079–1088, 2007.

[58] Nicolas Destainville. Cluster phases of membrane proteins. *Physical Review E*, 77 (1):011905, 2008.

[59] Frédéric Daumas, Nicolas Destainville, Claire Millot, André Lopez, David Dean, and Laurence Salomé. Confined diffusion without fences of a G-protein-coupled receptor as revealed by single particle tracking. *Biophysical journal*, 84(1):356–366, 2003.

[60] Eric Frank and Gerald D Fischbach. Early events in neuromuscular junction formation in vitro: induction of acetylcholine receptor clusters in the postsynaptic membrane and morphology of newly formed synapses. *The Journal of cell biology*, 83(1):143–158, 1979.

[61] James A Dix and A S Verkman. Crowding effects on diffusion in solutions and cells. *Annu. Rev. Biophys.*, 37:247–263, 2008.

[62] C Lesieur, B Vecsey-Semjen, L Abrami, M Fivaz, and F Gisou van der Goot. Membrane insertion: the strategies of toxins (Review). *Molecular membrane biology*, 14(2):45–64, 1997.

[63] J E Alouf. Pore-forming bacterial protein toxins: an overview. In *Pore-forming toxins*, pages 1–14. Springer, 2001.

[64] M R Gonzalez, M Bischofberger, L Pernot, F G Van Der Goot, and B Freche. Bacterial pore-forming toxins: the (w)hole story? *Cellular and molecular life sciences*, 65(3):493–507, 2008.

[65] J Ballard, Y Sokolov, W-L Yuan, BL Kagan, and RK Tweten. Activation and mechanism of clostridium septicum alpha toxin. *Molecular microbiology*, 10(3): 627–634, 1993.

[66] Valery M Gordon, Kim L Nelson, J Thomas Buckley, Victoria L Stevens, Rodney K Tweten, Patrick C Elwood, and Stephen H Leppla. *Clostridium septicum* alpha toxin uses glycosylphosphatidylinositol-anchored protein receptors. *Journal of Biological Chemistry*, 274(38):27274–27280, 1999.

[67] J Glenn Songer. Clostridial enteric diseases of domestic animals. *Clinical microbiology reviews*, 9(2):216, 1996.

[68] Daichi Yamashita, Takaki Sugawara, Miyu Takeshita, Jun Kaneko, Yoshiyuki Kamio, Isao Tanaka, Yoshikazu Tanaka, and Min Yao. Molecular basis of transmembrane beta-barrel formation of staphylococcal pore-forming toxins. *Nature communications*, 5, 2014.

[69] Cesare Montecucco, Emanuele Papini, and Giampietro Schiavo. Bacterial protein toxins penetrate cells via a four-step mechanism. *FEBS letters*, 346(1):92–98, 1994.

[70] Sayali S Karve and Alison A Weiss. Glycolipid binding preferences of shiga toxin variants. *PloS one*, 9(7):e101173, 2014.

[71] Peter H Fishman. Role of membrane gangliosides in the binding and action of bacterial toxins. *The Journal of membrane biology*, 69(2):85–97, 1982.

[72] Erwin London. Diphtheria toxin: membrane interaction and membrane translocation. *Biochimica et Biophysica Acta (BBA)-Reviews on Biomembranes*, 1113(1): 25–51, 1992.

[73] Nicholas F Endres, Rahul Das, Adam W Smith, Anton Arkhipov, Erika Kovacs, Yongjian Huang, Jeffrey G Pelton, Yibing Shan, David E Shaw, David E Wemmer, et al. Conformational coupling across the plasma membrane in activation of the egf receptor. *Cell*, 152(3):543–556, 2013.

[74] Inmaculada M Gonzalez-Gonzalez, Frederic Jaskolski, Yves Goldberg, Michael C Ashby, and Jeremy M Henley. Measuring membrane protein dynamics in neurons using fluorescence recovery after photobleach. *Methods in enzymology*, 504:127, 2012.

[75] Doan-Trung Luu, Alexandre Martiniere, Mathias Sorieul, John Runions, and Christophe Maurel. Fluorescence recovery after photobleaching reveals high cycling dynamics of plasma membrane aquaporins in arabidopsis roots under salt stress. *The Plant Journal*, 69(5):894–905, 2012.

[76] Jesse Stricker, Paul Maddox, ED Salmon, and Harold P Erickson. Rapid assembly dynamics of the *Escherichia coli* FtsZ-ring demonstrated by fluorescence recovery after photobleaching. *Proceedings of the National Academy of Sciences*, 99(5): 3171–3175, 2002.

[77] Laurence Salomé, Jean-Luc Cazeils, André Lopez, and Jean-François Tocanne. Characterization of membrane domains by FRAP experiments at variable observation areas. *European biophysics journal*, 27(4):391–402, 1998.

[78] Olivier Thoumine, Lucie Bard, Edouard Saint-Michel, Caroline Dequidt, and Daniel Choquet. Optical tweezers and fluorescence recovery after photo-bleaching to measure molecular interactions at the cell surface. *Cellular and Molecular Bioengineering*, 1(4):301–311, 2008.

[79] Dylan M Owen, Peter M P Lanigan, Christopher Dunsby, Ian Munro, David Grant, Mark A A Neil, Paul M W French, and Anthony I Magee. Fluorescence lifetime imaging provides enhanced contrast when imaging the phase-sensitive dye di-4-ANEPPDHQ in model membranes and live cells. *Biophysical journal*, 90(11): L80–L82, 2006.

[80] James A Levitt, Marina K Kuimova, Gokhan Yahioglu, Pei-Hua Chung, Klaus Suhling, and David Phillips. Membrane-bound molecular rotors measure viscosity in live cells via fluorescence lifetime imaging. *The Journal of Physical Chemistry C*, 113(27):11634–11642, 2009.

[81] Laure Wawrezinieck, Hervé Rigneault, Didier Marguet, and Pierre-François Lenne. Fluorescence correlation spectroscopy diffusion laws to probe the submicron cell membrane organization. *Biophysical journal*, 89(6):4029–4042, 2005.

[82] Hai-Tao He and Didier Marguet. Detecting nanodomains in living cell membrane by fluorescence correlation spectroscopy. *Annual review of physical chemistry*, 62: 417–436, 2011.

[83] Mats G L Gustafsson, Eric Betzig, Harald F Hess, George H Patterson, Jennifer Lippincott-Schwartz, and Michael W Davidson. Education in microscopy and digital imaging. URL http://zeiss-campus.magnet.fsu.edu/articles/superresolution/introduction.html.

[84] Sripad Ram, E Sally Ward, and Raimund J Ober. Beyond rayleigh's criterion: a resolution measure with application to single-molecule microscopy. *Proceedings of the National Academy of Sciences of the United States of America*, 103(12): 4457–4462, 2006.

[85] Birka Hein, Katrin I Willig, and Stefan W Hell. Stimulated emission depletion (STED) nanoscopy of a fluorescent protein-labeled organelle inside a living cell. *Proceedings of the National Academy of Sciences*, 105(38):14271–14276, 2008.

[86] Marta Fernández-Suárez and Alice Y Ting. Fluorescent probes for super-resolution imaging in living cells. *Nature Reviews Molecular Cell Biology*, 9(12):929–943, 2008.

[87] Birka Hein, Katrin I Willig, Christian A Wurm, Volker Westphal, Stefan Jakobs, and Stefan W Hell. Stimulated emission depletion nanoscopy of living cells using snap-tag fusion proteins. *Biophysical journal*, 98(1):158–163, 2010.

[88] Jochen J Sieber, Katrin I Willig, Carsten Kutzner, Claas Gerding-Reimers, Benjamin Harke, Gerald Donnert, Burkhard Rammner, Christian Eggeling, Stefan W Hell, Helmut Grubmüller, et al. Anatomy and dynamics of a supramolecular membrane protein cluster. *Science*, 317(5841):1072–1076, 2007.

[89] Christian Eggeling, Katrin I Willig, and Francisco J Barrantes. STED microscopy of living cells–new frontiers in membrane and neurobiology. *Journal of neurochemistry*, 126(2):203–212, 2013.

[90] V Mueller, A Honigmann, C Ringemann, R Medda, G Schwarzmann, and C Eggeling. Fcs in sted microscopy: studying the nanoscale of lipid membrane dynamics. *Methods in enzymology*, 519:1, 2013.

[91] Bo Huang, Mark Bates, and Xiaowei Zhuang. Super resolution fluorescence microscopy. *Annual review of biochemistry*, 78:993, 2009.

[92] Eric Betzig, George H Patterson, Rachid Sougrat, O Wolf Lindwasser, Scott Olenych, Juan S Bonifacino, Michael W Davidson, Jennifer Lippincott-Schwartz, and Harald F Hess. Imaging intracellular fluorescent proteins at nanometer resolution. *Science*, 313(5793):1642–1645, 2006.

[93] Michael J Rust, Mark Bates, and Xiaowei Zhuang. Sub-diffraction-limit imaging by stochastic optical reconstruction microscopy (storm). *Nature methods*, 3(10): 793–796, 2006.

[94] Mark Bates, Bo Huang, Graham T Dempsey, and Xiaowei Zhuang. Multicolor super-resolution imaging with photo-switchable fluorescent probes. *Science*, 317 (5845):1749–1753, 2007.

[95] Bo Huang, Wenqin Wang, Mark Bates, and Xiaowei Zhuang. Three-dimensional super-resolution imaging by stochastic optical reconstruction microscopy. *Science*, 319(5864):810–813, 2008.

[96] Samuel T Hess, Travis J Gould, Manasa V Gudheti, Sarah A Maas, Kevin D Mills, and Joshua Zimmerberg. Dynamic clustered distribution of hemagglutinin resolved at 40 nm in living cell membranes discriminates between raft theories. *Proceedings of the National Academy of Sciences*, 104(44):17370–17375, 2007.

[97] Ingolf Bernhardt, Lyubomira Ivanova, Patrik Langehanenberg, Bjoern Kemper, and Gert von Bally. Application of digital holographic microscopy to investigate the sedimentation of intact red blood cells and their interaction with artificial surfaces. *Bioelectrochemistry*, 73(2):92–96, 2008.

[98] Benjamin Rappaz, Alexander Barbul, Annick Hoffmann, Daniel Boss, Rafi Korenstein, Christian Depeursinge, Pierre J Magistretti, and Pierre Marquet. Spatial analysis of erythrocyte membrane fluctuations by digital holographic microscopy. *Blood Cells, Molecules, and Diseases*, 42(3):228–232, 2009.

[99] Benjamin Rappaz, Pierre Marquet, Etienne Cuche, Yves Emery, Christian Depeursinge, and Pierre Magistretti. Measurement of the integral refractive index and dynamic cell morphometry of living cells with digital holographic microscopy. *Optics express*, 13(23):9361–9373, 2005.

[100] Rolf Erni, Marta D Rossell, Christian Kisielowski, and Ulrich Dahmen. Atomic-resolution imaging with a sub-50-pm electron probe. *Physical review letters*, 102 (9):096101, 2009.

[101] Niels de Jonge and Frances M Ross. Electron microscopy of specimens in liquid. *Nature nanotechnology*, 6(11):695–704, 2011.

[102] Amélie Leforestier, Nicolas Lemercier, and Françoise Livolant. Contribution of cryoelectron microscopy of vitreous sections to the understanding of biological membrane structure. *Proceedings of the National Academy of Sciences*, 109(23): 8959–8964, 2012.

[103] KL Klein, IM Anderson, and N De Jonge. Transmission electron microscopy with a liquid flow cell. *Journal of microscopy*, 242(2):117–123, 2011.

[104] Gerd Binnig, Calvin F Quate, and Ch Gerber. Atomic force microscope. *Physical review letters*, 56(9):930, 1986.

[105] D J Johnson, S A Al Malek, B A M Al-Rashdi, and N Hilal. Atomic force microscopy of nanofiltration membranes: Effect of imaging mode and environment. *Journal of Membrane Science*, 389:486–498, 2012.

[106] Ignacio Casuso, Jonathan Khao, Mohamed Chami, Perrine Paul-Gilloteaux, Mohamed Husain, Jean-Pierre Duneau, Henning Stahlberg, James N Sturgis, and Simon Scheuring. Characterization of the motion of membrane proteins using high-speed atomic force microscopy. *Nature nanotechnology*, 7(8):525–529, 2012.

[107] Hong Qian, Michael P Sheetz, and Elliot L Elson. Single particle tracking. analysis of diffusion and flow in two-dimensional systems. *Biophysical journal*, 60(4):910–921, 1991.

[108] Rudolf Simson, Erin D Sheets, and Ken Jacobson. Detection of temporary lateral confinement of membrane proteins using single-particle tracking analysis. *Biophysical journal*, 69(3):989–993, 1995.

[109] Erik Meijering, Oleh Dzyubachyk, Ihor Smal, et al. Methods for cell and particle tracking. *Methods Enzymol*, 504(9):183–200, 2012.

[110] Michael J Saxton and Ken Jacobson. Single-particle tracking: applications to membrane dynamics. *Annual review of biophysics and biomolecular structure*, 26 (1):373–399, 1997.

[111] Daniel Aquino, Andreas Schönle, Claudia Geisler, Claas v Middendorff, Christian A Wurm, Yosuke Okamura, Thorsten Lang, Stefan W Hell, and Alexander Egner. Two-color nanoscopy of three-dimensional volumes by 4Pi detection of stochastically switched fluorophores. *Nature methods*, 8(4):353–359, 2011.

[112] Hendrik Deschout, Francesca Cella Zanacchi, Michael Mlodzianoski, Alberto Diaspro, Joerg Bewersdorf, Samuel T Hess, and Kevin Braeckmans. Precisely and accurately localizing single emitters in fluorescence microscopy. *Nature methods*, 11(3):253–266, 2014.

[113] Akihiro Kusumi, Taka A Tsunoyama, Kohichiro M Hirosawa, Rinshi S Kasai, and Takahiro K Fujiwara. Tracking single molecules at work in living cells. *Nature chemical biology*, 10(7):524–532, 2014.

[114] Dongmyung Oh, Yang Yu, Hochan Lee, Barry L Wanner, and Ken Ritchie. Dynamics of the serine chemoreceptor in the *Escherichia coli* inner membrane: A high-speed single-molecule tracking study. *Biophysical journal*, 106(1):145–153, 2014.

[115] Suliana Manley, Jennifer M Gillette, George H Patterson, Hari Shroff, Harald F Hess, Eric Betzig, and Jennifer Lippincott-Schwartz. High-density mapping of single-molecule trajectories with photoactivated localization microscopy. *Nature methods*, 5(2):155–157, 2008.

[116] Jean-Baptiste Sibarita. High-density single-particle tracking: quantifying molecule organization and dynamics at the nanoscale. *Histochemistry and cell biology*, 141 (6):587–595, 2014.

[117] Jean-Baptiste Masson, Patrice Dionne, Charlotte Salvatico, Marianne Renner, Christian G Specht, Antoine Triller, and Maxime Dahan. Mapping the energy and diffusion landscapes of membrane proteins at the cell surface using high-density single-molecule imaging and bayesian inference: application to the multiscale dynamics of glycine receptors in the neuronal membrane. *Biophysical journal*, 106 (1):74–83, 2014.

[118] Gerhard J Schütz, Gerald Kada, Vassili Ph Pastushenko, and Hansgeorg Schindler. Properties of lipid microdomains in a muscle cell membrane visualized by single molecule microscopy. *The EMBO journal*, 19(5):892–901, 2000.

[119] Osamu Shimomura. The discovery of aequorin and green fluorescent protein. *Journal of microscopy*, 217(1):3–15, 2005.

[120] Ryota Iino, Ikuko Koyama, and Akihiro Kusumi. Single molecule imaging of green fluorescent proteins in living cells: E-cadherin forms oligomers on the free cell surface. *Biophysical journal*, 80(6):2667–2677, 2001.

[121] Gregory S Harms, Laurent Cognet, Piet HM Lommerse, Gerhard A Blab, Heike Kahr, Roland Gamsjäger, Herman P Spaink, Nikolai M Soldatov, Christoph Romanin, and Thomas Schmidt. Single-Molecule Imaging of L-Type Ca^{2+} Channels in Live Cells. *Biophysical journal*, 81(5):2639–2646, 2001.

[122] W Klopper Leutwyler, S Leutwyler Bürgi, H Burgl, et al. Semiconductor clusters, nanocrystals, and quantum dots. *Science*, 271(5251):933–937, 1996.

[123] B O Dabbousi, J Rodriguez-Viejo, Frederic V Mikulec, JR Heine, Hedi Mattoussi, R Ober, K F Jensen, and M G Bawendi. (cdse) zns core-shell quantum dots: synthesis and characterization of a size series of highly luminescent nanocrystallites. *The Journal of Physical Chemistry B*, 101(46):9463–9475, 1997.

[124] M Nirmal, B O Dabbousi, M G Bawendi, J J Macklin, J K Trautman, T D Harris, and LE Brus. Fluorescence intermittency in single cadmium selenide nanocrystals. *Nature*, 383(6603):802–804, 1996.

[125] Peter Reiss, Joël Bleuse, and Adam Pron. Highly luminescent CdSe/ZnSe core/shell nanocrystals of low size dispersion. *Nano letters*, 2(7):781–784, 2002.

[126] Sungchul Hohng and Taekjip Ha. Near-complete suppression of quantum dot blinking in ambient conditions. *Journal of the American Chemical Society*, 126 (5):1324–1325, 2004.

[127] Benoit Mahler, Piernicola Spinicelli, Stephanie Buil, Xavier Quelin, Jean-Pierre Hermier, and Benoit Dubertret. Towards non-blinking colloidal quantum dots. *Nature materials*, 7(8):659–664, 2008.

[128] Maxime Dahan, Sabine Levi, Camilla Luccardini, Philippe Rostaing, Beatrice Riveau, and Antoine Triller. Diffusion dynamics of glycine receptors revealed by single-quantum dot tracking. *Science*, 302(5644):442–445, 2003.

[129] Alyona Sukhanova, Jérôme Devy, Lydie Venteo, Hervé Kaplan, Mikhail Artemyev, Vladimir Oleinikov, Dmitry Klinov, Michel Pluot, Jacques H M Cohen, and Igor Nabiev. Biocompatible fluorescent nanocrystals for immunolabeling of membrane proteins and cells. *Analytical biochemistry*, 324(1):60–67, 2004.

[130] Diane S Lidke, Peter Nagy, Rainer Heintzmann, Donna J Arndt-Jovin, Janine N Post, Hernan E Grecco, Elizabeth A Jares-Erijman, and Thomas M Jovin. Quantum dot ligands provide new insights into erbB/HER receptor–mediated signal transduction. *Nature biotechnology*, 22(2):198–203, 2004.

[131] Emmanuel Beaurepaire, Valérie Buissette, Martin-Pierre Sauviat, Domitille Giaume, Khalid Lahlil, Antoine Mercuri, Didier Casanova, Arnaud Huignard, Jean-Louis Martin, Thierry Gacoin, et al. Functionalized fluorescent oxide nanoparticles: artificial toxins for sodium channel targeting and imaging at the single-molecule level. *Nano Letters*, 4(11):2079–2083, 2004.

[132] J-B Masson, Didier Casanova, Silvan Türkcan, G Voisinne, Michel-Robert Popoff, Massimo Vergassola, and Antigoni Alexandrou. Inferring maps of forces inside cell membrane microdomains. *Physical review letters*, 102(4):048103, 2009.

[133] Silvan Türkcan, Jean-Baptiste Masson, Didier Casanova, Geneviève Mialon, Thierry Gacoin, Jean-Pierre Boilot, Michel R Popoff, and Antigoni Alexandrou. Observing the Confinement Potential of Bacterial Pore-Forming Toxin Receptors

Inside Rafts with Nonblinking Eu^{3+}-Doped Oxide Nanoparticles. *Biophysical journal*, 102(10):2299–2308, 2012.

[134] Didier Casanova, Domitille Giaume, Mélanie Moreau, Jean-Louis Martin, Thierry Gacoin, Jean-Pierre Boilot, and Antigoni Alexandrou. Counting the number of proteins coupled to single nanoparticles. *Journal of the American Chemical Society*, 129(42):12592–12593, 2007.

[135] Carol J Cogswell. Imaging immunogold labels with confocal microscopy. In *Handbook of Biological Confocal Microscopy*, pages 507–513. Springer, 1995.

[136] Frédéric Daumas, Honoré Mazarguil, Claire Millot, André Lopez, and Laurence Salomé. Probing functionalized gold colloids for single particle tracking experiments. *Biochemical and biophysical research communications*, 295(3):610–615, 2002.

[137] Akihiro Kusumi, Hiroshi Ike, Chieko Nakada, Kotono Murase, and Takahiro Fujiwara. Single-molecule tracking of membrane molecules: plasma membrane compartmentalization and dynamic assembly of raft-philic signaling molecules. In *Seminars in immunology*, volume 17, pages 3–21. Elsevier, 2005.

[138] Stéphane Berciaud, Laurent Cognet, Gerhard A Blab, and Brahim Lounis. Photothermal heterodyne imaging of individual nonfluorescent nanoclusters and nanocrystals. *Physical review letters*, 93(25):257402, 2004.

[139] David Lasne, Gerhard A Blab, Stéphane Berciaud, Martin Heine, Laurent Groc, Daniel Choquet, Laurent Cognet, and Brahim Lounis. Single nanoparticle photothermal tracking (SNaPT) of 5-nm gold beads in live cells. *Biophysical journal*, 91(12):4598–4604, 2006.

[140] YL Wang, John D Silverman, and Long-guang Cao. Single particle tracking of surface receptor movement during cell division. *The Journal of cell biology*, 127 (4):963–971, 1994.

[141] Patricia R Smith, Ian EG Morrison, Keith M Wilson, Nelson Fernandez, and Richard J Cherry. Anomalous diffusion of major histocompatibility complex class I molecules on HeLa cells determined by single particle tracking. *Biophysical journal*, 76(6):3331–3344, 1999.

[142] H Pin Kao and A S Verkman. Tracking of single fluorescent particles in three dimensions: use of cylindrical optics to encode particle position. *Biophysical journal*, 67(3):1291–1300, 1994.

[143] Lene Oddershede, Jakob Kisbye Dreyer, Sonia Grego, Stanley Brown, and Kirstine Berg-Sørensen. The Motion of a Single Molecule, the λ-Receptor, in the Bacterial Outer Membrane. *Biophysical journal*, 83(6):3152–3161, 2002.

[144] Domitille Giaume, Mélanie Poggi, Didier Casanova, Genevieve Mialon, Khalid Lahlil, Antigoni Alexandrou, Thierry Gacoin, and Jean-Pierre Boilot. Organic functionalization of luminescent oxide nanoparticles toward their application as biological probes. *Langmuir*, 24(19):11018–11026, 2008.

[145] Arnaud Huignard, Thierry Gacoin, and Jean-Pierre Boilot. Synthesis and luminescence properties of colloidal YVO_4:Eu phosphors. *Chemistry of materials*, 12 (4):1090–1094, 2000.

[146] Hellen C Ishikawa-Ankerhold, Richard Ankerhold, and Gregor PC Drummen. Advanced fluorescence microscopy techniques—FRAP, FLIP, FLAP, FRET and FLIM. *Molecules*, 17(4):4047–4132, 2012.

[147] Khuloud Jaqaman, Dinah Loerke, Marcel Mettlen, Hirotaka Kuwata, Sergio Grinstein, Sandra L Schmid, and Gaudenz Danuser. Robust single-particle tracking in live-cell time-lapse sequences. *Nature methods*, 5(8):695–702, 2008.

[148] Silvan Türkcan. *Investigation of Cell Membrane Architecture by Single-Molecule Tracking of Peptidic Toxins*. PhD thesis, Ecole Polytechnique, 2010.

[149] Didier Casanova. *Nanoparticule d'oxyde: développements et applications comme sondes biologiques*. PhD thesis, Ecole Polytechnique, 2008.

[150] Russell E Thompson, Daniel R Larson, and Watt W Webb. Precise nanometer localization analysis for individual fluorescent probes. *Biophysical journal*, 82(5): 2775–2783, 2002.

[151] Michael J Saxton. Single-particle tracking: models of directed transport. *Biophysical journal*, 67(5):2110–2119, 1994.

[152] Michael J Saxton. Single-particle tracking: effects of corrals. *Biophysical journal*, 69(2):389–398, 1995.

[153] Vishaal Rajani, Gustavo Carrero, David E Golan, Gerda de Vries, and Christopher W Cairo. Analysis of molecular diffusion by first-passage time variance identifies the size of confinement zones. *Biophysical journal*, 100(6):1463–1472, 2011.

[154] S Condamin, V Tejedor, R Voituriez, O Bénichou, and J Klafter. Probing microscopic origins of confined subdiffusion by first-passage observables. *Proceedings of the National Academy of Sciences*, 105(15):5675–5680, 2008.

[155] Michael J Saxton. Lateral diffusion in an archipelago. Single-particle diffusion. *Biophysical journal*, 64(6):1766–1780, 1993.

[156] Vincent Tejedor, Olivier Bénichou, Raphael Voituriez, Ralf Jungmann, Friedrich Simmel, Christine Selhuber-Unkel, Lene B Oddershede, and Ralf Metzler. Quantitative analysis of single-particle trajectories: mean maximal excursion method. *Biophysical journal*, 98(7):1364–1372, 2010.

[157] Fredrik Persson, Martin Lindén, Cecilia Unoson, and Johan Elf. Extracting intracellular diffusive states and transition rates from single-molecule tracking data. *Nature methods*, 10(3):265–269, 2013.

[158] Raibatak Das, Christopher W Cairo, and Daniel Coombs. A hidden Markov model for single particle tracks quantifies dynamic interactions between LFA-1 and the actin cytoskeleton. *PLoS computational biology*, 5(11):e1000556, 2009.

[159] Brian R Long and Tania Q Vu. Spatial structure and diffusive dynamics from single-particle trajectories using spline analysis. *Biophysical journal*, 98(8):1712–1721, 2010.

[160] Cédric Bouzigues and Maxime Dahan. Transient Directed Motions of $GABA_A$ Receptors in Growth Cones Detected by a Speed Correlation Index. *Biophysical journal*, 92(2):654–660, 2007.

[161] Silvan Türkcan, Antigoni Alexandrou, and Jean-Baptiste Masson. A Bayesian inference scheme to extract diffusivity and potential fields from confined single-molecule trajectories. *Biophysical journal*, 102(10):2288–2298, 2012.

[162] Marian Von Smoluchowski. Zur kinetischen Theorie der Brownschen Molekularbewegung und der Suspensionen. *Annalen der physik*, 326(14):756–780, 1906.

[163] Hannes Risken. The Fokker-Planck Equation. Methods of Solution and Applications, vol. 18 of. *Springer Series in Synergetics*, 1989.

[164] Guillaume Voisinne, Antigoni Alexandrou, and Jean-Baptiste Masson. Quantifying biomolecule diffusivity using an optimal bayesian method. *Biophysical journal*, 98 (4):596–605, 2010.

[165] Mohamed El Beheiry, Maxime Dahan, and Jean-Baptiste Masson. InferenceMAP: Whole-cell Mapping of Single-Molecule Dynamics with Bayesian Inference. *(Submitted)*.

[166] Maximilian U Richly, Silvan Türkcan, Antoine Le Gall, Nicolas Fiszman, Jean-Baptiste Masson, Nathalie Westbrook, Karen Perronet, and Antigoni Alexandrou. Calibrating optical tweezers with Bayesian inference. *Optics express*, 21(25):31578–31590, 2013.

[167] Arthur Ashkin, J M Dziedzic, J E Bjorkholm, and Steven Chu. Observation of a single-beam gradient force optical trap for dielectric particles. *Optics letters*, 11 (5):288–290, 1986.

[168] David G Grier. A revolution in optical manipulation. *Nature*, 424(6950):810–816, 2003.

[169] Keir C Neuman and Steven M Block. Optical trapping. *Review of scientific instruments*, 75(9):2787–2809, 2004.

[170] Michelle D Wang, Hong Yin, Robert Landick, Jeff Gelles, and Steven M Block. Stretching DNA with optical tweezers. *Biophysical journal*, 72(3):1335–1346, 1997.

[171] Peter Gross, Niels Laurens, Lene B Oddershede, Ulrich Bockelmann, Erwin J G Peterman, and Gijs J L Wuite. Quantifying how DNA stretches, melts and changes twist under tension. *Nature Physics*, 7(9):731–736, 2011.

[172] U Bockelmann, Ph Thomen, B Essevaz-Roulet, V Viasnoff, and F Heslot. Unzipping dna with optical tweezers: high sequence sensitivity and force flips. *Biophysical journal*, 82(3):1537–1553, 2002.

[173] Steven B Smith, Yujia Cui, and Carlos Bustamante. Overstretching B-DNA: the elastic response of individual double-stranded and single-stranded DNA molecules. *Science*, 271(5250):795–799, 1996.

[174] Steven M Block, Lawrence S B Goldstein, and Bruce J Schnapp. Bead movement by single kinesin molecules studied with optical tweezers. 1990.

[175] Scot C Kuo and Michael P Sheetz. Force of single kinesin molecules measured with optical tweezers. *Science*, 260(5105):232–234, 1993.

[176] Karel Svoboda and Steven M Block. Force and velocity measured for single kinesin molecules. *Cell*, 77(5):773–784, 1994.

[177] Amit D Mehta, Ronald S Rock, Matthias Rief, James A Spudich, Mark S Mooseker, and Richard E Cheney. Myosin-V is a processive actin-based motor. *Nature*, 400(6744):590–593, 1999.

[178] Claudia Veigel and Christoph F Schmidt. Moving into the cell: single-molecule studies of molecular motors in complex environments. *Nature Reviews Molecular Cell Biology*, 12(3):163–176, 2011.

[179] Nick J Carter and R A Cross. Mechanics of the Kinesin step. *Nature*, 435(7040): 308–312, 2005.

[180] Ahmet Yildiz, Michio Tomishige, Arne Gennerich, and Ronald D Vale. Intramolecular strain coordinates kinesin stepping behavior along microtubules. *Cell*, 134(6): 1030–1041, 2008.

[181] Alessandro Borgia, Philip M Williams, and Jane Clarke. Single-molecule studies of protein folding. *Annu. Rev. Biochem.*, 77:101–125, 2008.

[182] Ciro Cecconi, Elizabeth A Shank, Carlos Bustamante, and Susan Marqusee. Direct observation of the three-state folding of a single protein molecule. *Science*, 309 (5743):2057–2060, 2005.

[183] Miklós S Z Kellermayer, Steven B Smith, Henk L Granzier, and Carlos Bustamante. Folding-unfolding transitions in single titin molecules characterized with laser tweezers. *Science*, 276(5315):1112–1116, 1997.

[184] Josep Mas, Andrew C Richardson, S Nader S Reihani, Lene B Oddershede, and Kirstine Berg-Sørensen. Quantitative determination of optical trapping strength and viscoelastic moduli inside living cells. *Physical biology*, 10(4):046006, 2013.

[185] Min-Cheng Zhong, Xun-Bin Wei, Jin-Hua Zhou, Zi-Qiang Wang, and Yin-Mei Li. Trapping red blood cells in living animals using optical tweezers. *Nature communications*, 4:1768, 2013.

[186] Jeffrey R Moffitt, Yann R Chemla, Steven B Smith, and Carlos Bustamante. Recent advances in optical tweezers. *Biochemistry*, 77(1):205, 2008.

[187] Jaime Castillo-León, Winnie Edith Svendsen, and Maria Dimaki. *Micro and nano techniques for the handling of biological samples*. CRC Press, 2011.

[188] Iwijn De Vlaminck and Cees Dekker. Recent advances in magnetic tweezers. *Annual review of biophysics*, 41:453–472, 2012.

[189] Jochen Guck, Stefan Schinkinger, Bryan Lincoln, Falk Wottawah, Susanne Ebert, Maren Romeyke, Dominik Lenz, Harold M Erickson, Revathi Ananthakrishnan, Daniel Mitchell, et al. Optical deformability as an inherent cell marker for testing malignant transformation and metastatic competence. *Biophysical journal*, 88(5): 3689–3698, 2005.

[190] Koen Visscher, Steven P Gross, and Steven M Block. Construction of multiple-beam optical traps with nanometer-resolution position sensing. *Selected Topics in Quantum Electronics, IEEE Journal of*, 2(4):1066–1076, 1996.

[191] Yann von Hansen, Alexander Mehlich, Benjamin Pelz, Matthias Rief, and Roland R Netz. Auto-and cross-power spectral analysis of dual trap optical tweezer experiments using bayesian inference. *Review of Scientific Instruments*, 83(9): 095116, 2012.

[192] Koen Visscher, Mark J Schnitzer, and Steven M Block. Single kinesin molecules studied with a molecular force clamp. *Nature*, 400(6740):184–189, 1999.

[193] Matthew J Lang, Charles L Asbury, Joshua W Shaevitz, and Steven M Block. An automated two-dimensional optical force clamp for single molecule studies. *Biophysical journal*, 83(1):491–501, 2002.

[194] Kirstine Berg-Sørensen and Henrik Flyvbjerg. Power spectrum analysis for optical tweezers. *Review of Scientific Instruments*, 75(3):594–612, 2004.

[195] Karel Svoboda and Steven M Block. Biological applications of optical forces. *Annual review of biophysics and biomolecular structure*, 23(1):247–285, 1994.

[196] Antoine Le Gall, Karen Perronet, David Dulin, André Villing, Philippe Bouyer, Koen Visscher, and Nathalie Westbrook. Simultaneous calibration of optical tweezers spring constant and position detector response. *Optics express*, 18(25):26469–26474, 2010.

[197] Zan Gong, Zhong Wang, Yinmei Li, Liren Lou, and Shenghua Xu. Axial deviation of an optically trapped particle in trapping force calibration using the drag force method. *Optics communications*, 273(1):37–42, 2007.

[198] A Ashkin, Karin Schütze, J M Dziedzic, Ursula Euteneuer, and Manfred Schliwa. Force generation of organelle transport measured in vivo by an infrared laser trap. *Nature*, 348:346–348, 1990.

[199] Steven M Block, David F Blair, and Howard C Berg. Compliance of bacterial flagella measured with optical tweezers. *Nature*, 338:514–518, 1989.

[200] N Malagnino, G Pesce, A Sasso, and E Arimondo. Measurements of trapping efficiency and stiffness in optical tweezers. *Optics Communications*, 214(1):15–24, 2002.

[201] Iva Marija Tolić-Nørrelykke, Kirstine Berg-Sørensen, and Henrik Flyvbjerg. Matlab program for precision calibration of optical tweezers. *Computer physics communications*, 159(3):225–240, 2004.

[202] Poul Martin Hansen, Iva Marija Tolić-Nørrelykke, Henrik Flyvbjerg, and Kirstine Berg-Sørensen. tweezercalib 2.0: Faster version of MatLab package for precise calibration of optical tweezers. *Computer physics communications*, 174(6):518–520, 2006.

[203] Silvan Türkcan, Maximilian U Richly, Antigoni Alexandrou, and Jean-Baptiste Masson. Probing membrane protein interactions with their lipid raft environment using single-molecule tracking and Bayesian inference analysis. *PloS one*, 8(1): e53073, 2013.

[204] Erik Schäffer, Simon F Nørrelykke, and Jonathon Howard. Surface forces and drag coefficients of microspheres near a plane surface measured with optical tweezers. *Langmuir*, 23(7):3654–3665, 2007.

[205] Hilding Faxén. Der Widerstand gegen die Bewegung einer starren Kugel in einer zähen Flüssigkeit, die zwischen zwei parallelen ebenen Wänden eingeschlossen ist. *Annalen der Physik*, 373(10):89–119, 1922.

[206] Karen C Vermeulen, Gijs J L Wuite, Ger J M Stienen, and Christoph F Schmidt. Optical trap stiffness in the presence and absence of spherical aberrations. *Applied optics*, 45(8):1812–1819, 2006.

[207] Shinj Sato, Y Ogawa, M Ohyumi, H Shibata, and H Inaba. Optical trapping of small particles using a 1.3-μm compact InGaAsP diode laser. *Optics letters*, 16 (5):282–284, 1991.

[208] Ye Li, Vassiliy Lubchenko, and Peter G Vekilov. The use of dynamic light scattering and brownian microscopy to characterize protein aggregation. *Review of Scientific Instruments*, 82(5):053106, 2011.

[209] Charlie Gosse and Vincent Croquette. Magnetic tweezers: micromanipulation and force measurement at the molecular level. *Biophysical journal*, 82(6):3314–3329, 2002.

[210] Kurt D Wulff, Daniel G Cole, Robert L Clark, Roberto DiLeonardo, Jonathan Leach, Jon Cooper, Graham Gibson, and Miles J Padgett. Aberration correction in holographic optical tweezers. *Optics express*, 14(9):4169–4174, 2006.

[211] Andrew Callum Richardson, S Nader S Reihani, and Lene Broeng Oddershede. Non-harmonic potential of a single beam optical trap. *Optics express*, 16(20): 15709–15717, 2008.

[212] Silvan Türkcan, Maximilian U Richly, Cedric I Bouzigues, Jean-Marc Allain, and Antigoni Alexandrou. Receptor displacement in the cell membrane by hydrodynamic force amplification through nanoparticles. *Biophysical journal*, 105(1): 116–126, 2013.

[213] Ambrose R Cole, Maryse Gibert, Michel Popoff, David S Moss, Richard W Titball, and Ajit K Basak. *Clostridium perfringens* epsilon-toxin shows structural similarity to the pore-forming toxin aerolysin. *Nature structural & molecular biology*, 11 (8):797–798, 2004.

[214] Laetitia Petit, Maryse Gibert, Daniel Gillet, Christine Laurent-Winter, Patrice Boquet, and Michel R Popoff. *Clostridium perfringens* epsilon-toxin acts on MDCK cells by forming a large membrane complex. *Journal of bacteriology*, 179(20): 6480–6487, 1997.

[215] Susan E Ivie, Christine M Fennessey, Jinsong Sheng, Donald H Rubin, and Mark S McClain. Gene-trap mutagenesis identifies mammalian genes contributing to intoxication by Clostridium perfringens ε-toxin. *PLoS One*, 6(3):e17787, 2011.

[216] Hilde A Rinia, Margot ME Snel, Jan PJM van der Eerden, and Ben de Kruijff. Visualizing detergent resistant domains in model membranes with atomic force microscopy. *FEBS letters*, 501(1):92–96, 2001.

[217] Silvan Türkcan and Jean-Baptiste Masson. Bayesian decision tree for the classification of the mode of motion in single-molecule trajectories. *PloS one*, 8(12): e82799, 2013.

[218] Yasushi Sako and Akihiro Kusumi. Compartmentalized structure of the plasma membrane for receptor movements as revealed by a nanometer-level motion analysis. *The Journal of cell biology*, 125(6):1251–1264, 1994.

[219] Jonatan Dorca-Arévalo, Mireia Martín-Satué, and Juan Blasi. Characterization of the high affinity binding of epsilon toxin from *Clostridium perfringens* to the renal system. *Veterinary microbiology*, 157(1):179–189, 2012.

[220] Thomas M Cover and Joy A Thomas. *Elements of information theory*. John Wiley & Sons, 2012.

[221] Cécile Leduc, Otger Campàs, Konstantin B Zeldovich, Aurélien Roux, Pascale Jolimaitre, Line Bourel-Bonnet, Bruno Goud, Jean-François Joanny, Patricia Bassereau, and Jacques Prost. Cooperative extraction of membrane nanotubes by molecular motors. *Proceedings of the National Academy of Sciences of the United States of America*, 101(49):17096–17101, 2004.

[222] J Antoinette Killian. Hydrophobic mismatch between proteins and lipids in membranes. *Biochimica et Biophysica Acta (BBA)-Reviews on Biomembranes*, 1376 (3):401–416, 1998.

[223] Olaf S Andersen and Roger E Koeppe. Bilayer thickness and membrane protein function: an energetic perspective. *Annu. Rev. Biophys. Biomol. Struct.*, 36:107–130, 2007.

[224] Nancy J Lane. Microvilli on the external surfaces of gastropod tentacles and body-walls. *Quarterly Journal of Microscopical Science*, 3(68):495–504, 1963.

[225] T M Mukherjee and A Wynn Williams. A comparative study of the ultrastructure of microvilli in the epithelium of small and large intestine of mice. *The Journal of cell biology*, 34(2):447–461, 1967.

[226] Junichi Ikenouchi, Megumi Hirata, Shigenobu Yonemura, and Masato Umeda. Sphingomyelin clustering is essential for the formation of microvilli. *Journal of cell science*, 126(16):3585–3592, 2013.

[227] Kate Poole, Doris Meder, Kai Simons, and Daniel Müller. The effect of raft lipid depletion on microvilli formation in MDCK cells, visualized by atomic force microscopy. *FEBS letters*, 565(1):53–58, 2004.

[228] Yasuhiro M Umemura, Marija Vrljic, Stefanie Y Nishimura, Takahiro K Fujiwara, Kenichi G N Suzuki, and Akihiro Kusumi. Both MHC class II and its GPI-anchored form undergo hop diffusion as observed by single-molecule tracking. *Biophysical journal*, 95(1):435–450, 2008.

[229] Michio Tomishige and Akihiro Kusumi. Compartmentalization of the erythrocyte membrane by the membrane skeleton: intercompartmental hop diffusion of band 3. *Molecular biology of the cell*, 10(8):2475–2479, 1999.

[230] Yasushi Sako and Akihiro Kusumi. Barriers for lateral diffusion of transferrin receptor in the plasma membrane as characterized by receptor dragging by laser tweezers: fence versus tether. *The Journal of cell biology*, 129(6):1559–1574, 1995.

[231] Gideon Schwarz et al. Estimating the dimension of a model. *The annals of statistics*, 6(2):461–464, 1978.

[232] Kenneth P Burnham and David R Anderson. Multimodel inference understanding AIC and BIC in model selection. *Sociological methods & research*, 33(2):261–304, 2004.

[233] Nicolas Destainville and Laurence Salomé. Quantification and correction of systematic errors due to detector time-averaging in single-molecule tracking experiments. *Biophysical journal*, 90(2):L17–L19, 2006.

[234] Laurens Van der Maaten and Geoffrey Hinton. Visualizing data using t-SNE. *Journal of Machine Learning Research*, 9(2579-2605):85, 2008.

[235] Carl Lamanna. The Most Poisonous Poison: What do we know about the toxin of botulism? What are the problems to be solved? *Science*, 130(3378):763–772, 1959.

[236] D Michael Gill. Bacterial toxins: a table of lethal amounts. *Microbiological Reviews*, 46(1):86, 1982.

[237] CL Hatheway. Botulism: the present status of the disease. In *Clostridial Neurotoxins*, pages 55–75. Springer, 1995.

[238] Jeremy Sobel. Botulism. *Clinical Infectious Diseases*, 41(8):1167–1173, 2005.

[239] Lance L Simpson. Identification of the major steps in botulinum toxin action. *Annu. Rev. Pharmacol. Toxicol.*, 44:167–193, 2004.

[240] Andrew B Maksymowych and Lance L Simpson. Binding and transcytosis of botulinum neurotoxin by polarized human colon carcinoma cells. *Journal of Biological Chemistry*, 273(34):21950–21957, 1998.

[241] Jong-Beak Park and Lance L Simpson. Inhalational poisoning by botulinum toxin and inhalation vaccination with its heavy-chain component. *Infection and immunity*, 71(3):1147–1154, 2003.

[242] Lance L Simpson. Kinetic studies on the interaction between botulinum toxin type a and the cholinergic neuromuscular junction. *Journal of Pharmacology and Experimental Therapeutics*, 212(1):16–21, 1980.

[243] Yann Humeau, Frédéric Doussau, Nancy J Grant, and Bernard Poulain. How botulinum and tetanus neurotoxins block neurotransmitter release. *Biochimie*, 82 (5):427–446, 2000.

[244] Clifford C Shone, Peter Hambleton, and Jack Melling. Inactivation of Clostridium botulinum type A neurotoxin by trypsin and purification of two tryptic fragments. *European journal of biochemistry*, 151(1):75–82, 1985.

[245] N Yokosawa, Y Kurokawa, K Tsuzuki, B Syuto, N Fujii, K Kimura, and K Oguma. Binding of *Clostridium botulinum* type C neurotoxin to different neuroblastoma cell lines. *Infection and immunity*, 57(1):272–277, 1989.

[246] Clifford C Shone, Peter Hambleton, and Jack Melling. A 50-kDa fragment from the NH2-terminus of the heavy subunit of Clostridium botulinum type A neurotoxin forms channels in lipid vesicles. *European Journal of Biochemistry*, 167(1):175–180, 1987.

[247] Robert O Blaustein, William J Germann, Alan Finkelstein, and Bibhuti R DasGupta. The N-terminal half of the heavy chain of botulinum type A neurotoxin forms channels in planar phospholipid bilayers. *FEBS letters*, 226(1):115–120, 1987.

[248] Ornella Rossetto, Marco Pirazzini, and Cesare Montecucco. Botulinum neurotoxins: genetic, structural and mechanistic insights. *Nature Reviews Microbiology*, 12 (8):535–549, 2014.

[249] S K Sharma and B R Singh. Hemagglutinin binding mediated protection of botulinum neurotoxin from proteolysis. *Journal of natural toxins*, 7(3):239–253, 1998.

[250] Takuhiro Matsumura, Yingji Jin, Yuko Kabumoto, Yuki Takegahara, Keiji Oguma, Wayne I Lencer, and Yukako Fujinaga. The HA proteins of botulinum toxin disrupt intestinal epithelial intercellular junctions to increase toxin absorption. *Cellular microbiology*, 10(2):355–364, 2008.

[251] Shenyan Gu, Sophie Rumpel, Jie Zhou, Jasmin Strotmeier, Hans Bigalke, Kay Perry, Charles B Shoemaker, Andreas Rummel, and Rongsheng Jin. Botulinum neurotoxin is shielded by NTNHA in an interlocked complex. *Science*, 335(6071): 977–981, 2012.

[252] Joseph Jankovic, Kenneth Schwartz, and Donald T Donovan. Botulinum toxin treatment of cranial-cervical dystonia, spasmodic dysphonia, other focal dystonias and hemifacial spasm. *Journal of Neurology, Neurosurgery & Psychiatry*, 53(8): 633–639, 1990.

[253] J S Elston, J P Lee, C M Powell, C Hogg, and P Clark. Treatment of strabismus in adults with botulinum toxin a. *British journal of ophthalmology*, 69(10):718–724, 1985.

[254] Alan B Scott. Botulinum toxin injection of eye muscles to correct strabismus. *Transactions of the American Ophthalmological Society*, 79:734, 1981.

[255] Peter Hambleton. *Clostridium botulinum* toxins: a general review of involvement in disease, structure, mode of action and preparation for clinical use. *Journal of neurology*, 239(1):16–20, 1992.

[256] Edward J Schantz and Eric A Johnson. Properties and use of botulinum toxin and other microbial neurotoxins in medicine. *Microbiological reviews*, 56(1):80–99, 1992.

[257] Joseph Jankovic and M F Brin. Therapeutic uses of botulinum toxin. *The New England journal of medicine*, 324(17):1186, 1991.

[258] Jeffrey L Jackson, Akira Kuriyama, and Yasuaki Hayashino. Botulinum toxin a for prophylactic treatment of migraine and tension headaches in adults: a meta-analysis. *Jama*, 307(16):1736–1745, 2012.

[259] Stephen S Arnon, Robert Schechter, Thomas V Inglesby, Donald A Henderson, John G Bartlett, Michael S Ascher, Edward Eitzen, Anne D Fine, Jerome Hauer, Marcelle Layton, et al. Botulinum toxin as a biological weapon: medical and public health management. *Jama*, 285(8):1059–1070, 2001.

[260] Lance L Simpson. Identification of the characteristics that underlie botulinum toxin potency: implications for designing novel drugs. *Biochimie*, 82(9):943–953, 2000.

[261] Masaru Kitamura, Kogo Takamiya, Shinichi Aizawa, Keiko Furukawa, and Koichi Furukawa. Gangliosides are the binding substances in neural cells for tetanus and botulinum toxins in mice. *Biochimica et Biophysica Acta (BBA)-Molecular and Cell Biology of Lipids*, 1441(1):1–3, 1999.

[262] Roland WM Bullens, Graham M O'Hanlon, Eric Wagner, Peter C Molenaar, Keiko Furukawa, Koichi Furukawa, Jaap J Plomp, and Hugh J Willison. Complex gangliosides at the neuromuscular junction are membrane receptors for autoantibodies and botulinum neurotoxin but redundant for normal synaptic function. *The Journal of neuroscience*, 22(16):6876–6884, 2002.

[263] Brian C Yowler, Richard D Kensinger, and Cara-Lynne Schengrund. Botulinum neurotoxin A activity is dependent upon the presence of specific gangliosides in neuroblastoma cells expressing synaptotagmin I. *Journal of Biological Chemistry*, 277(36):32815–32819, 2002.

[264] Jennifer D Black and J Oliver Dolly. Interaction of 125I-labeled botulinum neurotoxins with nerve terminals. I. Ultrastructural autoradiographic localization and quantitation of distinct membrane acceptors for types A and B on motor nerves. *The Journal of cell biology*, 103(2):521–534, 1986.

[265] Jennifer D Black and J Oliver Dolly. Interaction of 125I-labeled botulinum neurotoxins with nerve terminals. II. Autoradiographic evidence for its uptake into motor nerves by acceptor-mediated endocytosis. *The Journal of cell biology*, 103 (2):535–544, 1986.

[266] Min Dong, Felix Yeh, William H Tepp, Camin Dean, Eric A Johnson, Roger Janz, and Edwin R Chapman. SV2 is the protein receptor for botulinum neurotoxin A. *Science*, 312(5773):592–596, 2006.

[267] Min Dong, David A Richards, Michael C Goodnough, William H Tepp, Eric A Johnson, and Edwin R Chapman. Synaptotagmins I and II mediate entry of botulinum neurotoxin B into cells. *The Journal of cell biology*, 162(7):1293–1303, 2003.

[268] Stefan Mahrhold, Andreas Rummel, Hans Bigalke, Bazbek Davletov, and Thomas Binz. The synaptic vesicle protein 2C mediates the uptake of botulinum neurotoxin A into phrenic nerves. *FEBS letters*, 580(8):2011–2014, 2006.

[269] Gary Matthews. Neurotransmitter release. *Annual review of neuroscience*, 19(1): 219–233, 1996.

[270] W J Betz and J K Angleson. The synaptic vesicle cycle. *Annual review of physiology*, 60(1):347–363, 1998.

[271] James E Keller, Fang Cai, and Elaine A Neale. Uptake of botulinum neurotoxin into cultured neurons. *Biochemistry*, 43(2):526–532, 2004.

[272] Lance L Simpson. The interaction between aminoquinolines and presynaptically acting neurotoxins. *Journal of Pharmacology and Experimental Therapeutics*, 222 (1):43–48, 1982.

[273] Lance L Simpson. Ammonium chloride and methylamine hydrochloride antagonize clostridial neurotoxins. *Journal of Pharmacology and Experimental Therapeutics*, 225(3):546–552, 1983.

[274] Andrew B Maksymowych and Lance L Simpson. Structural features of the botulinum neurotoxin molecule that govern binding and transcytosis across polarized human intestinal epithelial cells. *Journal of Pharmacology and Experimental Therapeutics*, 310(2):633–641, 2004.

[275] Aurélie Couesnon, Yannick Pereira, and Michel R Popoff. Receptor-mediated transcytosis of botulinum neurotoxin A through intestinal cell monolayers. *Cellular microbiology*, 10(2):375–387, 2008.

[276] Aurélie Couesnon, Takeshi Shimizu, and Michel R Popoff. Differential entry of botulinum neurotoxin A into neuronal and intestinal cells. *Cellular microbiology*, 11(2):289–308, 2009.

[277] Aurélie Couesnon, Jordi Molgó, Chloé Connan, and Michel R Popoff. Preferential entry of botulinum neurotoxin A Hc domain through intestinal crypt cells and targeting to cholinergic neurons of the mouse intestine. *PLoS pathogens*, 8(3): e1002583, 2012.

[278] Yukako Fujinaga, Kaoru Inoue, Sadahiro Watanabe, Kenji Yokota, Yoshikazu Hirai, Eiko Nagamachi, and Keiji Oguma. The haemagglutinin of *Clostridium botulinum* type C progenitor toxin plays an essential role in binding of toxin to the epithelial cells of guinea pig small intestine, leading to the efficient absorption of the toxin. *Microbiology*, 143(12):3841–3847, 1997.

[279] Yukako Fujinaga, Kaoru Inoue, Takako Nomura, Junzo Sasaki, Jean C Marvaud, Michel R Popoff, Shunji Kozaki, and Keiji Oguma. Identification and characterization of functional subunits of *Clostridium botulinum* type A progenitor toxin involved in binding to intestinal microvilli and erythrocytes. *FEBS letters*, 467(2): 179–183, 2000.

[280] Chowdhury R Ahsan, György Hajnóczky, Andrew B Maksymowych, and Lance L Simpson. Visualization of binding and transcytosis of botulinum toxin by human intestinal epithelial cells. *Journal of Pharmacology and Experimental Therapeutics*, 315(3):1028–1035, 2005.

[281] Tina I Lam, Larry H Stanker, Kwangkook Lee, Rongsheng Jin, and Luisa W Cheng. Translocation of botulinum neurotoxin serotype A and associated proteins across the intestinal epithelia. *Cellular Microbiology*, 2015.

[282] Lance Simpson. The life history of a botulinum toxin molecule. *Toxicon*, 68:40–59, 2013.

[283] Laurent Holtzer, Tobias Meckel, and Thomas Schmidt. Nanometric three-dimensional tracking of individual quantum dots in cells. *Applied physics letters*, 90(5):053902, 2007.

[284] Ignacio Izeddin, Mohamed El Beheiry, Jordi Andilla, Daniel Ciepielewski, Xavier Darzacq, and Maxime Dahan. PSF shaping using adaptive optics for three-dimensional single-molecule super-resolution imaging and tracking. *Optics express*, 20(5):4957–4967, 2012.

[285] Inge M Peters, Yvette van Kooyk, Sandra J van Vliet, Bart G de Grooth, Carl G Figdor, and Jan Greve. 3D single-particle tracking and optical trap measurements on adhesion proteins. *Cytometry*, 36(3):189–194, 1999.

[286] A Pralle, M Prummer, Ernst-Ludwig Florin, E H K Stelzer, J K H Hörber, et al. Three-dimensional high-resolution particle tracking for optical tweezers by forward scattered light. *Microscopy research and technique*, 44(5):378–386, 1999.

[287] Nathan P Wells, Guillaume A Lessard, Peter M Goodwin, Mary E Phipps, Patrick J Cutler, Diane S Lidke, Bridget S Wilson, and James H Werner. Time-resolved three-dimensional molecular tracking in live cells. *Nano letters*, 10(11): 4732–4737, 2010.

[288] Yujie Sun, Jennine Dawicki McKenna, John M Murray, E Michael Ostap, and Yale E Goldman. Parallax: high accuracy three-dimensional single molecule tracking using split images. *Nano letters*, 9(7):2676–2682, 2009.

[289] Erdal Toprak, Hamza Balci, Benjamin H Blehm, and Paul R Selvin. Three-dimensional particle tracking via bifocal imaging. *Nano letters*, 7(7):2043–2045, 2007.

[290] Sripad Ram, Dongyoung Kim, Raimund J Ober, and E Sally Ward. 3D single molecule tracking with multifocal plane microscopy reveals rapid intercellular transferrin transport at epithelial cell barriers. *Biophysical journal*, 103(7):1594–1603, 2012.

[291] Sara Abrahamsson, Jiji Chen, Bassam Hajj, Sjoerd Stallinga, Alexander Y Katsov, Jan Wisniewski, Gaku Mizuguchi, Pierre Soule, Florian Mueller, Claire Dugast Darzacq, et al. Fast multicolor 3D imaging using aberration-corrected multifocus microscopy. *Nature methods*, 10(1):60–63, 2013.

[292] Valeria Levi, QiaoQiao Ruan, and Enrico Gratton. 3-D particle tracking in a two-photon microscope: application to the study of molecular dynamics in cells. *Biophysical journal*, 88(4):2919–2928, 2005.

[293] Chloé Connan. *Neurotoxinogénèse et Passage des Neurotoxines botuliques à travers la Barrière Intestinale*. PhD thesis, Université Paris Sud, 2013.

[294] Melina Schuh. An actin-dependent mechanism for long-range vesicle transport. *Nature cell biology*, 13(12):1431–1436, 2011.

[295] Nobutaka Hirokawa. Kinesin and dynein superfamily proteins and the mechanism of organelle transport. *Science*, 279(5350):519–526, 1998.

[296] Kevin M McCarthy, Yinlee Yoong, and Neil E Simister. Bidirectional transcytosis of igg by the rat neonatal fc receptor expressed in a rat kidney cell line: a system to study protein transport across epithelia. *Journal of Cell Science*, 113(7):1277–1285, 2000.

[297] Erik Lindahl and Mark SP Sansom. Membrane proteins: molecular dynamics simulations. *Current opinion in structural biology*, 18(4):425–431, 2008.

[298] Daniel L Parton, Jochen W Klingelhoefer, and Mark S P Sansom. Aggregation of model membrane proteins, modulated by hydrophobic mismatch, membrane curvature, and protein class. *Biophysical journal*, 101(3):691–699, 2011.

[299] Naoki Watanabe and Timothy J Mitchison. Single-molecule speckle analysis of actin filament turnover in lamellipodia. *Science*, 295(5557):1083–1086, 2002.

[300] Anil K Jain. Data clustering: 50 years beyond k-means. *Pattern recognition letters*, 31(8):651–666, 2010.

[301] Geoffrey E Hinton and Sam T Roweis. Stochastic neighbor embedding. In *Advances in neural information processing systems*, pages 833–840, 2002.

Abstract

La membrane cellulaire est l'interface de communication et d'échange entre la cellule et le monde extérieur. En tant que telle, sa structure et composition ont une importance centrale à la viabilité de la cellule. Les protéines qui résident dans la membrane apportent la fonctionnalité nécessaire pour permettre à la membrane d'accomplir ces tâches. Ces récepteurs se retrouvent dans un environnement de haute hétérogénéité qui renforce leur efficacité. Nous avons étudié cet environnent en suivant des récepteurs uniques dans la membrane grâce aux nanoparticules dopées aux terres rares. Ces nanoparticules produisent des signaux continus, non-interrompus, permettant de suivre des trajectoires pendant plusieurs minutes. Nous avons ensuite utilisé une méthode basée sur l'inférence bayésienne pour analyser et comparer les trajectoires obtenues, et pour extraire le potentiel de confinement de forme arbitraire correspondant à chaque trajectoire.

Nous avons d'abord validé l'approche de l'inférence bayésienne en démontrant que cette méthode peut également être utilisée pour la calibration d'un montage de pinces optiques. Par ailleurs, nous avons démontré que cette approche est supérieure aux techniques couramment utilisées pour la calibration des pinces optiques. Puis, nous avons appliqué cette méthode aux trajectoires des récepteurs de la toxine ε (de *Clostridium perfringens*) dans des cellules rénales canines Madin-Darby (MDCK). En particulier, nous avons étudié l'évolution du potentiel de confinement et de la diffusivité à l'intérieur des domaines confinant les récepteurs pendant l'action d'un agent déstabilisant les domaines de confinement, ainsi que les événement de 'hopping' pendant lesquels le récepteur change de domaine de confinement, et déterminé les énergies de 'hopping' associées. De plus, nous avons observé l'effet d'une force externe appliquée au récepteur, produite par un flux hydrodynamique. L'application d'une force a mis en évidence une dépendance du confinement des récepteurs du cytosquelette d'actine en plus du confinement produit par la distribution des lipides.

Pour approfondir notre investigation du confinement des récepteurs de la membrane, nous avons classifié les potentiels de confinement obtenus pour les récepteurs résidant à l'intérieur et à l'extérieur des radeaux lipidiques. Les potentiels ressentis par les récepteurs en dehors des domaines lipidiques sont plus plats au centre du domaine de confinement et plus abrupts vers les bords du domaine par rapport aux potentiels ressentis par les protéines dans les radeaux.

Enfin, nous avons étendu la technique de suivi de particules uniques en 3D en utilisant la largeur de la fonction de réponse du signal de la nanoparticule. De cette manière, nous avons observé le mouvement d'internalisation de nanoparticules couplées à un fragment de la chaine lourde de la toxine botulique A de *Clostridium botulinum* dans des cellules intestinales de souris de la lignée m-IC_{cl2}.

Mots-clés: Suivi de molécules uniques (SMT), toxines, récepteur, radeaux lipidiques, force hydrodynamique, partitionnement de données, arbre de décision, potentiel de confinement, suivi en 3D

Abstract

The cell membrane is the interface of communication and exchange between the cell and the outside world. As such, its structure and composition is of integral importance to the cell's continued survival. The proteins within the membrane provide the necessary functionalities to the membrane for successfully acting out its role. The membrane receptors experience a highly heterogeneous environment in the cell membrane that enhances their efficiency. We studied this environment via single particle tracking of cell membrane receptors tagged with luminescent lanthanide-doped nanoparticles. The nanoparticles provided a continuous, uninterrupted signal of the movements, yielding trajectories of several minutes. We then used a method based on statistical Bayesian inference to analyse and compare the trajectories obtained and, hence, extract a confinement potential of arbitrary shape.

We first validated the Bayesian inference approach by demonstrating that this method can also be used to calibrate an optical tweezers setup. Furthermore, we showed that this method outperforms established calibration methods for optical traps. We then applied this approach to the confined trajectories of ε–toxin (produced by *Clostridium perfringens*) receptors in Madin-Darby canine kidney cells. In particular, we studied the evolution of the confinement potential and diffusivity within the domains upon addition of domain-destabilizing agents, as well as the occasional 'hopping' events, during which receptors are seen to hop into an adjacent confinement domain, and the associated 'hopping' energies. Additionally, we inquired into the effect of an externally applied force, implemented via a hydrodynamic flow on the receptors, and discovered an actin-dependent confinement of the microdomains in addition to the lipid-dependent confinement.

To further investigate the nature of membrane receptor confinement, we classified the potentials obtained from raft and non-raft proteins using a decision-tree method and a clustering algorithm. The results showed that non-raft proteins reside in domains that produce a steeper potential boundary with a flatter potential in the centre of the domain as compared to raft proteins.

Finally, we extended the single-particle tracking of toxins to three dimensions by registering the width of the point-spread function of the nanoparticle signal. In this way, we were able to observe the internalization trajectory of a heavy-chain segment of the botulinum toxin A of *Clostridium botulinum* in cells of the intestinal mouse cell line m-IC_{cl2}.

Keywords: Single Molecule Tracking (SMT), Toxins, Receptor, Lipid Rafts, Hydrodynamic Force, Data Clustering, Decision Tree, Confinement Potential, 3D Tracking